

Radio Frequency Atomic Magnetometer for Applications in Magnetic Induction Tomography

Patrick Bevington

National Physical Laboratory

University of Strathclyde

This dissertation is submitted for the degree of

Doctor of Philosophy

Declaration

This thesis is the result of the author's original research. It has been composed by the author and has not been previously submitted for examination which has led to the award of a degree. The copyright of this thesis belongs to the author under the terms of the United Kingdom Copyright Acts as qualified by University of Strathclyde Regulation 3.50. Due acknowledgement must always be made of the use of any material contained in, or derived from, this thesis.

Signed:

Date:

Patrick Bevington

2021

Acknowledgements

I am deeply grateful to all the people who have helped me with this piece of work. Firstly, I want to thank my NPL supervisor Witold Chalupczak for always taking the time to share his knowledge and enthusiasm, and for setting such an admirable pace. Secondly, I am indebted to Rafal Gartman for all the troubleshooting and advice in the lab; our interesting lunchtime conversations were a constant pleasure. To you both – ‘thank you from the mountain’. The example and encouragement from my Strathclyde supervisor, Paul Griffin, made me pursue a PhD in the first place. Thank you for faultless support, both academic and personal – especially at the end.

I owe thanks to all my colleagues, peers and friends for their material help and for making the day-to-day that bit easier. In particular, Rich Hendricks for his invaluable and insightful comments when reviewing my manuscripts; those in the NPL workshop for their speed in machining the samples I examined throughout my PhD; Stuart Ingleby for many stimulating conversations and the interest he’s shown in my work; and Carolyn O’Dwyer for the same, plus her patience in explaining the degree requirements to me.

Thank you to my Dad and Fiona for their enormous, and likely painful, proofreading efforts. This alleviated so much anxiety. Also thanks to my family and friends for all the fun and laughter.

Lastly, I want to thank those most important to me. My parents, for teaching me how to think and nurturing the curiosity that has brought me here. And Fiona, whose love and unwavering support makes everything better. This is for you.

Contents

Contents	vii
1 Introduction	1
2 Theory	5
2.1 Atoms	5
2.1.1 Fine and Hyperfine Structure	6
2.1.2 Zeeman States and Magnetic Sensitivity	9
2.1.2.1 Higher Order Magnetic Field Effects	10
2.1.3 Light shifts	11
2.2 Interaction with Light	12
2.2.1 Pumping	12
2.2.2 Probing	14
2.2.3 Propagation of Light and Complex Refractive Index	14
2.2.4 Birefringence	16
2.3 Atomic Coherences	17
2.4 Relaxation Processes	19
2.4.1 Wall collisions	19
2.4.2 Magnetic Gradients	20
2.4.3 Power Broadening of rf Coherences	21
2.4.4 Collisions	22
2.4.4.1 Spin Exchange Collisions	22
2.4.4.2 Spin Destruction Collisions	23
2.5 Atomic Magnetometer Operation	23

2.5.1	Resonance Lineshape	24
2.5.2	Measurement Limits	25
3	Magnetometer Performance	29
3.1	Laser Configurations	30
3.1.1	Pumping	30
3.1.2	Probing	32
3.1.3	Geometry	32
3.1.3.1	Separate Pump and Probe	32
3.1.3.2	Combined Pump and Probe	33
3.1.3.3	Repump	34
3.1.4	Summary	35
3.2	Two-Beam rf Magnetometer	35
3.2.1	Indirect-Pumping	36
3.2.2	Off-Resonant Probing	39
3.2.2.1	Probe Detuning	39
3.2.2.2	Sign of the Measured Coherence Amplitude	42
3.2.2.3	Probe Power	42
3.2.3	Sensitivity	44
3.2.4	Summary	47
3.3	Orientation with a Single Linearly Polarised Beam	48
3.3.1	Generation of an Oriented State	48
3.3.2	Practical Considerations	52
3.3.2.1	Narrow Feature for Locking Laser Frequency	52
3.3.2.2	Degenerate Pump and Probe	54
3.3.3	Summary	57
3.4	Conclusions	57
4	Experimental Setup	59
4.1	rf Magnetometer	59
4.1.1	Lasers	59
4.1.2	Vapour Cells	63

4.1.3	Detection	63
4.1.4	Measured Signal	63
4.2	Unshielded Operation	65
4.2.1	Experimental Setup	66
4.2.2	Environmental Magnetic Field	66
4.2.2.1	Compensation Coils	66
4.2.2.2	Magnetic Gradients	68
4.2.3	Magnetic Field Compensation in Finite-Sized Cells	70
4.2.3.1	Fluxgate as Source of Error Signal	71
4.2.3.2	Atomic Signal as Source of Error Signal	76
4.3	Shielded Operation	78
5	Magnetic Induction Tomography	81
5.1	Principle of Operation	82
5.1.1	Eddy Currents	82
5.1.2	Local Magnetisation	85
5.2	Secondary Field	86
5.2.1	Generation	87
5.2.2	Signal Response	87
5.2.2.1	Signal's Spatial Characteristics	87
5.2.2.2	Characteristic Signal Response from Ferromagnetic and Non-Ferromagnetic Materials	89
5.3	Sensors	91
5.3.1	Pick-Up Coils	92
5.3.1.1	Introduction	92
5.3.1.2	Operation	92
5.3.1.3	Properties	95
5.3.1.4	Applications for MIT	96
5.3.2	SQUIDs	97
5.3.2.1	Introduction	97
5.3.2.2	Operation	97
5.3.2.3	Properties	98

5.3.2.4	Applications for MIT	98
5.3.3	GMR Sensors	99
5.3.3.1	Introduction	99
5.3.3.2	Operation	99
5.3.3.3	Properties	100
5.3.3.4	Applications for MIT	101
5.3.4	Radio-Frequency Atomic Magnetometer	102
5.3.4.1	Introduction	102
5.3.4.2	Operation	102
5.3.4.3	Properties	103
5.3.4.4	Applications for NDT	104
5.3.5	Advantages and Disadvantages	104
6	Development of Imaging Technique	109
6.1	MIT Measurement Configuration	110
6.1.1	Experimental Setup	110
6.1.2	Signal Acquisition	112
6.1.3	Measurement Time	114
6.2	rf Magnetometer	115
6.2.1	Imaging Configurations	115
6.2.1.1	Normal Configuration	116
6.2.1.2	Primary Field Compensation	118
6.2.1.3	Self-Compensation Configuration	125
6.2.2	rf Compensation Factor	130
6.3	General Considerations of MIT	132
6.3.1	Imaging Resolution	132
6.3.1.1	Sub-mm Resolution	132
6.3.1.2	Lift-off	133
6.3.2	Defect Characterisation	136
6.3.2.1	Defect Depth	136
6.3.2.2	Optimum Operational Frequency	137
6.3.2.3	Defect on Inner Surfaces	141

6.3.2.4	Concealed Defects	144
6.4	Conclusions	147
7	Spin Maser For Defect Detection	149
7.1	Principle of Operation	149
7.1.1	System	149
7.1.2	Phase Matching Condition	151
7.2	Defect Detection	153
7.2.1	Frequency Shift	155
7.3	Dual Frequency Spin Maser	158
7.3.1	Dual Phase Matching Condition	158
7.3.2	Defect Detection	160
7.3.2.1	Active Stabilisation	162
7.4	Conclusions	163
8	Outlook	165
	References	167
A	Instrumentation	183
A.1	Translation Stage	183

List of acronyms and abbreviations

AOM - acousto-optical modulators

Cs - caesium

CW - continuous wave

DBR - distributed Bragg reflector

DFSM - dual frequency spin maser

EC - eddy current

ECT - eddy current testing

EM - electromagnetic

EMF - electromotive force

EOM - electro-optical modulators

FCOPM - flux concentrator optically pumped magnetometer

FFT - fast Fourier transform

FWHM - full width half maximum

GMR - giant magnetoresistance

HFS - hyperfine splitting

MCG - magneto electroencephalography

MEMS - microelectromechanical systems

MIT - magnetic induction tomography

MOSFET - metal–oxide–semiconductor field-effect transistor

MR - magnetoresistive

NDT - non-destructive testing

NLZ - non-linear Zeeman effect

OPM - optically pumped magnetometer

PBS - polarising beam splitter

PD - photodiode

PID - proportional-integral-derivative

PSD - power spectral density

PSU - power supply unit

Rb - rubidium rf radio frequency

SEC - spin exchange collisions

SERF - spin exchange relaxation free

SNL - shot noise limit

SNR - signal to noise ratio

SQUID - super conducting quantum interference device

TC - time constant

VCSEL - vertical cavity surface emitting laser

App. - appendix

Chap. - chapter

Equ. - Equation

Fig. - figure

Sec. - section

Chapter 1

Introduction

This thesis collects and structures the ideas and experiments from the last four years of the author's study, presenting them in a way to build a consistent narrative concerning the application of radio frequency (rf) atomic magnetometers for magnetic induction tomography (MIT). Although the first atomic magnetometers were demonstrated around 70 years ago [1–4], there has recently been a resurgence in their study. This is motivated by their extreme sensitivity ($< \text{fT}/\sqrt{\text{Hz}}$, which surpasses their closest competitor SQUIDs, without the need for cryogenics) and the fact they have become comparatively inexpensive to build, both of which are partly due to the increased availability of narrow band light sources (i.e. lasers). Within the community these sensors are also called optically pumped magnetometers, but this is interchangeable the term atomic magnetometer. This thesis uses 'rf atomic magnetometer' to align with the previous publications of the author and typically it is shortened to 'rf magnetometer'.

MIT is a non-destructive testing (NDT) scheme that utilises a magnetometer to monitor the response of an object that is inductively coupled to an oscillating magnetic field. The advantage of MIT over other NDT schemes is that oscillating magnetic fields penetrate materials, so it is possible to measure a subsurface defect or image through a barrier. Much of the research into atomic magnetometers has been carried out in magnetically shielded environments, but this is impractical for MIT measurements (as shielding is not portable and it is challenging to deliver samples to the sensor); hence, it is crucial to be able to undertake MIT measurements in an open, real-world environment. This thesis shows how to optimise the rf magnetometer for MIT measurements and for operation without magnetic shielding. It also demonstrates the efficacy of rf magnetometers for MIT in several scenarios, which in turn provides insight into the functionalities of the sensor.

This introduction begins with several observations about the motivations behind this thesis and

the work that it reports on. As a whole, the work was focused on the practical development of a sensor and an exploration of a particular application, MIT. The outcomes of this work are a set of ideas designed to increase the performance of the rf magnetometer for this application. As such, the work carried out during this study and the results presented in this thesis are predominantly experimental. This thesis is structured as follows:

- Chapter 2 introduces the most relevant underlying atomic physics theory required to understand the operation of an atomic magnetometer. Since this work is experimental, and since there are already many excellent theoretical descriptions of atomic magnetometers, efforts have been made to present intuitive arguments and descriptions where possible, and provide directions to further reading and explanations where appropriate.
- Chapter 3 describes how the performance of the rf magnetometer is influenced by the action of laser light, with particular attention paid to the number of laser beams used. For most of the thesis, a two-beam configuration is used as it is well studied and facilitates a sensor sensitivity on the order of $1 \text{ fT}/\sqrt{\text{Hz}}$ [5, 6]. The chapter ends by describing a novel laser scheme that operates the rf magnetometer in the same way as the two-beam configuration, but with a single laser, which drastically simplifies the experimental requirements of the sensor and will assist with the future miniaturisation of the setup.
- Chapter 4 details much of the technical details for the experimental setup. In particular, details are given on how the rf magnetometer is operated in an unshielded environment by actively compensating changes in the ambient magnetic field and magnetic field noise generated by mains electricity at 50 Hz.
- Chapter 5 discusses how MIT works and what the system measures. A section of this chapter introduces several other sensors that can be used for MIT. This chapter acts as a literature review of the field and sets the context for why the rf magnetometer is a good candidate for MIT.
- Chapter 6 covers the main topic of this thesis: the results of MIT with an rf magnetometer. The chapter is split into two sections, one that deals with issues specific to the use of the rf magnetometer, and the other covering more general topics concerning MIT.
- Chapter 7 introduces a mode of operation for the rf magnetometer, called the spin maser mode, which can be used to reduce the MIT measurement time and also enables operation in a magnetically noisy environment.
- Chapter 8 is the final chapter. It presents an overview of the progress this research has made and provides an outlook for future developments.

All of the experimental data collection for this thesis was done by the author in the Time and Frequency Department at the National Physical Laboratory; however, this work was not done in isolation. The results presented for the COMSOL simulations in Fig. 5.3 were carried out by the group of Prof. M. Fromhold at The University of Nottingham and Dr. R. Gartman wrote a numerical model that was used calculate the data in Fig. 5.4 and Fig. 6.8. The theoretical basis for the understanding of some of the results presented for the single-beam configuration in Sec. 3.3 was based on the previous work of Dr. W. Chalupczak. The results presented in this thesis were primarily recorded with an unshielded sensor that was built by the author. In a few cases, results are presented that were recorded with a shielded sensor, which was built before this body of work was undertaken. The author has benefited from working with postdoctoral researcher Dr. R. Gartman and academic supervisor Dr. W. Chalupczak and this thesis is accompanied by a series of publications, which are listed below.

- [7] P. Bevington, R. Gartman, W. Chalupczak, C. Deans, L. Marmugi, and F. Renzoni, "Non-destructive structural imaging of steelwork with atomic magnetometers", *Applied Physics Letters* 113, 6 (2018).
- [8] P. Bevington, R. Gartman, and W. Chalupczak, "Imaging of material defects with a radio-frequency atomic magnetometer", *Review of Scientific Instruments* 90, 1 (2019).
- [9] P. Bevington, R. Gartman, and W. Chalupczak, "Enhanced material defect imaging with a radio-frequency atomic magnetometer", *Journal of Applied Physics* 125, 9 (2019).
- [10] P. Bevington, R. Gartman, and W. Chalupczak, "Alkali-metal spin maser for non-destructive tests", *Applied Physics Letters* 115, 17 (2019).
- [11] P. Bevington, R. Gartman, and W. Chalupczak, "Generation of atomic spin orientation with a linearly polarized beam in room-temperature alkali-metal vapor", *Physical Review A* 101, 1 (2020).
- [12] P. Bevington, R. Gartman, and W. Chalupczak, "Magnetic induction tomography of structural defects with alkali-metal spin maser", *Applied Optics* 59, 8 (2020).
- [13] P. Bevington, R. Gartman, D. J. Botelho, R. Crawford, M. Packer, T. M. Fromhold, and W. Chalupczak, "Object surveillance with radio-frequency atomic magnetometers", *Review of Scientific Instruments* 91, 5 (2020).
- [14] P. Bevington, J. Rajroop, R. Gartman, and W. Chalupczak, "Role of the probe beam in a radio-frequency atomic magnetometer", *Applied Optics* 59, 20 (2020).

- [15] P. Bevington, R. Gartman, Y. V. Stadnik, and W. Chalupczak, "Dual-frequency cesium spin maser", *Physical Review A* 102, 3 (2020).
- [16] P. Bevington, R. Gartman, and W. Chalupczak, "Inductive Imaging of the Concealed Defects with Radio-Frequency Atomic Magnetometers", *Applied Sciences* 10, 19 (2020).

The chronology of these publications does not reflect the order in which the ideas and results are presented in this thesis. Also this thesis does not cover all of the topics presented in each publication, but the most relevant publications for each chapter are listed as follows: [11, 14] are included in Chap. 3, [7–9, 16] cover most of the results presented in Chap. 6, and [10, 12, 15] detail the investigations with the spin maser mode described in Chap. 7. The majority of the previously published data has been presented differently in this thesis so that it is more relevant to the arguments being presented; however as one might expect, there is significant overlap with the publications. The relevant publications for specific results will be detailed at the beginning of each chapter for the interested reader.

Chapter 2

Theory

This chapter describes the theory that underpins the operation of the atomic magnetometer. The aim is not for this to be an exhaustive survey of all of the interesting physics involved. As much as is appropriate, references will be given to works that already, often perfectly, describe the physics discussed throughout this thesis. Detailed theoretical descriptions will only be presented for concepts that help to explain the practical motivations behind this work and the experimental results presented throughout this thesis.

Care has been taken to only include details that are relevant to the arguments presented, and efforts have been made to avoid including ‘interesting’ asides.

2.1 Atoms

Much of the discrete atomic energy substructure originates in the internal interactions of electronic and nuclear angular momenta, and their interaction with external perturbations. These interactions give rise to energy structure or shifts. There is a hierarchy to interactions given by

$$\mathcal{H} = \mathcal{H}_e + \mathcal{H}_{FS} + \mathcal{H}_{HSF} + \mathcal{H}_B + \mathcal{H}_{\text{Light}}, \quad (2.1)$$

the ordering of which corresponds to the typical magnitude of the interaction in the energy scale. The first three terms are from internal interactions: atomic level of the electron (\mathcal{H}_e) and the coupling of electronic angular momentum states (electronic \mathcal{H}_{FS} and electronic with nuclear \mathcal{H}_{HSF}). The last two terms are from external interactions between the atom and a static magnetic field (\mathcal{H}_B) and the oscillating electric component of a light field ($\mathcal{H}_{\text{Light}}$). The magnitude of their interaction (expectation value) is a function of the field strength and is given by the induced splitting. The ordering shown in Equ. 2.1, i.e. $\mathcal{H}_B > \mathcal{H}_{\text{Light}}$, reflects the

regime considered in this work.

The alkali metals have a single valence electron, which reduces the number of available angular momentum states. This simplifies their energy structure with the result that it is relatively straightforward to control their atomic states, making them subjects of significant study in atomic physics. This work will only consider the alkali metals, in particular caesium [17–19]; however, it should be noted that rubidium [20–22] and potassium [5, 23, 24] are other popular choices for atomic magnetometry. Note: these references have been selected as a general sample.

The purpose of this section is to introduce the key topics that describe the atomic interaction energy as it underpins the operation of the atomic magnetometer. Much of this is fundamental and can be found at the beginning of any atomic physics textbook.

Before the description of the energy interaction, it is worth introducing the spectroscopic notation. It has a general form of $n^{2S+1}L_J$ and introduces the electronic angular momentum states where: n describes the principal atomic number, S is the spin quantum number while $|\mathbf{S}| = \sqrt{S(S+1)}$ ¹ is the spin angular momentum and $2S+1$ describes the spin multiplicity (number of degenerate spin states), L is the orbital angular momentum quantum number, and $\mathbf{J} = \mathbf{S} + \mathbf{L}$ is the total electron angular momentum quantum number. For an electron $S = 1/2$ and can be spin up ($m_s = +1/2$) or down ($m_s = -1/2$), while the orbital angular momentum quantum number can take values in the range of $L = 0, 1, 2, 3, \dots, n-1$. In spectroscopic notation, the numerical value of L is represented by a letter. The first four are given by: S, P, D and F (Sharp, Principal, Diffuse, Fundamental), while the rest follow onwards alphabetically from F (with the exception that there is no J state). The orbital angular momentum is given by \mathbf{L} , and like all angular momenta, its magnitude is given by $|\mathbf{L}| = \sqrt{L(L+1)}$. The ground state and the first excited state of the caesium (Cs) valence electron is given by $6^2S_{1/2}$ and $6^2P_{1/2}$. The most significant part of the energy structure, \mathcal{H}_e , is determined by the electronic atomic orbital, but this will not be considered any further since we are only considering the valence electron of the lowest manifold of Cs, where $n = 6$.

2.1.1 Fine and Hyperfine Structure

The next most significant energy structure, \mathcal{H}_{FS} , comes from the interaction of the electronic spin (\mathbf{S}) and orbital (\mathbf{L}) angular momentum to give a total electronic angular momentum J ($|L-S| \leq J \leq L+S$), which is called fine-structure (FS). Spin-orbital (LS)-coupling does not affect the ground state (since $L = 0$), but it creates two new sublevels in the first excited state ($L = 1$) that is characterised by $J = 1/2$ and $3/2$. The optical dipole transitions between

¹The \hbar is excluded from the notation used in this work.

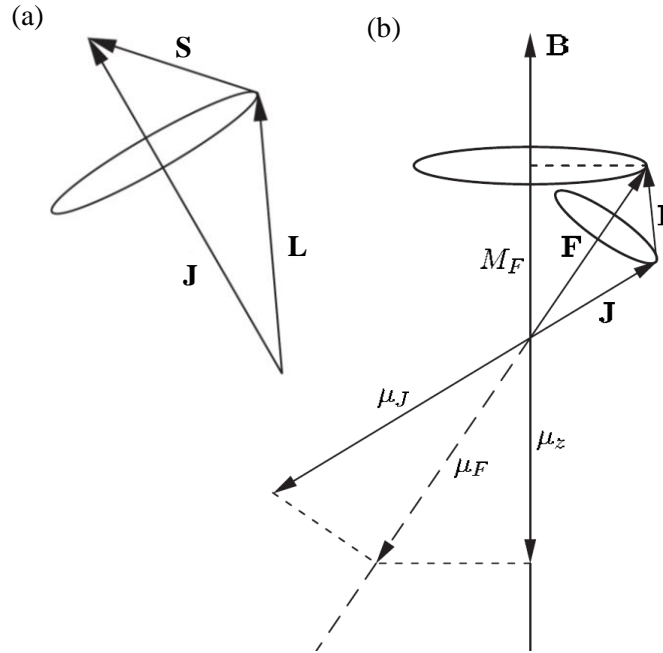


Figure 2.1: Vectorial representation of the interaction of atomic angular momentum: (a) LS-coupling resulting in total electronic momentum \mathbf{J} and leads to fine-structure, (b) coupling of \mathbf{J} with nuclear momentum \mathbf{I} to give total momentum \mathbf{F} and the hyperfine-structure is projected on to a quantisation axis defined by an external magnetic field. The total magnetic moment μ_F is projected along \mathbf{F} (modified from [25]). The nuclear magnetic moment μ_I is negligible compared with the electron (due to the difference in mass of the proton and the electron) and has not been included in this diagram .

these two excited states and the ground state are referred to as the D1 ($6^2S_{1/2} \rightarrow 6^2P_{1/2}$) and D2 ($6^2S_{1/2} \rightarrow 6^2P_{3/2}$) lines, which are at 894.6 nm and 852.3 nm, respectively. For brevity this work will only consider the D2 line, since it is the only optical transition used and the considerations for both are the same. LS-coupling is summarised by the simplistic vectorial picture shown in Fig. 2.1 (a).

The next in the series of internal interactions, \mathcal{H}_{HFS} , is the coupling of \mathbf{J} with the nuclear angular momentum, \mathbf{I} . These two combine to make the total atomic angular momentum $\mathbf{F} = \mathbf{I} + \mathbf{J}$ as shown in Fig. 2.1 (b), where $|I - J| \leq F \leq I + J$. For Cs the respective quantum number for the nuclear magnetic number is $I = 7/2$. Similarly to \mathcal{H}_{FS} , this coupling causes further splitting of the energy levels called hyperfine-structure (HFS). The associated magnetic moment μ with each angular momentum state is also represented in this figure. The ground state $6^2S_{1/2}$ is split into $F = 3$ and 4 levels, while for the excited state $6^2P_{3/2}$ is split into $F = 2, 3, 4$ and 5. The energy splittings between the hyperfine sublevels are given by Fig. 2.2.

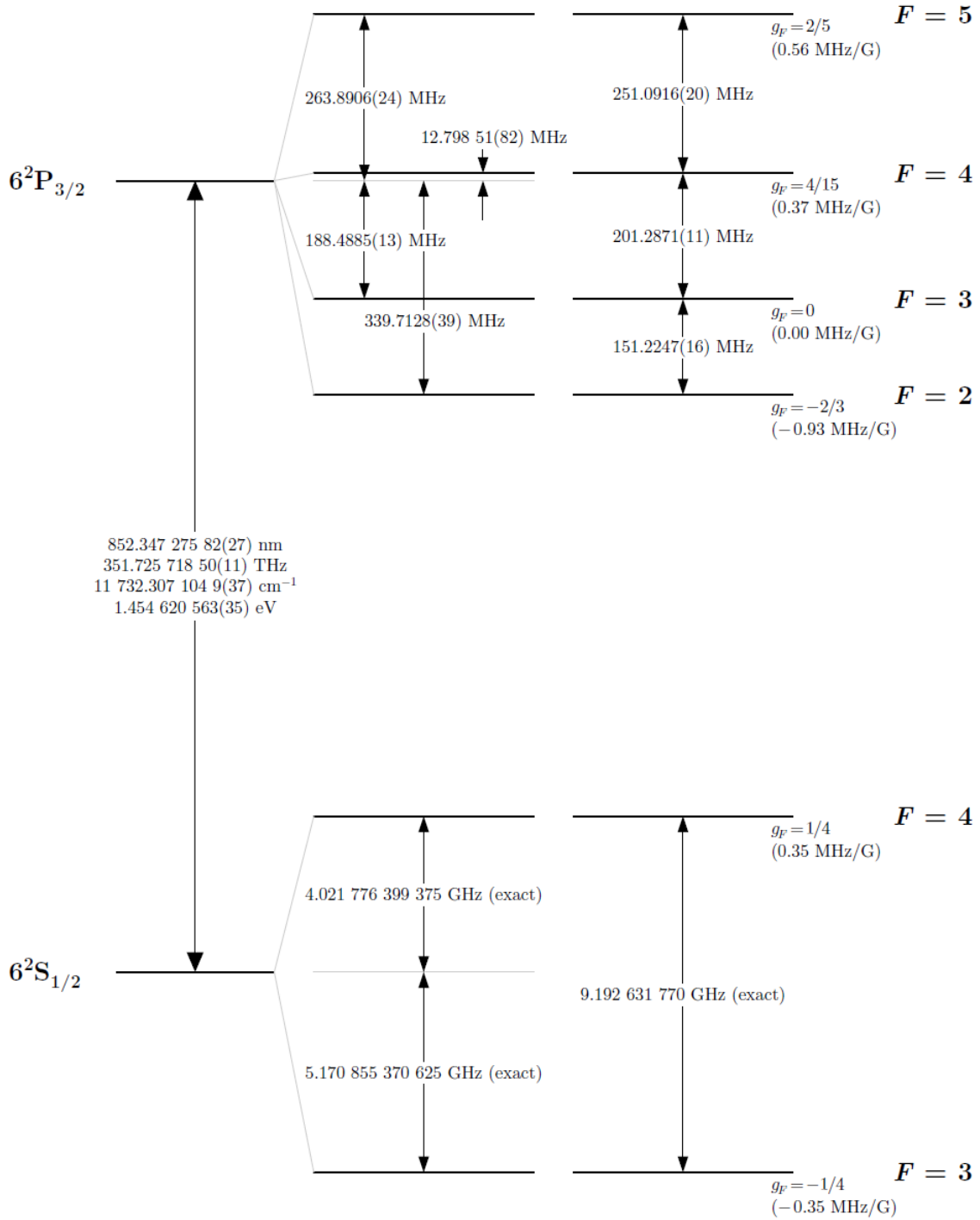


Figure 2.2: D2 line with hyperfine structure [26].

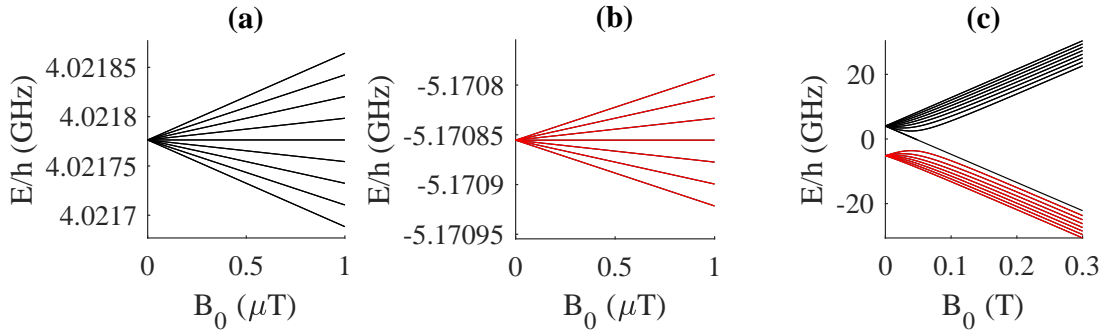


Figure 2.3: Energy of hyperfine ground state sublevels for $F = 4$ (black) and $F = 3$ (red) for increasing bias magnetic field B_0 . This is shown for the (a)-(b) low (Zeeman effect) and (c) high (Paschen-Back effect) magnetic field regimes. At high fields F is no longer a good quantum number, but the line colours are maintained to illustrate what happens to the energy structure.

2.1.2 Zeeman States and Magnetic Sensitivity

Next in the hierarchy of interactions is that of the atomic angular momentum with an external magnetic field, \mathcal{H}_B , which adds another layer to the energy level structure. Each hyperfine level is a manifold of $2F + 1$ sublevels, which are called the m_F , or Zeeman, sublevels. These can be interpreted as the angular distribution of the atomic magnetic moment with respect to the external magnetic field, i.e. the projection of the angular momentum (atomic magnetisation) on to the quantisation axis [25]. In zero field the levels are degenerate, but an external magnetic field will add an energy shift ΔE_B between the neighbouring levels. The magnetic sensitivity of these energy levels, and the energy (frequency) splitting between them, make them useful in magnetometry. The Hamiltonian of the magnetic field interaction depends on the strength of the magnetic field and is given by

$$\mathcal{H}_B = -\boldsymbol{\mu} \cdot \mathbf{B}_0, \quad (2.2)$$

where $\boldsymbol{\mu}$ is the atomic magnetic moment, which comprises of contributions from the angular momentum states and their corresponding Landé g -factor. The nuclear magnetic moment is small relative to the electronic magnetic moment. The former is dependent on the nuclear magneton $\mu_N \propto m_p^{-1}$, while the latter is dependent on the Bohr magneton $\mu_B \propto m_e^{-1}$, where m_p and m_e are the respective mass of the proton and the electron. To simplify the atomic projection (experimentally and numerically), the magnetic field is one dimensional and directed along the quantisation axis, typically denoted as the z -axis throughout this work.

The ordering of \mathcal{H}_B in the hierarchy of interactions depends on the strength of the magnetic

fields. For weak magnetic fields when $E_B \ll \Delta E_{HFS}$, then the magnetic moment is described by $\boldsymbol{\mu} = g_F \mu_B \mathbf{F}$, where g_F is the Landé hyperfine g -factors. The lowest order approximation of the energy shift of the Zeeman effect is given by

$$E_{|F, m_F\rangle} \approx g_F \mu_B m_F B_0. \quad (2.3)$$

The energy shift between neighbouring Zeeman sublevels, $E_{\Delta m_F = 1}$, in terms of frequency is

$$\omega_L = \frac{E_{\Delta m_F = 1}}{\hbar} = \frac{g_F \mu_B}{\hbar} B_0 = \gamma B_0, \quad (2.4)$$

where $\omega_L = 2\pi\nu_L$ is the Larmor frequency (this will be shown later to define the operational frequency of the magnetometer), or magnetic resonance frequency. For the caesium ground state, the gyromagnetic ratio is $\gamma_{Cs}/2\pi \approx 3.5 \text{ Hz/nT}^2$. Note: in this regime the energy splitting between each sublevel is equal. The approximation given in Equ. 2.3 is approximately valid for fields $< 30 \mu\text{T}$ (corresponds to $\nu_L < 105 \text{ kHz}$) and is called the linear Zeeman effect, as shown in Fig 2.3 for the (a) $F = 4$ and (b) $F = 3$ manifold. The work of this thesis is primarily concerned with magnetic fields within this range, but it should be noted that for higher magnetic fields, second order effects become significant.

2.1.2.1 Higher Order Magnetic Field Effects

The exact energy of an m_F sublevel can be calculated through the Breit-Rabi equation for the ground state levels when $L = 0$ through

$$E_{|F, m_F\rangle} = \frac{\Delta E_{HFS}}{2(2I+1)} + g_I \mu_B m_F B_0 + (-1)^F \frac{\Delta E_{HFS}}{2} \sqrt{1 + \frac{4m_F}{(2I+1)}x + x^2}, \quad (2.5)$$

where

$$x = \frac{(g_S - g_I)\mu_B}{\Delta E_{HFS}} B_0. \quad (2.6)$$

The energy of each m_F sublevel is plotted in Fig. 2.3 (c) for increasing B_0 . The second order, or nonlinear, Zeeman (NLZ) effect is a small correction to the linear regime and lifts the degeneracy in ω_L between Zeeman sublevels. It can be assumed that $g_I \approx -0.0004$ is zero, which simplifies the energy splitting between neighbouring m_F sublevels to [17]

$$\frac{E_{|F, m_F+1\rangle} - E_{|F, m_F\rangle}}{\hbar} = \omega_L \left(1 - \frac{\omega_L}{\Delta \omega_{HFS}} (2m_F + 1) \right). \quad (2.7)$$

²Experimentally it is preferable to use Hz rather than rads/s.

Hence the difference in energy in terms of the frequency between magnetic resonance frequencies, ω_{NLZ} , i.e. the difference between $\omega_{m_F+1 \leftrightarrow m_F} = E_{|F, m_F+1\rangle} - E_{|F, m_F\rangle} / \hbar$ and $\omega_{m_F \leftrightarrow m_F-1} = E_{|F, m_F\rangle} - E_{|F, m_F-1\rangle} / \hbar$, is given by

$$\omega_{\text{NLZ}} = \frac{2\omega_L^2}{\Delta\omega_{\text{HFS}}}, \quad (2.8)$$

where ΔE_{HFS} is the HFS between the ground state levels (this corresponds to $\Delta\nu_{\text{HFS}} \approx 9.193$ GHz in frequency). This shift is significant in rf magnetometers since the linewidths are typically on the scale of a few Hz. At high fields ($E_B > \Delta E_{\text{HFS}}$), the Zeeman effect at low fields can be seen to transition to a different regime called the hyperfine Paschen-Back effect.

It will only be mentioned that these regimes come about due to the precession of the different angular momentum states. A more complete description of the above considers when the different quantum numbers are ‘good’ (i.e. when the expectation value of the angular momentum operator remains constant with time) for the different regimes. For a weak field (Zeeman effect) F and m_F are good quantum numbers and for the strong field (hyperfine Paschen-Back effect) these are replaced with m_J and m_I . Further details and derivations can be found elsewhere [25, 27] since this does not add anything to the topics discussed in this thesis as this work only operates in a regime where F and m_F are good quantum numbers.

2.1.3 Light shifts

The final perturbation, $\mathcal{H}_{\text{Light}}$, to the energy structure is the light, or ac Stark, shifts. For magnetometry, the only shifts which are relevant³ are those that change the energy splitting between ground state m_F sublevels [28]. Consequently, these light shifts can be interpreted as the addition of a fictitious magnetic field. There are two interactions, called the vector (or Zeeman) and tensor light shifts, which occur for circularly and linearly polarised light, respectively.

These two effects appear in different measurement configurations [29]. The Zeeman light shift is caused by circularly polarised light and is equivalent to adding a static magnetic field either parallel (left circularly polarised) or anti-parallel (right) along the direction of the beam, leading to a linear change in ω_L with increasing interaction strength. The tensor light shift is caused by linearly polarised light and is equivalent to adding a static magnetic field along the polarisation axis of the beam. However, the tensor light shift has a nonlinear dependence between the atomic ground state spin and the strength of the light field. For most of the results

³There are other light shifts that change the centre of mass of the ground and excited state hyperfine levels simultaneously, either maintaining or modifying the hyperfine splitting.

presented in this work, the light powers (low) and optical detunings (far) for both circularly (pump) and linearly (probe) polarised beams are such that the light shifts are negligible - apart from a particular case presented in Sec. 3.3, where the effects of the tensor light shift are visible in Fig. 3.9.

2.2 Interaction with Light

The polarisation (angular momentum) of a photon interacts with, and is acted on by, the angular momentum states of the atom. Light can be used to prepare an atomic population in a specific angular momentum state (pumping), and is used to map the atomic angular momentum state on to the polarisation state of the light field (probing). Pumping transfers atomic population from one state to another by resonant (absorptive) interaction, i.e. the frequency ω of the light field is tuned near resonance with an atomic transition ω_0 (linear detuning $\Delta = (\omega - \omega_0)/2\pi \approx 0$). Probing can be achieved in a variety of ways [30, Chap. 13], but the method used in this work, the paramagnetic Faraday effect, is considered in terms of an off-resonant (dispersive) interaction.

A crude but useful description of these two types of interaction is that absorptive effects are when an angular momentum state of an atom is acted on by light after absorbing a photon, and dispersive effects are when the polarisation of a light field is acted on by the atom. This description implies absorptive effects are useful in atomic state preparation and dispersive effects are useful in measuring the atomic state.

2.2.1 Pumping

Figure 2.4 shows driving the D2 line $6^2S_{1/2}F = 4 \rightarrow 6^2P_{3/2}F' = 3$ transitions with a left circularly polarised beam that is directed along a bias magnetic field B_z on the z -axis. Due to the conservation of angular momentum, an atom will be transferred from the m_F ground state to the $m_{F'} = m_F + 1$ excited state. This is described as a σ^+ -transition, whereas right circularly polarised light drives σ^- -transitions where $m_{F'} = m_F - 1$. The excitation pathway is shown by the solid-black arrow. The excited state is short-lived (~ 35 ns [31]) and will spontaneously decay back to the ground state following the selection rules $\Delta m_F = -1, 0, +1$; i.e. the spontaneously emitted photon has a random polarisation in the case described in Fig. 2.4⁴, where the decay pathways are shown by the dashed-black arrows. The probability, or branching ratio, of the excitation and decay pathway is the same for a given transition and

⁴This work is only concerned with dilute vapours where radiation trapping is negligible.

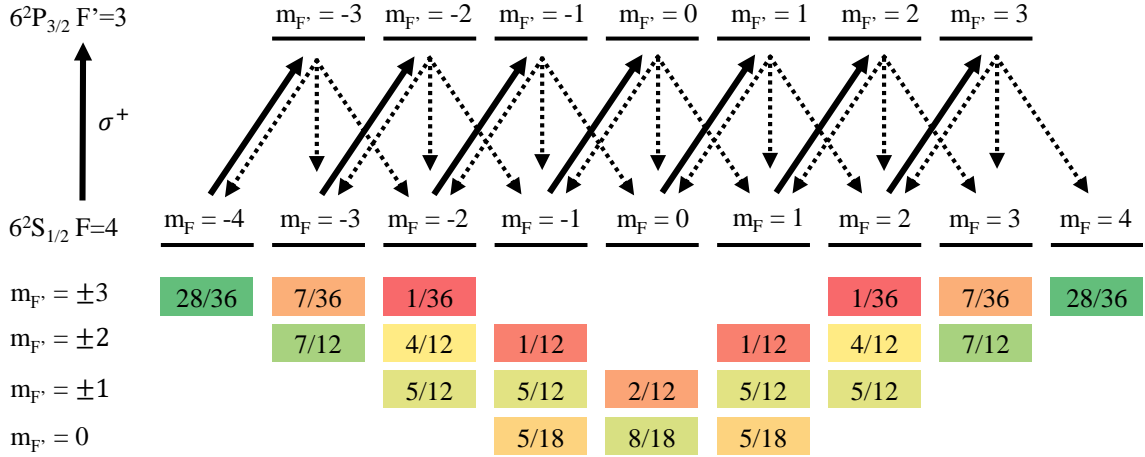


Figure 2.4: Depiction of pumping with left circularly polarised light tuned to the D2 line $6^2S_{1/2}F=4 \rightarrow 6^2P_{3/2}F'=3$ transition. Note: the energy shift between m_F sublevels due to the weak bias magnetic field is not visible on this energy scale. The solid and dashed black lines indicate the excitation ($\Delta m_F = +1$) and decay ($\Delta m_F = 0, \pm 1$) pathways. The probability, or branching ratio, of each pathway is arranged in rows and columns corresponding to the excited ($m_{F'}$) and ground state (m_F) sublevels, respectively. These are symmetric about $m_{F'} = 0 \rightarrow m_F = 0$, where the $m_{F'} = -1 \rightarrow m_F = 0$ and $m_{F'} = 1 \rightarrow m_F = 0$ have the same likelihood. The colour of these values indicates the highest (green) to lowest (red) probability.

they are described by the Clebsch-Gordan coefficients. The relevant numbers are given at the bottom of the figure and they have been arranged in rows and columns corresponding to the excited ($m_{F'}$) and ground state (m_F) sublevel, respectively. The colour of these values indicates the highest (green) to the lowest (red) probability.

In this example an atom will end up in either the $m_F = +F - 1$ or the $m_F = +F$ level (the latter is called the stretched state) after many pumping and decay cycles. These states are said to be ‘dark’ since they can no longer absorb any of the pump light. The presence of relaxation processes (discussed in Sec. 2.4) can either redistribute the atomic population amongst the $F = 4$ ground state level manifold, or move the atomic population to the $F = 3$ manifold. In the former, atoms will re-enter the pumping cycle and be returned to a stretched state. In the latter, the atoms are effectively lost from the atomic population since it is no longer part of the pumping cycle, unless the atom can be returned to the $F = 4$ level.

For a large population of N_{atoms} atoms in the same angular momentum state \mathbf{F} , the ensemble can be treated to have a macroscopic net angular momentum, often denoted as $\mathbf{M} = N_{\text{atoms}}\mathbf{F}$ as this is like a net magnetisation [32]. Pumping an atomic population in the previously described configuration (with circularly polarised light along B_z), will lead to a longitudinal magnetisation $M = M_0 F_z$, where M_0 represents the steady-state amplitude and $F_z = m_F \hbar$ [33]. In this case, the atomic spins are defined along a specified axis and direction. The atomic

population, or polarisation, is said to be oriented.

Pumping with linearly polarised light generates a different population distribution called atomic alignment, which has a net-zero magnetisation where the spins only have a specified axis [34]. One example of this is pumping the $F \rightarrow F' - 1$ transition with linearly polarised light, where the beam polarisation parallel to the bias magnetic field and the beams propagation axis perpendicular to the bias magnetic field [35]. In this geometry and since linearly polarised light is an equal superposition of left and right circularly polarised light, both polarisation components of the light pump atoms towards the $m_F = +F$ and $m_F = -F$ ground state level, respectively. This is just one pumping scenario with linearly polarised light, and it creates a longitudinal alignment. It is mentioned as it partially describes a novel pumping scheme detailed in Sec. 3.3.

The measured rf magnetometer signal (arising from Zeeman coherences that are discussed later in Sec. 2.3) is proportional to the population imbalance between the Zeeman sublevels. Hence, it is desirable to pump as many atoms as possible into a single stretched state, i.e. an oriented atomic polarisation. Pumping an oriented state with a circularly polarised beam is the primary method used in this work for polarising the atomic population; however, a special case is presented in Sec. 3.3. Further discussion is provided throughout Chap. 3 on the optimisation of pumping.

2.2.2 Probing

A common probing technique used in atomic magnetometers [5, 20, 36, 37], and the only one discussed in this thesis, analyses the polarisation rotation of a linearly polarised probe beam as it propagates through the sample. There are two key mechanisms involved in this type of atomic state probing: dichroism and birefringence [38]. Dichroism describes the difference in absorption of two orthogonal polarisation components of light, while birefringence describes the difference in refraction of the orthogonal polarisations. However dichroism is not explored any further in this work.

The rf magnetometer signal comes from measuring the modulation of the probe polarisation rotation due to Zeeman coherences. Zeeman coherences are described in Sec. 2.3, but they are not required to describe birefringent interaction.

2.2.3 Propagation of Light and Complex Refractive Index

The type of interaction of a light field with the atom is related to the real and imaginary components of the complex refractive index $\bar{n} = n + i\kappa$, where $n = kc/\omega$ is the real part of the

refractive index (indicating phase velocity) and κ is the extinction coefficient (attenuation of the light field). It should be noted that the physical properties $n(\omega)$ and $\kappa(\omega)$ of the atom are dependent on the frequency ω of the light field.

The presence of dichroic and birefringent interactions becomes clear when analysing the propagation equation for a linearly polarised light field $\mathbf{E}(z, t)$ propagating in free space along the z -axis. The field is a superposition of two orthogonal circularly polarised beams

$$\mathbf{E}(z, t) = \mathbf{E}_+(z, t) + \mathbf{E}_-(z, t), \quad (2.9)$$

where

$$\mathbf{E}_\pm(z, t) = E_0(\mathbf{x} \pm i\mathbf{y})e^{i(\bar{k}z - \omega t)}, \quad (2.10)$$

E_0 is the amplitude of the electric field and ω is the angular frequency of light. The wavenumber $\bar{k} = \omega\bar{n}/c$ (c is the vacuum speed of light) is complex and is related to the complex refractive index. Assuming there is a difference in absorption κ_\pm and refractive index n_\pm for the orthogonal circularly polarised beams, the field equations after propagating through a medium of length L becomes

$$\mathbf{E}_\pm(L, t) = E_0(\mathbf{x} \pm i\mathbf{y})e^{i(\omega L(n_\pm + i\kappa_\pm)/c - \omega t)} = E_0(\mathbf{x} \pm i\mathbf{y})e^{-\beta_\pm L}e^{i(k_\pm L - \omega t)}, \quad (2.11)$$

where $\beta_\pm = \omega\kappa_\pm L/c$ is the attenuation constant. The difference in absorption ($\beta_+ - \beta_-$) will cause a linearly polarised beam to become elliptical (dichroism) while a difference in refraction ($n_+ - n_-$) will cause a rotation of the linear polarisation (birefringence).

The Kramers–Kronig relation for an equation of the form $\bar{\chi} = \chi' + i\chi''$ states that [39]

$$\chi'(\omega) = \frac{2}{\pi} \int_0^\infty \frac{\chi''(\omega')}{\omega' - \omega} d\omega', \quad (2.12)$$

$$\chi''(\omega) = -\frac{2}{\pi} \int_0^\infty \frac{\chi'(\omega')}{\omega' - \omega} d\omega'. \quad (2.13)$$

This indicates that the components of absorption and refraction for the complex refractive index are causally interlinked; hence, dichroism and birefringence cannot be fully separated. However, it is possible to operate in a configuration where one effect is dominant over the other since $\kappa(\omega) \propto \Gamma/\Delta^2 + \Gamma$ (absorptive Lorentzian) and $n(\omega) \propto -\Delta/\Delta^2 + \Gamma$ (dispersive Lorentzian) [40], where Γ is the full-width-half-maximum (FWHM) of the Lorentzian line-shape.

2.2.4 Birefringence

Birefringence occurs for both linear and circular polarisations (refraction of the two orthogonal components of polarisation); however, only circular birefringence is used in this thesis. It can be assumed that the refractive index of an atom for the orthogonal polarisations of circularly polarised light depends on the angular momentum, i.e. ground state coherence (or spin), of the atomic ground state [41]. An anisotropy in the atomic population, such as for an oriented or aligned atomic ensemble, leads to birefringence. The difference in refractive index experienced by the left and right circular polarisations results in the rotation of a linearly polarised beam as it propagates through the atomic population. This is referred to as the paramagnetic Faraday effect⁵ [38]. Since birefringence is related to the refractive index, its interaction strength also has a dispersive dependence on optical frequency.

The rotation of the linearly polarised probe beam due to birefringence is defined by the coherences in the ground state, [42, Chap. 2] and [43, Chap. 6]; however, the rigorous proof provided in these references goes beyond the scope of this investigation. Regardless of the mechanism, the focus in this thesis is simply on the measurement of the polarisation rotation. For this thesis the probe beam measures the component of the precessing transverse spin that is co-linear with the beams propagation axis, typically denoted M_x , as will be described in Sec. 2.3. The direction of propagation of the probe beam is along the x -axis and the rotation angle is [30, Chap. 15]

$$\theta_{\text{Pol.}} \propto Ln_{\text{Cs}}M_xD(\omega) \quad (2.14)$$

for an optically thin medium (e.g. dilute vapour), where L is the propagation length of the beam through the atomic population, n_{Cs} is the atomic density, M_x is the net angular momentum of the sample directed along the x -axis (note: this is maximum when the probe is parallel to the spin component). D is the dispersive optical envelope

$$D(\omega) = \frac{\Delta}{\Delta^2 + \gamma_{\text{abs}}^2} \quad (2.15)$$

that originates from the dependence of the refractive index, where $\Delta = \omega - \omega_0$ is the detuning from the relevant atomic transition and γ_{abs} is the linewidth of the absorption profile. From Equ. 2.14 it is clear that the probing mechanism maps the projection of the transverse atomic spin on the polarisation of the probe beam. The evolution of M_x is described in Sec. 2.5.1.

⁵Birefringence also occurs when there is no population anisotropy and is described by the Faraday effect, which has uses in Faraday isolators/rotators.

2.3 Atomic Coherences

An atomic coherence describes the coherent superposition between two atomic states. An example of one is the coherent superposition between two Zeeman sublevels, where two neighbouring m_F levels are coupled via a resonant radio frequency (rf) magnetic field. In this thesis, these are referred to as Zeeman coherences⁶. The amplitude of the Zeeman coherence describes the strength of the coupling of the atoms to an external rf magnetic field. In the literature this interaction is often described semi-classically (summarised well in [44, Chap. 4]) as the precession of the collective atomic spin (magnetic moment) \mathbf{M} in a bias magnetic field. To align with other texts this is the description that is recalled here. The full quantum mechanical description of this interaction is not necessary for this work, but it can be found in [27].

Consider the oriented atomic ensemble described in Sec. 2.2.1, where the majority of the atoms are pumped into the same stretched state with a circularly polarised beam whose propagation axis is parallel to the direction of a static magnetic field \mathbf{B}_0 that defines the quantisation axis, and by convention is along the z -axis. The ensemble will be described by a net angular momentum $\mathbf{M} = (M_x, M_y, M_z)$, with a magnetic moment

$$\boldsymbol{\mu} = g_F \mu_B \mathbf{M} = \gamma \mathbf{M}, \quad (2.16)$$

where γ is the gyromagnetic ratio. A rotating magnetic field \mathbf{B}_{rf} perpendicular to the z -axis will tilt \mathbf{M} relative to \mathbf{B}_0 , which causes \mathbf{M} to precess about $\mathbf{B} = \mathbf{B}_0 + \mathbf{B}_{\text{rf}}$. The evolution of \mathbf{M} formulated by Bloch [45] is given by

$$\frac{d\mathbf{M}}{dt} = \gamma \mathbf{M} \times \mathbf{B} = \gamma \mathbf{M} \times (\mathbf{B}_0 + \mathbf{B}_{\text{rf}}) = \gamma \mathbf{M} \times \left(\frac{\omega_L}{\gamma} \hat{\mathbf{z}} + B_1 \cos(\omega_{\text{rf}} t) \hat{\mathbf{x}} \right), \quad (2.17)$$

where \mathbf{B}_{rf} is an rf magnetic field linearly polarised along an axis transverse to \mathbf{B}_0 , e.g. the x -axis, comprising of two counter rotating magnetic fields ($+\omega_{\text{rf}}$ and $-\omega_{\text{rf}}$) with an amplitude of $B_1 = \Omega/\gamma$. Ω is the Rabi frequency that describes the amplitude of the rf field in frequency units. The time dependence of the rf magnetic field can be removed by moving from a stationary frame of reference $(\hat{\mathbf{x}}, \hat{\mathbf{y}}, \hat{\mathbf{z}})$ to a rotating frame $(\hat{\mathbf{x}}', \hat{\mathbf{y}}', \hat{\mathbf{z}})$ that rotates around the z -axis at ω_{rf} . The classical rotation transform gives [46]

$$\frac{d\mathbf{M}}{dt} = \frac{d\mathbf{M}'}{dt} + \boldsymbol{\omega}_{\text{rf}} \times \mathbf{M}, \quad (2.18)$$

⁶Although they are sometimes called Hertzian coherences [27], as used in the title of Alfred Kastler's noble prize 'for the discovery and development of optical methods for studying Hertzian resonances in atoms'.

$$\frac{d\mathbf{M}'}{dt} = \gamma\mathbf{M} \times \mathbf{B} - \boldsymbol{\omega}_{\text{rf}} \times \mathbf{M}, \quad (2.19)$$

$$\frac{d\mathbf{M}'}{dt} = \gamma\mathbf{M} \times \left(\mathbf{B} - \frac{\boldsymbol{\omega}_{\text{rf}}}{\gamma} \hat{\mathbf{z}} \right), \quad (2.20)$$

which creates a fictitious magnetic field $B_f = -\omega_{\text{rf}}/\gamma$. The total magnetic field in the rotating frame now becomes

$$\mathbf{B}' = (B_0 + B_f) \hat{\mathbf{z}} + B_1 \hat{\mathbf{x}}'. \quad (2.21)$$

If $\boldsymbol{\omega}_{\text{rf}} = -\gamma B_0$, then \mathbf{B}' will appear stationary. In the rotating frame the rf magnetic field rotating at $+\omega$ appears very fast and can be neglected (rotating wave approximation), therefore \mathbf{M}' can be given by

$$\frac{d\mathbf{M}'}{dt} = \gamma\mathbf{M}' \times \left(\frac{\Delta\omega\hat{\mathbf{z}} + \Omega\hat{\mathbf{x}}'}{\gamma} \right), \quad (2.22)$$

where $\Delta\omega = \omega_L - \omega_{\text{rf}}$ is the detuning of the rf magnetic field frequency from the magnetic resonance (in this case the Zeeman splitting).

Decay (relaxation, described in Sec. 2.4) terms must be included to fully describe the temporal evolution of \mathbf{M} . The longitudinal (M_z) and transverse ($M_{x,y}$) relaxation mechanisms operate on different timescales, T_1 and T_2 respectively, and describes the tendency towards an equilibrium state where $M'_z = M_0$ and $M'_x = M'_y = 0$. Their inclusion gives

$$\frac{d\mathbf{M}'}{dt} = \gamma\mathbf{M}' \times \left(\frac{\Delta\omega\hat{\mathbf{z}} + \Omega\hat{\mathbf{x}}'}{\gamma} \right) - \left(\frac{M'_z - M_0}{T_1} \hat{\mathbf{z}} + \frac{M'_x \hat{\mathbf{x}}' + M'_y \hat{\mathbf{y}}'}{T_2} \right). \quad (2.23)$$

This description is now in the form of an ordinary differential equation that has stationary ($d\mathbf{M}'/dt = 0$) solutions given by [44, Chap. 4]

$$M'_x = -M_0 \frac{\Omega T_2}{(\Delta\omega T_2)^2 + (1 + \Omega^2 T_1 T_2)}, \quad (2.24)$$

$$M'_y = M_0 \frac{\Delta\omega \Omega T_2^2}{(\Delta\omega T_2)^2 + (1 + \Omega^2 T_1 T_2)}, \quad (2.25)$$

$$M'_z = M_0 \frac{1 + (\Delta\omega T_2)^2}{(\Delta\omega T_2)^2 + (1 + \Omega^2 T_1 T_2)}. \quad (2.26)$$

These terms describe the magnetic, or rf, resonance. Details of the shape of the resonance are given in Sec. 2.5.1

The lifetime of the longitudinal and transverse spin components related to the atomic ground

states relax at characteristic rates given by $\Gamma_1 = 1/T_1$ and $\Gamma_2 = 1/T_2$. The lifetime of the ground states are much longer than those of the excited states in the previous example of pumping Cs atoms on the D2 transition in Sec. 2.2.1. These slower ground state processes redistribute the atomic population built up in the ground-state hyperfine levels (depolarisation) and introduce dephasing between coherences (decoherence). Decoherence is described by T_2 processes, and depolarisation is described by T_1 . Assuming there is a pumping process to maintain a steady M_0 , the sensitivity of an atomic magnetometer is optimised by maximising T_2 (described in Sec. 2.5.2). This can be measured because the FWHM, or linewidth, of the magnetic resonance is equal to Γ_2 . The most relevant processes that lead to transverse relaxation are described in the following section.

2.4 Relaxation Processes

In this work the main relaxation processes that are of concern are from wall collisions and magnetic field gradients. Other processes that can have a significant effect are due to power broadening and atom-atom collisions. The source and description of all four are discussed in what follows. The total relaxation rate for Γ_2 is equal to the sum of all relaxation rates so it is desirable to minimise each.

2.4.1 Wall collisions

The atoms involved in the measurement are housed within a vapour cell. These atoms will rapidly depolarise when they interact with the local electric and magnetic fields of the cell walls, affecting both T_1 and T_2 processes. Due to the thermal velocity of the atoms at room temperature the collision rate per cell length is of the order of ~ 1 kHz/cm, which will likely dominate other processes unless the cell size is very large. However, Γ_{wall} can be mitigated by two main methods: filling the cell with a buffer gas or applying anti-relaxation coatings to the cell walls. Each method has important consequences that provide real constraints on the rf magnetometer. As such, the technical limitations of both will be discussed in what follows.

The purpose of the buffer gas (an inert noble gas) is to impede the diffusion of the atomic vapour to the cell walls through multiple alkali-buffer gas collisions, effectively pinning the atoms in space. In buffer gas cells only the polarised atoms that are being probed contribute to the measured signal, i.e. only the atoms in the intersecting volume of the pump and probe. This means the measurement volume can be much smaller than the cell, increasing the spatial resolution of the magnetic field measurement. It also enables independent field measurements within the same cell, which facilitates highly sensitive gradiometric measurements [47, 48].

However, there is a significant downside in the reduction of the number of atoms N_{atoms} in smaller measurement volumes as the signal to noise ratio (SNR) $\propto \sqrt{N_{\text{atoms}}}$. As a consequence, these cells are typically heated significantly above room temperature to increase the atomic vapour density.

The other method to avoid atomic depolarisation is to use an anti-relaxation coating that is chemically inert and has a very low polarisability. Paraffin coatings are widely used (maintaining atomic polarisation after $\sim 10^4$ wall collisions, giving $T_2 \sim 1$ s [49]), but have a relatively low melting point ($T_{\text{mp}} \approx 60^\circ\text{C}$) [50]. Above this temperature an anti-relaxation coating will begin to degrade. Other long-chain molecules such as deuterated polyethylene ($T_{\text{mp}} > 100^\circ\text{C}$) [51] or octadecyltrichlorosilane ($T_{\text{mp}} \approx 170^\circ\text{C}$) [52] exist, but are not as effective as paraffin. For some applications, e.g. the SERF regime (introduced in Sec. 2.4.4.2), it is desirable to operate at high atomic density n_{Cs} , which requires elevated temperatures. However, this work is only concerned with room temperature operation ($20 - 30^\circ\text{C}$). Even at room temperatures the time taken to traverse the cell is typically much less than the decoherence time. This means an atom can leave the pump beam, collide with the cell walls and enter the probe beam many times while remaining polarised. A benefit of this is that effectively all of the atoms within the cell are available for measurement, in contrast to only those in the intersecting volume of the pump-probe in buffer gas cells. However, this means the magnetic field is averaged across the whole cell and magnetic gradients lead to decoherence (discussed further in Sec. 4.2.2.2). This work uses a glass paraffin coated cell that was manufactured by Dr. M. Balabas, the author of [49] and whose cells are well respected within the community. These cells have residual wall relaxations of $\Gamma_{\text{wall}} \approx 1$ Hz.

It should be noted that historically cells have been made from glass (e.g. silica or borosilicate) due to its optical properties and ductility; however due to production techniques, glass cells are rather specialist products. Recently there has been considerable advancement in the construction of cells using microfabrication silicon-glass technology [53], which lends itself well to mass production. The cells are often called chip, or microelectromechanical system (MEMS), cells. They typically consist of a transparent (to the pump and probe beams, e.g. glass) window, or windows, anodically bonded to a silicon wafer that makes up the cell walls. Currently, these cells must operate with buffer gasses as the temperatures involved in anodic bonding ($250 - 400^\circ\text{C}$) far exceed the melting point of current anti-relaxation coatings.

2.4.2 Magnetic Gradients

Magnetic field gradients cause inhomogeneous broadening of the linewidth of the measured rf spectrum due to dephasing of the Zeeman coherences [54]. Due to the slow ground state

relaxation rates possible (e.g. $\Gamma_{\text{wall}} \approx 1 \text{ Hz}$) a polarised atom in a paraffin coated cell will bounce between the walls many times. Each collision will randomly modify the velocity of the atom, meaning the atom will experience a different path-dependent gradient ΔB as it traverses the cell between each collision. This intuitively leads to a phase shift $\Delta\phi_{\text{grad}}$ between the atoms. Since each atom will effectively sample the whole volume of the cell, $\Delta\phi_{\text{grad}}$ is proportional to the integral of the shift in Zeeman energy over the volume of the cell.

In rf magnetometers, the presence of the bias magnetic field breaks the symmetry across the cell, resulting in different sensitivities to gradients along the transverse and longitudinal axes. For large bias magnetic fields (ω_L is much faster than the collisional frequency), ΔB_z gradients will have a greater influence on B_0 than $\Delta B_{x,y}$, since $B_{x,y}$ are only second order corrections to the total field. One might expect gradients along the transverse axis to become negligible for increasing bias magnetic fields; however, a gradient along one axis requires a gradient in another (to satisfy $\nabla \cdot \mathbf{B} = 0$). Hence, if there is a gradient ΔB_x along the transverse direction, then there will be a longitudinal gradient equal to $\Delta B_z = -1/2\Delta B_x$ [54].

The broadening induced by gradients is given by [17]

$$\Gamma_{\text{grad}} \approx \gamma_{Cs}^2 \frac{L^3}{v} \Delta B_z^2, \quad (2.27)$$

which assumes an approximately cubic cell where L is its length and v is the atomic velocity. This work operates in an unshielded environment, in the presence of magnetic gradients. With gradient compensation and a 1.7 cm^3 cell, the broadening due to residual gradients is $\Gamma_{\text{grad}} \approx 20 \text{ Hz}$ (process described in Sec. 4.2.2.2 and 4.2.3). This relaxation process can be negated completely using good magnetic shielding.

2.4.3 Power Broadening of rf Coherences

In the field of atomic magnetometry power broadening describes processes where the absorption of a photon destroys a Zeeman coherence and occurs for both the pump and probe light. If light is resonant with a transition involving the state of interest there will be power broadening. The pumping rate to power broadening rate is optimised at the largest population anisotropy within the hyperfine ground state level manifold before the decoherence from power broadening begin to dominate - maximising the amplitude of the polarisation rotation signal. In the setup described in Sec. 3.2.1 for indirect pumping (used for the work on MIT in Chap. 6 and 7), the pump light is decoupled from the atomic state, which helps to reduce any decoherence from power broadening. This is evidenced in Sec. 3.2.2.1 by Fig. 3.3, where the presence of a weak pump beam coupled to transitions involving the $F = 3$ ground state broadens the

corresponding $F = 3$ rf resonance, relative to the $F = 4$ ground state rf resonance (which the pump light is decoupled from).

For the probe beam configuration used in this work (probe perpendicular to pump and described in Sec. 3.1.2), absorbing a photon will polarise the atom in a different basis, removing atomic population in addition to destroying the coherence. Power broadening for the probe can be mitigated by using off-resonant light and is optimised in the same way as the pump beam. Implementation of both these pumping and probing schemes means that power broadening of the rf coherences can always be set to zero.

2.4.4 Collisions

2.4.4.1 Spin Exchange Collisions

Spin exchange collisions (SECs) describe the transfer of angular momentum (e.g. spin up to spin down) between two atoms A and B , typically described by



where the total angular momentum is conserved [55]. Collisions between atoms in the same hyperfine manifold exchange m_F [56], while for collisions between atoms in different hyperfine ground states (e.g. Cs $F = 3$ and $F = 4$) collisions exchange F but maintain m_F [57]. Both of these processes lead to decoherence and depolarisation. It is clear that collisions between atoms in the stretched state, e.g. $|F = 4, |m_F| = 4 \rangle$, will not lead to the relaxation process caused by SECs; however, the full elimination of relaxation due to SECs requires $\sim 100\%$ polarisation (discussed further in Sec. 3.1.1)[58].

The broadening Γ_{SE} due to the rate of a spin exchange collisions, R_{SE} , is given by [42, 59]

$$\Gamma_{SE} = \frac{1}{q_{SE}} R_{SE} = \frac{1}{q_{SE}} \bar{v} n_{Cs} \sigma_{Self}^{SE}, \quad (2.29)$$

where $q_{SE} = 2I(2I - 1)/3I(2I + 1)$ is the broadening factor when $\omega_L \gg R_{SE}$, the relative velocity between atoms is given by $\bar{v} = \sqrt{2} \times \sqrt{8k_B T / \pi m_{Cs}}$, n_{Cs} is the atomic density, and $\sigma_{Self}^{SE} \approx 2 \times 10^{-14} \text{ cm}^2$ is the collision cross section between Cs atoms [23]. At the temperatures used in this work (22°C , $n_{atoms} = 3.3 \times 10^{10} \text{ cm}^{-3}$), the decoherence rate due to SEC is $\Gamma_{SE} \approx 1 \text{ Hz}$ and was confirmed by the measurements that supported [6] by Dr. W. Chalupczak et al. Although this is effectively negligible compared to decoherence experienced by magnetic gradients, SEC play an important role in the transfer of population between hyperfine levels. This facilitates the indirect pumping that is described in Sec. 3.2.1.

2.4.4.2 Spin Destruction Collisions

Intra-species collisions between alkali atoms can lead to spin-destruction, which describes cases where F and m_F is not conserved (momentum is transferred elsewhere), depolarising the atom. The rate of these spin-destruction collisions are much lower than SECs due to their significantly smaller cross-sectional area (Cs $\sigma_{\text{Self}}^{SD} = 2 \times 10^{-16} \text{ cm}^{-2}$) and their presence only becomes significant when SECs are negligible, in the so-called spin-exchange relaxation free (SERF) regime [23]. The SERF regime operates at elevated vapour temperatures (high density and spin-exchange rate) and low magnetic fields to enable rapid spin-exchange within a period of spin precession. In this way the average atomic spin interacts with the magnetic field and it does not see the decoherence from the SEC.

In buffer gas cells there is a low rate of spin-destruction collisions with polarised atoms and the buffer gas. The buffer gas pressure is set so that this is comparable to the other dominant spin-relaxation mechanisms, i.e. from walls and SECs [42, Chap. 2].

2.5 Atomic Magnetometer Operation

This section presents the concepts that have been presented in the preceding sections of the chapter to describe the fundamental operation of the rf magnetometer used throughout this work. The operation is typically described by the model of polarisation, evolution, and detection, described by Fig. 2.5 and below.

- **Polarisation:** Optical pumping is used to build up a population anisotropy within the hyperfine ground state manifold of m_F levels, aligning the atomic spins of an unpolarised atomic population Fig 2.5 (a)-(b). The pump beam is co-linear with a static bias magnetic field B_0 (e.g. directed along \hat{z}) that defines the quantisation axis and sets the Zeeman splitting (Larmor frequency) between m_F sublevels. The pump is circularly polarised, which directs the spins of the atomic ensemble along the pump and results in a net magnetisation $\mathbf{M} = M_0 \hat{z}$.
- **Evolution:** An rf magnetic field B_{rf} that is perpendicular to B_0 (e.g. directed along \hat{x}) and has a frequency ω_{rf} resonant with ω_L will induce coherences between m_F sublevels - this can be interpreted as the rf field tilting \mathbf{M} along \hat{x} and resonantly driving its precession around \hat{z} .
- **Detection:** Birefringence (difference in indices of refraction for left and right polarised light) maps the projection of the precessing component of angular momentum M_x to

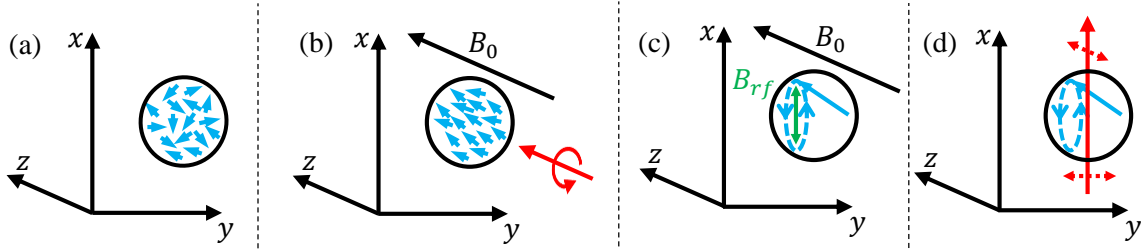


Figure 2.5: Initially an unpolarised atomic population (a) $\mathbf{M} = 0$ is polarised by a circularly polarised pump beam (b) $\mathbf{M} = M_0\hat{z}$ along B_0 ; (c) a rotating field B_{rf} which is resonant with ω_L and is perpendicular to B_0 will resonantly drive the precession of \mathbf{M} around B_0 ; (d) a linearly polarised probe beam perpendicular to B_0 can monitor the projection of \mathbf{M} along the probe via the paramagnetic Faraday effect.

the linear polarisation of a beam propagating along \hat{x} , leading to rotation of the beam polarisation.

2.5.1 Resonance Lineshape

The probe measures the co-linear projection of the transverse component of the precessing spin on to the axis of the probe beam, in the stationary frame of reference of the laboratory. In the literature it is standard for the probe to be aligned along the x -axis⁷, hence this configuration is referred to as an M_x magnetometer. The component will have the form $M_x = M'_x \cos(\omega_L t) + M'_y \sin(\omega_L t)$, describing a signal oscillating at ω_L with a Lorentzian amplitude envelope centred on $\omega_{rf} = \omega_L$, as depicted in Fig. 2.6 (a). Birefringence directly maps the component of angular momentum M_x on to the polarisation of the linearly polarised probe. Hence, monitoring the polarisation rotation of the probe (described in Sec. 4.1.3) gives a measure of M_x . The most useful information is the amplitude of M'_x and M'_y , which can be measured directly by demodulating⁸ the polarisation signal at $\cos(\omega_{rf} t)$ and $\sin(\omega_{rf} t)$, which

⁷projecting the probe along the y -axis will only introduce a 90° phase shift.

⁸This is typically done with a lock-in amplifier, which measure the amplitude and phase of a signal at a particular frequency. The input signal V_s is amplified and mixed with a reference signal V_f , effectively multiplying the two signals. If $f_s = f_R$ there will be a component at 0 Hz (DC signal) and $2f_R$. Low-pass filters are used to attenuate the non-DC component, which will include all frequency components of the input signal which are not at f_R . The output is a DC signal with an amplitude proportional to the component of the input signal at the reference frequency. The input signal is said to be demodulated at the reference frequency. The lock-in's time constant (TC) sets how close to DC the signal is filtered. Longer TCs have a lower frequency cut-off but they make the lock-in less reactive (measured DC amplitude typically takes 5-10 times the TC to settle). If by chance $\theta = \theta_S - \theta_R = 90^\circ$ the measured signal will be zero, even though the input signal is not. Another PSD can be implemented, which phase shifts the reference frequency by 90° . This gives two outputs, $X = A_S \cos \theta$ and $Y = A_S \sin \theta$, which are called the in-phase and quadrature component respectively. Further details can be found in [60]

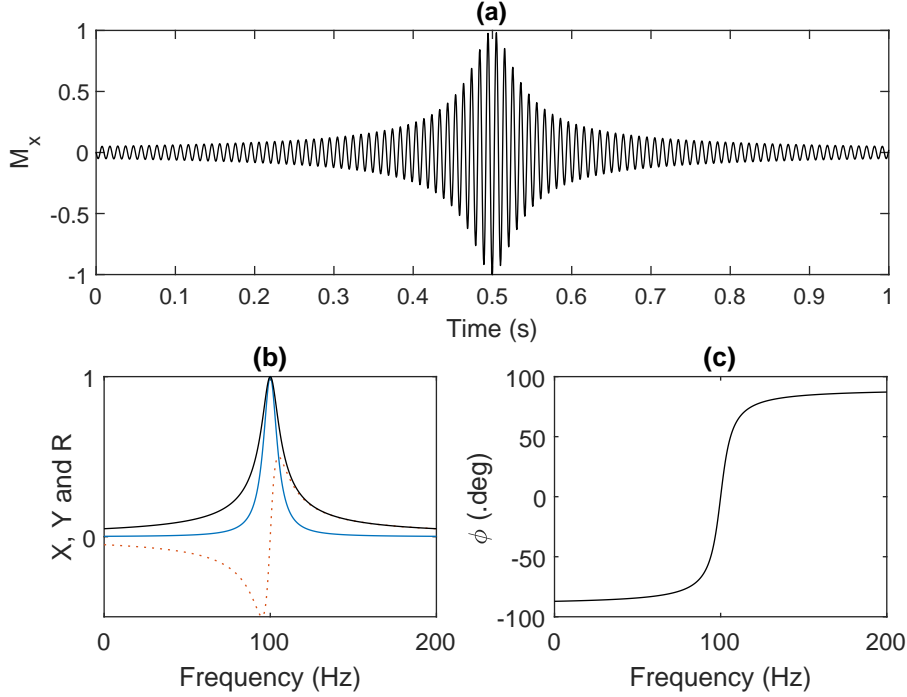


Figure 2.6: (a) Calculation of the M_x time-series as ω_{rf} increases linearly with time. In this model ω_{rf} is scanned through the resonance over a period of a second and the time series is centred at the point when $\omega_{\text{rf}} = \omega_L$. The M_x signal is demodulated at ω_{rf} into quadrature components X and Y , shown by the solid blue line and the dotted orange line in (b). The amplitude R and phase ϕ are shown by the black line in (b) and (c), respectively.

results in the components $X \propto M'_x$ (in-phase) and $Y \propto M'_y$ (quadrature), respectively. From the form of Equ. 2.24 and 2.25, X and Y will have an absorptive [$X(x) = 1/(1+x^2)$] and dispersive [$Y(x) = x/(1+x^2)$] Lorentzian lineshape, as shown by Fig. 2.6 (b) X (solid blue line) and Y (dotted orange line). The amplitude $R = \sqrt{X^2 + Y^2}$ and phase $\phi = \tan^{-1} Y/X$ of the demodulated signal are given by the black line in Fig. 2.6 (b) and (c), respectively. The data presented in Fig. 2.6 have been calculated for $\nu_L = 100\text{Hz}$ and has a linewidth of $\Gamma = 10\text{Hz}$ so that both the structure of the M_x signal and resonance are clearly visible.

2.5.2 Measurement Limits

Part of the excitement surrounding atomic sensors is that their sensitivity is quantum limited. For atomic magnetometers these topics are covered in depth in [44, Chap. 2] and [61], which deals with the fundamental sensitivity limits of atomic magnetometers more generally, while Savukov et al. [5] introduces the limits specifically for rf magnetometers. The work undertaken in this thesis is concerned with operating in an unshielded environment where there are

external factors, such as magnetic field gradients and 50-Hz electronic noise (as will be discussed in Sec. 4.2.3), that make it challenging to reach the quantum limit. However, it is worth introducing the dependencies of the quantum limited sensitivities on experimental parameters of the magnetometer to give a flavour of what is achievable.

The first limit is the atomic-shot-noise-limit (SNL), or spin projection limit. This originates from the random fluctuations (uncertainty) in atomic polarisation and affects the uncertainty in measuring the magnetic field, δB_{SNL} , given by

$$\delta B_{\text{SNL}} \approx \frac{2\pi}{\gamma_{Cs}} \sqrt{\frac{1}{N_{\text{atoms}} T_2 \tau}}, \quad (2.30)$$

where τ is the measurement time. Since the collective measurement is made up of measuring N_{atoms} many atoms, this shows the usual trend that the uncertainty will decrease with the inverse square root of the number of measurements and measurement time. Longer coherence lifetimes will also decrease the uncertainty. For the cell size (1.7 cm^3) used most frequently in this work and at room temperature, $N_{\text{atoms}} = 5.6 \times 10^{10}$ and typically $1/T_2 \approx 20 \text{ Hz}$, gives $\delta B_{\text{SNL}} \approx 5 \text{ fT}$ for $\tau = 1 \text{ s}$ integration time (note: $\gamma_{Cs}/2\pi = 3.5 \times 10^9 \text{ Hz/nT}$).

The second limit is the photon-shot-noise-limit. This originates for the stochastic arrival of photons at the detector and affects the uncertainty in measuring the angle of polarisation rotation $\delta \Phi_{\text{SNL}}$ given by

$$\delta \Phi_{\text{SNL}} \propto \frac{1}{2} \sqrt{\frac{1}{\phi_{\text{photons}} \tau}}, \quad (2.31)$$

where ϕ_{photons} is the number of photons arriving at the detector. The same consideration to δB_{SNL} applies here, where a greater number of photons N_{photons} measured over a longer period will decrease the measured uncertainty. There is also a quantum mechanical uncertainty that is associated with random fluctuations in the linear polarisation of the probe beam at the detector. Both these uncertainties are related to optical detection and their connection to the uncertainty in the measured magnetic field is somewhat involved (described fully in [61]); however, the details of this are not necessary for the magnetometer configuration considered here as its contribution is less than δB_{SNL} [6].

A technical limit of any measurement is the electronic, or detection noise, from the photodiodes monitoring the probe. At the fundamental limit this is the sum of the Johnson noise and $1/f$ noise in the electronics. Johnson noise is due to the current generated by the random, temperature dependent, motion of electrons in resistive components. This sums to zero over time, but has a broadband frequency component, while $1/f$ noise has a linear frequency response and typically dominates at low frequencies. In a real circuit there will be other larger noise contributions, but for modern photodiodes and commercial electronics, the noise level

should be significantly lower than δB_{SNL} and $\delta \Phi_{\text{SNL}}$.

The discussion in Sec. 3.2.3 details the calibration of the sensitivity of the rf magnetometer in a magnetically unshielded environment and shows that it is limited by technical noise at the level of $\sim 50 \text{ fT}/\sqrt{\text{Hz}}$.

Chapter 3

Magnetometer Performance

This chapter covers topics related to how the different configurations of laser light (pump and probe) impact the overall performance of atomic magnetometers; although, the context of the discussion is focused on the operation of the rf magnetometer. There is no ‘one size fits all’ method for constructing an atomic magnetometer, but there are design choices related to the configuration of the laser which must be considered with respect to their impact on performance. These design choices are: frequency, polarisation, the number of laser sources and their geometry (angle of the pump beam w.r.t bias magnetic field and the angle of the probe to atomic polarisation). Performance is a general term so the relevant issues are grouped as sensitivity and practicality.

- **Sensitivity:** discussed in terms of maximising the SNR of the polarisation rotation signal of the rf magnetometer. The primary considerations here are: the generation of a large number of polarised atoms (\propto polarisation rotation signal amplitude), maximising the Zeeman coherences lifetime T_2 , and the effective measurement of these coherences. These mechanisms are partially defined by optical pumping and probing. Note: the impact of technical noises, such as the effect of gradients (Sec. 4.2.2.2) and 50 Hz magnetic field noise (Sec. 4.2.3) on the operation of the rf magnetometer are discussed elsewhere.
- **Practicality:** pumping and probing can be achieved in a variety of ways, e.g. with different beam polarisations and geometries. However, the discussion of the practicality of the magnetometer is framed in the context of the number of laser sources (beams) required, since this parameter will influence the power consumption, dimensions, and overall complexity of the system.

These factors must be considered and balanced carefully when designing an rf magnetometer that can be miniaturised and developed into a real-world sensor. This chapter is by no means an

exhaustive review of the topics mentioned, but it does reference particular cases and studies where relevant. Section 3.1 discusses these topics in general terms, introducing issues that need to be considered in the operation of an atomic magnetometer. Section 3.2 describes the optimisation of the specific two-beam pumping and probing scheme used for the work presented in Chap. 6 and 7. The final section (Sec. 3.3) of this chapter introduces a novel pumping configuration that generates and probes an oriented atomic polarisation with a single, linearly polarised beam. The reduced complexity of the single-beam configuration makes it attractive for miniaturisation.

The author has discussed the results on the influence of the probe beam on the rf resonance presented in Sec. 3.2.2 in [11], and Sec. 3.3 covers the description of the single-beam pumping and probing configuration presented in [14].

3.1 Laser Configurations

The focus of this section is on the practical considerations of the pump (Sec. 3.1.1) and probe (Sec. 3.1.2) beam, and each section begins by recalling their functional requirements. Then in Sec. 3.1.3, three different laser configurations are discussed, focusing on how the number of beams affect the operation of the sensor. The cases are: two-beams with individual laser frequencies for pumping and probing, a single frequency beam that combines both functions, and the use of an additional pump beam (repump).

3.1.1 Pumping

The role of the pump beam is to achieve a large population imbalance between the ground state Zeeman sublevels, since the amplitude of the Zeeman coherences is proportional to the population difference between neighbouring sublevels ($\Delta m_F = \pm 1$). Several different parameters affect pumping. These are: the beam's optical frequency (detuning from the relevant atomic transitions), the polarisation of the light, and the number of beams and their geometry with respect to the quantisation axis (set by the bias magnetic field). Pumping is an absorptive effect so it typically requires an optical frequency resonant with an atomic transition. The choice of pump beam polarisation and geometry dictates the type of atomic polarisation achieved, while the number of beams typically impacts the degree of atomic polarisation, e.g. using a second pump called the repump to maximise polarisation. The pumping rate¹ influences the degree of atomic polarisation, but the optimum rate is dependent on the pumping scheme, e.g. pulsed or continuous wave (CW), or if the beam is on/ off-resonant with the relevant atomic transition.

¹In the low intensity regime (below saturation) this rate is proportional to the beam intensity

Although the considerations for pumping different atomic species and transitions are the same, this work only discusses pumping caesium atoms on the D2 line and with two distinct pump beam polarisations (described in Sec. 2.2.1). The first is left, or right, circularly polarised light propagating parallel the bias field to pump an oriented state that drives $m_F - m_{F'} = -1$, or $+1$, transitions. The second is linearly polarised light propagating perpendicular to the direction of the bias magnetic field to pump a longitudinal aligned state that drives $m_F - m_{F'} = 0$ transitions between the ground and excited state². For magnetometry, it can be desirable to pump atoms into an orientated state since there will be a greater population imbalance than compared to an aligned state. A more significant issue related to operating an rf magnetometer with an aligned state is that the measured polarisation rotation signal generated by the opposing stretched state have opposite amplitudes. Without separation of the m_F sub-levels, e.g. splitting from the nonlinear Zeeman effect or tensor light shifts, the signals from the opposing stretched states overlap and there will be no measurable signal present [35]. This results in a dependence of the measured signal amplitude on the bias field strength. The applications of MIT (discussed in Chap. 5 and 6) favour low frequency (low bias field strength) operation, meaning an aligned atomic state will not return a strong measurement signal.

Here issues associated with using a strong pump beam will be discussed. The function of the pump beam is to align the atomic spin with its propagation axis. The function of a resonant rf magnetic field is to generate and drive the precession of a spin component perpendicular to the pump beam. A strong pump beam can destroy Zeeman coherences by realigning the transverse spin component back along the pump beam. In pulsed operation a strong pulse of pump light can create near full atomic polarisation, but to avoid any decoherence it is required that the evolution of the atomic coherence is probed when the pump is off [17, 22]. However, measurement with pulsed operation has intrinsic issues for dc magnetometers due to dead-time (period of no measurement) and bandwidth limitations (e.g. Dick effect - aliasing signals with a frequency higher than the pulse frequency [62]). The alternate case is CW operation, which has neither issue and for the rf magnetometer enables the implementation of a continuous feedback mechanism, called the spin maser (described in Chap. 7). CW operation is also less complicated to implement, but the pumping configuration must be optimised to maximise the atomic polarisation while minimising any power broadening of the Zeeman coherence.

All the above examples in this section discussing the pump describe cases where the beam is resonant with a transition involving the ground state level of interest. Another scheme is off-resonant pumping, where the pump beam is optically decoupled from the target ground state, reducing power broadening effects. This scheme is described in detail in Sec. 3.2.1, but it can be considered to function in the same way as a repump (described in Sec. 3.1.3.3), by moving

²For this regime the beam polarisation vector is parallel to the bias magnetic field.

the atomic population out of the additional ground state whilst other processes generate atomic polarisation in the level of interest.

3.1.2 Probing

This work considers probing mechanisms where the atomic ensemble modifies the polarisation of a linearly polarised probe beam. This can be achieved through two processes, dichroism (absorption) or birefringence (dispersion/ refraction). The probing mechanism is mainly³ defined by the frequency of the probe light. As dichroism is an absorptive effect, the probe must be optically coupled to an atomic transition involving the spin states of interest, which will add to power broadening of the magnetic resonance. Whereas birefringence is an off-resonant interaction that can, in principle, perform a quantum non-demolition measurement of the spin state [36], i.e. the probe light does not polarise the atom, and power broadening is negligible.

3.1.3 Geometry

There are a plethora of options for beam polarisation, orientation, and detuning for both pump and probe. In this section examples will be discussed in the context of the number of beams required for pumping and probing. Beam number contributes significantly to the overall complexity of the sensor. This is exemplified by the fact that the first commercially available atomic magnetometers operated with a single light source⁴, i.e. single beam and optical frequency. To narrow the discussion of the different beam geometries, only examples of rf magnetometers are given. In this discussion, the use of devices that can modify the frequency of light, such as acousto-optical modulators (AOMs) and electro-optical modulators (EOMs), are considered to increase system complexity as much as using separate light sources.

3.1.3.1 Separate Pump and Probe

The main geometry used in this work has a separate pump and probe beam, requiring two light sources. The two-beam configuration is convenient since the action of the pump and probe can be separated to some degree, so that they can be considered to interact separately with the atoms. In particular, the probe beam can be detuned away from the atomic resonance so it does not interfere with the pumping mechanism. Beam power and polarisation can be optimised

³The polarisation of the probe light and also the character of the atomic population will also have an influence

⁴There have been different generation of sensors. While lamps were used in the 1950's [44], laser diodes are used in the present day by companies Twinleaf and QuSpin.

separately, although this is also possible when using a single light source and splitting the beams.

Another advantage of using two-beams is that the angle between them can be changed to achieve different pump-probe configurations. In one such case - which is used in this work and was first described in [5] - the optimum pumping of an oriented state is reached using a circularly polarised beam directed along the bias magnetic field. To create a Zeeman coherence, the rf magnetic field must be perpendicular to the axis that the ensemble of atoms are polarised along. The precessing spin (Zeeman coherence) only has a non-zero amplitude in the plane perpendicular to the axis of the bias magnetic field, i.e. the magnetometer has dead-zones along the bias magnetic field. The paramagnetic Faraday effect (described in Sec. 2.2.4) is used to monitor the projection of the precessing spins on to the propagation direction of the probe beam. The amplitude of the projection is maximum when the probe beam is parallel to the transverse spins. This is a convenient and well-used geometry [5, 20], including for all the results presented in this work (excluding Sec. 3.3).

3.1.3.2 Combined Pump and Probe

A special case of the separate pump and probe category is where the two-beams are identical, i.e. a single beam acting simultaneously as both. The benefit of using a combined beam is that the dynamics have been shown to be equivalent to using separate beams [63], while being easier to realise practically. However, a consequence is that the action of the pump and probe intermix further, complicating the atomic-light interaction. As a result there are many combinations of beam parameters (power, detuning, polarisation, and the angle between the beam and the quantisation axis) for the single-beam configuration.

In a single beam configuration, pumping is typically achieved using resonant light and hence the probing action takes the form of dichroism⁵. The intermixing of the two processes means that neither process can fully be optimised. One study increases pumping efficiency by using a beam ($\sim 30\text{mW}$, $1481\ \mu\text{W}/\text{mm}^2$) resonant with transitions involving one hyperfine ground state, $F = 3$, to generate atomic polarisation in the other hyperfine ground state, $F = 4$, (indirect pumping, described further in another case in Sec. 3.2.1) [65]. The consequence of using this scheme is inefficient probing⁶. In another study the beam is tuned near-resonant with

⁵Some of the original work studying magneto-optical effects used a combined pump and probe beam configuration, where the probe interaction was called ‘nonlinear Faraday interaction’ and was shown to be equivalent to the description of linear dichroism [64].

⁶This probing scheme monitors the transmission through the cell. Zeeman coherences induced by an rf magnetic field redistribute some of the atoms that were pumped into a highly oriented (95%) stretched state. SEC move stretched atoms to the other hyperfine ground state level, then absorption of the pump returns the atoms to the ground state level of interest.

the hyperfine ground state of interest. To mitigate the negative impact of the probing action on the pumping action, there is a reduced beam power ($4.7 - 8.9 \mu\text{W}$, $0.7 - 1.3 \mu\text{W}/\text{mm}^2$), which leads to inefficient pumping [66]. These two cases contrast with the novel single-laser case presented later in Sec. 3.3, which simultaneously achieves efficient pumping and probing (with a beam power 10mW , $32 \mu\text{W}/\text{mm}^2$).

From the inexhaustive survey conducted for this work, the atomic magnetometer sensitivity typically achieved with a single laser configuration is an order of magnitude worse than typically achievable with separate pump and probe beams [5, 6]. The best demonstrated sensitivity for a single-beam rf magnetometer that was found was a carefully considered experiment in magnetic shields that achieved a sensitivity of $\sim 10\text{fT}/\sqrt{\text{Hz}}$ (shot noise limited with beam power $40 \mu\text{W}$, $5.7 \mu\text{W}/\text{mm}^2$) [67]; although, it should be noted that this experiment was carried out with a large number of atoms ($N_{\text{atoms}} = 1.26 \times 10^{13}$). Higher sensitivities can only be achieved with more efficient pumping, e.g. with an additional pump. This is in agreement with the argument presented in the previous paragraph, where the mixing of the action of the pump and probe limit the performance of the sensor.

It is worth noting that the first commercially available atomic magnetometers from companies Quspín and Twinleaf operate with a single CW beam geometry. Both developed SERF and total field magnetometers, and although their operation differs significantly from that of an rf magnetometer, it exemplifies that the single-beam configuration is favourable when designing a commercial sensor. The University of Strathclyde has also followed this strategy in the design of their compact magnetometer [68].

3.1.3.3 Repump

During the pumping cycle some of the atomic population can be lost to the ‘other’ hyperfine ground state; e.g., when pumping $F = 4 \rightarrow F' = 3$ and population ends up in the $F = 3$ ground state. This is due to off-resonant scattering from the excited states and is exacerbated by the Doppler broadened pump coupling to the other excited states. There are also relaxation processes (Sec. 2.4) that redistribute the atomic population. An additional pump beam, called the hyperfine repumper (repump), can be used to increase the polarisation to $\sim 100\%$. The repump is tuned to resonance with transitions involving the hyperfine level that are not involved in the magnetic field measurement. After repeated pumping cycles, the atomic population in this level will be transferred to the ground state level of interest. This process increases the overall population in the target ground state, in addition to returning any population that has been lost [17, 19]. However, the experimental complexity of multiple beams operating at different frequencies limits the use of a repump in the development of a practical sensor.

3.1.4 Summary

With three independently tuneable beams the pumping and probing can be optimised separately. Pulsed pumping with a strong beam can be used to achieve a similar degree of atomic polarisation, but without the repumper, significantly reducing the experimental requirements of the system⁷. CW operation of an rf magnetometer is favourable over pulsed operation as it requires less experimental control, does not suffer from dead-time, and enables the use of the spin maser configuration (described in Chap. 7). The two-beam setup is a convenient configuration for partially separating the competing actions of the pump and probe. The next section discusses in greater detail the performance of the CW operation of the two-beam setup used for the MIT work presented in this thesis. From a practical point of view, it is favourable to design a sensor with a single laser that combines the functionalities of the pump and probe.

3.2 Two-Beam rf Magnetometer

This section briefly discusses how the pump and probe used in this work (excluding results in Sec. 3.3) affect the performance of the rf magnetometer, particularly with regard to sensitivity. The pumping and probing configurations used are described as indirect (or off-resonant) pumping and off-resonant probing. The term ‘off-resonant’ for both pumping and probing simply describes that the light is detuned from the relevant atomic transition frequency. Although they describe the same thing, for pumping there are other mechanisms at play so it is favourable to use the term ‘indirect’.

Sections 3.2.1 and 3.2.2 describe the influence the pump and probe have on the magnetometer; as such, the investigations in these sections have been carried out in magnetic shielding. The optimal operating conditions described in these two sections are used to run the rf magnetometer and Sec. 3.2.3 describes the estimation of the sensor’s sensitivity in an unshielded environment.

The laser used for both the pump and probe beam in these measurements are Vescent distributed Bragg reflector laser diodes (D2-100-DBR series) [69], described in Sec. 4.1.1.

⁷Pulsed pumping has only been introduced briefly to present the different options that are available for efficient pumping. Further information is available in works [17, 22]. Another case of general pulsed operation is the bell-bloom configuration where laser beam power, polarisation, or detuning, can be modulated [44].

3.2.1 Indirect-Pumping

Indirect-pumping combines pumping between the hyperfine ground state manifolds and SEC (see Sec. 2.4.4). The realisation of the scheme presented here was demonstrated first by Chalupczak et al. in 2012 [57]. The results presented in this section are reprinted from that work and were not carried out by the author of this thesis. They have been included since this is the pumping scheme used in all of the work presented in this thesis (excluding results presented in Sec. 3.3). Below is a brief summary of the effects that are relevant for the operation of this pumping scheme and it is discussed in relation to its impact on the performance of the magnetometer.

The aim is to use circularly polarised light to generate atomic orientation in the $F = 4$ manifold. As pumping is an absorptive process, the frequency of the beam would typically be tuned within the vicinity of the atomic transitions involving the spin state of interest, e.g. circularly polarised light that drives σ^- transitions tuned in the vicinity of $6^2S_{1/2}F = 4 \rightarrow 6^2P_{3/2}F' = 3$ transitions would pump orientation to the $F = 4, m_F = -4$ ground state. Although $m_F = -4$ is a dark state, the pump beam is still partially coupled to the spin state through coupling to the $F = 4 \rightarrow F' = 5$ transition. If the pumping rate is higher than the spin relaxation rate, i.e. causing power broadening, then it will lead to relaxation of the Zeeman coherence (described in Sec. 2.4.3). Indirect-pumping operates with the pump light optically decoupled from the target spin state, e.g. orientation of the same $F = 4, m_F = -4$ state can be achieved with the pump tuned to the $F = 3 \rightarrow F' = 2$ closed transition. The remainder of this section discusses the mechanism involved in indirect pumping. Note: the $6^2S_{1/2}$ and $6^2P_{3/2}$ notation will be dropped for the rest of this chapter, but all cases consider the Cs D2 line without exception.

By measuring the atomic population distribution within (and between) the $F = 3$ and $F = 4$ ground state manifolds, it is possible to determine the efficacy of the ground state pumping. This can be achieved with so-called ‘rf spectroscopy’ [17, 70], where the amplitude of the individual $\Delta m = \pm 1$ Zeeman coherences for each ground state can be measured. This technique takes advantage of the magnetic field dependent Zeeman shift between first, the $F = 3$ and $F = 4$ levels, and second, the individual Zeeman coherences within the same hyperfine ground state. Firstly, the difference in the Larmor frequency between the hyperfine ground state levels is due to the difference of Landé hyperfine g -factors

$$g_{F=I\pm 1/2} = \frac{1}{\mu_B} \left(-\frac{\mu_I}{I} \pm \frac{-\mu_I/J + \mu_I/I}{2I+1} \right), \quad (3.1)$$

where (for caesium, nuclear spin $I = 7/2$) the nuclear magnetic moment is $\mu_I = -2.582025(4)\mu_N$, where μ_N is the nuclear magneton, and the magnetic moment of the ground state electron

($J = I + L$ where $L = 0$) is $\mu_J = -1.001159652(41)\mu_B$ [17]. This results in $g_{F=4} = 0.250390$ and $g_{F=3} = -0.251194$ ($\gamma_{F=4}/2\pi \approx 3.505$ Hz/nT and $\gamma_{F=3}/2\pi \approx -3.516$ Hz/nT), which corresponds to approximately a shift between the $F = 3$ and $F = 4$ state of $\nu_{F=3} - \nu_{F=4} = 11.3$ Hz per $\nu_L = 35$ kHz ($B_0 = 1$ μ T). Secondly, the nonlinear Zeeman (NLZ) effect contributes a frequency shift ω_{NLZ} between the individual $\Delta m = \pm 1$ Zeeman coherences and is approximated by

$$\omega_{\text{NLZ}} \approx \frac{2\omega_L^2}{\omega_{\text{hfs}}}, \quad (3.2)$$

where $\nu_{\text{hfs}} = 9.193$ GHz is the frequency of the hyperfine splitting. Equation 3.1 and 3.2 can be found in [17].

The data shown in Fig. 3.1 (a) and (b) (reprinted from [57]) used rf spectroscopy to plot the change in amplitude of the individual Zeeman coherences in the $F = 4$ and $F = 3$ manifold, respectively. The Zeeman coherences were measured using the off-resonant probing configuration that is described in Sec. 3.2.2. The insets show the amplitudes of the individual $F = 4$, $m_F = -4 \leftrightarrow -3, \dots, 3 \leftrightarrow 4$ and $F = 3$, $m_F = -3 \leftrightarrow -2, \dots, 2 \leftrightarrow 3$ peaks, respectively. The coloured lines in plots (a) and (b) describe how the amplitude of the corresponding Zeeman coherence (marked with text) change with the power of the pump beam (tuned to $F = 3 \rightarrow F' = 2$). The bias magnetic field is set so that $\omega_{\text{NLZ}}/2\pi = 55$ Hz and the rf spectra shown in the insets were recorded with a pump power of ~ 0.5 μ W. The pump and probe beams were expanded to 38 mm before being passed through a 20-mm-diameter aperture to flatten the intensity profile so that it approaches a ‘top-hat’ beam. This is done to reduce the inhomogeneity in the vector light shift introduced by the inhomogeneities in the intensity profile of the pump beam (discussed in Sec. 2.1.3), i.e. strong gradients in intensity are equivalent to magnetic gradients. Both the pump and the probe beams fill the cell. The impact of the probe beam power and detuning is discussed in the following section, but for this experiment they are both constant and do not influence the pumping. These results were recorded within magnetic shielding.

Since the pump beam is tuned to the $F = 3 \rightarrow F' = 2$ transition, it is expected that atomic orientation of the $F = 3$, $m_F = -3$ state will begin to be built up as the pump power is increased, e.g. this is visible at ~ 10 μ W in Fig. 3.1 (b). However, atomic orientation is also built up in the $F = 4$, $m_F = -4$ state, which is unexpected since the pump is 9 GHz away from the transitions involving the $F = 4$ ground states. It was found that SECs between atoms in the $F = 3$ and $F = 4$ ground state replicates the resonantly-pumped polarisation seen in the $F = 3$ manifold in the $F = 4$ manifold. When the pump power was increased further (> 10 μ W), it begins to depopulate the $F = 3$ level by increasing the probability of $F = 3 \rightarrow F' = 3, 4$ transitions, which have a decay pathway to the $F = 4$ manifold. SECs redistribute some of

this population back to the $F = 3$ manifold. However, as the stretched states are partially immune to SECs, population will build up in the $F = 4$, $m_F = -4$ state after repeated cycles of pumping, decay, and SECs. It should be noted that with increasing beam power the pumping process is also assisted by the Doppler broadened transitions involving the $F = 3$ ground state; creating a non-negligible probability of $F = 3 \rightarrow F' = 3, 4$ transitions that transfer population to the $F = 4$ ground state through decay pathways from the excited state. This study found that a maximum orientation of 92% was achieved in the ~ 100 - $1000 \mu\text{W}$ pump power range

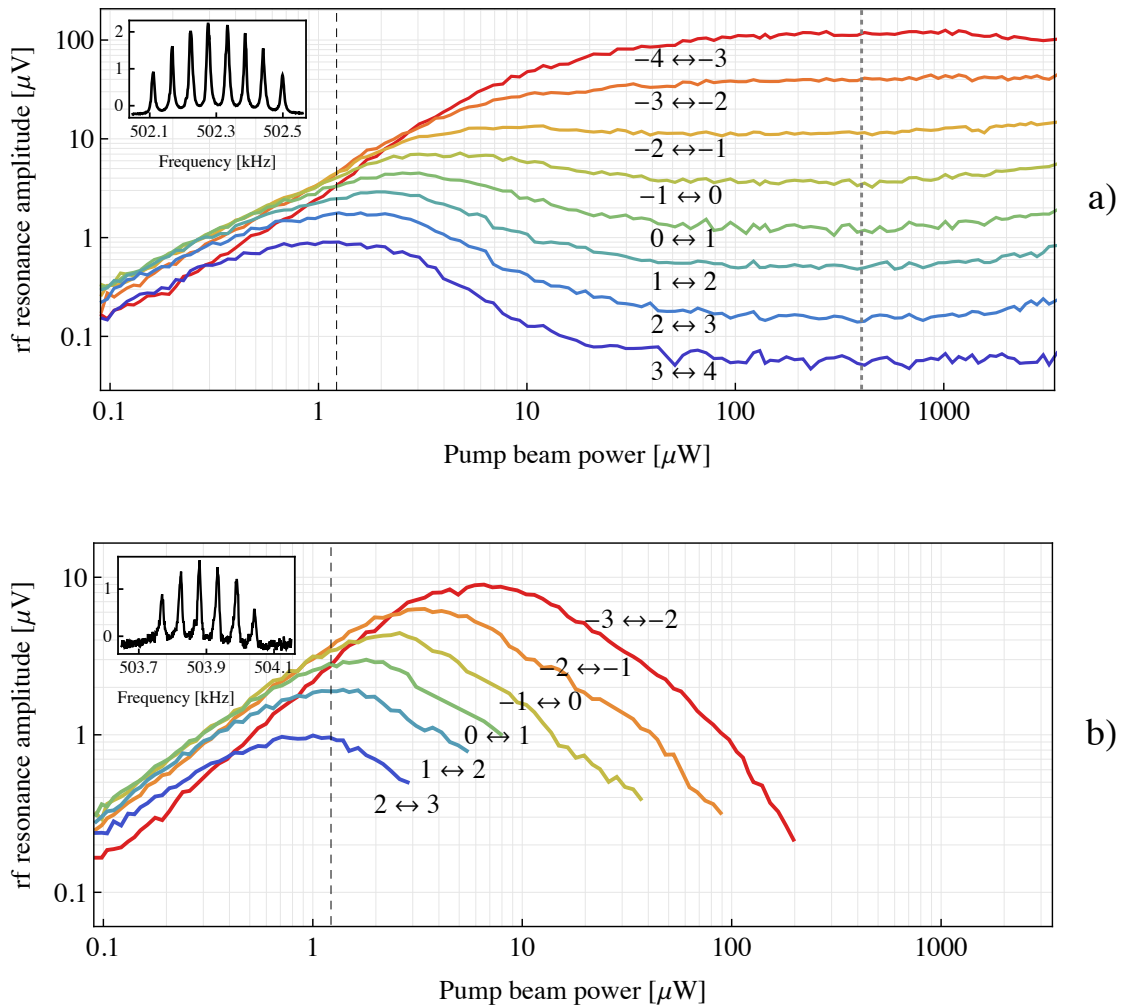


Figure 3.1: Plots of the amplitude of the individual Zeeman coherence for the (a) $F = 4$ and (b) $F = 3$ ground states for changing power of the pump tuned to $F = 3 \rightarrow F' = 2$. These are recorded from the individual peaks in the rf spectrum (e.g. inset in both recorded at $\sim 0.5 \mu\text{W}$) recorded at a magnetic field strength with a significant contribution from the nonlinear Zeeman effect. These results were recorded in magnetic shielding. This figure was reprinted from [57].

for a temperature of 32°C. At greater powers the coherence amplitude begins to contract. It is expected that this is due to the pumping strength leading to power broadening, although the exact dynamics of this process require further study. At temperatures > 32°C, SEC collisions become more dominant and the coherence amplitude also begins to contract. At the temperature used in this work (room temperature 22°C) it was found that the maximum orientation decreased to 85%. The decrease is likely due to the reduction in the population transfer between the $F = 3$ and $F = 4$ levels since this is partly facilitated by SEC.

When operating below $\nu_L = 100$ kHz the nonlinear Zeeman effect is smaller than the ground state relaxation rate (~ 2 Hz), i.e. there is negligible separation between m_F levels, and the rf spectrum has a single peak. The amplitude of this peak represents the sum of the collective Zeeman coherence amplitudes for the ground state manifold. The optimum pumping power can be determined by optimising the amplitude of the single measured peak. The orientation achieved in the work reported in this thesis is estimated to be at a similar level to that in [57].

3.2.2 Off-Resonant Probing

From the discussion of the probe in Sec. 3.1.2, it is desirable to minimise any perturbations introduced by the probe light on the measured spin state [36]. The two most significant contributing factors are the probe detuning from the relevant atomic transitions and the power of the beam. The effects of these parameters are linked, as demonstrated in Sec. 3.2.2.3. Studies presented on both parameters were carried out in magnetic shielding.

3.2.2.1 Probe Detuning

To investigate how the probe light interacts with the two ground state levels, the amplitude of the $F = 3$ and $F = 4$ Zeeman coherences were measured for different probe detunings. Unlike when investigating the power of the pump beam (where individual coherences are measured since it is important to know the individual sublevel populations), it is sufficient to consider the collective amplitude of the Zeeman coherences, i.e. the rf resonance can be measured at a bias magnetic field strength with a negligible contribution from the nonlinear Zeeman effect (discussed at the end of Sec. 3.2.1). Figure 3.2 shows the rf spectrum containing profiles for the $F = 4$ ($\nu_L = 22.454$ kHz) and $F = 3$ ($\nu_L = 22.523$ kHz) ground state recorded at $B_0 \approx 9.3$ μ T. The relevant information from these data are the peak amplitude and width of the blue (in-phase, see Sec. 2.5.1) component in Fig. 3.2.

For this investigation the pump beam is tuned to the $F = 3 \rightarrow F' = 2$ transition and has a power of 0.65 μ W, while the probe beam has a power of 1 mW (diameter of and intensity profile of

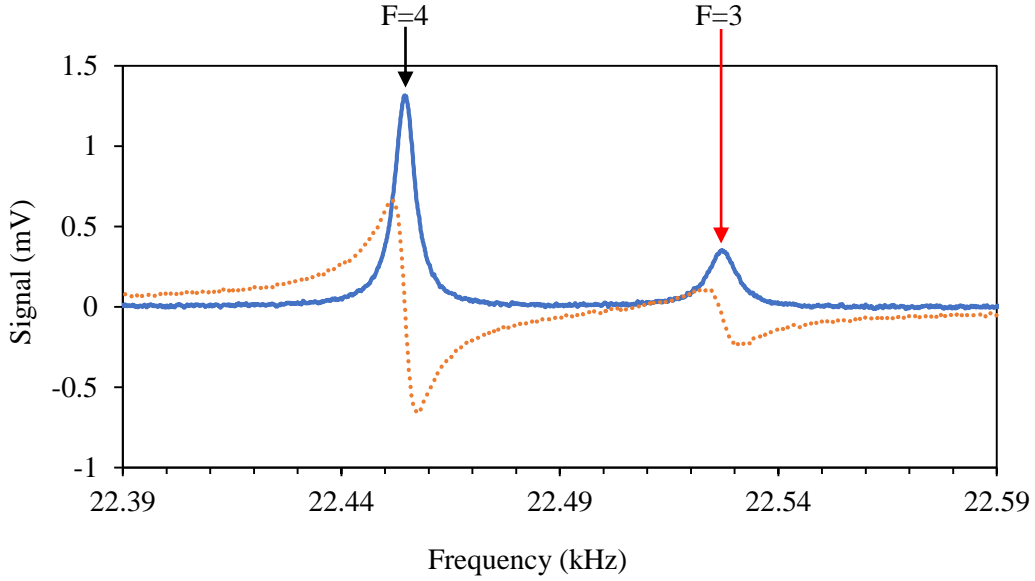


Figure 3.2: Plot of the two quadrature components, X (blue line) and Y (dotted orange line), of the rf spectrum containing contributions from the $F = 4$ and $F = 3$ Zeeman coherences, marked with black and red arrows, respectively. The power of the circularly polarised pump and the linearly polarised probe were $0.49 \mu\text{W}$ and $230 \mu\text{W}$, respectively, and the bias field was set to $B_0 = 9.3 \mu\text{T}$.

both beams are the same as the pump described in Sec. 3.2.1). The purpose is to investigate the region where the probe beam dominates the atomic-light interaction, which is why the probe beam is strong relative to the pump. However, a weak pump beam is still required so that there is a measurable signal when the detuning of the probe is large.

Figure 3.3 shows how the (a) amplitude and (b) linewidth of the rf spectra that represent the Zeeman coherences of the $F = 4$ (black diamonds) and $F = 3$ (red circles) ground states change as the detuning of the probe is scanned through the transitions involving the $F = 4$ (black vertical lines) and $F = 3$ (red vertical lines) ground states. The detuning is measured with respect to the frequency of the $F = 3 \rightarrow F' = 2$ transition. The amplitude is measured to be the peak value of the rf spectra and the linewidth is measured through fitting of a Lorentzian (where possible), as described in Sec. 2.5.1. Note: the figure inset here is relevant to the discussion in Sec. 3.3.1.

This study confirmed that the probe beam mostly exhibits an off-resonant interaction, as seen by the dispersive character of the amplitude dependence (centred on the respective group of transitions for each ground state) and is characterised by regions where the linewidth of the rf spectrum is constant and the amplitude varies slowly. For detunings in the vicinity of the atomic transitions that involve the state, there is an absorptive interaction that results in signif-

icant broadening of the measured linewidth. When the detuning of the beam is very close to the groups of atomic transitions, the state involved begins to experience a significant contribution from the tensor light shift (visible in the results presented later in Sec. 3.3.2.1) and the linearly polarised beam contributes to the pumping mechanism. These combine to drastically reduce the amplitude of the rf resonance and distort the lineshape. As such, these points have been excluded from the linewidth plot [Fig. 3.3 (b)]. For the same detunings, the rf spectral lineshape of the off-resonant state is also significantly distorted by the presence of the broad rf spectrum of the resonant state, e.g. the $F = 4$ component near 0GHz.

From visual inspection of the plots in Fig. 3.3, the region of dispersive interaction is much broader than the region of absorptive interaction, i.e. the broadening of the atomic resonance

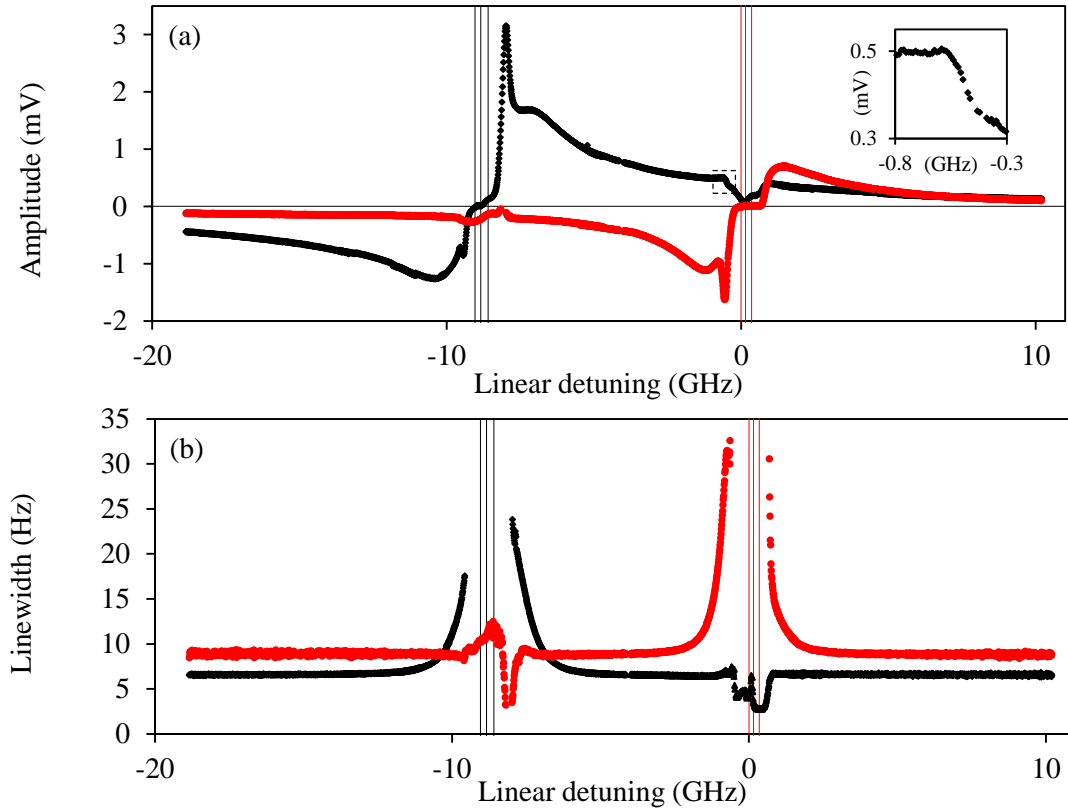


Figure 3.3: Dependence of the (a) amplitude and (b) linewidth of the rf spectrum of the $F = 4$ (black diamonds) and $F = 3$ (red circles) on the detuning of the linearly polarised probe beam. The linear detuning of the probe is measured with respect to the $F = 3 \rightarrow F' = 2$ transition and the beam has a power of 1 mW. The pump is tuned to the $F = 3 \rightarrow F' = 2$ transition and has a power of $0.65 \mu\text{W}$. The group of transitions involving the $F = 4$ and $F = 3$ ground states are marked by black and red vertical lines, respectively. Note: the inset in (a) plots the data within the dashed black box and is relevant to the discussion in Sec. 3.3.1.

decreases more rapidly than the amplitude. The difference in the rate of change of these parameters presents an optimum detuning where there is negligible broadening, but still a considerable amplitude. This follows with what is expected from the Kramers–Kronig relation in Sec. 2.2.3 where the absorptive and dispersive Lorentzian profiles respectively follow a $1/\Delta^2$ and $1/\Delta$ dependence away from resonance ($\Delta > \Gamma$).

It should be noted that the presence of weak magnetic field gradients within the magnetic shield cause ~ 5 Hz of broadening of the measured linewidth. The source of gradients is from the partial electrification of the magnetic shields. This is due to perishing of the insulation that covered the wires supplying current to the solenoid that defines the bias magnetic field. Also, the linewidth of the $F = 3$ ground state is broadened by an additional ~ 3 Hz, since the pump beam is directly coupled to $F = 3$ level. This shows the benefit of using the indirect pumping scheme described in Sec. 3.2.1.

3.2.2.2 Sign of the Measured Coherence Amplitude

Figure 3.3 (a) shows the amplitude of the polarisation rotation signal (demodulated X component). Since the dependence of the amplitude on the probe detuning is dispersive, the sign of the amplitude changes when passing through the resonance, i.e. from red (+) to blue (-). The direction of the rf magnetic field also influences the sign of the coherence amplitude. In this experiment, the rf magnetic field is directed along the probe beam. The influence of the rf field direction is described fully in Sec. 7.3.1. However, at this stage it is sufficient to say that although the $g_{F=4}$ and $g_{F=3}$ factors have opposite signs (see Sec. 3.2.1) - meaning the $F = 3$ and $F = 4$ states precess in opposite directions - when the rf magnetic field is directed along the probe beam the amplitude of both the $F = 3$ and $F = 4$ Zeeman coherence have the same sign. Hence the measured amplitude of both states is positive and negative for red and blue detuning, respectively.

3.2.2.3 Probe Power

A key finding of these investigations was that the same SNR could be achieved for different probe power detunings by changing the power of the probe beam. Figure 3.4 (a) plots the amplitude of the rf spectrum (blue circles) and total noise (brown squares) - sum of electronic, atomic, and photon-shot noise - for different probe beam powers (recorded within magnetic shielding). The probe beam is detuned by +1.4 GHz from the $F = 3 \rightarrow F' = 2$ transition and the green diamonds represent the SNR ratio. The SNR can be seen to saturate at $\times 10^4$ for a power of $500 \mu\text{W}$. A pump power close to saturation of the rf coherence ($100 \mu\text{W}$) was used for these measurements so that a significant SNR ratio could be measured. Specific

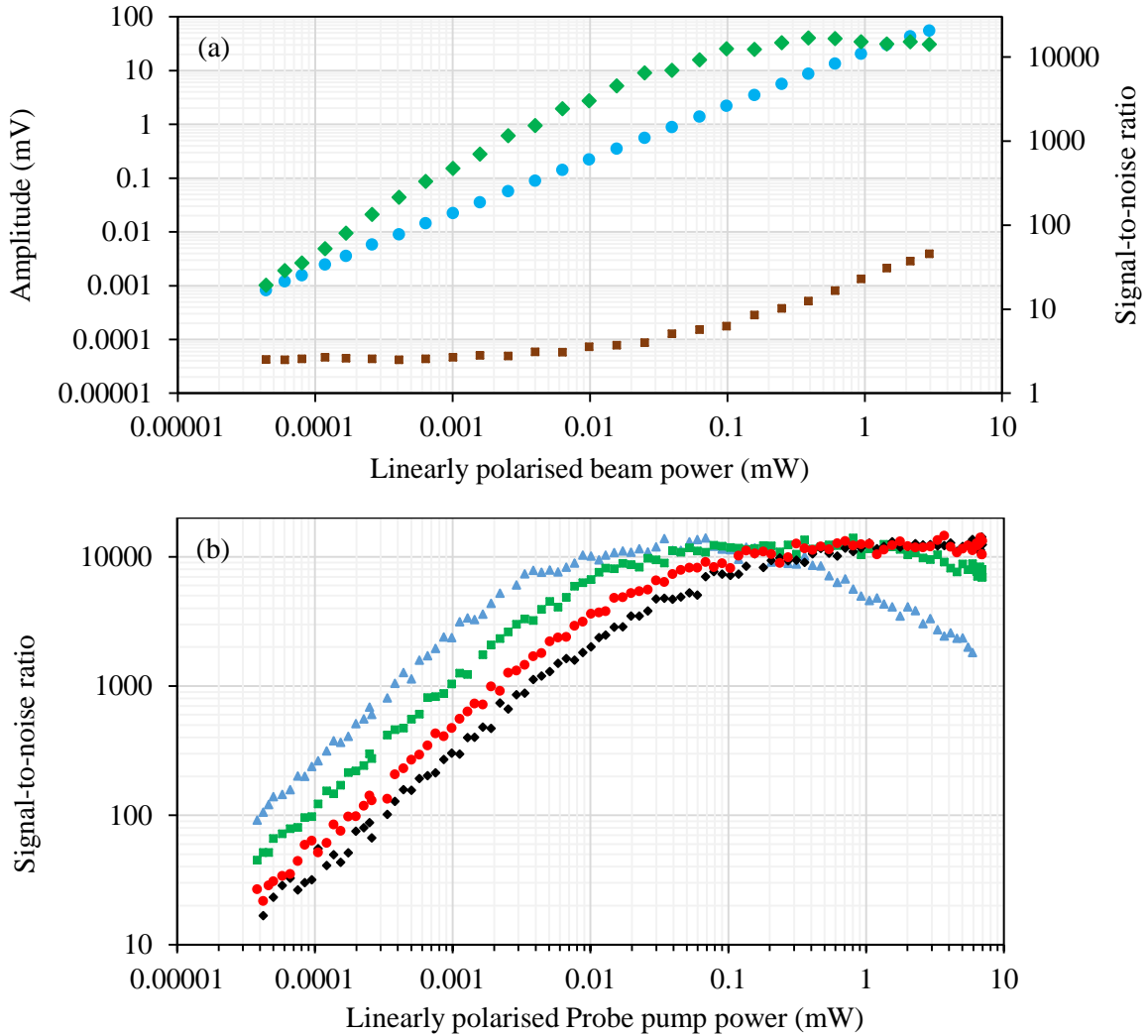


Figure 3.4: Plot of how probe beam power affects the SNR ratio. (a) Amplitude of the rf spectrum (blue circles) and total sum of electronic, atomic, and photon-shot noise (brown squares). The probe beam is detuned by 1.4 GHz from the $F = 3 \rightarrow F' = 2$ transition and the green diamonds represent the SNR ratio. (b) SNR ratio for a linear detuning of +0.6 GHz (blue triangles), +1.2 GHz (green squares), +2.4 GHz (red circles) and +3.9 GHz (black diamonds).

studies on the influence of pump power on SNR have not been conducted in this work as this would be similar to that presented in [57] (Sec. 3.2.1), but the pump power is set such that it does not contribute to power broadening of the magnetic resonance (i.e. below saturation). Figure 3.4 (b) plots the SNR ratio against probe power for linear detunings of: $\Delta = +0.6$ GHz (blue triangles), $\Delta = +1.2$ GHz (green squares), $\Delta = +2.4$ GHz (red circles) and $\Delta = +3.9$ GHz (black diamonds). This plot shows that the same SNR can be achieved for different detunings by changing the power of the probe beam, e.g. to achieve an SNR = 1000 with $\Delta = +0.6$ GHz

requires a power of $P \approx 0.4 \mu\text{W}$ while for $\Delta = +3.9 \text{GHz}$ it requires a power of $P \approx 3.8 \mu\text{W}$. It can also be seen that the optimum becomes broader for higher detunings. This is related to the rapid saturation of the atomic transition when the probe is close to the resonance (visible in the change of linewidth of in Fig. 3.3). Generally, this broad optimum is useful as it reduces the dependency on the stability of the laser frequency. Note: a smaller pump power was used in Fig. 3.4 (b) than in (a), which accounts for the factor of 2 difference in peak SNR. The presence of an optimum in the SNR ratio as the probe power is increased indicates the transition from a regime of negligible absorption, to a regime where the probe light begins to pump the atoms (i.e. interplay between absorption and dispersion). The choice of probe power or detuning then simply becomes an issue of experimental convenience.

3.2.3 Sensitivity

The two-beam (indirect-pumping and off-resonant probing configuration) that has just been described is used for the rf magnetometer that was built to carry out MIT measurements in a magnetically unshielded environment. The setup is described in Chap. 4; however, this section, which is on the estimation of its sensitivity, is given here to follow on with the discussion of the magnetometer performance. This section provides an estimation of the sensitivity of the rf magnetometer operating in an unshielded environment. The aim of this work was not to squeeze the greatest possible sensitivity out of the sensor, but to construct one that can operate in a functional environment, e.g. in the presence of magnetic gradients and noises.

The magnetometer's sensitivity can be determined by calibrating the amplitude of the rf spectrum against a known magnetic field. The work of Chalupczak et al. [57] (presented in Sec. 3.2.1) used a cell volume of 14.5cm^3 that was heated to 32°C to achieve an atomic projection noise limited sensitivity of $1 \text{fT}/\sqrt{\text{Hz}}$ [6]. This sensitivity was determined by calculating the strength of an rf field that saturates the Zeeman coherence and calibrating the measured magnetometer signal in units of magnetic field. The field strength was calculated through two separate methods. First, the strength of the rf field that saturates the Zeeman coherence was calculated from the broadening of the rf resonance. Second, the rf field strength determined from the first method was verified through simulation of the rf coil with the Biot-Savart equations and the current supplied to the coil. The former methodology was used in this work and it gives a conservative estimate of the sensitivity of the rf magnetometer. It is described in what follows.

In the same way as a light field would saturate an optical transition, the rf magnetic field can be said to saturate the Zeeman coherence when the linewidth of the rf resonance is broadened by a factor of $\sqrt{2}$. In the work that supported Chalupczak et al. [6], the unsaturated linewidth was

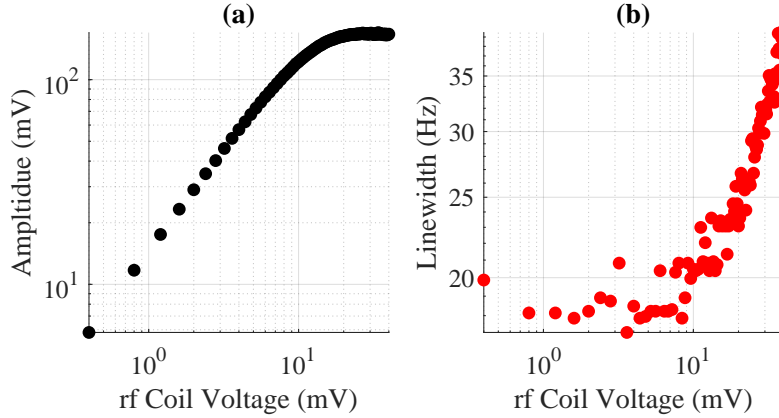


Figure 3.5: Data for (a) amplitude (black circles) and (b) linewidth (red circles) of the rf spectrum recorded as the driving voltage of the rf coil is increased. The averaged unbroadened linewidth is determined to be $\Gamma = 18.5$ Hz for an rf coil voltage of ≤ 18 mV. Saturation of the atomic coherence occurs when the linewidth of the rf spectrum is $\sqrt{2} \times \Gamma = 26.2$ Hz, for an rf coil voltage of 25.2 mV.

found to be $\Gamma_0 = 2.408$ Hz. The rf field that saturated the Zeeman coherence broadened the linewidth to $\sqrt{2}\Gamma_0 = 3.406$ Hz. Here, the atomic density was $n_{Cs} = 3.3 \times 10^{10} \text{ cm}^{-3}$ (22 °C), which is the same as was used in this work. It is assumed that this broadening (defined as $\Delta\Gamma_{\text{SAT}} = \sqrt{2}\Gamma_0 - \Gamma_0 = 0.998$ Hz) in terms of Larmor frequency can be translated linearly to an rf magnetic field amplitude of 0.285 nT ($B_{\text{rf}} = \Delta\Gamma_{\text{SAT}}/\gamma$). This value was supported by the simulation of the magnetic field strength through the dimensions of the rf coil and the supplied current⁸. The determination of the strength of the saturating rf magnetic field meant that the magnetometer signal could be calibrated.

This work used the same methodology and results from Chalupczak et al. [6] to estimate the sensitivity of the rf magnetometer built for this thesis. Figure 3.5 shows the dependence of the amplitude (a) and linewidth (b) of the rf spectrum on the voltage that drives the rf field coil. The 1.7 cm^3 cell used in this work has an intrinsic linewidth of $\Gamma_0 = 2$ Hz, which due to inhomogeneous broadening increases to $\Gamma = 18.5$ Hz. If an rf field broadens Γ_0 by a factor of $\sqrt{2}$, it is *assumed* that the same rf field strength will also broaden Γ by a factor of $\sqrt{2}$. This assumption effectively ignores the inhomogeneous broadening due to the presence of magnetic field gradients and residual 50-Hz magnetic field noise, assuming that when the rf magnetic field saturates the Zeeman coherence the resonance will always be broadened by a factor of $\sqrt{2}$. The rf spectrum saturates at $\Gamma_{\text{SAT}} = 26.2$ Hz with an rf coil voltage of 25.2 mV. This corresponds to an rf magnetic field amplitude of 0.285 nT (found through the systematic

⁸Unpublished accompaniment to [6].

measurements that supported [6] described in the previous paragraph).

What follows describes how the measured polarisation rotation signal can be calibrated in units of magnetic field. When the saturating rf field is applied, the amplitude of the polarisation rotation signal will correspond to a known field value. This field will also correspond to a known voltage that has been supplied to the rf coil. Since it can be assumed that the relationship between applied voltage and resultant rf field strength is linear, the coil voltage can be calibrated in terms of field strength. For rf field amplitudes less than the saturating value, the relationship between rf field strength and the amplitude of the polarisation rotation signal is also linear. From these relations, it is possible to calibrate the measured amplitude of the polarisation rotation signal in units of magnetic field.

A spectrum analyser (Keysight Technologies Agilent N9010A Swept Spectrum Analyser) was used to record the amplitude spectral density of the polarisation rotation signal, which gives a measure of the amplitude per bandwidth (units $V_{\text{rms}}/\sqrt{\text{Hz}}$) [71]. Applying an rf field that saturates the atomic coherences results in an on resonance ($\omega_{\text{rf}} = \omega_L$) polarisation rotation signal amplitude of $R_{\text{peak}} = 167\text{mV}$, which is equal to the peak value of the on resonance signal. The signal is then normalised by the value R_{peak} (units $1/\sqrt{\text{Hz}}$) and then multiplied by the saturating field strength. The spectrum is now in units $\text{T}/\sqrt{\text{Hz}}$. The black line in Fig. 3.6 shows the on-resonant rf magnetometer signal for an rf field of $\sim 44\text{pT}/\sqrt{\text{Hz}}$, normalised against the calibrated rf field. Also plotted are the atomic projection (red), shot noise (cyan), and electronic (magenta) noise. The data is an average of 50 measurements, recorded with a 1 Hz bandwidth on a spectrum analyser.

The contribution from atomic projection noise is expected to be $\sim 5\text{fT}/\sqrt{\text{Hz}}$ ⁹ and is measured by removing the rf magnetic field. The presence of ambient oscillating magnetic fields over a broad range of frequencies is responsible for elevating the profile of the atomic noise contribution to $\sim 50\text{fT}/\sqrt{\text{Hz}}$ - the broad pedestal visible for both the black and red line in Fig. 3.6. For example, this ambient field consists of resolved frequency components, like the spike visible at 30kHz. Such noise features only become apparent in the magnetometer signal when they are close to ω_L and their presence slightly raises the amplitude of the broad pedestal the closer the noise spike is to ω_L . The measurement was recorded at this frequency as it is between nearby noise spikes. In other investigations it was found that an rf magnetic field with a broadband (0 – 100kHz) white noise frequency profile could be used to elevate the amplitude of this broad pedestal¹⁰ [13]. The ambient rf magnetic field likely contains similar

⁹Atomic projection noise scales with $1/\sqrt{N_{\text{atoms}}}$. In [6] projection noise is $1\text{fT}/\sqrt{\text{Hz}}$ and has a factor of ~ 30 times the number of atoms than in this work. This is in agreement with prediction in Sec. 2.5.2.

¹⁰The atoms act as bandpass filter and are driven by the frequency components of the white noise that span the ‘bandwidth’ of the rf resonance. This bandwidth can be defined as the linewidth of the rf spectrum. Since the atoms are driven by noise, there is no phase information contained within this signal.

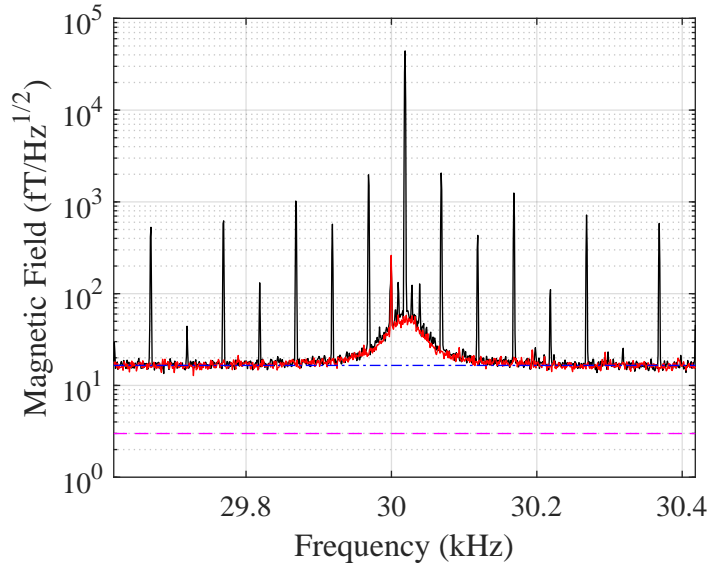


Figure 3.6: FFT of the on-resonant rf magnetometer signal (black line) calibrated in terms of rf magnetic field strength. The atomic projection noise (red line) has been elevated by some broadband environmental magnetic field noise. The blue dashed-dotted and magenta dashed lines represent the shot and electronic noise level, respectively.

broadband noise components, with a broad frequency profile that adds to the amplitude of the broad pedestal in the rf magnetometer signal.

From the calibration of the rf magnetic field, the level of the shot (dashed-dotted blue line) and electronic (dashed magenta line) noise in Fig. 3.6 are measured to be $16 \text{ fT}/\sqrt{\text{Hz}}$ and $3 \text{ fT}/\sqrt{\text{Hz}}$, respectively. The electronic noise of the same photodetector was measured to be $< 0.4 \text{ fT}/\sqrt{\text{Hz}}$ (the shot-noise level) by Chalupczak et al. when operating in a magnetically shielded environment [6]. From this it can be inferred that the sensitivity calculation here is a conservative estimate. Additionally, in the work carried out by Dr. J. Rajroop [72] (operating in a partially shielded environment, but with an unsaturated linewidth of $\Gamma = 25 \text{ Hz}$ - broader than that achieved in this work) the sensitivity was determined to be $\sim 7 \text{ fT}/\sqrt{\text{Hz}}$, through careful optimisation of the sensor.

3.2.4 Summary

The optimised two-beam configuration presented here is ideal for evaluating the general characteristics of the rf magnetometer for applications in MIT. Its operation is well understood, making it easy to untangle effects related to the magnetometer and those related to MIT. From a practical perspective it would be preferable to operate the sensor with a single laser. As

such, the following section presents a novel configuration for achieving a similar pumping and probing geometry with a single light source.

3.3 Orientation with a Single Linearly Polarised Beam

This section introduces the observation of an interesting and highly non-trivial laser configuration for generating an oriented atomic polarisation with a single linearly-polarised beam. The role of the laser beam in this configuration goes beyond the simple action of the pump and probe, since the effect includes the nonlinear interaction (tensor light shift) and evolution (SEC) of the spin states driven by the laser light. However, the focus of this discussion is centred on how to prepare this configuration. The nonlinear dynamics involved are the subject of their own topic, and a full description would require further investigations in a dedicated piece of work. However, it is still worth including these results in this thesis to show how the rf magnetometer can be simplified in future applications of this sensor.

The results presented here were recorded within magnetic shielding as the purpose was to explore the fundamental aspects of the operation of the rf magnetometer. However, the same findings were confirmed in the unshielded setup. The performance of the configuration is only compared qualitatively to the optimised two-beam laser configuration presented in the previous section.

The single laser used in this section is the same as the Vescent laser used for the probe beam in the previous section. It has been assumed that the linewidth of the laser frequency spectrum is narrow (< 1 MHz) [69].

3.3.1 Generation of an Oriented State

In the analysis of the role of the probe detuning in Sec. 3.2.2.1, the inset in Fig. 3.3 shows a slight upturn in the amplitude of the $F = 4$ state when the probe detuning is around -600 MHz from the $F = 3 \rightarrow F' = 2$ transition, before it sharply decreases due to the on-resonant interaction of the light with the group of $F = 3$ transitions. The data was recorded with a pump and probe beam power of $1 \mu\text{W}$ and 1mW respectively. Since the pump beam is so weak, the slight upturn in the $F = 4$ signal indicates that the off-resonant probe beam contributes to the polarisation of the $F = 4$ ground state level manifold. Further investigation found that increasing the power of the linearly polarised beam increased the amplitude of the $F = 4$ signal. The results and discussion in this section present the dependence of the $F = 4$ signal amplitude

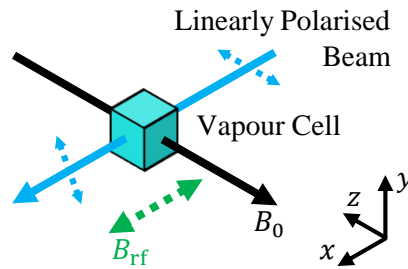


Figure 3.7: Schematic diagram of the setup for the single-laser configuration consisting of a linearly polarised beam propagating along the x -axis, perpendicular to the bias magnetic field B_0 (directed along the z -axis). This beam pumps an atomic polarisation. The polarisation of the beam is parallel to B_0 and an rf magnetic field B_{rf} (directed along the x -axis) drives Zeeman coherences, rotating the angle of linear polarisation via the paramagnetic Faraday effect.

on the power of a linearly polarised beam that is far detuned from transitions involving the $F = 4$ hyperfine ground state level and show that this beam generates atomic orientation in this hyperfine manifold.

To investigate the role the linearly polarised beam is playing, the circularly polarised beam that propagates parallel to the bias magnetic field and acts as the pump was removed. This leaves only a single linearly polarised beam that propagates orthogonally to the bias magnetic field, as depicted in Fig. 3.7. The angle of the polarisation is parallel to the bias magnetic field and the beam has a diameter of 20mm (the beam is the same as the probe used for the two-beam configuration, Sec. 3.2). The power of the single linearly polarised beam was increased while measuring the amplitude of the Zeeman coherence. These data are shown by the black triangles Fig. 3.8 (a). As the beam power is increased then the amplitude dependence changes (at 2mW) from linear to quadratic, indicating the start of a nonlinear process. It was suspected that this change in dependence was caused by the transition from pumping an aligned atomic polarisation in the $F = 4$ ground state manifold, to pumping an oriented atomic polarisation. To check this, the amplitude dependence was measured again in the presence of a weak (constant $17\mu\text{W}$) circularly polarised beam. This beam is applied along the bias magnetic field and acts like the pump beam described in Sec. 3.2.1 for the two-beam configuration. The blue diamonds and red points in Fig. 3.8 (a) represent measurements with the two orthogonal polarisations of the circularly polarised beam. For powers $< 2\text{mW}$, the amplitude of the signal created with the addition of the two orthogonality polarised beams is equal. For powers $> 2\text{mW}$ the amplitudes generated by the two begin to diverge. This indicates that the polarisation generated by either beam is either aiding (blue diamonds), or competing (red points), with the atomic polarisation generated by the linearly polarised beam. Since it is known that a circularly polarised beam generates an oriented atomic polarisation, it

can be inferred that the linearly polarised beam is generating an oriented atomic polarisation. This is also confirmed by analysing the lineshape of the rf spectra. Figure 3.8 (b) and (c) show the X and Y component of the $F = 4$ rf spectrum in the three conditions just described. These were measured with a linearly polarised beam power of 12.4 mW. The black line represents the profile recorded with only the linearly polarised beam. The blue dotted line represents the case where the orientation generated by the circularly polarised beam coincides with that generated by the linearly polarised beam, increasing the amplitude. The red dashed line describes

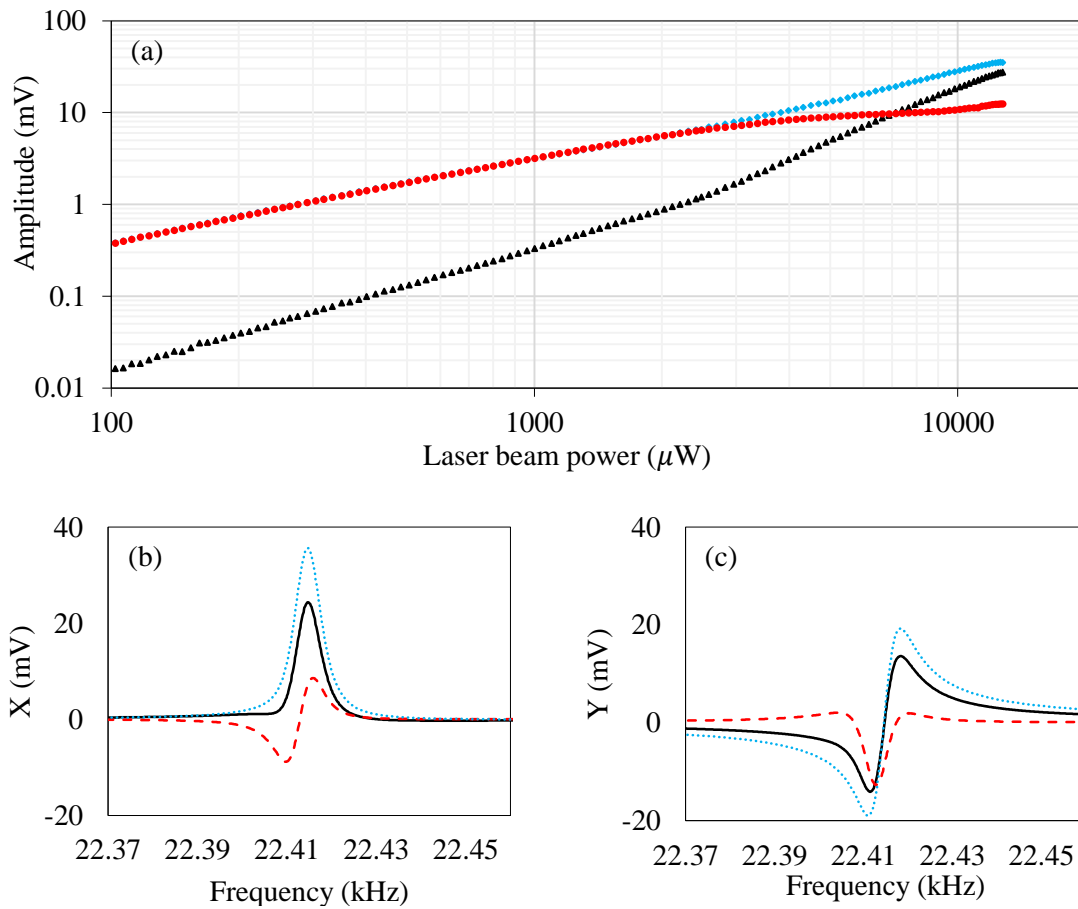


Figure 3.8: (a) Plot of the dependence of the amplitude of the $F = 4$ Zeeman coherence on the power of the linearly polarised beam recorded for the three configurations: linearly polarised beam only (black triangles) and in the presence of a weak pump beam (power $17 \mu\text{W}$) with either of the two orthogonal circular polarisations, which aids (blue dotted) and competes (red dashed) with the pumping generated by the linearly polarised beam. Plots of the (b) X and (c) Y component of the rf spectrum recorded for the same three configuration: only the linearly polarised beam (solid black line), with an additional beam which aids (blue dotted), and competes (red dashed) with the orientation of the single beam. All three were recorded with a linearly polarised beam power of 12.4 mW.

the case where the pump has the opposite circular polarisation, i.e. generating a competing orientation to that created by the linearly polarised beam. In this latter case, the pumping of two oppositely oriented states describes the pumping of an aligned state characterised by a dispersive X component and the ‘wings’ on the Lorentzian-like Y component [38] (also seen in the supporting work to [35]). The lineshape generated by the linearly polarised beam only [black line in Fig. 3.8 (b)] is not a perfect Lorentzian, indicating some of the population is still distributed across the $F = 4$ hyperfine manifold.

Since this measurement has been carried out at a field strength where there is negligible splitting between the individual Zeeman coherences, the single line plot presented in Fig. 3.8 (a) is equivalent to taking the sum of the individual Zeeman coherence amplitudes plotted in Fig. 3.1 (a). The data for the individual Zeeman coherence amplitudes for the power scan of the single linearly polarised beam [Fig. 3.8 (b)] cannot be presented in the same way as Fig. 3.1 (a) because the generation of orientation collapses after a threshold Larmor frequency. This is detailed further in Sec 3.3.2.2.

The maximum SNR ratio of this single laser pumping and probing scheme was found to be ~ 0.75 times that of the optimum SNR achieved in the separate pump and probe configuration described in Sec. 3.2. Removing the need for a second laser drastically reduces the complexity of the sensor, while maintaining a comparable SNR ratio to the two-beam configuration. A full sensitivity calibration was not carried out; however since the sensitivity of the separate pump and probe configuration was $1 \text{ fT}/\sqrt{\text{Hz}}$, a conservative estimate is that this single laser scheme will be $< 10 \text{ fT}/\sqrt{\text{Hz}}$, which is the limit of the best demonstrated sensitivity with a single laser found in the literature [67].

The reader should note that the purpose of this thesis is to present and review the practical consideration of the rf magnetometer, specifically for applications in MIT. Although a similar effect has been seen in other situations¹¹, further theoretical and experimental investigations are required to fully untangle the effects at play. The model of the generation of orientation with a linearly polarised beam is thought to combine three elements. (i) A linearly polarised laser beam moves the atomic population from the $F = 3$ to the $F = 4$ manifold through indirect pumping, creating alignment within both levels. The particular frequency detuning of the beam ($\Delta \approx -500 \text{ MHz}$ from $F = 3 \rightarrow F' = 2$) ensures that the majority of the population transferred within the $F = 3$ ground state goes to either stretched state (alignment). This population distribution is then replicated in the $F = 4$ manifold due to indirect-pumping. While the dynamics within the $F = 3$ level is defined by the resonant coupling to the laser field, the $F = 4$ atomic spins evolve only in the presence of weak far-off-resonant optical coupling and SEC. (ii) The weak coupling to the optical field drives nonlinear spin dynamics that

¹¹Private conversation with Dr. Stuart Ingleby.

breaks the population distribution symmetry (tensor light shift leads to a process similar to so-called alignment-to-orientation-conversion¹² [73]) by moving some of the population out of one of the stretched states, effectively making the atoms more prone to SEC relaxation (iii). It is thought that the consequence of these two factors (nonlinear spin dynamics and SEC) suppresses one of the components representing one of the spin directions that contribute to alignment, leading to a single oriented state.

Evidence has been provided that a single linearly polarised beam with a frequency tuned in the vicinity of the $F = 3 \rightarrow F' = 2$ transition, propagating perpendicular to the bias magnetic field (condition for pumping alignment described in Sec. 2.2.1), can build up atomic population in the $F = 4$ hyperfine ground state, while simultaneously probing the Zeeman coherences in the same hyperfine manifold. Tests adding orthogonal circularly polarised beams indicate that for powers of the linearly polarised beam > 2 mW the $F = 4$ hyperfine ground state has an oriented atomic polarisation. These results have been included in this work to highlight the fact that the off-resonant pumping and probing of an oriented atomic polarisation with the two-beam configuration presented in Sec. 3.2 (used for the results for MIT with an rf magnetometer presented in Chap. 6 and 7) can be simplified to a single beam.

3.3.2 Practical Considerations

This section discusses two properties of the single-laser configuration that influence the practicality of this setup for use in an rf magnetometer. First discussed is the amplitude dependence of the $F = 4$ Zeeman coherence on the detuning of the laser, second is the range of Larmor frequencies over which an oriented atomic polarisation can be achieved. Also, a modification is provided, which extends the operational range of Larmor frequencies and improves the pumping mechanism.

3.3.2.1 Narrow Feature for Locking Laser Frequency

Figure 3.9 plots the R component of the rf spectrum as the beam's linear detuning is scanned across the group of transitions involving the $F = 3$ ground state. The position of the rf profiles corresponding to the $F = 4$ and $F = 3$ hyperfine ground state levels are marked with black and red arrows, respectively. There is only the single linearly polarised beam present, with a power of 6.75 mW that is the range that generates orientation in the $F = 4$ state. Significant

¹²It should be noted that the outcome of the light interaction shown here is different to alignment-to-orientation-conversion. Alignment-to-orientation-conversion describes a *periodic oscillation* between an aligned and orientated state. The scheme presented in this thesis shows the transition from pumping a *stable* aligned atomic polarisation to a *stable* oriented atomic polarisation.

splitting of the $F = 3$ state is visible in the range of $\Delta = -500$ MHz to -1500 MHz. This is due to the tensor light shift created by the near-resonant, strong, linearly polarised beam. In the range ($\Delta = -500$ MHz to 750 MHz) there is no signal from the $F = 3$ state as the on-resonant light pumps atoms out of this manifold. The on-resonant interaction of the $F = 3$ state is likely to be the cause of the complicated dependence of the amplitude of the $F = 4$ state over a similar range of detunings ($\Delta = -250$ MHz to 1000 MHz). The purpose of this figure is to show that there is a relatively narrow range over which the linearly polarised beam acts as an off-resonant pump for the $F = 4$ state.

For this measurement the signal maximum is at $\Delta = -500$ MHz. Usefully, the feature is relatively narrow (FWHM ≈ 450 MHz) and can be used to identify the optimal laser frequency to achieve atomic orientation with a single laser. This procedure was successfully tested with a vertical-cavity surface-emitting laser (VCSEL), by scanning the laser current and monitoring the rf magnetometers signal amplitude. At the optimum linear detuning the VCSEL emitted 4 mW of light and was able to enter the regime where orientation is generated; however, VCSELs are not yet available that generate a significantly larger power than this - meaning the sensor would be poorly optimised. The motivation behind testing the VCSEL is that they are low power, compact lasers that are highly attractive for miniaturised atomic sensors [74]. Demonstrating that this scheme is feasible for the rf magnetometer configuration presented in this thesis is a significant step forward in developing a practical sensor. It is suspected that using rubidium (Rb) atoms would be a better choice for the single-laser scheme. The energy splitting between the hyperfine ground state levels in terms of frequency for Cs is $\Delta_{HFS} \approx 9.2$ GHz, while for ^{87}Rb and ^{85}Rb it is $\Delta_{HFS} \approx 6.8$ GHz and 3.0 GHz, respectively. This means the detuning of the off-resonant probe action is much lower. From the studies presented in Sec. 3.2.2 it was shown that it is possible to reach the optimum SNR ratio at lower detunings with less power. Hence, with the use of ^{85}Rb it is expected that it will be possible to reach the optimum SNR, which was not achievable with the power available in this investigation with Cs, and would perform better with the low power available from a VCSEL. This configuration has not yet been tested due to lack of the appropriate lasers.

The frequency spectrum of the single mode diode lasers typically have a single, large frequency component (the laser mode) that sits on top of a low-amplitude, broad ‘pedestal’. It is possible that this single laser pumping process is aided by a low power component of the laser frequency spectrum that is detuned from the central frequency. Further investigations using a very narrow laser, such as the M Squared Ti:Sapphire laser, would be required to unpack the origin of this process.

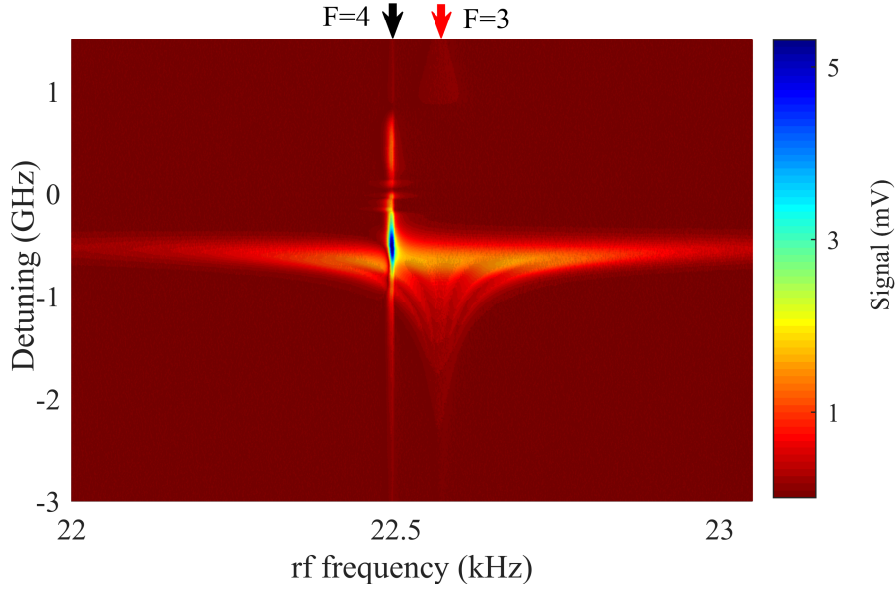


Figure 3.9: Map of the change in amplitude of the rf spectrum, R , with the linear detuning of the single linearly polarised beam from the $F = 3 \rightarrow F' = 2$ transition. The position of the $F = 4$ and $F = 3$ rf resonances are marked with a red and black arrow, respectively. The measurements were made with a laser beam power of 6.75 mW.

3.3.2.2 Degenerate Pump and Probe

A key feature of the described method of atomic orientation through the action of a single linearly polarised beam is that it only occurs over a particular range of Larmor frequencies. Figure 3.10 is a map of the normalised (a) X and (d) Y component of the rf spectrum as the magnetic field is varied. The normalisation compares the rf spectrum recorded in this single-beam case with the optimised two-beam pump and probe configuration to account for any change in the amplitude and phase of the rf spectrum as the bias field is increased. This measurement was recorded with the single linearly polarised laser (beam power of 4.6 mW). The field is plotted in terms of Larmor frequency, while the frequency of the rf field is expressed in terms of detuning from the central frequency of the rf spectrum. Figure 3.10 (b) and (e) plots the X and Y component of the rf spectrum recorded at a field equivalent to $\nu_L = 0.6$ kHz, while the X and Y component shown in Fig. 3.10 (c) and (f) were recorded at a field equivalent to $\nu_L = 204.7$ kHz. As ν_L is increased there is a transition in the lineshape, which corresponds to a change from an oriented [Fig. 3.10 (b, e)] to an aligned [Fig. 3.10 (c, f)] state. The transition between these two polarisation states begins for $\nu_L > 20$ kHz. Once again, the dynamics of the transition between an oriented and aligned state is beyond the scope of this work, which focuses on practical considerations of the rf magnetometer. Further discussion of this process is provided in [11].

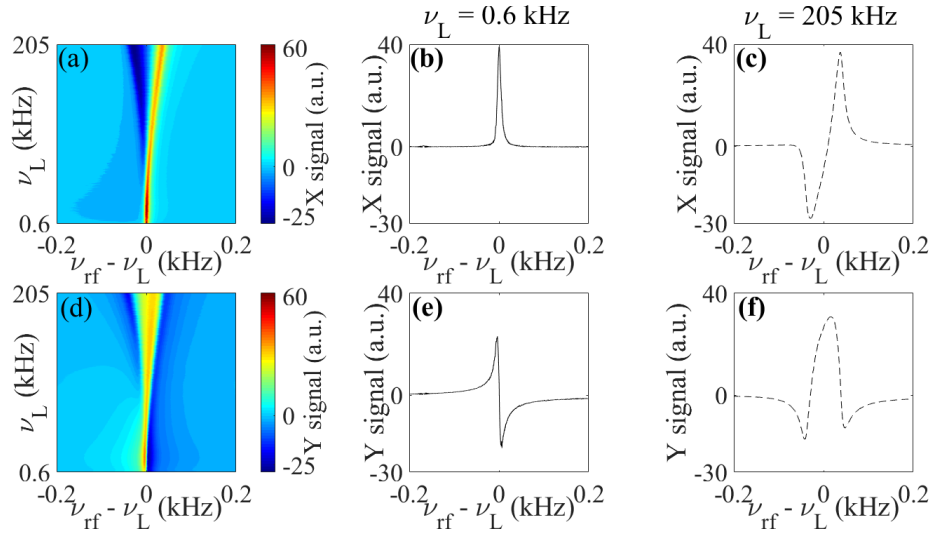


Figure 3.10: Map of the change of (a) X and (d) Y quadrature components of the rf spectrum on the offset magnetic field strength in terms of Larmor frequency, measured with the single linearly polarised beam at a power of 4.6 mW. The frequency of the rf spectra is expressed in terms of the difference from the centre of the rf resonance. Plots (b) and (e) are the X and Y components measured at Larmor frequency of 0.6 kHz, while (c) and (f) are measured at 204.7 kHz.

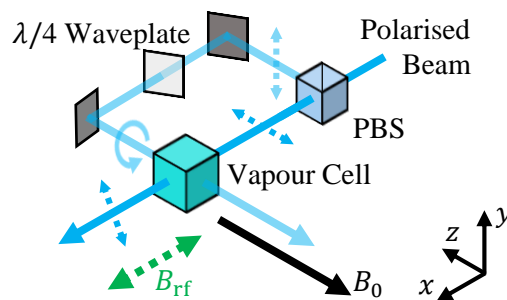


Figure 3.11: Setup for the degenerate pump and probe configuration. Light is split by a polarising beam splitter (PBS). The strong, horizontally-polarised beam that is transmitted by the PBS acts as the linearly polarised beam in the single-laser configuration. The reflected light is circularly polarised with a $\lambda/4$ waveplate such that it aids the polarisation generated by the linearly polarised beam.

The dependence of the generation of an oriented state on the Larmor frequency is introduced to partially disclose the limitation of this novel single laser configuration, but mainly to present a solution to this problem. This issue does not significantly influence applications in magnetic induction tomography, since the rf field frequency range of most interest is $\nu_L < 10\text{kHz}$, as will be discussed in Chap. 5 and 6. However, it is possible to modify the setup (shown in in Fig. 3.11) for the single-laser case to mitigate the dependence of the atomic polarisation on Larmor frequency. Here, the laser light from a single source is split such that there are two-beams with a degenerate frequency. One beam remains as the linearly polarised beam, as described in Fig. 3.7 for the single-beam configuration, and the additional beam that is directed along the bias field is circularly polarised to act as a pump. The circular polarisation of this additional degenerate beam is set so that it assists the orientation generated by the linearly polarised beam, as described in Fig. 3.8. This generates an oriented atomic polarisation across the full range of bias magnetic fields tested in Fig. 3.10. This configuration is still classed as operation with a single laser as there is a single source, but it's referred to as the degenerate pump and probe configuration. The circularly polarised beam is interpreted to be acting as an off-resonant pump for the $F = 4$ atoms in the same way as described in Sec. 3.2, aiding the overall pumping process. Figure 3.12 is a map of the amplitude to the $F = 4$ component of the rf spectrum as the power of the circularly polarised beam and the linearly polarised beam is changed. This measurement was not made in the setup shown in Fig. 3.11 (although this was shown to work), but with two separate beams at the same detuning so that their power could

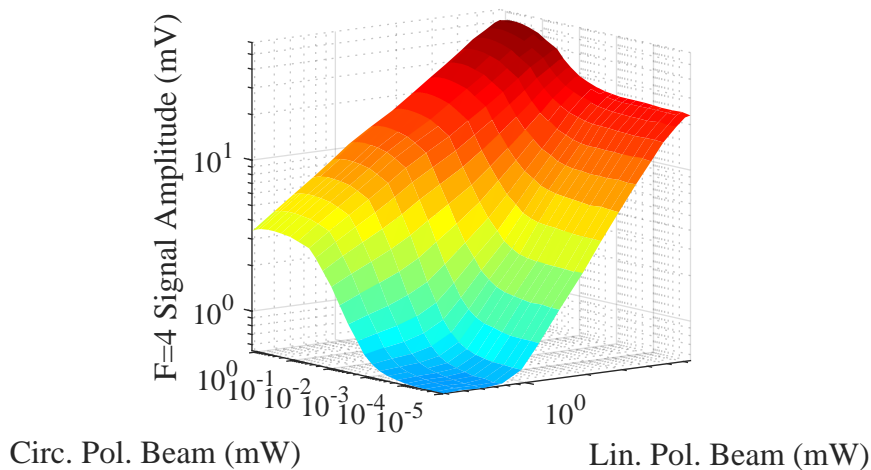


Figure 3.12: Map of the change in amplitude of the $F = 4$ component of the rf spectrum with power of the degenerate circular and linearly polarised beam. A power of $\sim 0.8\text{mW}$ for the circularly polarised beam optimises the measured amplitude, while the optimum for the linearly polarised beam is in excess of the power available.

be changed independently. The optimum beam power for the circularly polarised beam was found to be ~ 0.8 mW, while powers in excess of 6.5 mW are required to reach the optimum power for the linearly polarised beam.

3.3.3 Summary

The risk of failure of apparatus increases with complexity, in addition to: weight, power consumption, and cost. Hence, the implementation of the single laser configuration will significantly aid in the miniaturisation of the sensor and will be used as the focus of research moving forward.

As stated in Sec. 3.2, the single laser configuration is not used in the rigorous investigation of MIT presented in Chap. 6, however ‘proof of principle’ experiments were carried out to show the operation was the same. There is no fundamental difference between the operation of the rf magnetometer with one or two-beams, so the MIT results can be extended to the single-beam case, albeit with a slightly reduced amplitude/ sensitivity.

The optimum signal amplitude was not achievable with the power available. One option to improve this would be to use the ^{85}Rb atoms, since the D2 line hyperfine splitting is $\Delta\nu_{\text{HFS}} = 3.035$ GHz; which is 6.157 GHz less than for caesium, decreasing the detuning of the beam from an indirectly pumped state. A smaller detuning would increase the amplitude of the polarisation rotation signal, potentially improving the SNR. Additionally one of the nonlinear effects being employed (tensor light-shift) scales with Δ^{-2} , reducing the power threshold for the generation of orientation.

3.4 Conclusions

A broad range of connected subjects has been covered in this chapter. The purpose of Sec. 3.1 was to act as a brief summary of some of the relevant issues affecting the choice of pumping and probing configuration for the rf magnetometer. In particular, attention was paid to how the choice of beam geometry influences the performance of the system. Experimentally it is favourable to use a single-beam configuration, since it reduces the overall complexity of the system; however, due to the intermixing of the action of the pump and probe, the sensor sensitivity is worse than can be achieved for systems with separate beams. The two-beam pump and probe configuration used for the majority of the work presented in this thesis (found in Chap. 6 and 7, described in Sec. 3.2), utilises an off-resonant interaction for both the pumping and probing, which optimises the performance of the magnetometer. The final section, Sec. 3.3,

presents a novel laser scheme which achieves similar off-resonant pumping and probing with a single beam. The measurement was not calibrated, but it is likely that this scheme can achieve greater sensitivity than other single-beam schemes, which will be the subject of future study. The single-beam configuration reduces the complexity of the sensor and the use of a VCSEL as a light source will help with miniaturisation. These steps show a path forward for taking the rf magnetometer system used in this thesis out of the laboratory and into the real world.

Chapter 4

Experimental Setup

This chapter is split into two sections that describe the key components required for the operation of an rf magnetometer (Sec. 4.1) in a magnetically unshielded environment (Sec. 4.2). The setup described here has been explicitly designed for making the magnetic induction tomography measurements in Chap. 6.

4.1 rf Magnetometer

4.1.1 Lasers

Laser light plays two functions in the operation of an rf magnetometer; pumping an imbalance in the population within the hyperfine manifold and probing the precession of the Zeeman coherence. For atomic magnetometers (both dc and rf) these actions are summarised by the generation and probing of the evolution of a collective atomic spin. This can be achieved with a single, or multiple, lasers acting as the pump and the probe. The latter generally leads to more efficient pumping and probing. The purpose of this section is to describe the lasers used, how the role of the pump and the probe benefit from different methods of frequency stabilisation and, finally, how the beams are configured experimentally.

This work primarily uses separate pump and probe lasers, both of which are Vescent distributed Bragg reflector (DBR) laser diodes (D2-100-DBR series [69]). The laser module contains beam condition optics to shape the elliptical output of the edge emitting diode to be an 1-mm-diameter (approximately) circular beam, and a Faraday isolator to minimise unwanted optical feedback. The laser is designed to operate at 852nm (caesium D2 line). The frequency of the laser can be tuned by both the temperature and the current supplied to the diode, both of which are controlled via the Vescent D2-105-200 Laser Controller.

As pumping is a resonant interaction, it is convenient to stabilise the beam's frequency relative to an atomic transition of interest [75]. This can be done by locking the beam to the groups of caesium D2 transitions¹ or cross-over transitions² with the Vescent D2-210 Spectroscopy Module and the Vescent D2-125 Laser Servo. Ideally, the probe laser is used to make a non-perturbative measurement of the atomic coherence. This can be achieved using light that is detuned, e.g. 1 GHz (although this detuning can be greater or smaller depending on the available probe power, see Sec. 3.2.2.3), from the relevant atomic transitions. This is achieved by locking the probe to the pump using the D2-135 Offset Phase Lock Servo. The pump and probe are overlapped in the D2-150 Heterodyne Module and a fast photodiode monitors the beatnote between them. The servo compares the phase and the frequency of the beatnote to a reference frequency with a phase-frequency detector. For DBR lasers (used here) where there are phase slips, the phase-frequency detector acts as a frequency comparator [76] and locking is achieved through frequency offset locking. This setup can be used to detune the frequency of the probe ± 10 GHz from the frequency of the pump beam.

Both the lasers have an output power of 80 mW and are contained within the same sealed box. The light from both diodes are coupled into separate polarisation maintaining single-mode fibres via acousto-optical modulators (AOMs) (Crystal Technology 3080-122) in a single pass configuration. The light output from the laser is linearly polarised and is passed through a half waveplate to match the polarisation angle to the fast angle of the polarisation maintaining fibre. This reduces the polarisation noise introduced by changes in the refractive index of the fibre, typically caused by temperature gradients and vibrations. Schäfter Kirchhoff 60SMS fibre couplers were used, typically achieving coupling ratios of $\sim 50\%$. The AOMs are primarily used to control the amplitude of the laser light transmitted through the fibre. They also shift the frequency of laser light by +80 MHz; however, this detuning is inconsequential in the experiments carried out in this thesis, since the beams are Doppler broadened³. The result is that there is experimental control over the power of the beams output from the box. The power of the free space propagating beams is typically < 0.2 mW for both beams during experiments. Figure 4.1 is a schematic diagram of the laser box layout. The fibre outputs for the pump and probe beam are mounted with collimating lenses and the relevant polarising elements ($\lambda/4$ and $\lambda/2$ waveplate for the pump and probe respectively) on separate optical breadboards. Each beam is passed through a polariser (Thorlabs Glan-Taylor, 10^{-5} extinction ratio) that cleans the polarisation of the beam and converts any polarisation noise to amplitude noise. It is then possible to actively stabilise the amplitude of the beam by monitoring a portion of the beam's

¹ $6^2S_{1/2}F = 3 \rightarrow 6^2P_{3/2}F' = 2, 3, 4$ and $6^2S_{1/2}F = 4 \rightarrow 6^2P_{3/2}F' = 3, 4, 5$.

² $6^2S_{1/2}F = 3 \rightarrow 6^2P_{3/2}F' = 2/3, 2/4, 3/4$ and $6^2S_{1/2}F = 4 \rightarrow 6^2P_{3/2}F' = 3/4, 3/5, 4/5$.

³At room temperature ($T = 295$ K) the Doppler broadening for caesium atoms (mass $m_{Cs} = 2.21 \times 10^{-25}$ kg [26]) is $\Delta\omega_D = 2\sqrt{2\ln 2}k_B T/m_{Cs}c^2 = 360$ MHz.

power and modulating the AOM transmission accordingly. However, laser amplitude noise was not a limiting factor in this work so the scheme was not explored any further than an initial demonstration. A periscope raises the beams so that they intersect with the cell. Due to the high extinction ratio of the polariser, the periscope mirrors have a negligible impact on the polarisation of the beam. The light out of the fibre was collimated to ~ 5 mm for both beams before being passed through a 2 mm iris, hence the beams have approximately a ‘top-hat’ intensity profile.

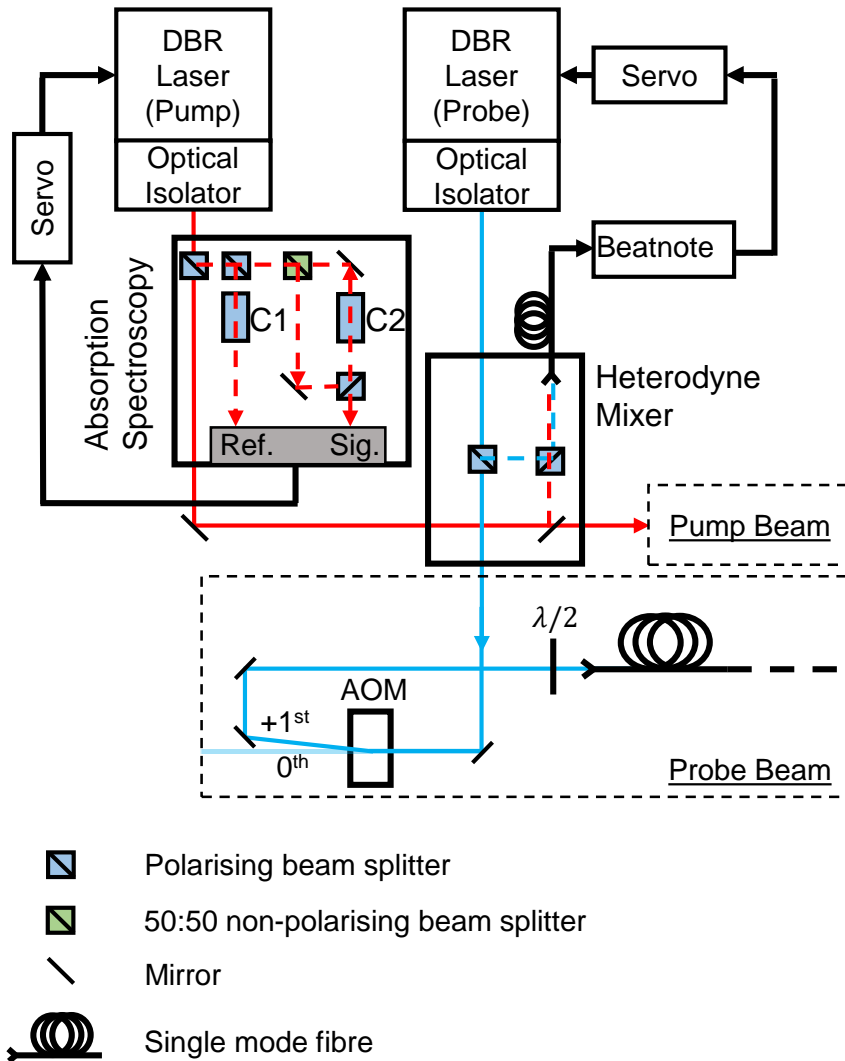


Figure 4.1: Note: this diagram is to give an indication of the setup and not all of the details have been included (such as the waveplates used to optimise beam power reflected or transmitted through the polarising beam splitter). The pump laser (left) is frequency locked to the atomic transition of interest via the absorption spectroscopy module [A small portion of the beam is directed through two glass vapour cells containing caesium, marked as C1 and C2. The signal recorded at the photodiode marked as Ref. from C1 (the reference cell) provides a Doppler broadened absorption profile. The atoms in the same velocity group in cell C2 are pumped and probed in a counter-propagating configuration and the probe is monitored with the photodiode marked as Sig. The two photodiode signals are subtracted from each other to provide an Doppler-broadening free absorption probe]. The probe laser (right) is offset locked to the pump after they mix in the heterodyne module. After the optics for the frequency stabilising modules, the lasers are passed through an AOM and the 1st order output is coupled into a polarisation maintaining single mode fibre. The AOM is used to control the power of the laser input to the fibre and a $\lambda/2$ waveplate matches the laser polarisation to the fast axis of the fibre. The whole probe beam setup was repeated for the pump beam.

4.1.2 Vapour Cells

This work uses a paraffin-coated, 1.7 cm^3 -cubic (unless stated otherwise) glass cell at room temperature $T = 22 \pm 0.2^\circ\text{C}$ (stabilised with air-conditioning), containing $N_{\text{atoms}} \approx 5.6 \times 10^{10}$ atoms (atomic density $n_{\text{Cs}} = 3.3 \times 10^{10}\text{ cm}^{-3}$ [57]⁴). With the off-resonant pumping scheme used in this work (described in Sec. 3.2.1), only moderate heating of the cell to $T = 32^\circ\text{C}$ is required to achieve a $\sim 1\text{ fT}/\sqrt{\text{Hz}}$ sensitivity [6]. The relaxation due to wall collisions in this cell was measured to be $\approx 1\text{ Hz}$ by the manufacturer and the relaxation due to SEC at this temperature was measured to be $\approx 1\text{ Hz}$ [78], giving the residual cell linewidth to be 2 Hz . It is noted that this type of cell is unlikely to be suitable for long term sensor development due to the scale of production and cost, but it is an excellent choice for exploring the underlying principles and testing the detection limits of MIT with an rf magnetometer. Figure 4.4 (a) is picture of a 1.7 cm^3 paraffin coated cell that is used for the majority of the work presented in this thesis.

4.1.3 Detection

Birefringence maps the precessing atomic polarisation on to the polarisation of the linearly polarised probe beam. This results in an optical polarisation rotation, which can be measured with a polarimeter consisting of a polarising beam splitter (PBS) and a balanced photodiode (PD) to monitor the amplitude of the reflected (vertical) and transmitted (horizontal), as described in Fig. 4.2. In this work a commercially-available balanced PD (Thorlabs PDB150A) was used.

4.1.4 Measured Signal

The primary measurement in this work is that of the amplitude and phase of the Zeeman coherence. This is recorded as an rf spectrum (see Sec. 2.5.1). The spectra are recorded by monitoring the balanced photodiode signal as the frequency of an rf field ω_{rf} is scanned across the Larmor frequency ω_L . This measurement lends itself well to lock-in detection, but can also be done by directly monitoring the photodiode output. In essence, lock-in detection measures the amplitude R and phase ϕ (with respect to the reference) of a particular frequency component of the input signal. This is achieved by demodulating the measured signal at the reference frequency $\omega_{\text{ref}} = \omega_{\text{rf}}$ into two orthogonal components, X and Y ($R = \sqrt{X^2 + Y^2}$ and $\phi = \tan^{-1} Y/X$). This work uses the SRS 865A lock-in amplifier and an example of a measured

⁴Determined through absorption measurements in the work of Chalupczak that accompanied [57] and verified through calculations [77].

rf spectrum is given in Fig. 4.3, where (a) plots the X (blue line), Y (dotted orange line) and R (black line) component, while (b) plots ϕ (black line).

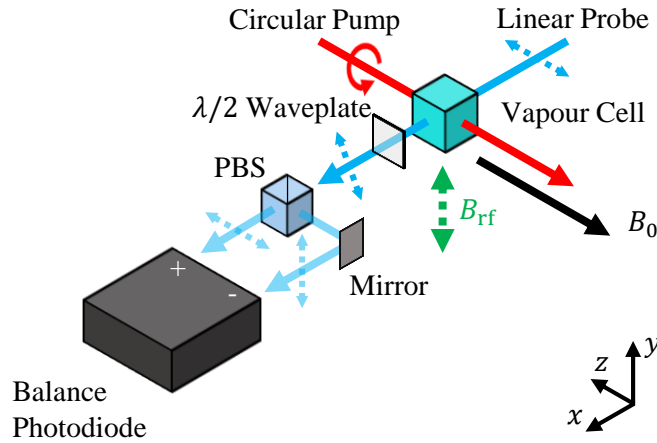


Figure 4.2: Schematic layout of the operation of the rf magnetometer, including the polarimeter setup. The atoms are pumped with a circularly polarised beam (red arrow) along a bias magnetic field B_0 (black arrow). A resonant rf magnetic field B_{rf} (green dashed arrow) drives Zeeman coherences, which are coupled to the linear polarisation of the probe beam (blue arrow). The vertical and horizontal components of the probe beam are monitored by separate photodiodes and are subtracted from each other to create an oscillating signal with dc common mode rejection, e.g. power fluctuations. A $\lambda/2$ waveplate is used so that the polarisation of the input beam is at 45° to the polarising beam splitter (PBS) to balance the power between the reflected and transmitted components.

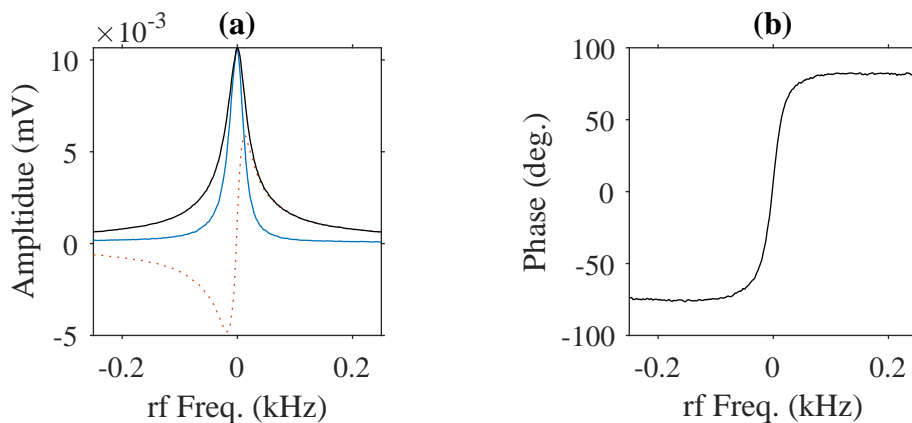


Figure 4.3: Recording (a) X (blue line), Y (orange dotted line) and R (black line), and (b) ϕ (black line) component of an rf spectra.

4.2 Unshielded Operation

This section discusses the experimental setup and the environmental magnetic field conditioning used to operate the rf magnetometer in a magnetically unshielded environment, and discusses some of the consequences of doing so.

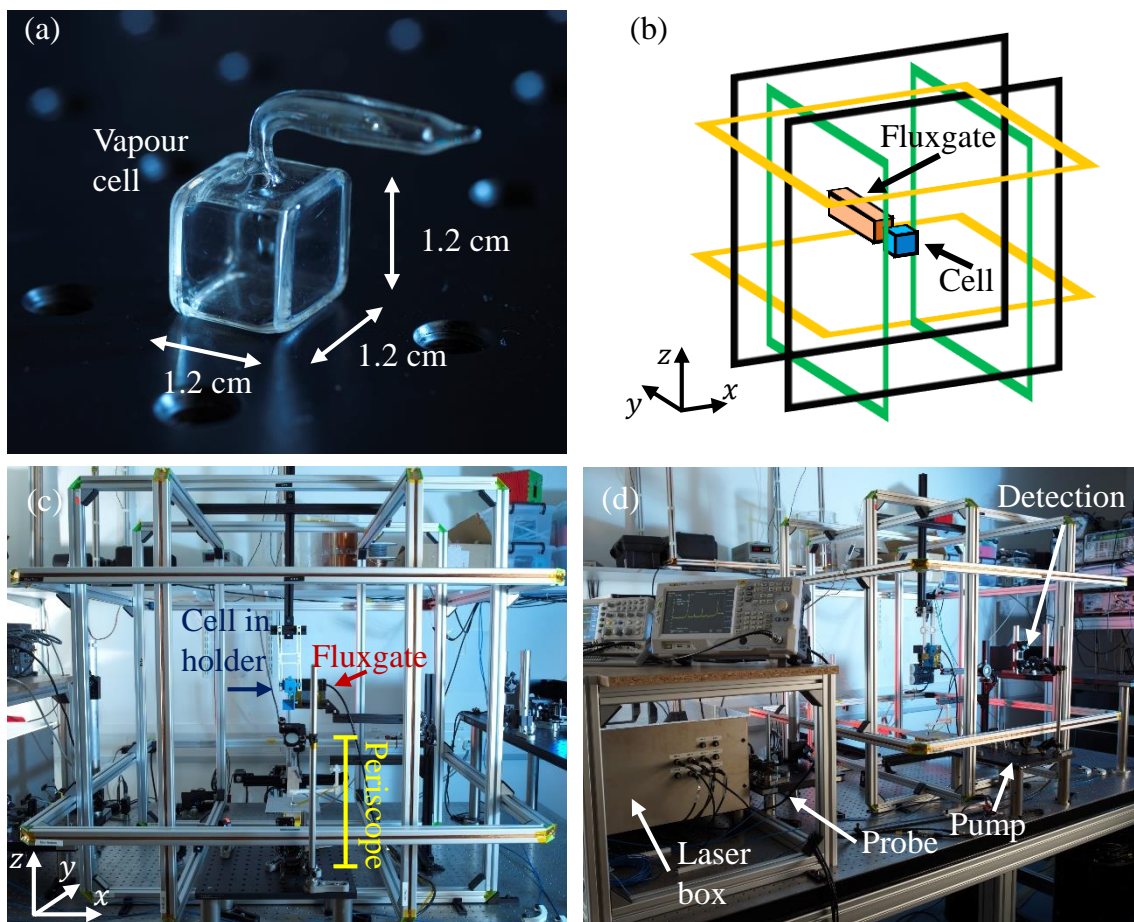


Figure 4.4: Images describing the experimental setup. Picture (a) is an image of the 1.7cm^3 paraffin coated vapour cell used for the majority of the results presented in this thesis. The schematic (b) shows the interlocking coil array used to define and actively stabilise the bias magnetic field. Each orthogonal coil pair has its own colour (green, black, and orange coils are directed along x , y , and z , respectively). Picture (c) shows the experimental coil arrangement. The gradient coils have been omitted from (b-d) for clarity. Picture (d) shows the whole experimental setup (laser, pump and probe beam conditioning optics, vapour cell, detection, and coils) sitting on top of a optical table.

4.2.1 Experimental Setup

Figure 4.4 depicts the experimental setup. The atoms contained in the paraffin coated vapour cell (a) are optically pumped and probed. The cell is in the centre of a coil array (described in Sec. 4.2.2.1) used to define the bias magnetic field. A fluxgate close to the cell is used to monitor the ambient magnetic field and it is used as an error signal to actively stabilise changes in the field (described in Sec. 4.2.3). The schematic in (b) represents the orthogonal coil pairs (green, black, and orange coils are directed along x , y , and z , respectively) with the fluxgate and vapour cell at their centre. Picture (c) shows the experimental arrangement of the coils, vapour cell, and fluxgate. Picture (d) shows the whole experimental setup: box containing the pump and probe lasers, which are coupled to optical fibres; fibres deliver the light to breadboards that contain the beam conditioning optics for the pump and probe beam, which are then raised with periscopes [marked in (c)] to intersect within the cell; probe beam propagates through the cell to a breadboard containing the optics and photodiodes for detection. The whole setup sits atop a $48'' \times 96''$ optical bench. The table top has not been vibrationally stabilised or demagnetised. These two features, combined with nearby PSUs and electronics, create a harsh working environment for the magnetometer.

4.2.2 Environmental Magnetic Field

4.2.2.1 Compensation Coils

Magnetic Field Homogeneity

Magnetic coils are used to define the amplitude and direction of the bias magnetic field throughout the experiments described in this work. One key feature of their performance is the inhomogeneity of the field they create. This can be determined by the fractional variation ΔB_{In} , defined as the difference in the magnetic field at point i , which is a distance L from the central magnetic field B_0 , given by

$$\Delta B_{\text{In}} = \frac{(B_0 - B_i)}{B_0} = \frac{\Delta B}{B_0}, \quad (4.1)$$

where ΔB and B_0 are only related to the magnetic field created by the coils. It is desirable that the inhomogeneity in the field is as small as possible. Since $\Delta B \propto B_0$, a homogeneity factor must be chosen with respect to the field strength. In this work, operating frequencies are typically $\nu_L < 100\text{kHz}$ ($\sim 35\ \mu\text{T}$). A limit in the allowable inhomogeneity was set at the order of $\Delta B = 10\text{Hz}/\gamma_{\text{Cs}}$ at $B_0 = 100\text{kHz}/\gamma_{\text{Cs}}$, which corresponds to $\Delta B_{\text{In}} = 0.01\%$. Multiple coils can be configured in an array to construct a particular magnetic field landscape. The most

Helmholtz coil	Separation	Homogeneity length scaling factor: $\Delta L_B = L_{In}/r$ or L_{In}/a		
		$\Delta B_{In} = 0.1\%$	$\Delta B_{In} = 0.01\%$	$\Delta B_{In} = 0.001\%$
Circular	r	0.20	0.10	0.045
Square	$1.089 \times a$	0.20	0.09	0.05

Table 4.1: Values of the homogeneity length scaling factor for circular and square Helmholtz coils for different homogeneity lengths.

well known and simplest coil design to make a homogeneous magnetic field is the circular-Helmholtz coil, where a pair of identical coils are separated by their radius. In this arrangement the first three spatial derivatives of the field are zero [79]. This is referred to as the Helmholtz condition. In the analysis that follows, square-Helmholtz coils are also considered. In this arrangement, the Helmholtz condition is met when a pair of square coils with length⁵ $b = 2a$ are separated by $\approx 0.5445b$ [79].

A figure of merit of the coil design is the homogeneity length $L_{In} = 2L$, which is defined as twice the distance from the position of B_0 at which the field variation is less than chosen ΔB_{In} . The distance is doubled as the field is symmetric in both the positive and negative direction along the coil axis, where B_0 should be in the centre of the cell. A useful parameter for deciding the coil size is the ratio between the homogeneity length L_{In} and a dimension of the coil. Here this ratio is called the homogeneity length scaling factor ΔL_B . For a circular coil the relevant dimension is its radius r , while for a square coil it is a . Table 4.1 gives the simulated values for the ΔL_B for a circular and square-Helmholtz coil⁶. Simulations found that square coils have a $\sim 10\%$ worse homogeneity length when compared with circular coils, which is supported by the literature [80, 81]. The coil array built for this work chose square coils, as they have an acceptable homogeneity and are simpler to construct out of commercially available aluminium profiles. From the data in the table it is simple to determine L_{In} from a desired ΔB_{In} and known coil size and shape; e.g, for $\Delta B_{In} = 0.01\%$ and a square-Helmholtz coil ($\Delta L_B = 0.09$) of length $2a = 1$ m, $L_{In} = 90$ mm.

⁵Measured as the length of the side of the coil, i.e. the perimeter of the coil.

⁶A coil has two axes: the coil axis which runs through the centre of each coil and the axis that runs orthogonal to this (identical other orthogonal), both intersecting at the centre of the coil array. L_{In} along either axis can differ significantly depending on the design of the coil array. For the two Helmholtz coils considered here, L_{In} is similar on either axis; but since the cell is cubic, the smaller of the two values is given in the table.

Design

The largest vapour cell used in this work has a length of 37 mm (50.7 cm^3 volume). This sets the approximate minimum homogeneity length required for a compensation coil. A compensation coil array of three nested mutually-orthogonal square-Helmholtz coils was designed, with coil lengths $2a = 1000 \text{ mm}$, 940 mm , 880 mm . For $\Delta B_{\text{In}} = 0.01\%$ the homogeneity length of the smallest coil is $L_{\text{In}} = 79 \text{ mm}$, which exceeds the dimensions of the minimum homogeneity length. The scale of the coil array was set for a gradiometric field measurement, which required a large L_{In} . However, these experiments have not been included in this work. The coils were constructed with $30 \text{ mm} \times 30 \text{ mm}$ square aluminium profiles and made up of 50 turns of 0.5-mm-diameter copper wire. The field-control-system that drives the coils was powered by a digital three-channel power supply unit (PSU) (Rigol DP831).

4.2.2.2 Magnetic Gradients

Anti-Helmholtz Coils

Anti-Helmholtz coils are common coil arrays used to cancel the 1st-order magnetic field gradients, e.g. ΔB_z , that meet the Helmholtz condition [82]. For a circular anti-Helmholtz coil the design is a coil-pair separated by $1.732r$ [83], energised by equal currents that flow in opposite directions. The field from either coil cancels each other at the centre of the coil array generating a linear magnetic field gradient. The homogeneity of anti-Helmholtz coils must also be considered, but since these coils generate a much smaller field, their homogeneity can be reduced to $\Delta B_H = 0.1\%$. A coil design of $r = 200 \text{ mm}$ with 20 turns of 0.5-mm-diameter wire was chosen, which has an estimated homogeneity length of $0.36r$. The design for the coil formers were for three orthogonal, interlocking coils. The diameter of the coil, and therefore the track for winding each coil, are equal for each coil pair. Consequently the wire paths overlapped, causing the wire loops to deviate from a perfect circle. Since the homogeneity length is significantly greater than the largest coil, it is assumed that deformation of the wire paths did not limit the gradient compensation, which is discussed in the following section.

Gradient Compensation

Corrective gradients can be applied across the cell to reduce the rf spectral linewidth. This can be achieved with a simple iterative approach by sequentially applying gradients along the three orthogonal axes and setting the gradient that minimises the linewidth. This is shown by Fig. 4.5, where the current in the anti-Helmholtz coil is scanned, creating a gradient (a) ΔB_x , (b) ΔB_z and (c) ΔB_y , while recording the resonance linewidth. The bias field is directed

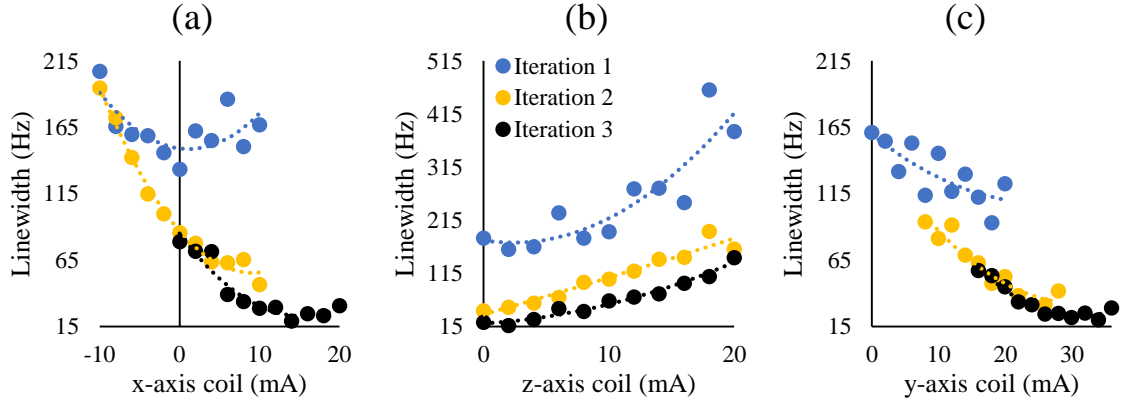


Figure 4.5: Plot of the change of resonance linewidth as the current supplied to the anti-Helmholtz coils is changed, applying gradients (a) ΔB_x , (b) ΔB_z and (c) ΔB_y across an 8.4 cm^3 volume cell. The current which minimised the linewidth is selected for each current scan per anti-Helmholtz coil. These optimum current values are used as the initial current values for the next iteration.

along the z -axis and the data in this figure are recorded for an 8.4 cm^3 (cylindrical cell 22 mm long, with a 11 mm radius) cell. Note: these measurements have been carried out with active stabilisation of the bias magnetic field, which is described in detail in the following section. The currents applied to each coil are scanned sequentially, starting from 0 mA in each, then applying the current for that coil that minimises the linewidth, before scanning the current in the next coil. This process is iterated until the linewidth cannot be reduced any further. In the case presented for the 8.4 cm^3 cell, the optimum linewidth was $\Gamma_{\text{opt}} \approx 15\text{ Hz}$, which is better than typically achieved for the two other cell volumes that are considered in the following section. The linewidth shows a quadratic dependence on the applied gradient and exhibits a greater dependence on gradients applied along the bias field [Fig. 4.5 (b)], both of which are expected from [54]. It should be noted that the same total gradient can be produced by different combinations of applied gradients ($\nabla \cdot B = 0$).

An estimate of the broadening from magnetic gradients is given by Julsgaard in [17];

$$\Gamma_{\text{grad}} \approx \gamma_{Cs}^2 \frac{L^3}{v_{\text{atoms}}} \Delta B_z^2, \quad (4.2)$$

where $v_{\text{atoms}} \approx \sqrt{k_B T / m_{Cs}} = 136\text{ m/s}$ (in a single direction) at $T = 295\text{ K}$ and $L = 22\text{ mm}$ (cylindrical cell with same length and diameter) - giving

$$\Gamma_{\text{Grad}} = 0.96\text{ Hz}(\text{cm/nT})^2 \Delta B_z^2. \quad (4.3)$$

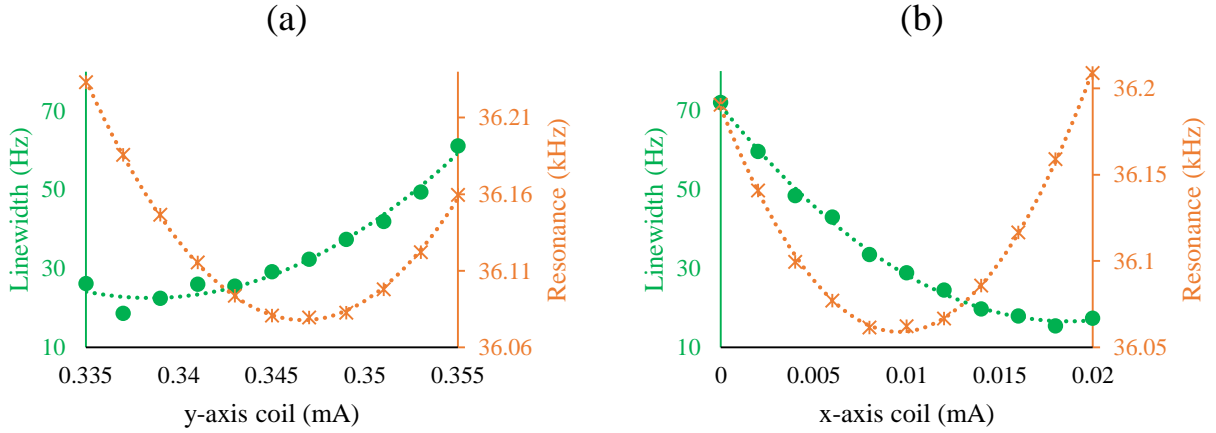


Figure 4.6: Plot of the change in linewidth (green circles) and resonant frequency (orange stars) as the current applied to the coils that create transverse static fields along the (a) y -axis and (b) x -axis.

Using Equ. 4.2 and the data in Fig. 4.5 for the initial [(a) iteration 1 at 0 mA; $\Gamma \approx 165$ Hz] and final [(c) iteration 3 at 30 mA; $\Gamma \approx 15$ Hz] linewidths, the ambient and residual uncompensated gradients are found to be on the order of $\Delta B_z = 13$ nT/cm and $\Delta B_z = 4$ nT/cm, respectively (assuming all broadening comes from gradients).

An interesting feature was that the minimum linewidth was recorded when there were non-zero transverse fields present, as shown in Fig. 4.6. In this figure the current supplied to y - and x -axis Helmholtz coils is scanned through the region where the transverse fields are minimised, i.e. minimum resonance frequency. The resonance linewidth is minimised when a static field equivalent to ~ 0.1 kHz is added on each axis. This could be explained by asymmetries, i.e. curvature, in the local magnetic field. This idea is also supported by an experiment where two 1.7 cm^3 cells were placed 5 cm apart and each measured a linewidth of 20 Hz and 40 Hz, respectively. Additional compensatory coils would be required to correct this field curvature, so this was not explored any further.

4.2.3 Magnetic Field Compensation in Finite-Sized Cells

As previously stated, rf magnetometers can be used to measure either the magnitude of a bias magnetic field B_0 or the amplitude and phase of an rf magnetic field. However, for measurements of the rf field magnitude, B_0 must be relatively stable while the measurement is being carried out. The dominant noise source in a built-up environment is 50-Hz magnetic field noise from the mains electrical supply and local electronics. This noise manifests as a modulation of the bias magnetic field. Noise directed along the bias magnetic field, e.g. z -

axis, dominates as the transverse fields B_x and B_y are only secondary corrections to B_0 (i.e. for $B_z \gg B_x$ and B_y , $B_0 \approx B_z$). However, it is still beneficial to compensate the noise on all three axes. This can be achieved passively by using magnetic shielding, which can achieve a reduction of many orders of magnitude in the background magnetic field; however, shields are cumbersome and expensive in large volumes. Shields are also unsuitable for this work, as its main aim is to use the rf magnetometer image metal plates via MIT. This would require placing the object inside the shielding, which is impractical, and any magnetisation of the object would negate the action of the shield.

A different method is active compensation of the environmental field. The active field control system designed in this work stabilises dc and low frequency (primarily 50-Hz electronic noise) changes in the bias magnetic field. The system comprises of a magnetometer, to generate an error signal, and a proportional-integral-derivative (PID) servo controller (SRS SIM960 PID, bandwidth dc-3 kHz). The output of the PID controller is used to modulate the output of a current control circuit (PSU and a MOSFET), which modulates the field generated by the coils aligned along the axis of the fluxgate - providing feedback to the system. The performance of this system as a whole is discussed further in the following section. Such a system is open and more flexible than passive shielding, making it possible to deliver a sample close to the rf magnetometer.

The feedback control was tested with two separate sources of error signal, a commercial fluxgate magnetometer (Bartington Mag690, bandwidth dc-1 kHz) and one of the quadrature components of the rf magnetometer's rf spectrum. First, the performance of the fluxgate as a source of the error signal is evaluated. It should be noted that since the fluxgate is spatially separated from the vapour cell, the magnetic field it monitors does not fully represent that seen by the vapour cell. The fluxgate sensing volume is $\sim 1 \text{ cm}^3$.

4.2.3.1 Fluxgate as Source of Error Signal

The performance of the magnetic field compensation for the rf magnetometer was investigated using two cubic cells with volumes 1.7 cm^3 (length 1.2 mm)⁷ and 50.7 cm^3 (37 mm length cell); studying how these two volumes are influenced by the background magnetic field gradients and noise. Smaller volume cells are less sensitive to magnetic field gradients relative to larger volumes ($\Gamma \propto L^3$ from Equ. 4.2). Figure 4.7 shows the rf spectra recorded for the two cell volumes: (a) in the ambient magnetic field (in the presence of magnetic field noise and gradients), (b) with active field stabilisation with the fluxgate as the source of the error signal,

⁷Like the 50.7 cm^3 volume, the length of both cells is the measured outside dimension. The glass is said to be 2 mm thick, but the thickness can be seen to vary for both cells. The outside dimension has been taken as it is a consistent measurable for both, although it does not represent the true volume of both cells.

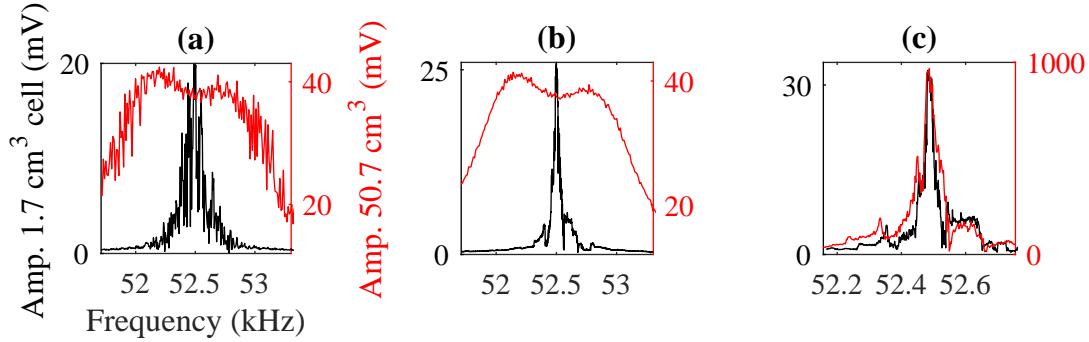


Figure 4.7: Plots of the rf spectra recorded for 1.7 cm^3 (small cell plotted on left axis and black line) and 50.7 cm^3 (large cell plotted on right axis and red line) volume cells in: (a) in the ambient environmental magnetic field noise and gradients, (b) with active stabilisation of the bias field and (c) with active stabilisation and gradient compensation. The frequency step between each point in the rf spectrum for the 1.7 cm^3 cell is: (a) 5 Hz, (b) 1 Hz and (c) 1 Hz, and for the 50.7 cm^3 cell is: (a) 10 Hz, (b) 10 Hz and (c) 1 Hz [larger frequency steps are sufficient when recording broad resonances, 1.7 cm^3 (a) and 50.7 cm^3 (a-b)] - recorded with 100 ms between each point. Note: all results in the work are recorded at room temperature.

and (c) with active field stabilisation and magnetic gradient compensation. These spectra have been constructed by recording a single value of the instantaneous amplitude (R) with a fast time constant $\tau = 100\ \mu\text{s}$ and a 6 dB/oct roll-off filter (1st order)⁸ so that some of the noise in the polarisation rotation signal is represented in the rf spectrum.

To investigate the noise present for each condition described in Fig. 4.7, the on resonance ($\omega_{\text{rf}} = \omega_L$) power spectral density (PSD)⁹ of the magnetometer signal for the two cells (1.7 cm^3 black line, 50.7 cm^3 red line) are analysed. The results are given by: Fig. 4.8 (a) ambient magnetic field, Fig. 4.8 (b) with active field stabilisation, and Fig. 4.8 (c) with active field stabilisation and magnetic gradient compensation. This data has been normalised so that a comparison in the relative SNR can be made.

First, consider the results recorded in the ambient magnetic field. The linewidth of the rf spectrum shown in Fig. 4.7 (a) for the small (black line) and large (red line) cell are $\Gamma_S \sim 180\text{ Hz}$ and $\Gamma_L \sim 1.5\text{ kHz}$, respectively. The linewidths of both are estimated from the raw data due to their distorted lineshape. Magnetic gradients and 50-Hz noise dominate the recorded lineshape and linewidth; however as will be discussed, the two cells are affected by these factors differently. Also it should be noted that there is considerable variation in the measured point-to-point value of the amplitude in the raw data since the magnetic field varies in time ($\sim 100\text{ ms}$

⁸ n^{th} order RC filter will roll-off at $6 \times n\text{ dB/oct}$ at corner frequency $f_{-3\text{ dB}} = f_c \sqrt{2^{(1/n)} - 1}$, where $f_{-3\text{ dB}} = f_c = 1/2\pi\tau = 1591\text{ Hz}$ for $n = 1$ and $\tau = 100\ \mu\text{s}$.

⁹Square of the amplitude spectral density described in 3.2.3.

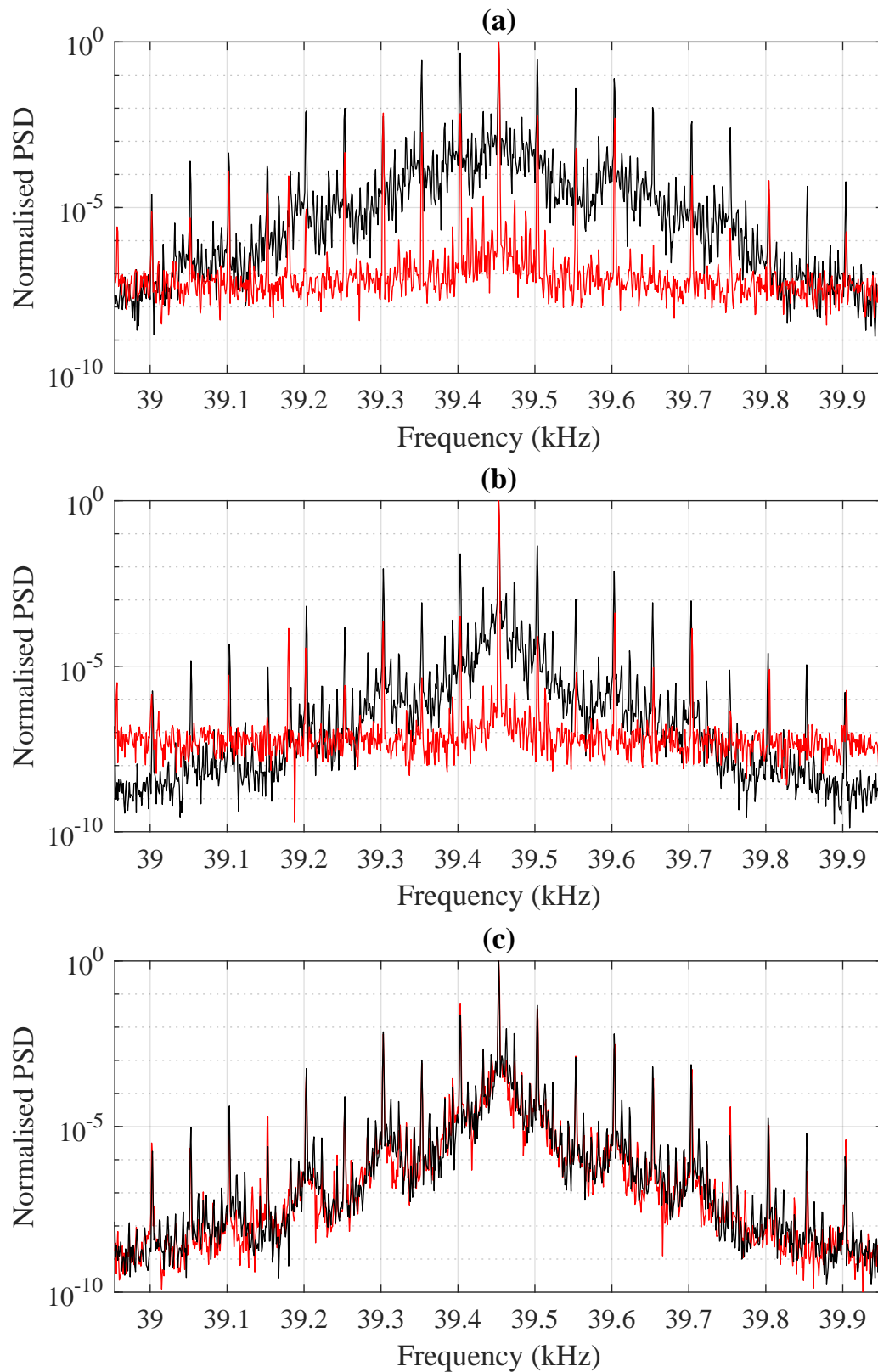


Figure 4.8: On resonance ($\omega_f = \omega_L$) normalised power spectrum for the 1.7 cm^3 (back line) and 50.7 cm^3 (red line) cell for: (a) ambient laboratory magnetic field, (b) bias field stabilised using the fluxgate as the source of the error signal for the active field control system, and (c) bias field stabilised with corrective gradients applied across both cells.

between each data point). Analysis of the on resonance power spectrum [Fig. 4.8 (a)] shows the presence of large 50Hz sidebands for both cells. At this stage in the analysis it should just be noted these sidebands are much more prominent for the small cell (black line). The 50-Hz noise also adds a significant low frequency pedestal to the small cell in Fig. 4.8 (a).

Figure 4.7 (b) shows the rf spectra recorded for the two cell volumes with active stabilisation of the bias magnetic field, using a fluxgate as an error signal for the field control system. The point-to-point variation in amplitude can be seen to be significantly lower when active stabilisation is applied, e.g. this difference can be clearly seen for the data recorded for the large cell (red line) in Fig. 4.7 (a) and (b) where both are recorded with the same frequency step. The active stabilisation also reduces the linewidth of the 1.7 cm^3 cell to approximately $\Gamma_S \approx 23\text{ Hz}$ calculated from fitting (reminder that this cell has an intrinsic linewidth of $\approx 2\text{ Hz}$ and is broadened due to gradients and residual 50-Hz electronic noise), while there is negligible change in the linewidth of the 50.7 cm^3 cell. The difference in linewidth seen here approximately follows what is expected from the volume (L^3) dependence on magnetic gradients in Equ. 4.2. From the double peak structure visible in the rf spectra for the 50.7 cm^3 cell, there is some other factor contributing to the broadening for this cell. Since the presence of 50-Hz magnetic field noise has a significant broadening effect on the 1.7 cm^3 cell, it can be assumed that the depth of the modulation is comparable to the linewidth of the rf spectrum if it was unperturbed by mains noise. The amplitude of the modulation, $B_{50\text{Hz}}$, will be proportional to the amount of broadening experienced by the cell 1.7 cm^3 ($\sim 160\text{ Hz}$); hence, it can be estimated that $B_{50\text{Hz}} \sim 46\text{ nT}$. The PSD for both cells are shown in Fig. 4.8 (b). The active stabilisation reduces the 50Hz sidebands seen at both cells, in addition to the low-frequency pedestal seen for the 1.7 cm^3 cell, by a factor of 10.

Lastly, Fig. 4.7 (c) shows the rf spectra once corrective gradients have been applied across both cells. This reduces the linewidth of the 1.7 cm^3 and 50.3 cm^3 cell to $\Gamma_S \approx 14\text{ Hz}$ and $\Gamma_L \approx 24\text{ Hz}$, respectively. For both cells the linewidth has been determined by fitting. The rf spectra for the respective cells now have the same shape and the ratio of signal amplitudes [shown in Fig. 4.7 (c)] is proportional to the ratio of the number of atoms in each cell¹⁰. Both of these features would be expected for two cells being measured in the same magnetic environment. Although it should be noted that, it is harder to compensate the residual gradients across the large cell, hence the 50.7 cm^3 cell has a slightly larger linewidth than the 1.7 cm^3 cell. Figure 4.8 (c) shows the PSD for both cells recorded in the same conditions as Fig. 4.7 (c). The PSD for the 50.7 cm^3 cell now follows the same character as the 1.7 cm^3 cell. However some interesting behaviour has now become apparent; the ratio between the peak of the normalised PSD and the largest 50Hz sideband ($\text{SNR}_{50\text{Hz}}$) for the 50.7 cm^3 cell

¹⁰ $\text{Signal}_{\text{Large}}/\text{Signal}_{\text{Small}} \approx \text{Volume}_{\text{Large}}/\text{Volume}_{\text{Small}}$.

is smaller when corrective gradients are applied [Fig. 4.8 (c)] relative to when they are not [Fig. 4.8 (b)]. In other words, it appears like the noise profile for the 50.7 cm^3 cell gets worse when corrective gradients are applied. The decrease in $\text{SNR}_{50\text{Hz}}$ is related to the ratio between the unmodulated linewidth of the rf spectrum and the magnitude of the field modulation, i.e. size of $B_{50\text{Hz}}$ relative to Γ . This same behaviour is visible when comparing the PSD for the two cells when there is no field stabilisation or magnetic gradient compensation [Fig. 4.8 (a)]. For this case, 50-Hz noise affects the 1.7 cm^3 cell (narrow linewidth) more than the 50.7 cm^3 cell (broad linewidth). These two cases can be described as the condition when the amplitude of the modulation is greater or smaller than the linewidth of the spectrum. When the gradients across the 50.7 cm^3 cell are compensated and there is no active stabilisation of the bias magnetic field, the normalised PSD for both cells have the same character, i.e. they both look like the trace for the 1.7 cm^3 cell in Fig. 4.8 (a). Once active stabilisation is applied, the same order of magnitude reduction in 50-Hz magnetic field noise is seen for the 50.7 cm^3 cell as the 1.7 cm^3 cell. The signal for the 50.7 cm^3 cell might appear to be better without corrective gradients; however, this does not take into account the reduction in linewidth (increase in Zeeman coherence lifetime) by a factor of 75 when gradients are applied, which also leads to an increase in resonance amplitude. The compensation of 50-Hz noise is important for improving the quality of the rf spectrum, as this is the measurable parameter in the applications for MIT, and the reduction in linewidth is beneficial for improving the sensitivity of the measurement as a whole.

It should be noted that the 50Hz sidebands are slightly higher for the larger cell. This is due to the position of the fluxgate. For both measurements the fluxgate was placed $\approx 10\text{ mm}$ from the side of the cell, which is $\approx 16\text{ mm}$ and $\approx 28\text{ mm}$ from the centre of the 1.7 cm^3 and 50.7 cm^3 cell, respectively. As a result, the field measured by the fluxgate better represents the field at the small cell.

Fluxgate Position

Figure 4.9 depicts the layout of the cell and fluxgate, where the sensing volumes are spatially separated by d_c . Since two spatially separated sensors will experience different magnetic fields, the performance of the active compensation will be influenced by how close the fluxgate is to the cell, as shown in Fig. 4.10. In this figure, the amplitude and linewidth of an rf spectrum, and the $\text{SNR}_{50\text{Hz}}$ was recorded for the 1.7 cm^3 cell as the fluxgate was moved along the bias field axis (z). Distance $d_f = 0\text{ mm}$ represents when the fluxgate is flush with the side of the cell. Away from the cell, the $\text{SNR}_{50\text{Hz}}$ is inversely proportional with the fluxgate separation distance, as it better monitors the 50Hz seen by the atoms close to the cell. However, for

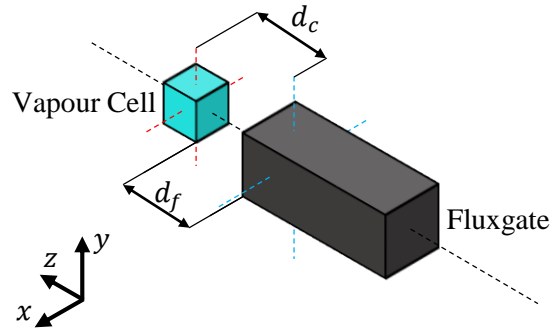


Figure 4.9: Layout of the vapour cell and fluxgate. Their center lie on the same z -axis and are respectively marked by the red and blue dashed lines along the x - and y -axis. The centre of each sensing volume is separated by d_c and the distance between the closest faces is given by d_f . The latter is what is measured to define the fluxgate position.

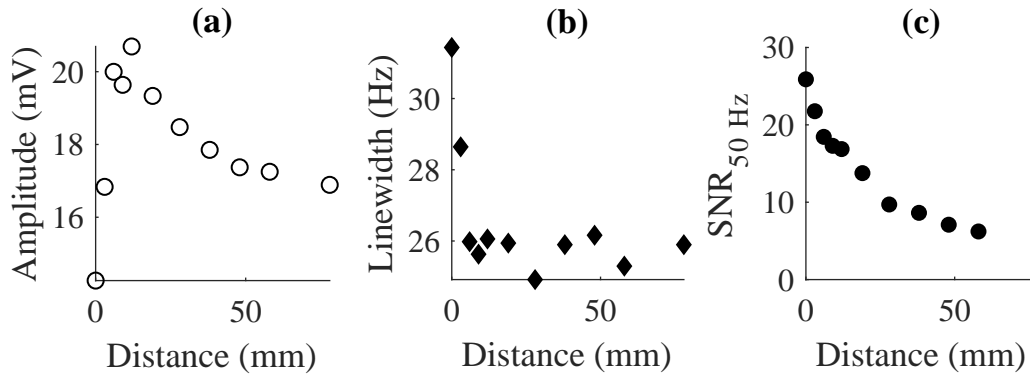


Figure 4.10: The (a) amplitude and (b) linewidth of the rf spectrum recorded as the distance of the fluxgate to the vapour cell is changed. (c) $\text{SNR}_{50\text{Hz}}$ of the peak signal to largest 50Hz sideband is measured at each point.

distances less than 12 mm the signal amplitude begins to decrease and the linewidth broadens. The broadening and reduction in amplitude are due to the influence of the residual magnetic field produced by the fluxgate and its electronics. The Mag690 is energised at 16kHz, well above the operating bandwidth of the fluxgate and PID controller, but it is a significant source of magnetic field noise. Since the data shown in the above analysis were recorded far from this frequency, it is not visible in the PSD or rf resonances.

4.2.3.2 Atomic Signal as Source of Error Signal

The rf magnetometer signal itself can also be used as an error signal for the field control system. The amplitude of the dispersive-like component of the rf spectrum has a zero-crossing

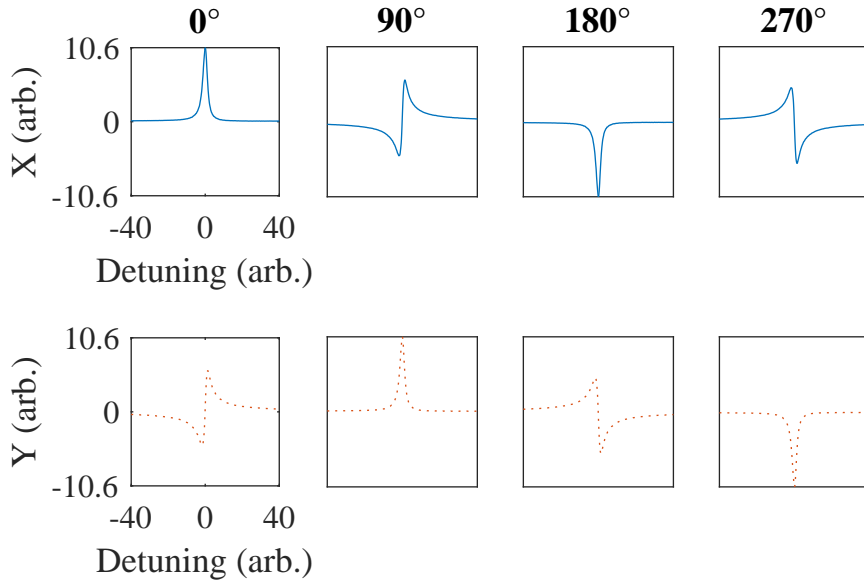


Figure 4.11: Plots describing the lineshape of the X and Y components of the rf spectrum for different phases of rf spectrum. The detuning is measured from ω_L and is in arbitrary units, along with the X and Y .

when $\omega_{\text{rf}} = \omega_L$, e.g. shown by the Y component (orange dotted line) in Fig. 4.11 (0°). The position of the zero-crossing is a scalar representation of the bias magnetic field (since $B_0 = \sqrt{B_x^2 + B_y^2 + B_z^2}$), hence it can only be used to provide feedback along a single axis. Assuming the noise directed along the transverse axes is not significantly greater than the noise directed along the bias field, one-dimensional noise compensation along B_z will still work well since $B_z \gg B_y, B_x$.

Figure 4.12 shows the PSD for the 1.7 cm^3 and 50.7 cm^3 cell with the rf spectrum providing the error signal for field stabilisation along B_z . The data for both cells were recorded with corrective gradients applied and is an equivalent measurement to Fig. 4.8 (c), where the fluxgate was the source of the error signal. The $\text{SNR}_{50\text{Hz}}$ when using the rf magnetometer as the error signal is $\times 10^4$ and $\times 10^5$ for the 50.7 cm^3 and 1.7 cm^3 cells respectively, compared with $\times 10^1$ when using the fluxgate magnetometer. Since the rf magnetometer fully describes the magnetic field measured at the cell, the error signal from the rf magnetometer will describe the noise measured at the cell better than the error signal from the fluxgate.

A drawback is that the lineshape of the X and Y components are dependent on the relative phase between the reference signal and the measured polarisation rotation signal, as shown in Fig. 4.11 for four different phases¹¹. Any change in phase will shift the zero-crossing such

¹¹The phase in these plots represent the phase of the reference signal. The value of the phase is arbitrary,

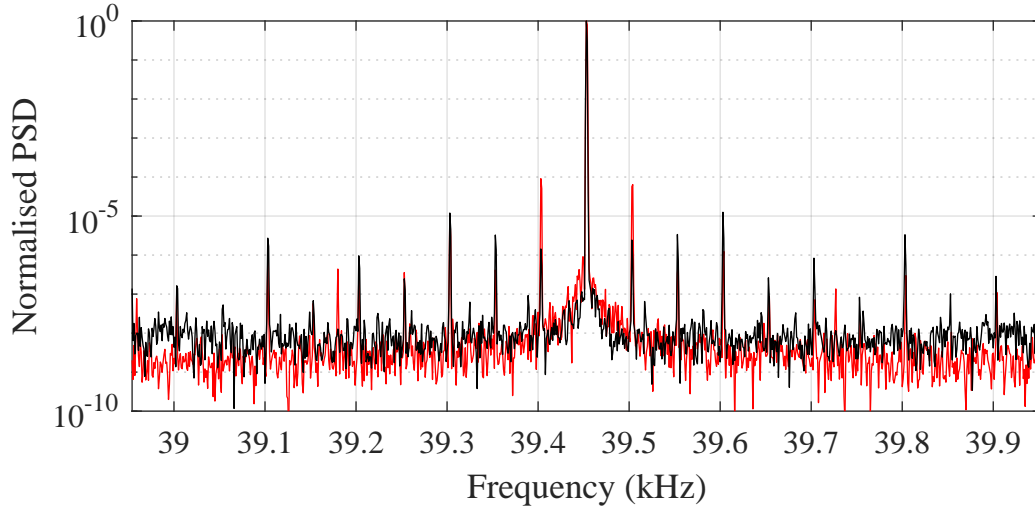


Figure 4.12: On resonance ($\omega_{\text{rf}} = \omega_L$) normalised PDS for the 1.7cm^3 (back) and 50.5cm^3 (red) cell measured with the bias field stabilised using the dispersive component of the rf spectrum as the source of the error signal for the active field control system. Corrective gradients have been applied across both cells.

that it does not occur on resonance and will be indistinguishable from magnetic field noise. However in many MIT experiments described later in this thesis, the amplitude will be zero for a time and the phase will change by 360° during a measurement. Both these factors will break the feedback loop: meaning that although the increase in $\text{SNR}_{50\text{Hz}}$ is impressive, this method is not practical for providing field stabilisation for MIT measurements.

4.3 Shielded Operation

Although the purpose of this work is to develop an rf magnetometer for operation in an unshielded environment, some experiments investigating the single-laser configuration (Sec. 3.3) and the spin maser (parts of Chap. 7) were carried out within magnetic shields to analyse fundamental aspects of the operation of the sensor.

Magnetic shielding can be achieved in a number of ways depending on the application. It operates by making the field flow around the perimeter of the shield, rather than through it. As a result, shielding works best when it encloses a volume, rather than when used as a screen. Any thickness of a highly electrically-conductive material (any metal, e.g. aluminium) can shield high-frequency magnetic fields to some degree. A Faraday cage is a particular

while the change in lineshape between two different phases is always constant; for example, the lineshape seen at 0° could occur at any value phase value, while the absorptive Lorentzian shape seen at 0° will always become dispersive when the phase of the reference signal is shifted by $\pm 90^\circ$.

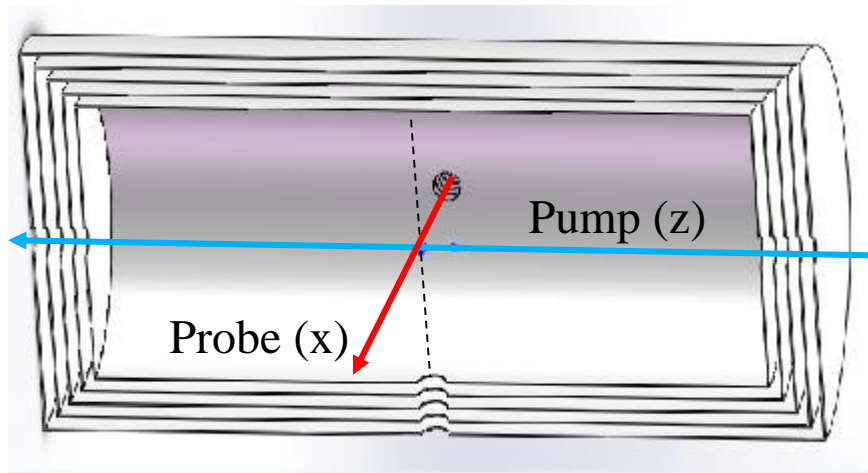


Figure 4.13: Experimental schematic of the 5 layers of magnetic shielding. The vapour cell (not shown) is placed in the centre of the shielding, where the pump and probe intersect, and rf coils (not shown) surrounding the vapour cell generates an rf magnetic field. The bias magnetic field is defined by a solenoid (not shown) contained within the inner shield.

example, where the spacing in the mesh is an order of magnitude smaller than the wavelength of the field. Slowly oscillating fields, such as 50Hz, will be partially shielded by magnetic induction [42] (discussed in Chap. 5). However, dc fields can only be shielded by highly magnetically permeable materials such as mu-metal. Mu-metal can effectively attenuate all external magnetic fields. A limitation is that thermal fluctuations in the material itself generate their own magnetic field noise (Johnson noise), which sets the baseline noise level. This can only be removed at cryogenic temperatures (discussed again in Sec. 5.3.2) and reduced when using low conductivity shields, e.g. the innermost ferrite shield in [84].

The shielding used in this work consists of five nested cylinders of mu-metal, each 2 mm thick [57]. A schematic is shown in Fig. 4.13. The cylinders consist of tubes with removable endcaps with a hole in their centre to allow longitudinal optical access (pump). There are also holes through the centre of the tube sections to allow transverse optical access (probe). The smallest and largest shield has an outer diameter/ length of 200mm/ 400mm and 280mm/ 560mm respectively, with a 20 mm air-gap between each layer¹². Each layer is separated by a plastic spacer so the centre of each shield aligns along the same axis. This setup has a shielding factor of the order of 10^6 and a solenoid generates a highly uniform bias magnetic field, with a homogeneity of $\Delta B_{\text{In}} < 0.001\%$ over the volume of the cell. Using the calculations detailed in [86] (equation 16, using geometry factor $G = 0.438$), the magnetic Johnson noise generated by the inner shield is calculated to be $8 \text{ fT}/\sqrt{\text{Hz}}$ at 1 Hz with $f^{-1/4}$ frequency dependence.

¹²It has been shown that a shield made up of layers and air-gaps has the same shielding efficiency as a solid shield of the same dimensions, drastically reducing weight and cost [85].

This value is not a limitation for the measurements presented in this thesis, and a ferrite shield was not deemed necessary.

Chapter 5

Magnetic Induction Tomography

Magnetic induction tomography (MIT), is a well established technique for non-destructive testing (NDT). A general scheme for MIT is based on the inductive coupling between an oscillating magnetic (primary) field and an electrically conductive and/ or magnetically permeable object. This object generates a response (secondary) field, which is then monitored by any type of magnetometer. The presence of a defect, such as a structural change (e.g. crack, hole, or cavity) or material change (e.g. corrosion, stress, or strain), will be imprinted on the secondary field through a change in its phase and/or amplitude. The defect can then be mapped by measuring the secondary field across the object.

Historically MIT has been referred to as eddy current testing (ECT), where traditionally the magnetometer is a pick-up coil and the secondary field is generated by circulating eddy currents induced in electrically conductive materials by the primary field. This work has found that in magnetically permeable samples, the secondary field is generated by local magnetisation. Due to the difference in the mechanism that generates the secondary field, the name ECT is somewhat misleading, so it is described as MIT throughout this thesis. There is some variety in the terminology used for this technique¹ but the name MIT has been chosen to be in keeping with older literature discussing how this general technique is separate from pick-up coils [87], and it is what has been used throughout the previous publications of the author. The term tomography describes the ability to image different spatially separated sections, which is achievable by varying the frequency of the primary rf field, as will be described in the following section. Many of the results presented in Chap. 6 are recorded at a single frequency because they are concerned with understanding and optimising the measurement, rather than gaining extra information about the sample (see Sec. 6.3.2.2 for variable frequency mea-

¹It is interchangeably called mutual inductance tomography[87], electromagnetic induction tomography [88], electromagnetic tomography [89], electromagnetic imaging [20] or, the erroneously named, eddy current testing [90, 91, Chp. 5].

surements). As such, some of the results in this chapter could be called ‘magnetic induction imaging’; however, the term MIT will be used throughout for simplicity.

It should be noted that there are two fields that are both some times called the ‘magnetic field’, the magnetic flux density \mathbf{B} and the magnetic field strength \mathbf{H} , which are related by $\mathbf{B} = \mu_0(\mathbf{H} + \mathbf{M}) = \mu\mathbf{H}$ [92, Chap. 3]. $\mathbf{M} = \chi\mathbf{H}$ is the magnetisation of the point in space where \mathbf{H} exists, χ is the magnetic susceptibility. $\mu_r = \mu/\mu_0 = (1 + \chi)$ is the relative permeability of the medium, where μ_0 is the permeability of free space. \mathbf{M} effectively describes how strongly the medium interacts with \mathbf{B} , and for free space $\mathbf{M} = 0$ and $\mu_r = 1$. \mathbf{B} is defined by the magnetic flux Φ_B through an area A and is measured in units tesla T. The terminology of the magnetic fields are often used interchangeably, but \mathbf{H} can be thought of as the applied field and \mathbf{B} as the measured field. In atomic physics the ‘magnetic field’ typically used is \mathbf{B} , a convention which is also used here.

5.1 Principle of Operation

5.1.1 Eddy Currents

Eddy currents (EC) are one of the mechanisms used to detect defects. This section details their formation and introduces a key concept called skin depth δ , which describes the penetration of ECs beneath the surface of the medium. This feature enables the detection of subsurface defects, or the detection of objects through screening materials, setting MIT technology apart from other NDT methods, for example; infrared, ultrasound, and magnetic particle inspection [90], to name a few.

Eddy currents² are closed loops generated by the displacement of electrons induced by a changing magnetic field. As an electromagnetic (EM) wave can propagate through media, ECs can be induced at depth. The penetration depth of the EM field depends on its frequency and the properties of the medium. The change in the density of ECs with propagation distance can be inferred from the attenuation of the primary field through the medium. The arguments below describe this theoretically and follow the description in [90, Chap. 5].

Starting with Maxwell’s equations in their usual form

$$\nabla \cdot \mathbf{D} = \rho \quad (5.1)$$

²They are sometimes called Foucault’s currents in French speaking countries after one of their first discoverers.

$$\nabla \cdot \mathbf{H} = 0 \quad (5.2)$$

$$\nabla \times \mathbf{E} = -\mu \frac{d\mathbf{H}}{dt} \quad (5.3)$$

$$\nabla \times \mathbf{H} = \mathbf{J} + \frac{d\mathbf{D}}{dt}, \quad (5.4)$$

where the electric flux density is given by $\mathbf{D} = \epsilon \mathbf{E}$ ($\epsilon = \epsilon_r \epsilon_0$ and ϵ_r is the relative permittivity and ϵ_0 is the permittivity of free space), ρ is the free electric charge and \mathbf{J} is the free current density. Substituting Ohm's law ($\mathbf{J} = \sigma \mathbf{E}$, where σ is the conductivity of the medium) into Equ. 5.4 (Ampère's circuital law) then

$$\nabla \times \mathbf{H} = \sigma \mathbf{E} + \epsilon \frac{d\mathbf{E}}{dt}. \quad (5.5)$$

Using the vector identity $\nabla \times \nabla \times \mathbf{H} = \nabla(\nabla \cdot \mathbf{H}) - \nabla^2 \mathbf{H}$ and Equ. 5.2, Equ. 5.5 becomes

$$-\nabla^2 \mathbf{H} = \nabla \times \left(\sigma + \epsilon \frac{d}{dt} \right) \mathbf{E}. \quad (5.6)$$

Applying Equ. 5.3 (Faraday's law of induction) gives

$$\nabla^2 \mathbf{H} = \left(\sigma + \epsilon \frac{d}{dt} \right) \mu \frac{d\mathbf{H}}{dt}. \quad (5.7)$$

Assuming the magnetic field can be described by a plane wave $\mathbf{H} = \mathbf{H}_0 e^{i(\mathbf{k}\mathbf{r} - \omega t)}$, where $d\mathbf{H}/dt = i\omega \mathbf{H}$ and $d^2 \mathbf{H}/dt^2 = -\omega^2 \mathbf{H}$, then Equ. 5.7 can be given in the form of the Helmholtz equation

$$\nabla^2 \mathbf{H} = (i\omega\sigma - \omega^2\epsilon) \mu \mathbf{H} = k^2 \mathbf{H}, \quad (5.8)$$

where the propagation constant k is entirely dependent on the properties of the medium.

Assuming the field is propagating along the x -axis, through an infinite air/surface boundary in the yz -plane, the magnetic field will point along \hat{z} , perpendicular to \hat{x} . Equation 5.8 can now be described by

$$\frac{d^2 H_z}{dx^2} - k^2 H_z = 0, \quad (5.9)$$

where the plane wave approximation gives

$$H_z = H_{0z} e^{i(\omega t - kx)} \quad (5.10)$$

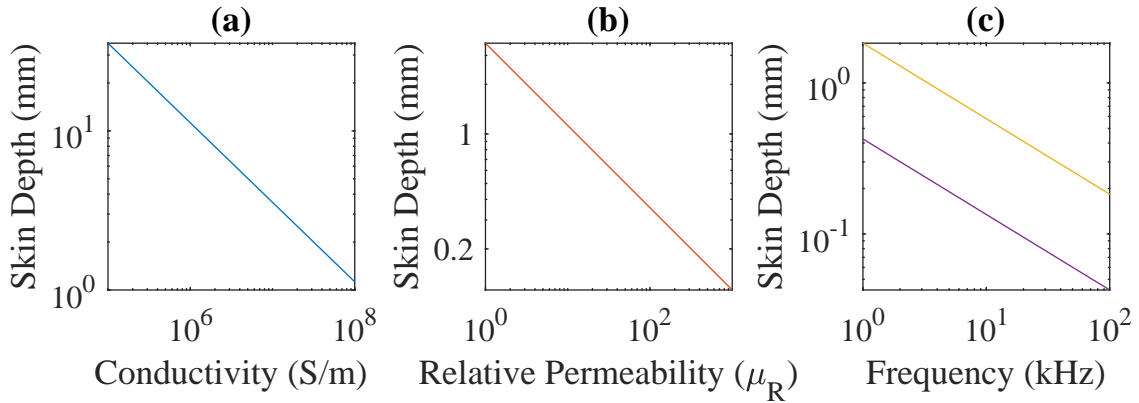


Figure 5.1: Numerical value of δ over the range of parameters applicable in this work. The frequency for (a) and (b) is 1 kHz, with a permeability and conductivity of $\mu_R = 1$ and $\sigma = 1 \times 10^7$ S/m, respectively. (c) Plots δ for aluminium (yellow), $\mu_R = 1$ and $\sigma = 3.77 \times 10^7$ S/m, and carbon steel (magenta), $\mu_R = 100$ and $\sigma = 6.99 \times 10^6$ S/m.

and H_{0z} is the field strength at the surface of the boundary. Rearranging $k^2 = (i\omega\sigma - \omega^2\epsilon)\mu$ to $k^2 = (\sigma + i\omega\epsilon)i\omega\mu$, one can see that for $\sigma \gg \omega\epsilon$, $k \approx \sqrt{i\omega\sigma\mu} = \sqrt{i2\pi f\sigma\mu}$ (by convention only the positive root is taken [92, Chap. 6]). This is true for all metals ($\sigma \gtrsim$ MS/m) in the radio frequency range ($f \lesssim$ MHz) [93]. Using the identity $\sqrt{i} = (1+i)/\sqrt{2}$, k can be separated out into real and imaginary parts to give

$$k = \sqrt{\pi f\sigma\mu} + i\sqrt{\pi f\sigma\mu} = k' + ik'' . \quad (5.11)$$

Substituting Equ. 5.11 into Equ. 5.10 it becomes

$$H_z = H_{0z}e^{-i\omega t}e^{-k'x}e^{-ik''x} . \quad (5.12)$$

The real $e^{-k'x}$ and imaginary $e^{-ik''x}$ spatial components represent the attenuation and phase lag of the field as it propagates through the medium. When $x = 1/k' = 1/\sqrt{\pi f\sigma\mu}$ the amplitude of the internal field will be e^{-1} smaller than its surface value and the phase lag will be $\theta = 1$ rad. This distance is called the skin depth δ ; and although this depth is somewhat arbitrary, δ is a useful metric for discussing the variation in eddy current depth in different materials or over a range of frequencies as shown in Fig. 5.1.

From Faraday's law of induction (Equ. 5.3), a current will be induced by the oscillating field \mathbf{H} . These are eddy currents and their amplitude and phase will follow the attenuation dynamics

of \mathbf{H} as it propagates through the conductor, giving the current density amplitude of

$$|J_y| = |J_{0y}|e^{-z/\delta}, \quad (5.13)$$

with a phase of

$$\theta_y = \theta_{0y}e^{-z/\delta}, \quad (5.14)$$

where J_{0y} and θ_{0y} is the eddy current density and phase at the surface. From Fig. 5.1 (c) it can be seen that even moderate penetration (1 mm) is only achievable at frequencies < 1 kHz for aluminium, while the penetration for steel is a factor of ~ 4.3 less than for aluminium. These are the two materials which are considered in this work. Lastly, from Ampère's circuital law (Equ. 5.4), the presence of these eddy currents generate their own magnetic field, which is in the opposite direction to the field which created it due to the negative sign in Equ. 5.3 - sometimes referred to as Lenz's law.

This description is summarised by: the circulating eddy currents induced in a conductive material by an oscillating magnetic field (primary field \mathbf{B}_{rf}) generate their own opposing magnetic field (secondary field \mathbf{b}_{rf}).

5.1.2 Local Magnetisation

From the survey of the literature regarding the different applications of MIT it was found that there is effectively no thorough discussion regarding the creation of a secondary field due to local magnetisation of the sample. What has been found only discusses how magnetisation competes with EC [90, Chap. 5]. It is beyond the scope of this work to present a functional model to describe this behaviour, but what follows presents a simplistic picture to describe the generation of the secondary field in magnetically permeable samples.

First consider a static magnetic field $B_{\text{coil}}\hat{\mathbf{z}}$ generated by a coil that is close to a magnetically susceptible object. This field will magnetise the object, creating a field $B_{\text{mag}}\hat{\mathbf{z}} = \mu_0\mathbf{M}\hat{\mathbf{z}}$ where $\mathbf{M} = \chi\mathbf{H}$. If the direction of the field created by the coil inverts, then so will that created by the magnetisation. There is a nonlinear dependence of \mathbf{M} with \mathbf{H} that is due to hysteresis in the ascending or descending dependence of $M_+ \leftrightarrow M_-$ with $H_+ \leftrightarrow H_-$ as shown by Fig. 5.2 (a) and the saturation of $\chi(\mathbf{H})^3$ [92, Chap. 3]. If the magnetic field applied by the coil regularly changes direction (e.g. generating an rf magnetic field \mathbf{B}_{rf}) then the \mathbf{B}_{mag} will simply follow \mathbf{B}_{rf} - albeit with an amplitude that is related to the hysteresis cycle. The amplitude of the magnetisation field will also have some dependence on frequency due to the relation of the

³Saturation does not need to be considered in this work as the magnetic samples studied are steel, which saturate at fields of the order of 1 T and is significantly greater than the fields applied here ($< 100 \mu\text{T}$).

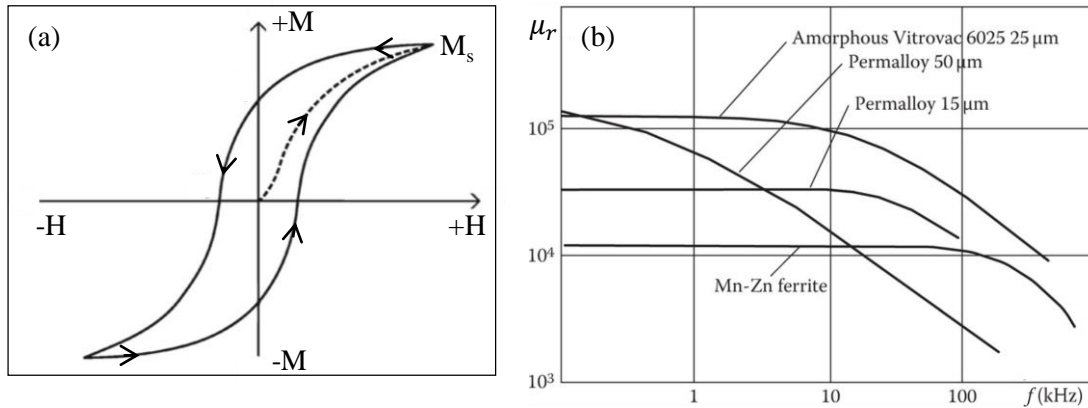


Figure 5.2: Two plots related to the magnetisation of a material. (a) Describes a hysteresis curve between \mathbf{M} and \mathbf{H} , saturating at \mathbf{M}_s (edited from [92]). The dashed line represents the initial magnetisation curve. The hysteresis loop will be smaller when the field is less than the saturating field, with a M_{\max} value which lies along the initial magnetisation curve. (b) Relationship between $\mu_r = (1 + \chi)$ and the frequency for the oscillating magnetic field for several different materials with a high permeability (reprinted from [94]).

permeability μ with frequency; a few examples are given in Fig. 5.2 (b). From the description of these effects it is clear that an oscillating field (primary field) will create an additional field (secondary field) through local magnetisation of the sample.

Something that has not been included in this description is the penetration of local magnetisation in the sample, which becomes important when considering the measuring of subsurface defects. The change of local magnetisation with depth will be different to the attenuation of an EM wave as it propagates through a highly conductive material. Local magnetisation would be better described by the bulk magnetisation of a local area that will spread to some depth in the material. The full theoretical study of the depth of local magnetisation requires its own dedicated study and is beyond the scope of this thesis; but, it can be assumed that the depth of local magnetisation that generates a detectable secondary field will be proportional to \mathbf{M} and from Fig. 5.2 (b) it will be greater at lower frequencies, both of which are material dependent factors.

5.2 Secondary Field

This section discusses general properties and dynamics of the secondary field. These considerations are relevant to any method of MIT.

5.2.1 Generation

The primary field used in this work, and the sensors described in Sec. 5.3, is generated by an rf coil. The only component of rf coil design which is considered here is the number of turns and coil diameter, parameters which can be interpreted as defining the strength and spatial distribution of the rf field. As the secondary field is proportional to the primary field, it is desirable to maximise the primary field strength. It is also desirable to decrease the diameter as it relates to imaging resolution of MIT. The reasoning for this is described in detail in Sec. 6.3.1; but to summarise, the secondary field strength is defined by the density of eddy currents or local magnetisation, which in turn are defined by the spatial distribution of the primary field. Smaller diameter coils will create a tighter distribution of rf fields in the radial direction leading to an increased imaging resolution. Coils were wound with a large number of turns N to increase the primary field strength generated. To decrease the coil diameter, 20- μm -diameter wire was used, leading to a high turn density. Examples of coils wound had $N = 1000$ and outer/ inner diameter of $D_o = 5 \text{ mm}/ D_i = 2 \text{ mm}$, or $N = 300$ turns and $D_o = 2 \text{ mm}/ D_i = 1 \text{ mm}$. The length of coil winding influences the coil's inductance, but this has not been considered in the coil design. In some cases in this thesis a ferrite core has also been used, which concentrates the flux, defining the spatial distribution of the rf field by the diameter of the core. It also acts as a former to wind the coil around. The specific details of the coil used for each measurement will be given in the relevant section.

5.2.2 Signal Response

5.2.2.1 Signal's Spatial Characteristics

Numerical modelling was carried out to gain some insight into the dynamics of the secondary field \mathbf{b}_{rf} . The arguments presented here are in the context of eddy currents; however, they can be directly transferred to local magnetisation, since it describes how a change in the spatial distribution of the source of \mathbf{b}_{rf} affects the spatial distribution of \mathbf{b}_{rf} - where the source can be either EC or local magnetisation. The primary field \mathbf{B}_{rf} will induce ECs that form closed loops, following the path of least resistance. This path is either defined by the sample geometry (flowing around or under edges) or the material properties (e.g. changes in conductivity due to corrosion); however, the investigations in this thesis only consider changes in sample geometry. This is illustrated in Fig. 5.3 in which the EC density induced by a 5-mm-diameter coil (not shown) is simulated with COMSOL⁴ near (b) and far (a) from a 24-mm-diameter hole in a $90 \times 90 \text{ mm}^2$ square plate. From these simulations it can be seen that, over a homogeneous

⁴Work carried out by Prof. M. Fromhold's group at the University of Nottingham [13].

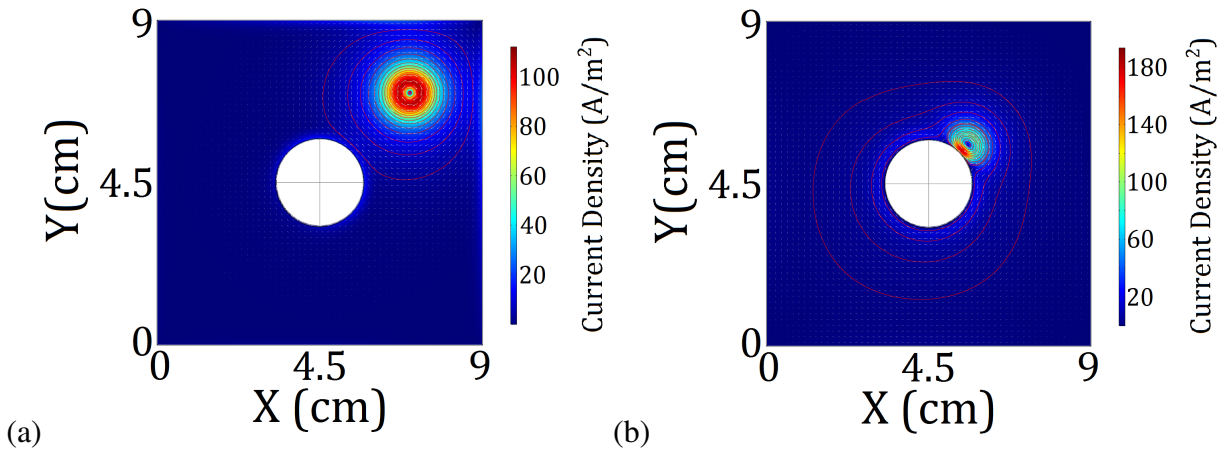


Figure 5.3: COMSOL simulation of the deformation of the eddy current density by a circular hole in a square plate (this work was carried out by Prof. Mark Fromhold's group at the University of Nottingham). In (a) the coil is over a homogeneous region of the plate and there is minimal disturbance of the eddy current paths. In (b) the coil is in the vicinity of the circular hole (representing a defect), which breaks the symmetry of the eddy current paths and concentrates them along the edge of the conductor. The coil is not shown on either plot, but for scale, it is exactly the same shape and size as the darkest red region in (a).

region of the plate, the greatest density of ECs occurs directly underneath the circumference of the coil. When approaching the recess, the spatial distribution of currents is a convolution of that defined by the coil and the object geometry. The presence of the defect can also be seen to concentrate the ECs around the perimeter of the hole.

For the rest of the discussion 'rf' will be dropped from the primary \mathbf{B}_{rf} and secondary \mathbf{b}_{rf} field, but the primary field should not be confused with the static bias magnetic field \mathbf{B}_0 . In a homogeneous region of the sample [Fig. 5.3 (a)], the geometry of the EC paths will be defined by the coil, which is circular in all the cases considered in this work. These currents will generate a \mathbf{b} field that will be parallel to the surface normal of the sample, i.e. $b_x = b_y = 0$. From the plot shown in Fig. 5.3 (b), the hole (defect) deforms the path of the eddy currents, which generates non-zero horizontal components of \mathbf{b} .

Figure 5.4 is the simulated⁵ amplitude images of the (a) b_x , (b) b_y and (c) b_z components of the \mathbf{b} field generated by the ECs as the coil is scanned over a $64 \times 64 \text{ mm}^2$ area over a sample with a defect in the form of a 48-mm-diameter circular hole. A large diameter hole was simulated so that the secondary field generated by the opposite edges of the hole did not overlap

⁵Simulations carried out by colleague at NPL with a different model than used to generate Fig. 5.3. These simulations simply modelled ECs as current loops and calculated \mathbf{b} using the Biot-Savart equations [95, Chap. 5] in Matlab. The problem was confined entirely to the surface of object, since it was concerned with modelling the radial distribution of the secondary field. The current loops were centred on the coil and defined by the coil size.

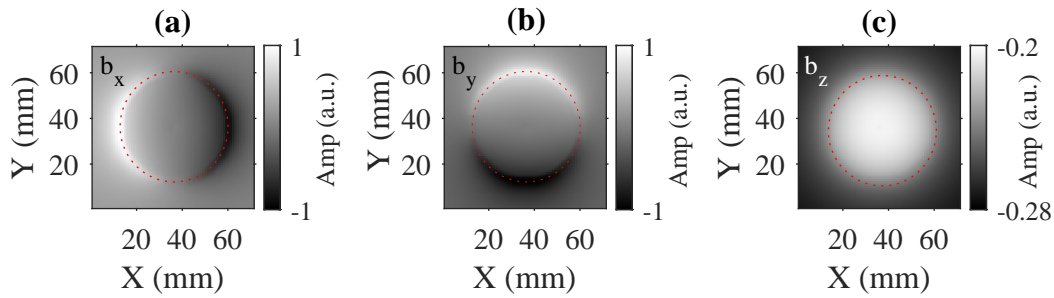


Figure 5.4: Simulated images of how the amplitude of the (a) b_x , (b) b_y and (c) b_z components of the secondary field change as a coil is scanned across a 48-mm-diameter circular hole. The image comprises of 70×70 pixels.

significantly (the consequence this overlap is discussed further in Sec. 6.3.1). The units of this figure are normalised by the maximum amplitude of the three field components. From these simulations it can be seen that the edges of the hole perpendicular to the horizontal component (e.g. x -axis for b_y) generate a maximum amplitude, while the edges that run parallel create no signal. In all three components of \mathbf{b} it can be seen that there is a signature of the defect (hole); however, the most significant measurable signal is the generation of non-zero b_x and b_y components. The large amplitude of these components is due to the concentration of EC at the defect edge and the change in sign of both components indicates that they change direction at opposite sides of the recess. There is only a small reduction in the amplitude of b_z due to lack of material to generate a signal.

When considering \mathbf{b} produced by local magnetisation (in a magnetically permeable sample), the same assumptions considered for these simulations do not hold; however, the spatial distribution of the local magnetisation will still be defined by \mathbf{B} and the geometry of the sample. Hence, the dynamics of the change in the components of \mathbf{b} around a defect are expected to be same for local magnetisation and eddy currents. Here it has been shown that a simple model for the generation of the secondary field predicts the spatial distribution of its components. The efficacy of this model is confirmed and discussed further in Sec.'s 6.2.1.2 and 6.2.1.3 in the context of measurements.

5.2.2.2 Characteristic Signal Response from Ferromagnetic and Non-Ferromagnetic Materials

The results presented here⁶ are to qualitatively show how the secondary field produced by eddy currents and local magnetisation have opposite directions, as described in Sec. 5.1.1

⁶The details of how the measurements presented in this section were carried out are described fully in Chap. 6.

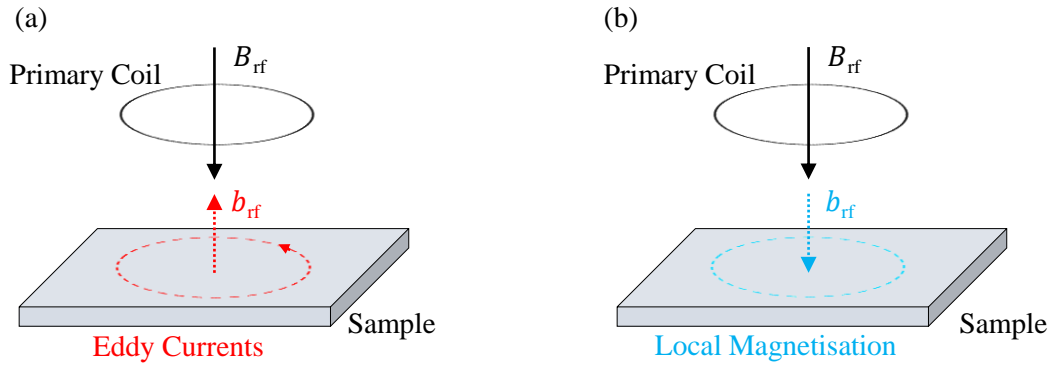


Figure 5.5: Schematic diagram of the direction of the secondary field produced by (a) eddy currents and (b) local magnetisation.

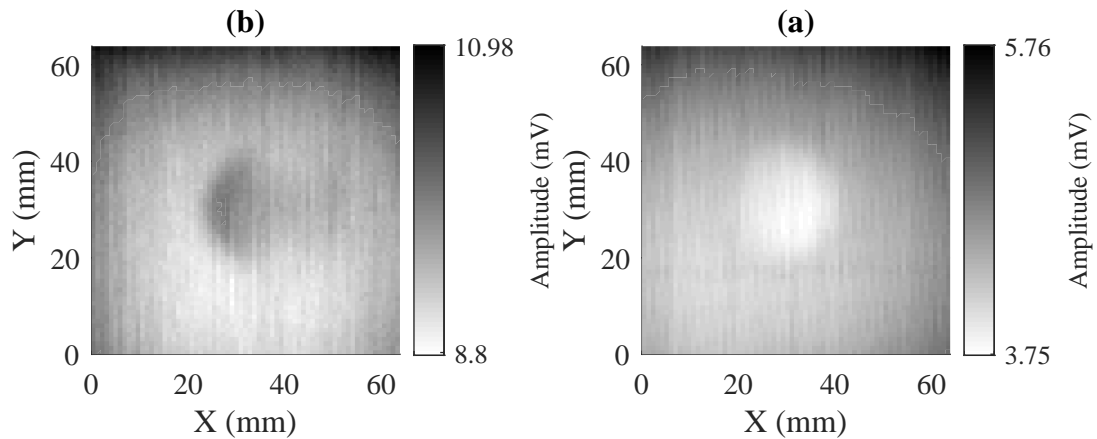


Figure 5.6: Measured change in the amplitude of the rf spectrum recorded over a 24-mm-diameter recess in (a) an aluminium and (b) a steel plate. Note: the colour scale is inverted (light to dark) to highlight the signature of the recess in this low contrast image.

and 5.1.2. The secondary fields produced by the two mechanisms are depicted schematically in Fig. 5.5, where the sample is a homogeneous flat object. This difference in the direction of the secondary field was experimentally confirmed by recording the magnetometer signal amplitude while scanning over a $64 \times 64 \text{ mm}^2$ area (70×70 pixels) of both a steel (low electric conductivity, high magnetic permeability) and an aluminium (high electric conductivity, low magnetic permeability) plate. The square ($150 \times 150 \text{ mm}^2$), 6-mm-thick plates each contain a defect in the form of a 24-mm-diameter recess that is 2.4-mm-deep. These measurements were performed in the same experimental conditions and with the coil and rf magnetometer on the same side of the plate as the recess. Figures 5.6 (a) and (b) show the amplitude images recorded for the aluminium and steel plate, respectively. The colour scale has been inverted to make the features more pronounced. The rf magnetometer is configured to measure the total rf field $\mathbf{B}_{\text{Tot}} = \mathbf{b} + \mathbf{B}$ over the plate and the amplitude of the rf resonance is proportional $|\mathbf{B}_{\text{Tot}}|$. For the aluminium plate, the \mathbf{b} field is generated by eddy currents and opposes \mathbf{B} . Since there is less material to generate a response (as shown by simulations in Fig. 5.4) the signal amplitude will be larger over the recess. For the steel plate the secondary field is generated by local magnetisation; hence, the \mathbf{b} field is generated in the same direction as \mathbf{B} . This is confirmed in the measurements presented here, where the amplitude increases over the recesses for the aluminium plate [Fig. 5.6 (b)] and decreases for steel [Fig. 5.6 (a)].

5.3 Sensors

This section describes different sensors used for MIT. First discussed are pick-up coils, which are the accepted tool currently used for this technique. Then the implementation of two other sensors, superconducting quantum interference devices (SQUIDs) and giant magnetoresistive (GMR) sensors, will be discussed. Finally, there is a brief summary of aspects of the rf magnetometer that are relevant for comparison with all three sensors. Pick-up coils are not ideally suited to low frequency operation (e.g. for MIT) since they measure the rate of change of the rf field. SQUIDs, GMRs and rf magnetometers are more attractive since they measure the amplitude of the rf magnetic field. SQUIDs and GMR sensors measure the temporal change of a static field, while rf magnetometers are intrinsically sensitive to the rf magnetic field.

The section for each sensor is laid out as a short report: introducing the technology and why it is being considered, describing how it operates, detailing some relevant properties and how these sensors have been implemented for MIT. The properties that have been considered - dead-zones, sensitivity, and spatial resolution - are only discussed in relation to the operation of the sensor. For each case the electronics and signal processing will be considered sufficient

not to limit the operation of the sensor. Dead-zones describe the angular region over which the sensor operates poorly or not at all. Sensitivity, or resolution, is the smallest change in magnetic field that the magnetometer can detect. Examples of optimum sensitivities for each sensor is discussed to give context, but a more useful indicator is the sensitivity per sensor volume, which is detailed further in Sec. 5.3.5. The spatial resolution of the sensor is only relevant when applied to MIT. In this context, the resolution is discussed in terms of what limits the size of defect detectable by the sensor. This section aims to describe these sensors qualitatively, describing general aspects of each sensor and how their fundamental operation influences their application to MIT. It is challenging to draw direct comparison across different sensors as they are often suited to different scenarios, but Sec. 5.3.5 summarises some of the advantages and disadvantages of the four sensor types.

5.3.1 Pick-Up Coils

5.3.1.1 Introduction

As was said in the introduction to this chapter, MIT technologies historically use a pick-up coil to monitor the secondary field induced in a sample by a primary field. Commercially they are readily available and have a long history of practical use in many environments. Greater attention is given to this sensor as pick-up coils are to be considered as the baseline which any new sensors have to beat, and the concepts related to pick-up coils are also relevant for the rf coils used to generate the primary field.

The pick-up coil is either the same as the coil which generates the primary field, called the primary coil, or is a separate coil. The simplicity of such instruments is highly attractive; however, they have a reduced sensitivity at low frequencies [96] and exhibit a strong dependence of sensitivity on coil size [97]. It is worth bearing in mind that simple, high quality pick-up coils can become expensive as they are artisan products that are time consuming to make and are challenging to reproduce effectively [98, 99].

5.3.1.2 Operation

A pick-up coil is used to measure the strength of an oscillating magnetic field, usually tuned to a particular frequency range. In addition to eddy currents, an oscillating magnetic field will also induce a voltage in a closed loop of wire, often referred to as the electromotive force (EMF). This is formulated by Faraday's law of induction

$$V = -\frac{d\Phi_B}{dt}, \quad (5.15)$$

where the induced voltage V is proportional to the rate of change of the magnetic flux Φ_B through a loop of wire (different form of Equ. 5.3 [92, Chap. 5]). The magnetic flux generated by a current I in a coil is related to the coil's inductance L via

$$\Phi_B = IL. \quad (5.16)$$

A coil's inductance is defined by the properties of the coil, in particular its geometry (shape and size), number of turns, permeability of the coil's core and wire conductivity. Other than for simple coil designs, L is challenging to calculate and the coil must be either fully simulated or built and measured [100].

Regardless of whether one uses a combined or separate primary and pick-up coil, V and I are the measurable properties of the pick-up coil. For applications in MIT, one analyses changes in the ratio of these two, which is given by the impedance $Z = V/I = R' + i\omega L$, where R and L are the resistance and inductance of the coil. The results are present in so-called impedance plane diagrams (represented in Fig. 5.7) that plot $\text{Re}(Z)$ against $\text{Im}(Z)$. These factors respond differently to changes in the material characteristics, which is why impedance is monitored and not just voltage or current. Although these plots capture much information, they are rather convoluted, require considerable experience to translate, and must be fully calibrated. Several sources offer an approachable explanation on their formation and use thereof [90, 92, 93, 101]. The dynamics of how R and L change during an MIT measurement are briefly described as follows, with the descriptions following these sources.

Figure 5.7 (a) represents the impedance plane curve, which maps the reflected impedance from the sample back on the pick-up coil. If there is no sample ($\sigma = 0$), no eddy currents are generated and the free space impedance is measured (marked in Fig. 5.7 (a) by the left arrow). Often the impedance plane is normalised by dividing $Z/\omega L_0$ and this is given by Fig. 5.7 (b) (point of free space impedance marked by an arrow). As a sample with $\sigma \neq 0$ is brought to the coil then eddy currents are generated and create a resistive loss $R_{EC} = R' - R_0$, which changes the impedance of the coil [marked in 5.7 (a) by right arrow] [90, Chap. 5]. If the conductivity of the sample increases [as shown by the arrow in 5.7 (b)] towards a perfect conductor, then eddy currents will be generated without loss and $R_{EC} = 0$. Also if the sample is a perfect conductor, the secondary field will be an exact reflection of the primary field and will cancel the field at the coil, meaning $L = 0$. This is the description of the impedance curve for the example of a changing conductivity. If, for example, the conductivity is constant, but there is a defect which deforms the eddy currents, similar dynamics in the curve will be seen as this will change the density of eddy currents induced and the amplitude of the secondary field measured at the coil.

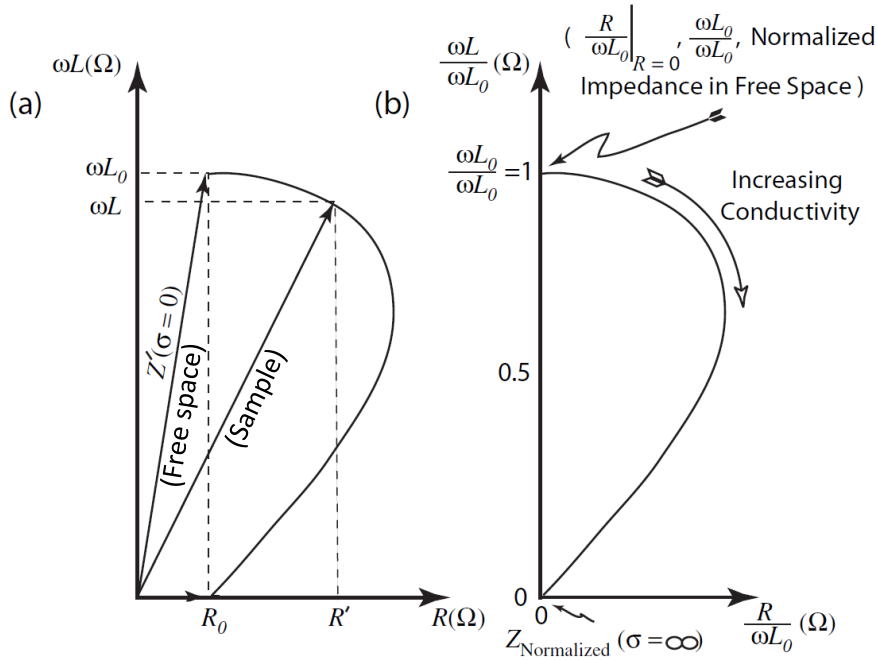


Figure 5.7: Plots of the change of the $Re(Z)$ and $Im(Z)$ in the (a) impedance plane and (b) normalised impedance plane. In free space (i.e. not in the presence of a sample) the pick-up coil has $Re(Z) = R_0$ and $Im(Z) = \omega L_0$, which is marked by the arrow on the left in (a) ($Z(\sigma = 0)$). When the coil is measuring the response from a sample with $\sigma \neq 0$, the coil parameters are now R' and L , and the position of the impedance is now marked with the arrow on the right. As the conductivity of the sample increases, the impedance will follow the path of the solid curve (edited from [90, Chap. 5]).

In non-ferromagnetic samples, EC create a secondary field $-\mathbf{b}$ that opposes the primary field \mathbf{B} , which reduces the field at the pick-up coil $\mathbf{B}_{Tot} = \mathbf{B} - \mathbf{b}$ and therefore the coil's inductance. In ferromagnetic materials, the permeability leads to an increase in \mathbf{B} from the coil⁷. If the increase in \mathbf{B} is larger than the decrease in \mathbf{B}_{Tot} due to the secondary field from eddy currents, then overall the ferromagnetic materials will lead to an increase in the coil's inductance. Due to the competition between the respective increase (\mathbf{B}) and decrease (\mathbf{b}) in field components, ferromagnetic samples are difficult to inspect. Often a saturating dc magnetic field is applied to ferromagnetic samples so that $\mu_r = 1$, at which point the eddy currents are monitored and it behaves in the same way as a non-ferromagnetic sample [90, Chap. 5].

⁷This description does not include any influence from local magnetisation, the increase in \mathbf{B} is due to the ferromagnetic material acting as a core. Local magnetisation would further complicate this description and has not been included.

5.3.1.3 Properties

Dead-zones: The magnetic flux Φ_B is defined as the amount of field \mathbf{B} through a vector area \mathbf{S} given by $\Phi_B = \mathbf{B} \cdot \mathbf{S} \cos \theta$, where θ is the angle between the field and the surface normal. Hence, they have a dead-zone in the plane in which the area enclosed by the coil lies. For MIT, pick-up coils are oriented such that their coil axis is parallel with the surface normal of the object to maximise the secondary field flux through the coil. These are scalar sensors, which can measure the direction of the rf field through analysis of the sign of the measured signal.

Sensitivity: The construction of high quality pick-up coils is challenging. In particular, small differences in windings cause significant variation in individual coil performance (inductance), even when sourced from the same manufacturer [102]. Many parameters affect the pick-up coil's sensitivity. As a result they are usually designed for operation over a particular frequency range. Their sensitivity is strongly linked to their size as they measure a changing magnetic flux through a particular area. Design choices, such as the coil height H_{coil} and inner D_i and outer D_o diameters, influence the performance of the coil. Analysis by Mooney et al. [97] found that the diameter to length ratios that optimise the coil sensitivity are $D_o : D_i : H_{\text{coil}} = 1 : 0.425 : 0.69$ - achieving a sensitivity of $57 \text{ fT}/\sqrt{\text{Hz}}$ at 30 Hz for $D_o = 120 \text{ mm}$. Another group [103] used algorithmic design to optimise coils with peak sensitivities at 10.5 kHz: one with dimensions $D_o : D_i : H_{\text{coil}} = 1 : 0.914 : 0.15$ where $D_i = 120 \text{ mm}$ achieved a sensitivity of $3.9 \text{ fT}/\sqrt{\text{Hz}}$, and another with the dimensions $D_o : D_i : H_{\text{coil}} = 1 : 0.523 : 0.526$ where $D_i = 38 \text{ mm}$ achieved $23.7 \text{ fT}/\sqrt{\text{Hz}}$ ⁸. It should be noted that the pick-up coils designed in both these studies use carefully considered electronics to achieve such high sensitivities.

Ferromagnetic cores act as a flux concentrator, meaning coils can achieve higher sensitivities in a smaller geometry, but typically lead to a nonlinear response that depends on temperature, frequency and field strength [104]. However, it should be noted that well-designed ferromagnetic cores have been shown to have similar linearity to air core coils [105]. The optimisation of a coil with a core is more complicated than an air coil, but a rule of thumb for the dimensions of the coil windings should be a core diameter of $D_c \approx 0.3D_o$ and height $H_{\text{coil}} = 0.7-0.9H_{\text{core}}$ [104, 106]. An example of an ultra-sensitive, compact, cored pick-up coil was designed for a satellite - achieving $4 \text{ fT}/\sqrt{\text{Hz}}$ at 6 kHz with a coil ($D_o = 9.5 \text{ mm}$ and $H_{\text{coil}} = 78.2 \text{ mm}$) and ferromagnetic core ($D_o = 4.7 \text{ mm}$, $H_{\text{core}} = 170 \text{ mm}$) by Sèran and Fergeau [107].

Spatial Resolution: The surface area of the coil defines the spatial resolution of the pick-up coil. A pick-up coil with a small diameter will be able to resolve spatially separated changes in the field, while a large coil will average this change across the surface enclosed by the coil. A

⁸ D_i is estimated from figure given in the paper

reduction in coil diameter will increase spatial resolution, but from the previous discussion it will compromise the sensitivity. The configurations and geometries required to make a highly sensitive pick-up coil are not the same as those required for useful MIT measurements, as large diameter coils are unwieldy and reduce the measurement's spatial resolution. A quoted rule of thumb is that the smallest defect size detectable with a pick-up coil is approximately half the size of the coil diameter [108].

5.3.1.4 Applications for MIT

There are many different configurations of coil design [92, 101, 109, 110], the choice of which is often application specific; e.g. 'surface (pancake) coils' where the axis of the pick-up coil is parallel to the surface normal of the sample, 'encircling coils' where the coil encloses the sample (typically a pipe), or a 'bobbin coil' where the coil is enclosed by the sample (typically a pipe). While the whole sensor (probe) can consist of; a combined drive and pick-up coil (absolute probe), separate coils (drive pick-up probe), or an array of varying numbers of drive and pick-up coils. The references above present thorough reviews of all the above configurations and more. The coil that has the closest resemblance to the other sensors examined in this section is the surface coil, with a single drive and pick-up coil.

The depth at which a subsurface defect can be detected increases with coil size [100, Chap. 5], but larger coil sizes have worse spatial resolution. Lower operating frequency also increases penetration depth, but also reduces the sensor's sensitivity. These parameters must be balanced to optimise the sensor for specific applications, but generally pick-up coils are limited to surface and near-surface (1-2 mm) defect detection. The advantage of pick-up coils for a commercial sensor is their simplicity but they will not have such a highly optimised sensitivity as the specialist cases presented earlier. Although there are commercial pick-up coils for MIT (e.g. Olympus [108] and Zetec [111]), no literature on the comparison of the performance of commercial products was found. Companies do not typically publish the sensitivity due to the variation in size and operational frequency range of their different sensors, but it can be assumed that a typical pick-up coil has a sensitivity at the $nT/\sqrt{\text{Hz}}$ level [101]. The main difference from the $fT/\sqrt{\text{Hz}}$ sensitivities quoted earlier, is that for a coil to be useful for MIT it must be reasonably small since one is typically interested in small (mm scale) defects. Also, the cost of an ultra-sensitive pick-up coil will likely be exclusionary for most applications.

5.3.2 SQUIDS

5.3.2.1 Introduction

Superconducting quantum interference devices (SQUIDS) and rf magnetometers are each other's main competitors as they have a comparable $\text{fT}/\sqrt{\text{Hz}}$ sensitivity⁹. The development of SQUIDS is ~ 20 -30 years ahead of the current generation of highly sensitive atomic magnetometers, hence there are more commercially available products and there has been more research in this field. However, atomic magnetometers appear to be cheaper and are more versatile. These sensors could replace SQUIDS in some applications, such as for magnetoencephalography (MCG) [112] where around 20,000 SQUIDS have been installed in systems worldwide as of 2006 [113] (it can be assumed this is ~ 200 systems, also supported by [114]). Much of the details presented here on SQUIDS comes from an excellent primer by R. L. Fagaly [113].

5.3.2.2 Operation

When a material is made to become superconducting while a magnetic flux exists within it, the flux will be completely expelled¹⁰. If the material forms a loop and has some flux through its centre when it becomes superconducting, the flux becomes trapped as it cannot flow through the encircling material. A consequence of this is any attempt to change this flux will induce a current through the loop, called the shielding current, to maintain $\Delta\mathbf{B} = 0$. This trapped flux is quantised in units of $\Phi_0 = h/2e \approx 2.068 \text{ fTm}^2$.

A current will flow between a weak resistive barrier, called a Josephson junction, that separates the two bulk superconductors via quantum tunnelling. Typically this is a non-superconducting barrier, thinner than some characteristic length, varying from 0.1-100nm depending on the material. More recently micro bridges (constrictions) in the material are used¹¹. The current I flowing through this junction is equal to $I = I_c \sin \Phi$, where I_c is the critical current (maximum that can be sustained with zero resistance) for the junction, and $\Phi = \phi_1 - \phi_2$ is the phase difference between the two superconducting regions. This is called the dc Josephson effect and describes the basis of a SQUID.

A SQUID is a superconducting loop that consists of two arms, each containing a Josephson junction. Terminals across the loop supply a bias current $I_B < I_c$. For a static I_B , the voltage

⁹The dimensions of the highly sensitive pick-up coils described earlier are not suitable for MIT so will not be compared to these sensors.

¹⁰The flux can penetrate a very shallow layer of the material. This is called the London penetration depth and is typically $\sim 100 \text{ nm}$.

¹¹This concentrates the current so that it exceeds I_c

across the loop will be modulated between V_{min} and V_{max} with a period of Φ_0 as the flux enclosed by the loop is increased. The output voltage of the feedback loop is proportional to the change in flux. The feedback voltage can be calibrated against a known field to make a magnetic flux measurement.

To take advantage of the sensitivity of SQUIDs they are kept within magnetic shielding and are inductively coupled to the environment via an induction coil with an input circuit. In this configuration, an input circuit converts some measurable quantity into a magnetic flux at the SQUID. To make a SQUID magnetometer the input circuit acts as a so-called superconducting flux transformer, i.e. a superconducting pick-up coil.

5.3.2.3 Properties

Dead-zones: The properties of a SQUID as a magnetometer are partially defined by the pick-up coil used to couple the secondary field to the SQUID circuit. Hence, the dead-zones of a SQUID magnetometer are the same as a pick-up coil. SQUIDs are scalar sensors that measure the absolute amplitude of the field.

Sensitivity: When configured as a magnetometer, the SQUIDs sensitivity is also dependent on the design of the superconducting inductive pick-up circuit. This pick-up circuit consists of an input coil (L_i) that is inductively coupled to the SQUID in series with a larger pick-up coil (L_p). With a carefully considered multi-loop pick-up coil, SQUID magnetometers have been demonstrated with a sensitivity down to $1\text{fT}/\sqrt{\text{Hz}}$ in a range of $\sim 1 - 10^6\text{Hz}$ at 4.2 K (liquid helium), which increased to $36\text{fT}/\sqrt{\text{Hz}}$ at 77 K (liquid nitrogen) [115].

Spatial Resolution: Like dead-zones, the spatial resolution of the SQUID will be limited to the dimensions of the pick-up coil and will have the same relationship with sensitivity and coil size. The extreme sensitivity of the SQUID should enable the size of the pick-coil to be reduced considerably without compromising defect detection.

5.3.2.4 Applications for MIT

Here the focus is on applications of SQUIDs in MIT, but several other examples of NDT have been demonstrated, such as the detection of magnetic anomalies due to fatigue [116] and structural defects [117]. Some of the initial work on MIT coupled a standard EC pick-up coil probe to the SQUID [117]. This system is limited to the sensitivity of the pick-up coil and the SQUID is simply acting as a high fidelity amplifier. Gains can only be made if the pick-up coil is contained within the cryostat and is superconducting. This presents a challenge for high- T_c SQUIDs, as ceramics are the only material that exhibit high- T_c and they cannot be extruded

into wires, so pick-up coil circuits must be printed. The first significant demonstration of MIT with a SQUID was carried out by W. N. Podney [118]. A 4-mm-diameter pick-up coil at 5.3 K with a minimum lift-off of 4 mm was used to detect a 1-2 mm sized defect through 5-8 mm of aluminium at 88 Hz. More recently, a high- T_C SQUID at 77 K was used to detect 5-mm-long cracks under 2.25 mm of aluminium with a minimum lift-off of 7 mm at 990 Hz [119], while operating in an unshielded environment with an active feedback system [120] (similar to that discussed in 4.2.3). This sensor was attached to a robot arm to enable programmable scanning measurements, which could be advantageous in production line measurements. An issue with both the described configurations is that the integrated cryostat is on the order of ~ 1 m. This is, addition to the requirement of access to refrigerant, makes SQUIDs rather unsuited for MIT measurements, unless in very specific circumstances.

5.3.3 GMR Sensors

5.3.3.1 Introduction

Giant magnetoresistance (GMR) sensors¹² are nano-scale circuits built from multiple thin films. As they are manufactured through semiconductor device fabrication techniques, they can be mass-produced, drastically reducing their cost. These devices are inherently very small and low power [121]. Their primary use is as read heads for computer storage hard disks, although they have also been developed as operational magnetometers. The expendability of individual GMR sensors relative to pick-up coils, SQUIDs, and rf magnetometers, makes them highly attractive for sensor development.

5.3.3.2 Operation

There are different configurations of GMR sensors [121–123], but this description considers the four-layer type [124], described in Fig. 5.8. A conductive non-magnetic layer is sandwiched between two ferromagnetic layers. The magnetic moment of one layer is fixed, or pinned (Fig. 5.8, ‘Pinned ferro’ dark-orange), by a fourth antiferromagnetic layer on top (Fig. 5.8, ‘Antiferro’ blue layer). The direction of the magnetic moment of the other layer is free to move (Fig. 5.8, ‘Free ferro’ light-orange layer) with the direction of an applied field. This layer is configured so that in zero field its magnetic moment is orthogonal to the direction of the magnetic moment in the antiferromagnetic layer. Consider the case in Fig. 5.8 (c) where the presence of a magnetic field aligns the magnetic moment of the free layer in the opposite direction to the pinned layer. The electrons in the conduction band of the two magnetic layers

¹²This is the name of the effect which is utilised in these sensors. They are also-called spin value sensors.

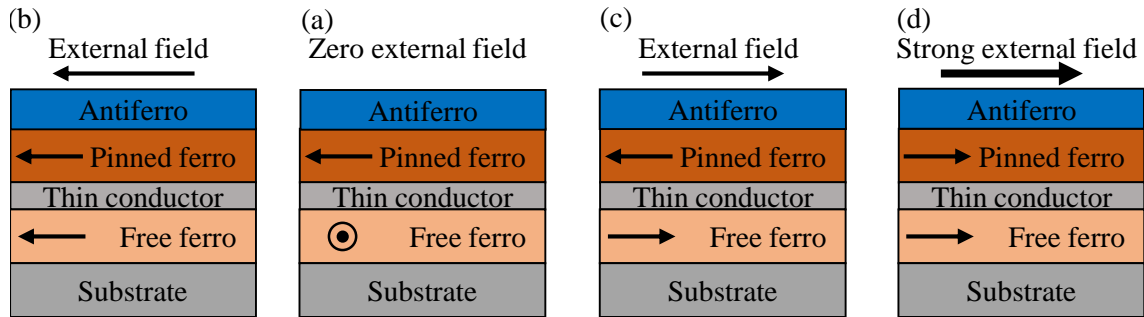


Figure 5.8: Diagram of the operation of the four-layer GMR sensor. (a) Low resistive state; an external magnetic field aligns the free layer ('Free ferro' light orange) with the layer which is pinned ('Pinned ferro' dark orange) by the antiferromagnetic layer ('Antiferro' blue). (b) Resistive state; there is zero magnetic field and the free layer is aligned perpendicular to the pinned layer. (c) Highly resistive state; field in opposite direction to the case in (a). (d) Low resistive state [opposite case to (a)]; a strong enough magnetic field aligns the pinned layer with the already aligned free layer.

are in opposite spin up and spin down states. The non-magnetic conductive layer has an equal portion of spin up and spin down electrons. Since the conductive layer is only ~ 10 atoms thick, a spin up/ down electron travelling along the conductor will have an increased probability of being scattered by the spin down/ up magnetic layer. This increases the resistance since resistance is proportional to the mean-free-path of the conduction electrons. The presence of a magnetic field will change the alignment of the magnetic moments of the magnetic layers. When the magnetic moments are parallel [Fig. 5.8 (a)] this significantly reduces the scattering of electrons in the conductive layer and therefore the resistance. When the magnetic moments are orthogonal, the conductor will be in an intermediate resistive state [Fig. 5.8 (b)]. There is a final low resistive state when a strong external field aligns the magnetic moment of the pinned layer with the direction of the field [Fig. 5.8 (d)].

This circuitry is referred to as a magnetoresistive (MR) component. The change of resistivity (10 – 20%) is considered giant, hence the name. A magnetometer constructed for a GMR sensor simply integrates this component into a circuit and measures changes in its resistance.

5.3.3.3 Properties

Dead-zones: GMR sensors are scalar sensors which can be configured to detect the component of the field directed along either a single direction ($+x$ -axis) or along an axis ($\pm x$ -axis).

Sensitivity: GMR sensors have a limited operational range as once the layers are fully aligned with the magnetic field, the response of the resistance saturates [125] and they have a baseline sensitivity at the $\text{nT}/\sqrt{\text{Hz}}$ level [98, 126]. They have been configured as part of a supercon-

ducting circuit, demonstrating $1.5 \text{ fT}/\sqrt{\text{Hz}}$ in the kHz range at 4K [127]; however, this has the same disadvantages as the SQUID and will not be considered further.

Spatial Resolution: The main benefit of GMR sensors is their small sensing volume. For NDT applications GMR sensors are typically configured gradiometrically by constructing a Wheatstone bridge out of multiple sensors. Combined as an array and with circuitry, the sensing volume is on the order of $\sim 1 \text{ mm}^3$ [128] or smaller [126]. For such a sensor the primary coil size is less important and the imaging resolution is defined by the sensor size (see Sec. 6.3.1). For this, the sensor must be very close to the sample to measure small local variations in the field. This can be utilised to make high resolution images [129] or construct arrays like in [130], where 16 sensors were aligned on a 8 mm wide probe head, and [131], where a 10×10 GMR sensor array was integrated into a probe with an array of Hall sensors.

5.3.3.4 Applications for MIT

From a review of the literature for GMR sensors applied to MIT, typically the sensor is placed in the centre of a coil and the resistance of the GMR circuit is measured as it is scanned across a sample. An ac measurement is made by monitoring the temporal dc change in the GMR sensor's resistance. The presence of some defect will influence the amplitude or phase of the secondary field, and therefore the same components of the measured signal. Demonstrations of this were carried out by Dogaru and Smith [132, 133]. This work takes advantage of the sensors 1D measurement axis. Large edges pose a problem for MIT as they concentrate eddy currents and local magnetisation, increasing the secondary field response relative to a homogeneous surface. This makes it difficult to detect the signature of defects on or near an edge. Dogaru and Smith align the sensing axis of the GMR sensor such that it minimises the contributions of the secondary field generated by the edge to the measured signal (parallel to the edge) and can easily detect the signal contribution of the defect, even if it has a magnitude of a few per cent compared to the edge signal. They also showed that the sensor has a flat signal response from dc to 100kHz.

Some other studies showed that there was conflicting performance between pick-up coils and GMR sensors. Ward and Moulder [134] demonstrated that the signal response of a GMR sensor was ~ 10 larger than a pick-up coil when applied to low-frequency ($<1\text{kHz}$) pulsed eddy current inspection (described in 6.3.1.2); while in another study, Ribeiro et al. [135] concluded that a differential pick-up coil outperformed a GMR sensor.

A study of particular interest regarding GMR sensors for NDT was carried out between Tata Steel Europe and the German Federal Institute for Materials Research and Testing [136]. This application looked at comparing a GMR sensor (configured to monitor magnetic flux leakage)

with a pick-up coil (configured for ECT). Although the character of this measurement is different from MIT, it shows there is active interest from industrial companies and representatives in this area of research.

5.3.4 Radio-Frequency Atomic Magnetometer

Although the final two chapters of the thesis are directly concerned with the operation and performance of the rf atomic magnetometer, this section aims to contextualise the rf atomic magnetometer for comparison with the other sensors. Note: in this thesis this sensor is just referred to as an rf magnetometer.

5.3.4.1 Introduction

While pick-up coils and SQUIDs measure the change in inductance of an electrical circuit and GMR sensors effectively measure a time varying dc field, rf atomic magnetometers are intrinsically sensitive to rf fields. When applied to MIT, the amplitude and phase of the secondary field measured across a sample can be directly measured from the polarisation-rotation signal of the optical probe.

5.3.4.2 Operation

The sensor's fundamental operation is described in Sec. 2.5. Some key details will be recalled here, but the focus is on practical considerations of the sensor and features that are of relevance to MIT.

A circularly polarised pump beam directs the spins of a population of alkali metal atoms along a bias magnetic field. This defines the magnetometer axis and is usually set along the z -axis. An rf magnetic field in the xy -plane that is resonant with the Larmor frequency set by the bias field will cause precession of the atomic polarisation. The precession of the atomic polarisation rotates the optical polarisation of a linearly polarised probe beam directed somewhere along the xy -plane. A balanced polarimeter converts the optical polarisation rotation to an electronic signal. The amplitude and phase of the signal can be measured directly by analysing the polarimeter signal, however this measurement lends itself well to lock-in detection.

Something that needs to be considered is that rf magnetometers have a non-sensitive axis that runs parallel to the magnetometer axis. The rf field tilts the projection of the atomic spins in the direction of the rf field and drives their precession. This only occurs if the rf field is perpendicular to the magnetometers quantisation axis (parallel bias field and pump beam). A lock-in amplifier demodulates the signal with respect to the frequency of the rf field.

Assuming this field has a constant phase, the measured phase of the polarisation-rotation signal will change linearly with a change in the angle of the rf field relative to the probing axis. The amplitude of the signal will also have a linear relationship with the rf field amplitude, so long as the field is below the saturation strength of the atomic coherences. With a linear response to the rf field direction and magnitude (below saturation), the rf magnetometer provides 2D vectorial information about the rf field, which can be directly measured. This feature is highly advantageous for MIT, where the aim is to map the secondary field generated by an object.

5.3.4.3 Properties

Dead-zones:

The rf magnetometer used in this work (described in 3.2) can make a dc measurement of a magnetic field ($|\mathbf{B}_0| = \sqrt{\mathbf{B}_x^2 + \mathbf{B}_y^2 + \mathbf{B}_z^2}$), but it is also intrinsically sensitive to rf magnetic fields in the plane which are perpendicular to the magnetometer axis ($|\mathbf{B}_{\text{rf}}| = \sqrt{\mathbf{B}_{\text{rf},x}^2 + \mathbf{B}_{\text{rf},y}^2}$). The non-sensitive axis of the rf magnetometer can be used in a similar way to the GMR sensor, so that the primary field does not dominate the measurement of the secondary field (described in Sec. 6.2.1.3).

Sensitivity: The sensitivity limit of the rf magnetometer has been determined to be $10 \text{ aT}/\sqrt{\text{Hz}}$ [5] and is shown to reach $\sim 1 \text{ fT}/\sqrt{\text{Hz}}$ in magnetically shielded environments [5, 6]. The setup used for the work presented in this thesis is $50 \text{ fT}/\sqrt{\text{Hz}}$ (unshielded), as shown in Sec. 3.2.3. It should be noted that progress in developing miniature atomic magnetometers has produced sensors with mm^3 volumes and sensitivities in the $\sim 100 \text{ fT}/\sqrt{\text{Hz}}$ range [137, 138].

Spatial Resolution: For MIT with an rf magnetometer it is advantageous to reduce the size of the rf coil that generates the primary field such that the induced secondary field generated by the structural inhomogeneity is well defined locally. Changes in this field can then be measured by the sensing volume of the rf magnetometer (the cell) that can have a radial length scale greater than the primary rf field coil. This maintains a large number of atoms, and therefore SNR, while achieving a spatial resolution which is defined by the primary coil. This subject is described in detail in Sec. 6.3.1. It should be noted that the sensing volume of an rf magnetometer can also be made small (either by using a small cell or using a buffer-gas cell where the sensing volume is determined by the intersection of the pump and probe beam) and configured in the same way as a GMR sensor with a primary field coil that is much greater than the sensing volume.

5.3.4.4 Applications for NDT

The first demonstration of MIT with an atomic magnetometer was carried out by Prof. F. Renzoni's group at University College London in 2014 [139], with the detection of different aluminium shapes with a magnetometer in the so-called Bell-Bloom configuration. The work at UCL was continued with an rf atomic magnetometer that operates in the same way as the two-beam configuration used and described in this thesis. This group has gone on to publish several papers (publications [20, 140, 141] provide a representative sample) and undertaken several PhD projects ([142, 143]) on this subject. However, the focus of the UCL group has shifted to imaging lower conductivity samples, with the aim of measuring conductivity maps of the heart (conductivity of $0.7\text{-}0.9\text{ Sm}^{-1}$, compared with $\sim 10^6\text{ Sm}^{-1}$ for metal) [19, 144]. Dr. A. Wickenbrock, who was involved with the publication [139], subsequently published a paper using an rf magnetometer for MIT with a different group at Johannes Gutenberg University [145]. More recently in this group, the same author has demonstrated MIT with nitrogen vacancy centres in diamond [146], and a different group at the National Optical Institute in Florence has demonstrated MIT with a Bose-Einstein condensate. Although these last two references use a different class of sensor, these are included in this short survey to present all of the groups who are interested in MIT with an atomic interaction based magnetometer (to the knowledge of the author of this thesis).

The work that has been done previously using the MIT with an rf magnetometer has demonstrated the detection of mm scale defects [140]; however, it has been primarily concerned with discriminating between different materials [141, 145] and imaging through barriers [20]. The following chapter will thoroughly detail the progress of investigating defect detection, with particular focus on understanding the secondary field produced by the defect and how it affects the rf magnetometer signal. Also studied is the imaging resolution of the MIT system and how to characterise properties of the defect, demonstrating the detection of defects through mm-thick barriers and mapping of sub-mm scale features. Like the GMR sensor, the non-sensitive axis of the rf atomic magnetometer is hugely beneficial as it can be aligned along the primary magnetic field axis. This increases the measurement contrast as the primary field can be much greater than the secondary field.

5.3.5 Advantages and Disadvantages

The main details regarding each sensor when applied to MIT are summarised as follows:

- **Pick-up coil:** Simple sensors that are commercially available for use in MIT measurements. They have a reduced sensitivity at low frequencies where rf field penetration

depth is greatest, which combined with the practical limits of probe size means that they are typically only used for surface and near surface (1-2 mm) detection.

- **SQUID:** Ultra-sensitive device that has demonstrated detection of mm scale concealed defects, at depths approaching a cm. However, due to requirements for cryogenics the sensor is bulky and is unlikely to approach a handheld device.
- **GMR:** Cheap to manufacture due to links to the computer industry and has a miniature sensing volume ($< \text{mm}$) which is useful for high resolution measurements; although combining this with a poor sensitivity ($\text{nT}/\sqrt{\text{Hz}}$), requires negligible stand-off from the sensor and sample - significantly reducing its practicality. The sensor only has a single measurement axis, which can be exploited by aligning the non-sensitive axis along the dominant primary field to enhance the measurement of the secondary field.

The following discussion compares the size, power, and cost of the rf magnetometer to the other magnetometers, presenting several advantages. Figure 5.9 (a) plots the theoretical sensitivity against operating frequency for an rf magnetometer (dotted-dashed line) and a pick-up coil (dotted lines represent the asymptotic limits for low and high frequency, solid line for single solid wire, dashed line for Litz wire with 1000 strands) that both have the same sensing volume [96]. This figure shows that while the sensitivity of the pick-up coil exhibits a strong dependence on operating frequency, the sensitivity of the rf magnetometer is effectively constant across the full frequency range. For the frequency ranges that are interesting for MIT (kHz), the rf magnetometer significantly outperforms the pick-up coil. As mentioned in Sec. 5.3.1, the parameters that optimise coil sensitivity (large cross-section to increase the measured flux and high frequency to maximise induction) are the opposite to the desirable features for a pick-up coil for MIT (small coil diameter for high resolution measurements and low frequency to increase primary field penetration). As will be detailed in the Sec. 6.3.1, cell size does not affect the measurement resolution, and the rf magnetometer performs well at low frequencies. For these reasons the rf magnetometer is better suited for MIT measurements than the pick-up coil. Due to the significant burden of cryogenics, it can also be easily said that an rf magnetometer is superior to a SQUID in terms of size, while demonstrating at least a comparable sensitivity. Significant progress has been made in miniaturising atomic magnetometers, and although the smallest developed so far are approximately an order of magnitude larger than a GMR, they demonstrate 4 orders of magnitude better sensitivity.

Figure 5.9 (b) presents an *impression* of sensor price against power consumption [121]. For the analysis in this thesis the focus is on sensor cost. This figure is 20 years old, but it can still be used for a reasonable comparison. The unit price for manufacturing a GMR sensor (black circle) has likely decreased significantly due to growth in computer manufacturing; however,

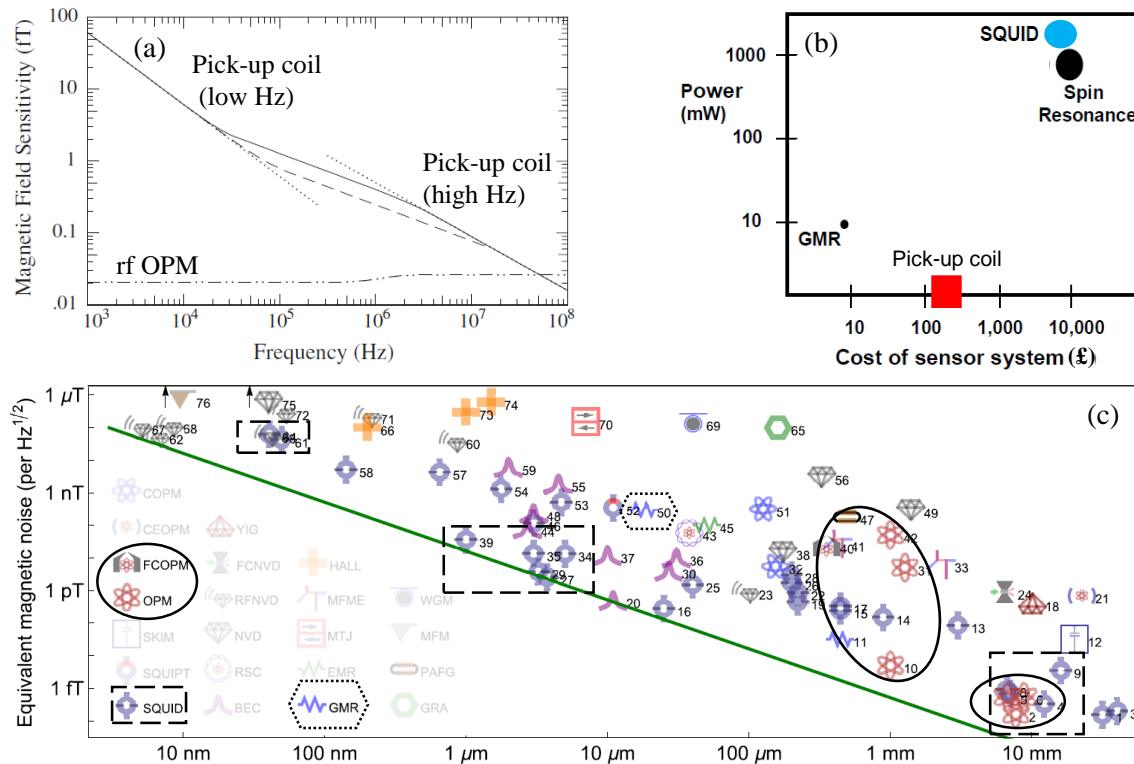


Figure 5.9: Figures from a survey of the literature comparing different sensors. (a) Compares the sensitivity and operating frequency for a pick-up coil and an rf magnetometer with the same sensing volume (edited from [96]). The dotted-dashed line is for the rf magnetometer, and the solid line and dashed line is for a pick-up coil made with a single wire and Litz wire with 1000 strands, respectively. (b) Provides an indicative estimation of the cost and power consumption for the sensors relevant to this analysis, where spin resonance is an atomic magnetometer (edited from [121]). (c) Plots the size and sensitivity of different magnetometers from a thorough survey of the literature (edited from [147]). Only the sensors that have been discussed in this section are highlighted; GMR, SQUID and OPMs (FCOPM is an OPM that uses a flux concentrator). Sensors that have an interesting size/sensitivity have been marked with a solid ellipse (OPM), dashed rectangle (SQUID), and a dotted hexagon (GMR).

this would be a low estimate for the cost of a whole sensor for MIT applications - but there are no commercially available sensors for comparison. The figure was edited to add the price of commercial pick-up coil sensors (red square), e.g £327 for a single probe from Olympus [148] or £5.5k for a 2×16 flexible coil array (£170 per coil) from Zetec [149]¹³. A pick-up coil is a passive system so technically requires no power to operate. In practice the sensor circuitry will require power operate, but this parameter has not been considered for the other sensors. The cost of the SQUIDs (blue oval) was updated, and it gives the price of the bare sensor (£5-10k),

¹³Note; the Olympus and Zetec probes require a £30.5k (single channel) and £16k (up to 32 probe channels) acquisition module to operate.

but the cost of a whole system is much higher (required cryogenic cooler system >£100k and liquid helium for low- T_c systems ~£1.5k per 2-3 days)¹⁴. Also, the power required to run the whole system would be larger than that given in this reference. The price estimated in 1999 for a spin resonance (atomic magnetometer) sensor was a good prediction of the prices from companies Twinleaf (founded 2007) and QuSpin sensors (founded 2012), both £7.5-10k per sensor. In these fledgeling companies there is significant cost on research and manufacture. The cost of individual components for a mass produced sensor is not prohibitive to reducing the price, so it is expected that this could be in the low £1000s, while the price of SQUIDs and pick-up coils are unlikely to be reduced further.

Figure 5.9 (c) is reprinted from Mitchell and Alvarez [147], which is an exhaustive survey plotting the size of the sensing region of a magnetometer against sensitivity for a huge range of sensors. Only the sensors which are relevant for the discussion in this thesis have been highlighted. They empirically find that there seems to be an energy resolution limit related to sensor size given by the green line. The closer a sensor lies to this line indicates that it is possibly operating near the ‘optimum’ sensitivity per sensor size. From their analysis it can be seen that SQUID sensors span the full range of sensor size; however, the previously discussed price and physical requirements are prohibitive for MIT measurements. The GMR sensor quoted demonstrates good spatial resolution¹⁵ at a sensitivity comparable to pick-up coils that would be several orders of magnitude larger. The atomic magnetometer exhibits the highest sensitivity and approaches the optimum sensor size. The sensitivity worsens when the sensor size is reduced; however for MIT, the cell size does not dictate the imaging resolution. SQUIDs [118] and GMR [134] sensors have been proposed for MIT since the 1990’s but have failed to become adopted technologies. Given the likelihood of the price of an atomic magnetometer reducing in the near future and the advantages they have over pick-up coils and GMR sensors in terms of sensitivity, and SQUIDs in terms of size and practically, it is clear the rf magnetometer is a promising candidate for applications in MIT.

¹⁴Costs given by users at the National Physical Laboratory

¹⁵The other entry shown for the GMR sensor has been integrated with a superconducting circuit and has the same issues as a SQUID for MIT.

Chapter 6

Development of Imaging Technique

This chapter presents the results regarding the development of the rf magnetometer as a tool for defect detection via MIT. The first section, Sec. 6.1, describes how MIT measurements are carried out. It begins by explicitly detailing the experimental setup and then discusses the best way to read out the signal from the rf magnetometer, as well as the practical topic of the measurement time for recording an MIT image. The following sections in this chapter present experimental results. The first, Sec. 6.2, describes aspects of MIT that are specifically influenced by using an rf magnetometer as the sensor. Most notably how its non-sensitive axis influences the MIT measurement (Sec. 6.2.1.3) and how it is used to avoid saturation of the atomic coherence (Sec. 6.2.2). The second section, Sec. 6.3, discusses general issues related to MIT that are present regardless of what sensor is used. These topics are; the resolution of MIT as an imaging system, how properties of the measured signal relate to the detection of defects at depth, and how the distance of rf coil to object (lift-off) influence the measurement. Although the observations presented in this section influence MIT generally, it should be noted that certain aspects of the results presented will still be specific to rf magnetometers as they were the tool used to investigate the topics.

The findings discussed in Sec. 6.2.1 regarding the understanding of the sensors response to the secondary magnetic field were first introduced by the author in [7, 9], and the topics related to defect characterisation were covered in [7, 16].

6.1 MIT Measurement Configuration

6.1.1 Experimental Setup

Although parts of the experimental setup have been described before, [lasers (Sec. 4.1.1), detection (Sec. 4.1.3), the physical setup (Sec. 4.2.1) and the field control system (Sec. 4.2.3)], a succinct overview of the arrangement used to carry out MIT with an rf magnetometer is given in Fig. 6.1 and the following text.

The whole experimental apparatus sits atop a 48" \times 96" optical bench and is supported by an aluminium frame. The table top has not been vibrationally stabilised or demagnetised. These two features, combined with nearby PSUs and electronics, create a harsh working environment for the magnetometer. A 3D-printed plastic housing [blue holder in Fig. 6.1 (a)] for a cubic paraffin coated glass vapour cell (volume 1 cm³) is positioned in the centre of an array of nested orthogonal square Helmholtz coils [lengths $2a = 1$ m, 0.94 m and 0.88 m - represented by the orange, green and back coils in 6.1 (a) and visible in (b)]. The housing is attached to the interlocking coil frame. The rf coil, which drives the primary field used for MIT, is centred directly below the cell [marked in 6.1(c)]. The rf coil is affixed to a support that enables its distance and orientation, relative to the cell, to be changed. The pump and probe beams are output from a sealed box via polarisation maintaining fibres. Both fibres are mounted to optical breadboards and conditioned with a collimating lens, an iris, and a polariser. The iris sets the beam diameter (2 mm) smaller than the collimated beam waist (~ 5 mm), increasing the power homogeneity across the beam. The pump and probe are respectively polarised by $\lambda/4$ and $\lambda/2$ waveplates and are raised via periscopes to intersect within the cell. The probe beam propagates through the cell to the polarimeter [detection in Fig. 6.1 (a) and (b)] mounted on a raised breadboard. Due to their size, all three optical breadboards are positioned outside the coil array. Consequently, the probe beam propagates ~ 1 m from the cell to the photodiodes. The relatively poor quality of the cell walls imprints optical aberrations on the probe beam, inhibiting a tight focus on to the photodiodes leading to detection losses (5 – 10%).

The output of the balanced photodiode is input to a lock-in amplifier that references the oscillating polarisation rotation signal at the frequency of the signal that drives the rf coil. This particular model of lock-in amplifier (SRS865) can be self-referenced to an inbuilt 2 V signal generator (dc-2.5 MHz). The whole rf spectrum can be read out at once by sweeping the rf frequency and storing the lock-in output to an internal buffer, simplifying the measurement process. A desktop PC controls the frequency of the signal generator output and reads the demodulated lock-in output data. It also controls much of the experiment by setting; the power levels of the pump and probe beam via the rf voltage supplied to their respective AOM

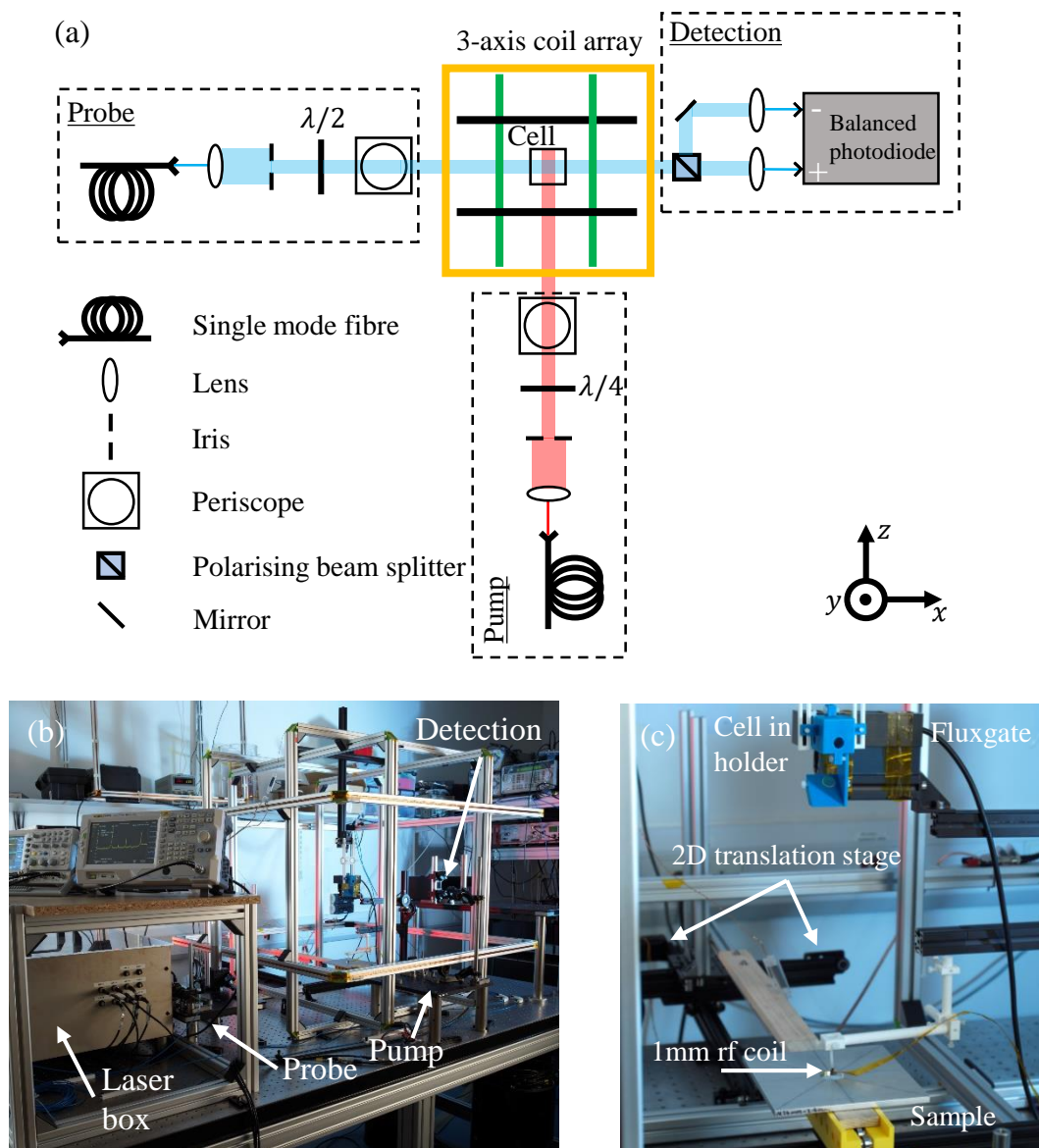


Figure 6.1: Figures that describe the experimental setup of the rf magnetometer for MIT. (a) gives a schematic of the laser setup and the positioning of the components, while (b) is a photograph of the physical setup. The parts outlined in dashed boxes in (a) correspond to the separate optical breadboards that contain the respective optical elements for each component indicated in (b). For practical reasons these elements are far from the cell; however, the spatial footprint of these components mean that this setup could be contained within an area of a few cm. (c) is a photograph of the parts of the experimental setup relevant to MIT; including the rf coil and a sample sitting atop a 2D translation stage.

by a direct digital synthesis (DDS) generator, the setpoint values of the field-control-system, the current supplied to the anti-Helmholtz coils and the positioning of a 2D translation stage [marked in Fig. 6.1 (c)] for moving samples under the rf magnetometer (details given in App. A.1).

The rf coil is typically 20-30cm from the magnetometer to simulate the case where a thick insulating material covers the sample (e.g. cladding on a pipe) and the coil is typically 1-5 mm above the sample surface (lift-off). Although the coil to magnetometer distance represents a practical operating range, the lift-off is still unrealistically close for many applications. An improved delivery method (such as strong rf coils or magnetic waveguides) will increase the lift-off, but this is outwith the scope of this work. These two distances, along with the dimensions of the rf coil, are stated alongside their relevant results. Lift-off is discussed further in Sec. 6.3.1.2.

6.1.2 Signal Acquisition

MIT measures the change in amplitude and phase of the secondary field created by an object in response to a primary field. It is possible to measure both these parameters from the on resonance ($\omega_{\text{rf}} = \omega_L$) polarisation rotation signal of the rf magnetometer, a measurement which a lock-in amplifier is particularly well suited to. However, due to operation in an unshielded environment, this data cannot be recorded with accuracy or precision in a single shot. To investigate the optimum averaging time, the statistical uncertainty (Allan deviation) of the resonance amplitude was continuously measured at a rate of $500 \mu\text{s}$ with a lock-in time-constant (TC) of $200 \mu\text{s}$, shown by black points in Fig. 6.2 (a). This data shows a $\tau^{-1/2}$ (dotted black line) dependence for $\tau \leq 200 \text{ms}$, where τ is the measurement time, indicating the amplitude exhibits white (uncorrelated) noise characteristics [150]. Over this time scale the Allan deviation of the resonance amplitude is at a similar level to the shot noise, indicating that this is a major component of the noise budget. The difference may come from the atomic noise that has the same dependence on the integration time. For $\tau \geq 1 \text{s}$ the noise dependence flattens out (dashed black line), implying ‘flicker’ noise, which is due to fluctuations in the magnetic field and is attributed to the residual 50 Hz noise and instabilities in the power supply units.

Another way of acquiring data is to record an rf spectrum and fitting to one of the demodulated outputs from the lock-in. The fit function used is given by

$$f_{\text{fit}} = X_{\text{fit}} + Y_{\text{fit}} + R_{\text{offset}} = \frac{\alpha\Gamma}{(\omega_L - \omega_{\text{rf}})^2 + (\Gamma/2)^2} \cos(\phi) - \frac{2\alpha(\omega_L - \omega_{\text{rf}})}{(\omega_L - \omega_{\text{rf}})^2 + (\Gamma/2)^2} \sin(\phi) + R_{\text{offset}} \quad (6.1)$$

where the amplitude and phase are given by $R = 4\alpha/\Gamma$ and ϕ . Γ is the full-width half-maximum (FWHM), ω_L and ω_{rf} are the Larmor and rf field frequency respectively, and the R_{offset} is an additional parameter to account for any background level in the recorded data. This fit accommodates the change in character of the two components as the phase changes [$X(\phi = 0^\circ) = Y(\phi = 90^\circ)$] as in Fig. 4.11]. The green squares in Fig. 6.2 (a) represent the uncertainty of fitting to an rf resonance which spans $\pm 150\text{Hz}$ around the resonance, recorded over 1 s and 10 s. This data was also recorded with $\text{TC} = 200\ \mu\text{s}$. The measured data for the 1 s scan time and the corresponding fit are plotted in Fig. 6.2 (b). The elevated uncertainty is a result of fitting to five independent variables (α , ω_L , Γ , ϕ and R_{offset}) and the fact that the fit does not fully represent the rf spectral profile, e.g. the presence of a small asymmetry in the data at 28.62 kHz (thicker spread of points) relative to the opposite side of the resonance in Fig. 6.2 (b) will increase the fitting uncertainty. From this analysis, the optimum measurement strategy is the identification of the resonance frequency and averaging individual measurements over $\sim 200\ \mu\text{s}$. For the investigations undertaken in this work, it is desirable to compromise the data read out in return for an increase in measurement speed by recording a single point with a lock-in at $\text{TC} = 10\ \text{ms}$ to provide additional averaging of the signal. When scanning magnetic samples, it is not practical to continuously record the on resonance amplitude due to shifts in the local magnetic field at the cell caused by imperfections in the field control system. However, this increases measurement time (discussed in the next section).

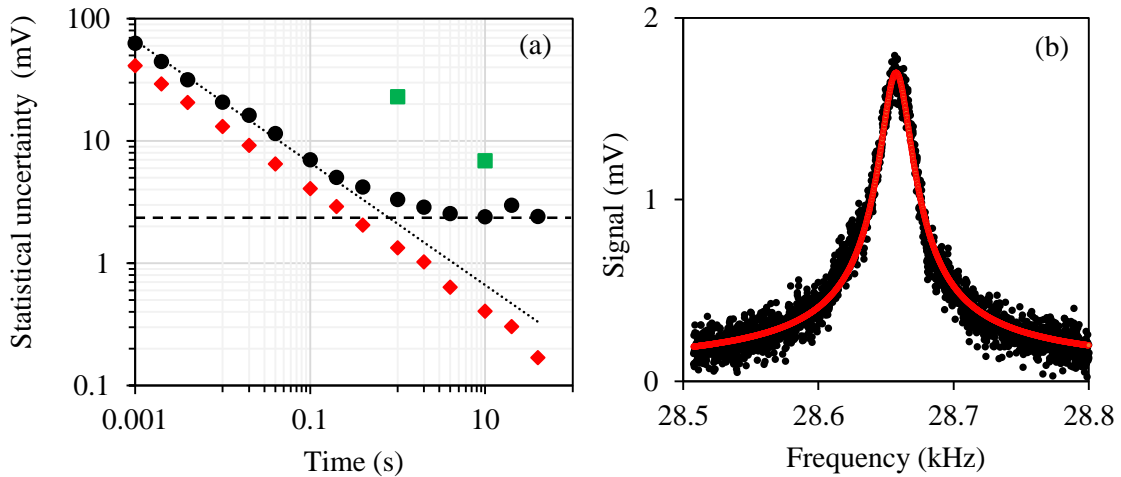


Figure 6.2: (a) Plot of the statistical uncertainty (Allan deviation) of the on resonance amplitude of the rf spectrum (black circles), the photonic shot noise (red diamonds). The green squares represent the uncertainty of fitting the amplitude to an rf resonance recorded over 1 s [plot in (b)] and 10 s. (b) Data for an rf spectrum recorded over 1 s (black circles) plotted with a fit function (solid red line).

6.1.3 Measurement Time

Measurement time is a serious consideration in all NDT methods. Although this is a general issue, it is discussed before Sec. 6.3 as it describes the processes used to record the images presented in Sec. 6.2. All the images shown in this work are recorded as a raster scan (rows and columns built of individually measured points). The total measurement time is doubled because data is only recorded when scanning in one direction on both axes, i.e. scanning along $+x$, returning to $x = 0$ before incrementing one step along $+y$. This is because the stepper motor is magnetically driven, and the change of step direction causes periodic changes in the local magnetic field. Due to the step speed of the stepper motor (~ 25 ms per $\sim 184 \mu\text{m}$) used in this work, the movement time alone for an $N_{\text{pix}} = 70 \times 70$ pixel image with a 0.92 mm step is $t_{\text{stepper}} \approx 20$ min (including the time taken for the stepper motor to return to $x = 0$ each increment along $+y$). Note: this is the typical image size recorded in this work. The most significant factor contributing to the measurement is the time taken to record an rf spectrum t_{rf} , since $t_{\text{tot}} = t_{\text{stepper}} + (t_{\text{rf}} \times N_{\text{pix}})$. The SRS865 lock-in amplifier is configured to record its X and Y quadrature outputs, while simultaneously scanning the frequency of its internal signal generator (used to drive the rf field) over a given frequency range and in a time equal to an integer number of seconds, i.e. minimum $t_{\text{rf}} = 1$ s. Therefore an image where $t_{\text{rf}} = 1$ s and $N_{\text{pix}} = 70 \times 70$, the measurement time will be $t_{\text{tot}} \approx 100$ min. The time t_{rf} can be mitigated by recording a single data point for each pixel. Ideally, this is data point is the on-resonant amplitude and phase (i.e. at a single frequency $\omega_{\text{rf}} = \omega_L$) of the rf spectrum as the object is being scanned. In this configuration, t_{tot} is limited on t_{stepper} . Although this method is subject to short and long term magnetic field perturbations and does not acquire data over the optimised measurement time, the results are more than sufficient for most of the tests carried out in this work.

Due to imperfections in the field stabilisation system, this method does not work when imaging magnetic samples. One method that can be employed to speed up the scanning time of magnetic samples is to modulate the bias magnetic field while maintaining a fixed rf field. If the magnetic field sweeps ω_L through ω_{rf} , an individual rf spectrum will be recorded with a period that is the same as the modulation period of the magnetic field. The amplitude R output of the lock-in is now an oscillating signal that can in turn be demodulated at the frequency of modulation of the bias field. A second lock-in amplifier can be used to achieve this. In such a configuration, a magnetic sample can be scanned continuously and the relative change in the amplitude of the modulated rf spectra will be recorded. It is essential that the amplitude of the modulating magnetic field is sufficient to sweep ω_L through ω_{rf} and that the period of modulation is greater than the time taken to recorded a pixel. The modulation frequency was typically set to 20 Hz. With this technique it is possible to increase the measurement speed to

match the continuous measurement speed for non-magnetic samples. Additional analysis of the rf spectrum output from the first lock-in would be required to gain information about the phase change, likely requiring off-line analysis to maintain the increase in measurement speed this method provides.

6.2 rf Magnetometer

This section describes how functionalities that are specific to the operation of the rf magnetometer influence the MIT measurement. The first section evaluates the performance of three imaging configurations that are achieved by changing the components of the rf field which contribute most to the rf magnetometer signal. The second section details how saturation of the rf atomic coherence sets the operational limit of rf field amplitude.

6.2.1 Imaging Configurations

In MIT measurements, the amplitude and phase images of an object are created by recording the relevant parameters of the rf spectrum as a sample is moved under the rf coil. It is possible to configure the magnetometer such that it is sensitive to different components of the secondary rf field. Three distinct configurations are listed below. A steel and aluminium sample, with the same dimensions (6-mm-thick, $150 \times 150 \text{ mm}^2$ plate with a 2.4-mm-deep, 24-mm-diameter circular recess), was adopted as a test-bed for investigating the different imaging configurations. The material used will be explicitly mentioned with the relevant results. The rf coil used for all the results presented in this section is a hand wound air cored coil with $N = 1000$ turns of 20- μm -diameter wire and has dimensions $D_o : D_i : H_{\text{coil}} = 5 : 2 : 10 \text{ mm}$. The rf coil is placed 30 cm from, and directly underneath, the cell. The coil lift-off from the sample surface is 1-2 mm and it is directly driven by the lock-in amplifier's internal 2 V signal generator.

For the magnetic (steel) sample, the whole rf spectrum must be recorded due to shifts in the magnetic field at the cell as the plate is moved. For the aluminium sample it is sufficient to measure the on resonance amplitude and phase as the plate is continuously scanned. The images presented consist of 70×70 pixels, with a step of 0.92 mm. The rf spectra recorded for the steel samples have a span of 200 Hz recorded over $t_{\text{rf}} = 8 \text{ s}$ with a lock-in TC = 10 ms, giving a total scan time of $\sim 12 \text{ hrs}$. The continuous measurement for the aluminium sample has a scan time of $\sim 20 \text{ mins}$.

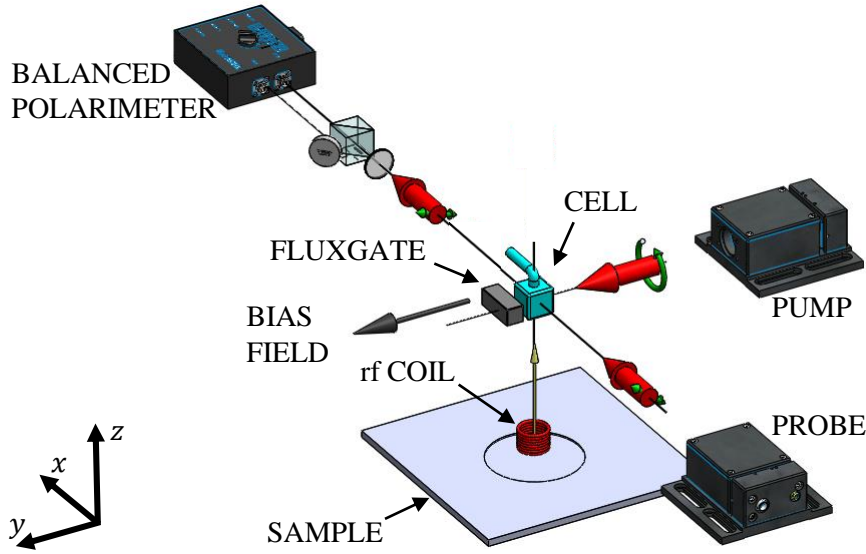


Figure 6.3: Experimental setup of the so-called normal configuration, where the magnetometer axis (parallel bias magnetic field and pump beam) and rf magnetic field are orthogonal.

6.2.1.1 Normal Configuration

The typical setup for an rf magnetometer is to align the rf field such that it maximises signal strength. With the pumping configuration used in this work, this is achieved when the magnetometer axis (bias magnetic field parallel to the direction of the pump beam) is orthogonal to the rf magnetic field axis defined by the rf coil, as shown in Fig. 6.3. The magnetometer axis and rf field are aligned along the y and z -axis, respectively. In this work this geometry is named the normal configuration. As the sample is scanned under the coil, the magnetometer measures a combination of the primary rf field \mathbf{B}_{rf} from the coil and the secondary field \mathbf{b}_{rf} generated by the sample. As in the previous chapter 'rf' will be dropped from \mathbf{B} and \mathbf{b} , and the primary field should not be confused with the static bias magnetic field \mathbf{B}_0 . Assuming the surface normal of the plate is parallel with the rf coil axis, the rf field measured by the magnetometer is given by

$$\mathbf{B}_{\text{tot}} = \mathbf{B}_x + \mathbf{B}_z + \mathbf{b}_x + \mathbf{b}_z \quad (6.2)$$

since it is not sensitive to fields along the y -axis. The amplitude of the rf spectrum R is proportional to the magnitude of the measured rf field

$$R = A_{\text{rf}} \sqrt{(B_x + b_x)^2 + (B_z + b_z)^2}, \quad (6.3)$$

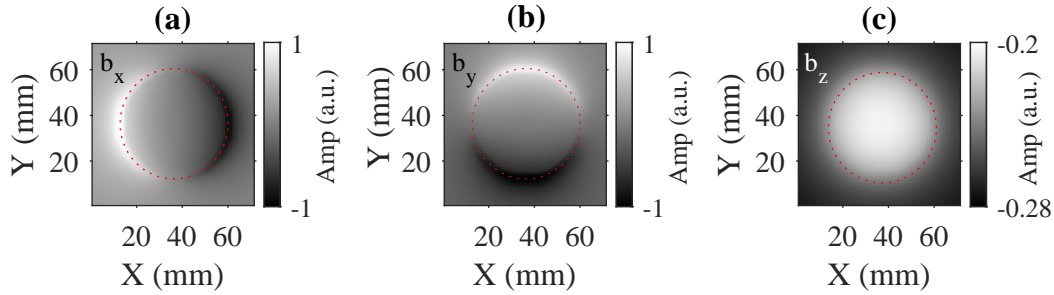


Figure 6.4: Simulated images of how the amplitude of the (a) b_x , (b) b_y and (c) b_z components of the secondary field change as a coil is scanned across a 48-mm-diameter hole. The image comprises of 70×70 pixels. The red dashed line outlines the edge of the recess.

and its phase ϕ is related to the direction of the rf field

$$\phi = \tan^{-1} \left(\frac{B_x + b_x}{B_z + b_z} \right), \quad (6.4)$$

where A_{rf} is some scaling factor between the measured rf field and signal. Since the distance between the coil and magnetometer is so much greater than the coil diameter, it can be assumed that the rf coil generates a well defined primary field, i.e $\mathbf{B} \approx \mathbf{B}_z$, and that $\mathbf{B} \gg \mathbf{b}$. Equation 6.3 and 6.4 can now be approximated to

$$R \approx A_{rf}(B_z + b_z) \quad (6.5)$$

$$\phi \approx \frac{b_x}{B_z + b_z}, \quad (6.6)$$

using the small angle approximation for the latter. From the simulations shown in Fig. 6.4 [reproduced from Sec. 5.2.2.1], the change in (a) b_x is much greater than (c) b_z so it can be assumed that $\phi \approx b_x/B_z$. This result in mapping of the orthogonal components of the weak secondary field on the strong primary field.

Figure 6.5 shows the (a) amplitude and (b) phase images recorded for the steel plate. It can be clearly seen that the amplitude and phase correspond to the simulated values of the b_z and b_x components in Fig. 6.4 (c) and (a), respectively. A change in phase is only visible along the x -axis since the secondary field generated by edges perpendicular to the magnetometer axis are not detectable. The phase carries a better signature of the recess since the change has a much greater dynamic range than the amplitude. Also the amplitude is strongly affected by the presence of the plate edges and any angle between its surface normal and the rf field, which accounts for the change in background signal. Comparison between Fig. 6.5 and Fig. 6.4

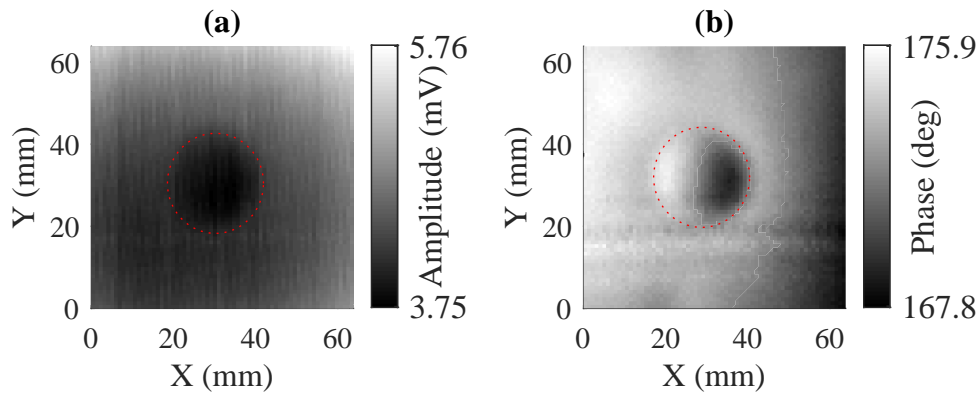


Figure 6.5: The amplitude (a) and phase (b) of the rf spectrum recorded in the normal configuration for the steel plate [amplitude image is the same as Fig. 5.6 (a)]. The red dashed line outlines the edge of the recess.

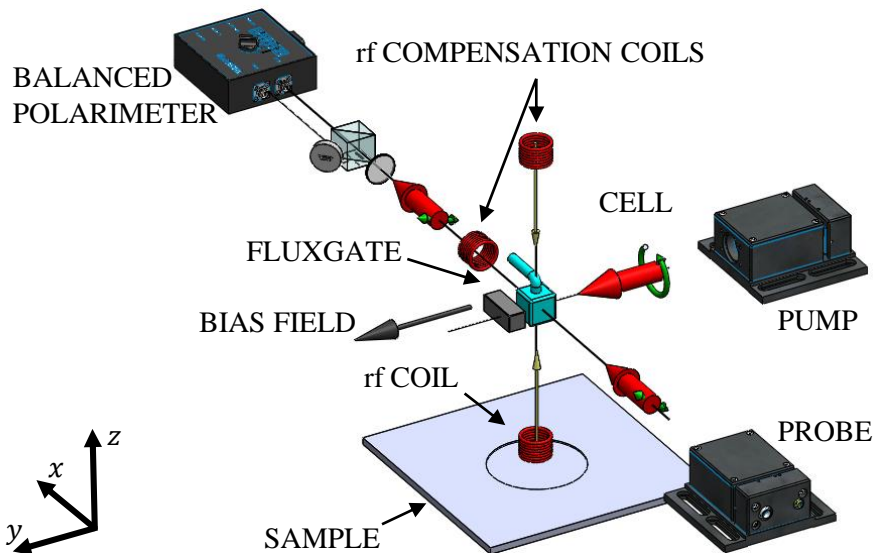


Figure 6.6: Experimental setup of the so-called compensated configuration, where the magnetometer axis (parallel bias magnetic field and pump beam) and rf magnetic field are orthogonal, and one or two rf compensation coils are aligned along the sensitive axis of the magnetometer to compensate the primary field at the cell.

shows that the rf magnetometer is performing a vector measurement of the rf field, which will be elaborated further in Sec. 6.2.1.3.

6.2.1.2 Primary Field Compensation

Maintaining the same experimental setup as the normal configuration, the logical next step to improve the imaging contrast is to compensate \mathbf{B} at the cell, as depicted in Fig. 6.6. This

is called the compensation configuration and can be achieved by applying a compensatory field \mathbf{B}_c with an additional rf coil placed on the opposite side of the cell and aligned with the primary rf field coil along the z -axis. If required, additional coils can be used to create an rf field along the horizontal axis, like the coil directed along the x -axis in Fig. 6.6. The field measured by the magnetometer is now

$$\mathbf{B}_{\text{tot}} = \mathbf{B} + \mathbf{B}_c + \mathbf{b} = \mathbf{B}' + \mathbf{b}, \quad (6.7)$$

and R and ϕ will become

$$R = A_{rf} \sqrt{(B'_x + b_x)^2 + (B'_z + b_z)^2}, \quad (6.8)$$

$$\phi = \tan^{-1} \left(\frac{B'_x + b_x}{B'_z + b_z} \right). \quad (6.9)$$

Figure 6.7 shows the simulated dependence of the amplitude of the \mathbf{b}_x (dashed red line) and \mathbf{b}_z (solid blue line) component as the primary coil (aligned along the z -axis) is scanned along a 1D-axis over a plate with a recess in the form of a 24-mm-diameter hole centred at 0mm. \mathbf{b} is assumed to be generated from eddy currents and was calculated in the same way as was described Sec. 5.2.2.1. In the vicinity of the recess (edge at $X = \pm 12$ mm) the symmetry of the eddy currents are broken and a large \mathbf{b}_x component is produced. The asymmetry of the eddy current flow is mirrored on the other side of the recess ($X = -12$ mm), resulting in a change of sign in the amplitude, i.e. the \mathbf{b}_x component points in the opposite direction on either side of the recess. In the centre of the recess, these \mathbf{b}_x components cancel each other to zero. It should be noted that there is a slight asymmetry in the amplitude of the \mathbf{b}_x profiles that correspond to the opposite edges of the recess. This asymmetry is erroneous and is due to the resolution of the simulation in mapping circular current loops (the eddy currents) and a circular hole to a square point grid. Since the secondary field points in the opposite direction to the primary field, the \mathbf{b}_z component is negative. Over the recess there is less material so the magnitude of the \mathbf{b}_z component decreases.

The model used to simulate Fig. 6.7 can then be used to calculate how the amplitude R and phase ϕ changes as the coil is scanned across the recess. The plots in Fig. 6.8 represent the numerical simulations of the R (red line) and ϕ (dashed line) for different compensation fields, \mathbf{B}_c . Moving between the plots arranged in rows and columns is equivalent to changing the $\mathbf{B}_{C,x}$ and $\mathbf{B}_{C,z}$ components of the applied field, respectively. The applied field is given in terms of resultant field $\mathbf{B}' = \mathbf{B} + \mathbf{B}_c$ at the top of each plot. In each plot, the two peaks in amplitude at $X = \pm 12$ mm correspond to the signal amplitude generated by the opposite edges

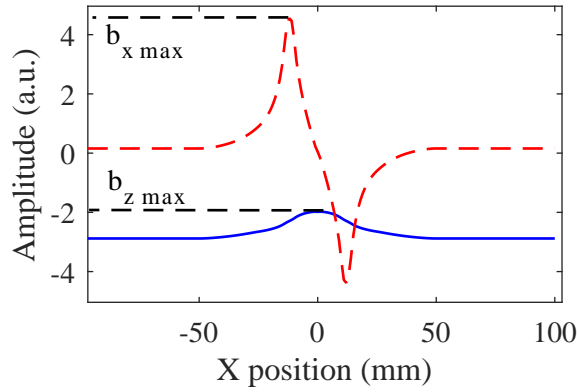


Figure 6.7: Simulation of the distribution of the secondary field components b_x and b_z (marked with dashed red and solid blue lines, respectively). The coil is moved along the x -axis across the centre of a 24-mm-diameter recess [equivalent to a cross-section along the x -axis over the centre of the recess in Fig. 6.4 (a) and (c)]. Maximum values of b_x and b_z within the recess boundaries are referred to as $b_{x\max}$ and $b_{z\max}$.

of the recess. Since the amplitude is a measure of the magnitude of the secondary field, it is always positive. Where possible the relationship between the change in amplitude and phase profile will be described quantitatively, but for some cases only qualitative comparisons can be made.

A figure of merit can be defined to evaluate the efficacy of the compensation. This is the amplitude C_r and phase C_ϕ contrast of the change in R and ϕ as the coil is scanned over the recess, given by

$$C_R = \frac{R_{\max} - R_{\min}}{R_{\max} + R_{\min}}, \quad (6.10)$$

$$C_\phi = \phi_{\max} - \phi_{\min}, \quad (6.11)$$

where these are the maximum and minimum of the values recorded from the data. These have a respective maximum of $C_R = 1$ and $C_\phi = 180^\circ$. Note for C_ϕ , this is only considering the change measured across a 1D scan over the recess. $C_R = 1$ can only be achieved if $R_{\min} = 0$, while the condition for $C_\phi = 180$ requires a change in sign of the nominator and a singularity in the denominator of ϕ . Counterintuitively both contrast conditions are not maximised when the primary field is fully compensated, i.e. for $B' = 0$ then $R = A_{rf} \sqrt{b_x^2 + b_z^2}$ and $\phi = \tan^{-1}(b_x/b_z)$. From the results in Fig. 6.7, neither b_x or b_z are zero at the same time. The optimum contrast will be reached when $B'_x = 0$ and $B'_z = b_{z\max}$ (note: from Fig. 6.7 $b_{z\max}$ is negative so is canceled when a positive field is applied), so passing through the centre of the recess both

$b_x = b_z = 0$ and \mathbf{b}_x changes sign. This condition is called the compensation point and is depicted by the plot in the second (middle) column and third (from top) row, with the simulations giving $C_R = 0.98$ and $C_\phi = 179^\circ$. It is not possible to reach the maximum contrast value for both amplitude and phase simultaneously due to the residual component of the \mathbf{b}_z component. If \mathbf{b}_z is fully compensated over the centre of the recess then it will not be non-zero over the edge, thus $C_\phi < 180^\circ$. If the \mathbf{b}_z component from the edge is compensated then $C_\phi = 180^\circ$, but $R_{\min} \neq 0$ anywhere over the plate or recess. Another possible reason for the difference in calculated contrast from their possible maximum value is due to the resolution of the simulation.

From this point it is possible to study what effect applying the components of \mathbf{B}'_z and \mathbf{B}'_x have on the measured profile, which is useful when trying to realise the compensation point experimentally and understanding MIT images recorded in this configuration. First, consider the change in amplitude profile when adding a \mathbf{B}'_x component when $B'_z = 0$ [plots in the second (from top) row]. For $B'_x = 0$ then the amplitude profiles from either edge should be symmetrical from the simulations shown in Fig. 6.7. The addition $B'_x = -b_{x,\max}$ (plots in first column) or $B'_x = b_{x,\max}$ (plots in third column) either opposes or aids the secondary field generated by opposite edges of the recess. In these cases the amplitude contrast remains high, but the phase contrast is drastically reduced, e.g. for $B'_x = b_{x,\max}$ in the plot in the third (right) column and second (from top) the values are $C_R \approx 0.92$ and $C_\phi \approx 62^\circ$. The change in amplitude and phase profiles for the $B'_x = -b_{x,\max}$ and $B'_x = b_{x,\max}$ should be symmetrical. The slight difference between them is again due to the resolution of the simulation. This applies to all of the plots shown in Fig. 6.8.

Now, consider the change in amplitude profile when adding a \mathbf{B}'_z component. It is simplest to consider cases where $B'_x = 0$ (plots in second column) and $b_x = 0$ (e.g. at $X = -100$ mm away from the recess), since the dependence on amplitude reduces to $R \propto B'_z + b_z$. For the case where $B'_z = 0$ (third row), only the secondary field contributes to the measured amplitude. From this point it can be seen that adding a \mathbf{B}'_z field changes the dc level of the amplitude and at $X = 100$ mm, $R_{100\text{mm}} \sim 0.63$ a.u. Adding a field of $B'_z = -2.3b_{z,\max}$ (plot in fourth row) in the same direction increases the amplitude to ~ 1.63 a.u. (change of 1 a.u.) Adding the same field in the opposite direction, $B'_z = 2.3b_{z,\max}$ (plot in first row), opposes the secondary field generated by the plate, reducing it through zero and resulting in $R \sim 0.37$ a.u. (change of -1 a.u.) This shows a linear relationship between the R and $\mathbf{B}' = \mathbf{B}'_z$. For the other plots and features where \mathbf{B}'_x and \mathbf{b}_x are non-zero the influence of \mathbf{B}'_z is less obvious. From visual inspection on the plots in the second column, it is clear the contrast of both the amplitude and phase decreases when \mathbf{B}'_z moves away from the compensation point.

The following argument describes the change in phase for the plots described in the second

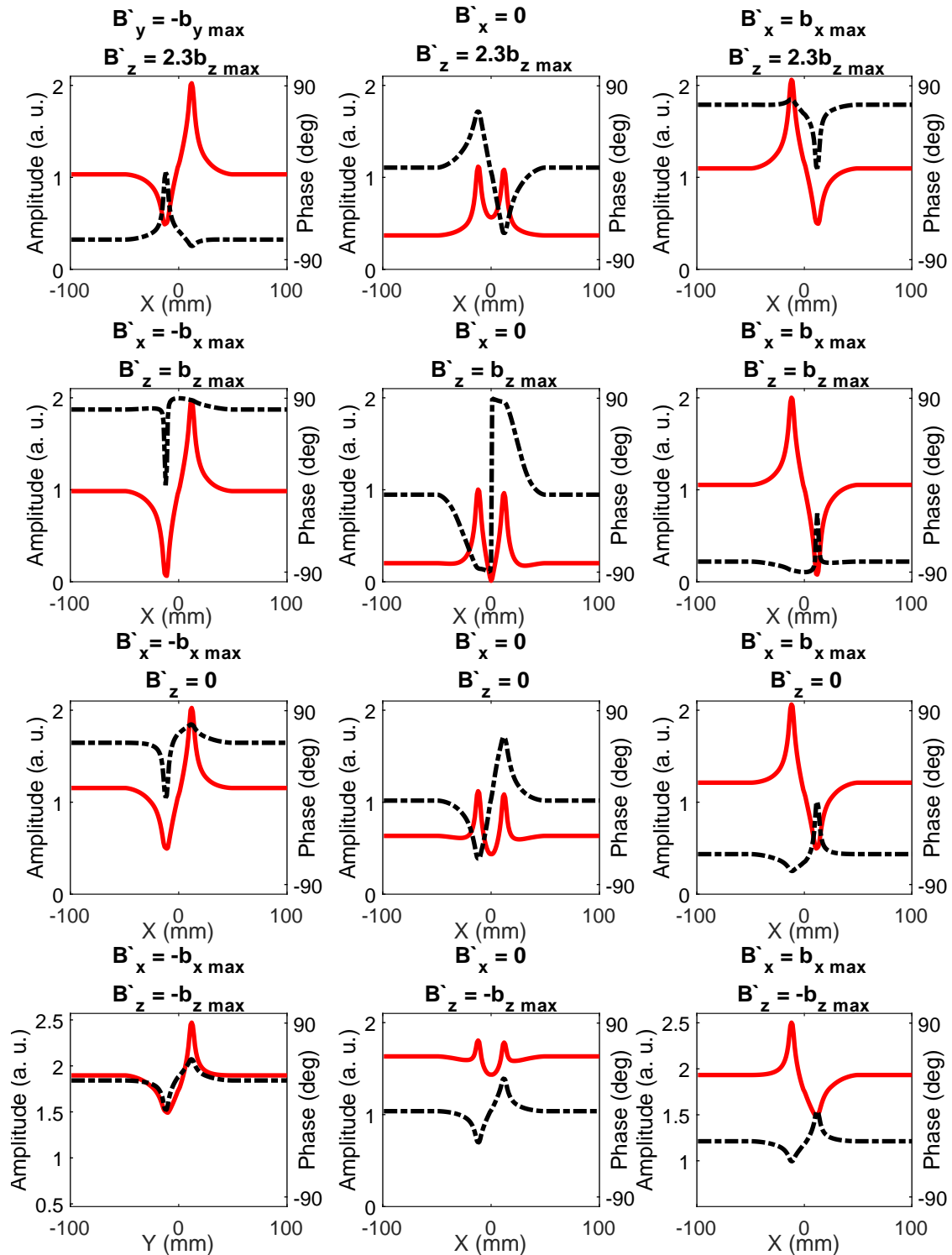


Figure 6.8: Simulated change of the signal amplitude (solid red line, left y-axis) and phase (dashed black line, right y-axis) of the rf spectrum for various amplitudes of B' (given in plots titles) as the coil is scanned across a 24-mm-diameter recess. Plots along the vertical and horizontal axes represent changes in the field along the z -axis and x -axis, respectively. The amplitude is expressed in arbitrary units of b_x .

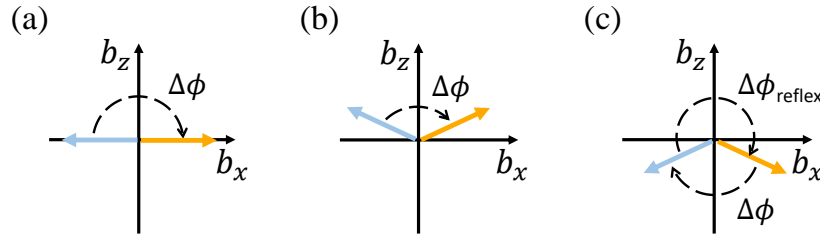


Figure 6.9: Light blue and yellow arrows represent the secondary field generated by the opposite edges of the recess for different field compensations. The angle between these secondary fields corresponds to the measured phase difference $\Delta\phi$ between the two fields. (a) At the compensation point where the secondary field is defined by the \mathbf{b}_x component and $\Delta\phi \approx 180^\circ$. For (b) and (c) \mathbf{b}_z has a non-zero positive and negative amplitude respectively, resulting in $\Delta\phi < 180^\circ$.

column as it is useful for the description of the experimental realisation of the compensation point in the following paragraph. The change in angular distribution of the secondary field maps directly on to the phase change $\Delta\phi$, i.e. 180° phase shift between fields that point in opposite directions. This angle is in the xz -plane in which the rf magnetometer is sensitive to rf magnetic fields. At the compensation point $\Delta\phi \approx 180^\circ$, since the angular distribution is defined by the \mathbf{b}_x component generated by opposite edges of the recess. Vectorially this is shown by Fig. 6.9 (a). Away from the compensation point, as \mathbf{b}_z is either positive or negative and \mathbf{b}_x remains the same size, the angle between them is $\Delta\phi < 180^\circ$, as shown by Fig. 6.9 (b) and (c), respectively.

Experimentally the compensation point can be realised by placing the centre of the recess directly beneath the primary field coil (aligned along the z -axis) and compensating the amplitude of the rf spectrum with an additional coil above the cell, which is on the same axis as the primary coil. For the results presented here, the second coil was identical to the primary coil. This procedure assumes the primary coil is parallel to the surface normal of the plate. If this is not the case, a third or fourth coil can be used to compensate any field along the x or y -axes. Typically, additional coils were only required for magnetically permeable samples. In both cases, the amplitude of \mathbf{B}_c was tuned by changing the distance of the compensation coil to the cell.

First the compensation point was realised with an aluminium plate and a single compensation coil. Figure 6.10 shows the (a) amplitude contrast C_R (red diamonds) and the (b) phase contrast C_ϕ (red triangles) measured by recording the change in amplitude and phase as the aluminium plate was scanned under the rf coil, for different positions of compensation coil (value of \mathbf{B}'_z), e.g. similar to the simulated values in the middle (second) column in Fig. 6.8. The plotted values for C_ϕ must be adjusted since practically $0^\circ \leq C_\phi \leq 180^\circ$, i.e. the phase (direction)

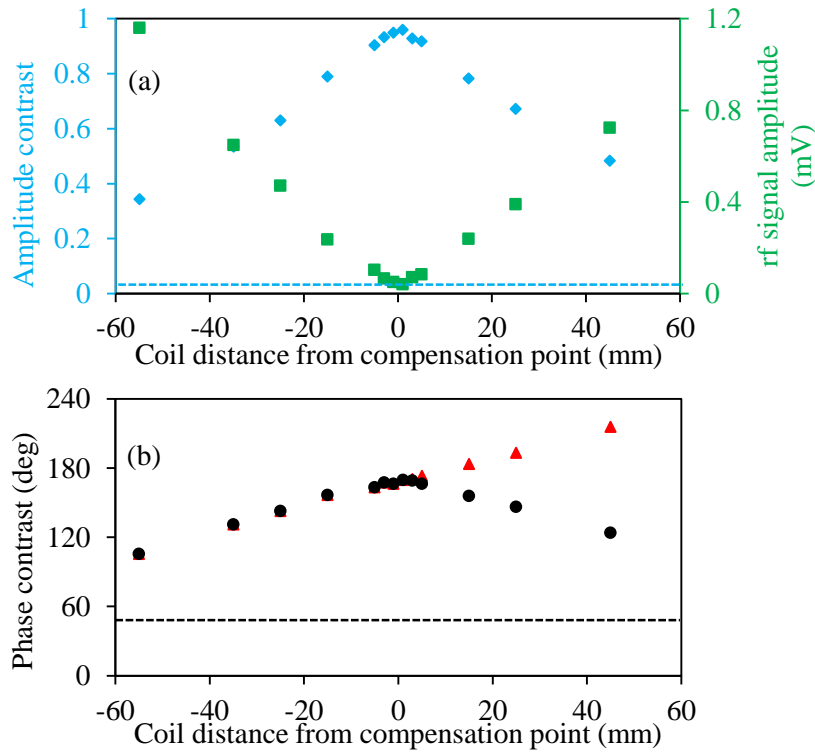


Figure 6.10: Plots of the (a) amplitude (cyan diamonds) and (b) phase (black circles) contrast of the rf spectrum as the position of the second compensation coil is changed along the z -axis. 0mm represents the position of the secondary coil above the cell where the compensation point is reached. The green squares in (a) represent the amplitude of the rf spectrum at the centre of the recess, while the red diamonds in (b) show the unadjusted values for the phase contrast. The (a) cyan and (b) back dashed lines mark the amplitude and phase contrast in the absence of the compensation field, i.e. in the so-called normal configuration.

of the secondary field generated by the opposite edges of the recess edge can only change by a maximum of 180° . The meaning of the values $C_\phi \geq 180^\circ$ can be interpreted as the measurement of the reflex angle described in Fig. 6.9 (c). When this occurs the values for C_ϕ can be corrected by setting $C_\phi = 360^\circ - C_{\phi,\text{reflex}}$ ($0^\circ = 360^\circ$) and are represented by the black circles in Fig. 6.10 (b). The compensation point, marked as 0mm, occurs when the C_R and C_ϕ are maximised. The amplitude of the rf spectrum recorded over the centre of the recess [green squares in Fig. 6.10 (a)] is also minimised at the compensation point. Both of these effects correspond with what is expected from the simulations in Fig. 6.8. It should be noted that C_R and C_ϕ do not reach their ideal values, i.e. maximum of $C_R = 1$ and $C_\phi = 180^\circ$. This is due to misalignment between the surface normal of the plate and the primary field (not parallel), and the primary field and the magnetometer axis (not perpendicular). The difference of $\approx -10^\circ$ from maximum phase contrast is a measure of the systematic error in the alignment

and compensation of the field and is taken into account in the determination of $C_{\phi, \text{refelx}}$. The dashed cyan (a) and back (b) lines mark the amplitude and phase contrast in the absence of a compensation field, i.e. in the so-called normal configuration described in Sec. 6.2.1.1, where $C_R = 0.03$ and $C_\phi = 47^\circ$. In the compensated configuration these improve to $C_R = 0.77$ and $C_\phi = 170^\circ$.

To demonstrate the compensation of the \mathbf{B}'_x component, measurements were made with the steel plate and a small misalignment of the rf coil with the surface normal of the plate. This required a third coil aligned along the x -axis, like the one directed along the x -axis in Fig. 6.6. The compensation point is reached in the same way as for the aluminium plate with a single coil, by changing the respective position of the compensation coils directed along the x and z -axis. For illustrative purposes, Fig. 6.11 shows the amplitude (a-c) and phase (g-i) images for the steel plate recorded for different values of \mathbf{B}'_x , once the compensation point on the z -axis has already been reached (i.e. $B'_z + b_{z, \text{max}} = 0$). Cross-sections for the amplitude and phase (black line) along the x -axis are plotted in (d-f) and (j-l), respectively, along with the results from their corresponding numerical simulations (dotted-dashed red line). The images in this figure are equivalent to the data in the second row of plots in Fig. 6.8, where Fig. 6.11 (b) and (h) represent the amplitude and phase images expected at the compensation point. The edge of the plate causes the amplitude to increase at the image edge, e.g. Fig. 6.11 (b) $0 \text{ mm} \leq X \leq 10 \text{ mm}$ and $55 \text{ mm} \leq X \leq 64 \text{ mm}$. The asymmetry in amplitude across the plate, i.e. dark ring encircling the edge at $\sim X = 25 \text{ mm}$ and bright corners at $Y = 0 \text{ mm}$ and 64 mm , is likely due to imperfections in the compensation of the transverse field components as the plate is scanned underneath the coil.

Away from the compensation point C_R is near its maximum value [Fig. 6.11 (d) and (f)]; however, C_ϕ is significantly reduced [Fig. 6.11 (j) and (l)] relative to that achieved at the compensation point [Fig. 6.11 (k)]. In addition to this, the area where there is any significant change in the phase is drastically reduced. This should be considered for cases when only monitoring the phase and scanning with a coarse spatial step, as it would be easy to miss the signature of the recess. It should be noted that results with the aluminium plate have a similar character as these images, although \mathbf{B}_x components must be applied to generate images shown in the first and third rows.

6.2.1.3 Self-Compensation Configuration

While the compensated configuration shows it is possible to approach the maximum contrast regimes for both the amplitude and phase, not all of the spatial information about the recess is available since the magnetometer axis (non-sensitive axis) is aligned along the y -axis. A more

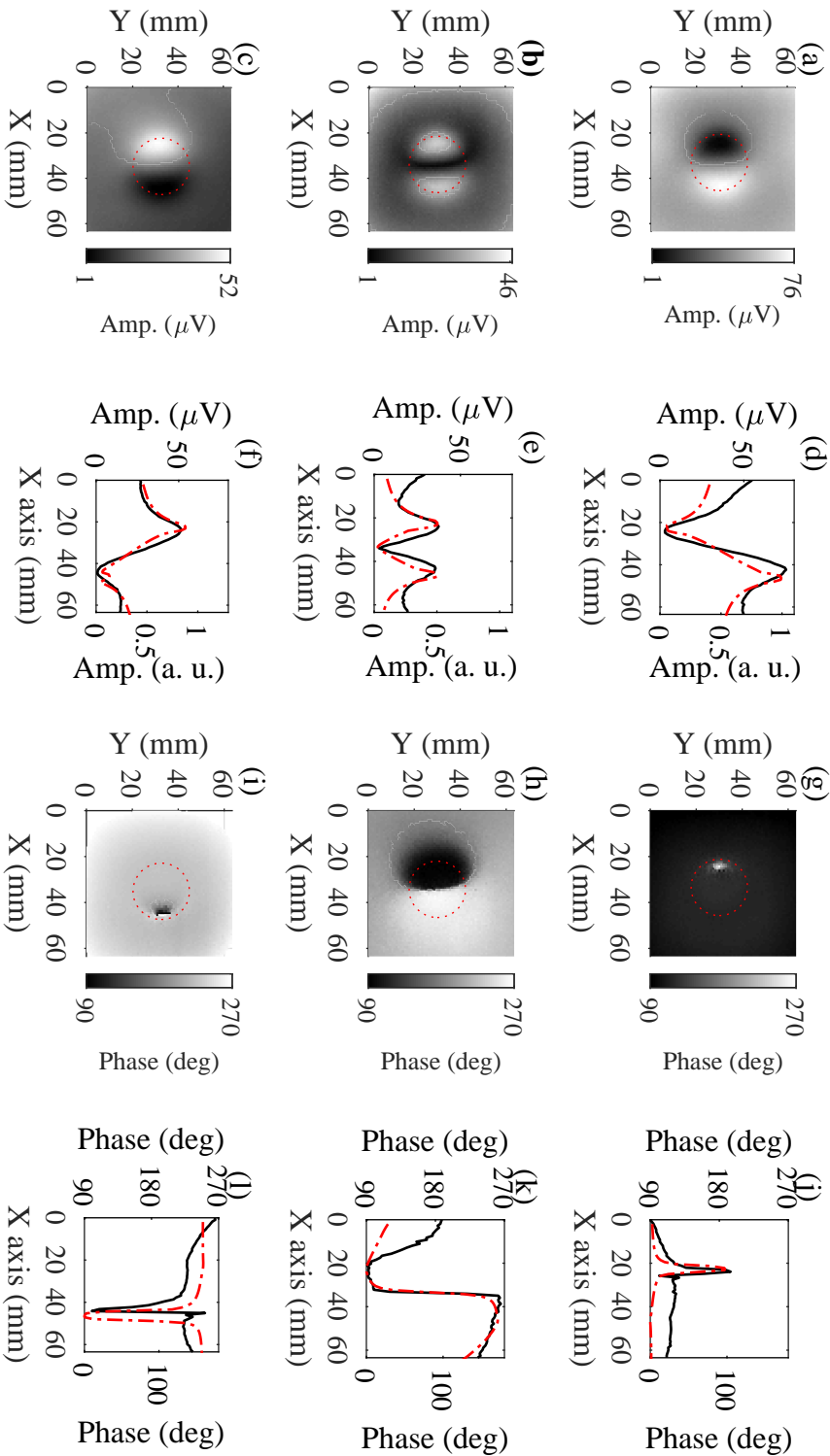


Figure 6.11: Amplitude (a-c) and phase (g-i) images of the steel plate recorded for three values of B_x with the field along z properly compensated. Cross-sections along X for the amplitude (d-f) and phase (j-l) (black lines) are compared against numerical simulations (dotted-dashed red lines). Moving along the vertical axis of these plots is equivalent to moving along the second row of plots in Fig. 6.8. The outline of the recess is given by the dashed red line in (a-c) and (g-i).

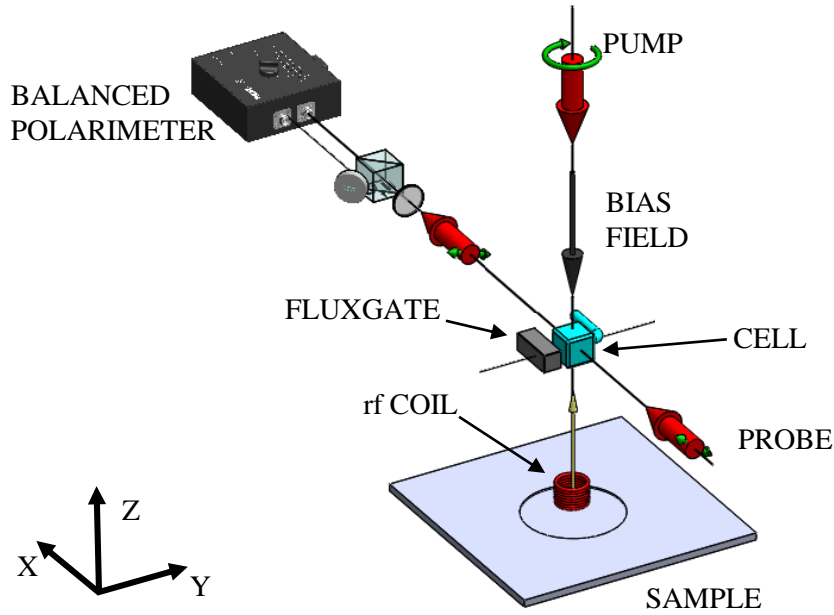


Figure 6.12: Experimental setup of the so-called self-compensated configuration, where the magnetometer axis (parallel bias magnetic field and pump beam) and rf magnetic field are parallel.

an elegant solution is to align the magnetometer axis such that it is parallel to the primary field and the surface normal of the plate (directed along the z -axis) as shown in Fig. 6.12. Since $\mathbf{B} \approx \mathbf{B}_z$, this geometry fully meets the condition for compensation, removing the need for any compensation coils and enables the full reconstruction of the secondary field generated along the surface of the object, i.e. the components generated by the edges of the recess. This is called the self-compensated configuration. The amplitude and phase measured by the magnetometer are now given by

$$R = A_{rf} \sqrt{b_x + b_y}, \quad (6.12)$$

$$\phi = \tan^{-1} \left(\frac{b_x}{b_y} \right). \quad (6.13)$$

Figure 6.13 shows the experimentally measured amplitude and phase images for the normal (a-b), compensated (c-d) and self-compensated (e-f) configurations, respectively. All three have been recorded for the aluminium plate at an operational frequency of 30kHz. It can clearly be seen that the amplitude image for the self-compensated configuration fully reconstructs the signature of the circular recess. Notably, the amplitude of the background (over the homogeneous region of the plate) has an amplitude approaching 0mV.

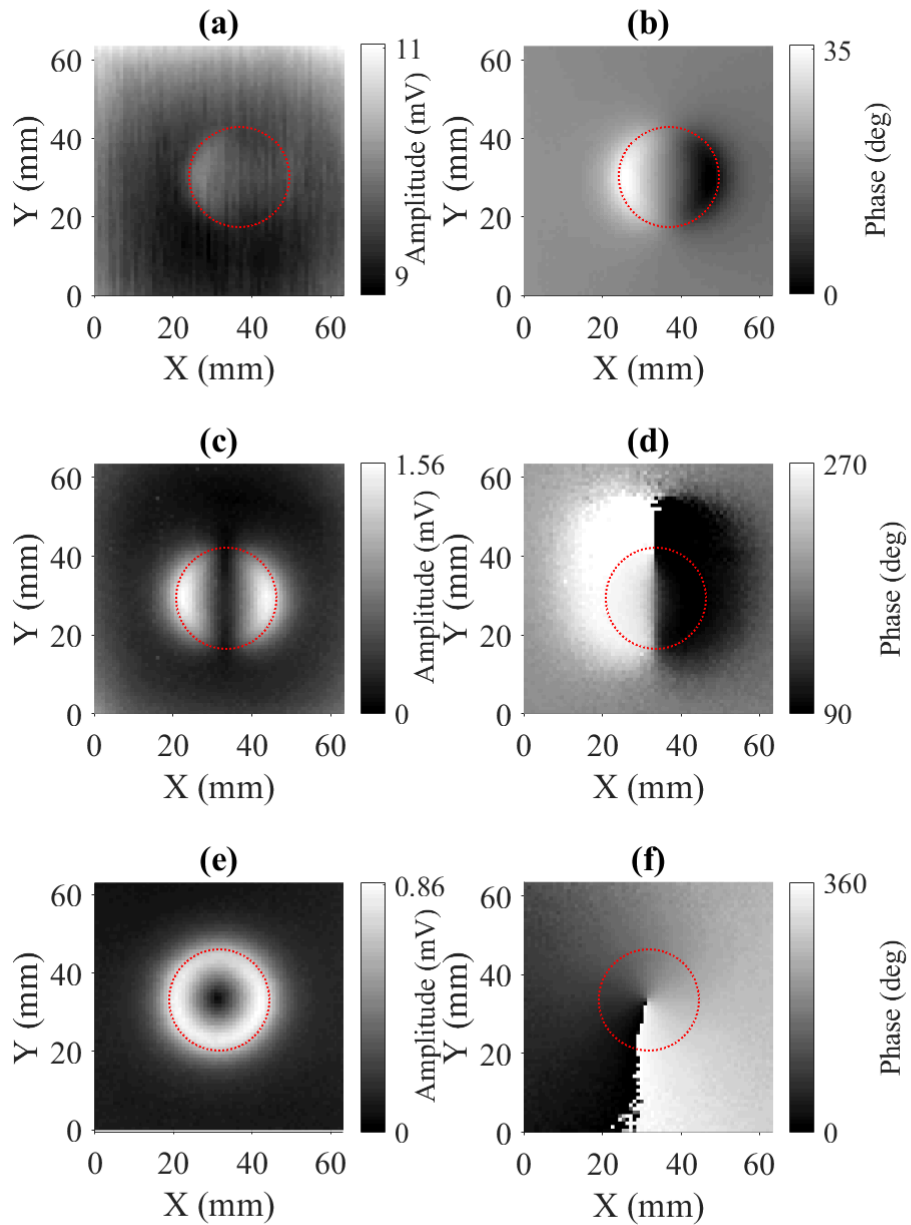


Figure 6.13: Amplitude and phase images for the (a-b) normal, (c-d) compensated, and (e-f) self-compensated configurations. A dashed red line outlines the edge of the recess in each configuration.

The phase image Fig. 6.13 (f) shows full 360° rotation, which describes the full rotation of the secondary field as the coil is scanned around the perimeter of the recess. This is vortex-like and will be referred to as such for the remainder of this thesis. Although the dynamic range of this data is at its maximum 360° , the maximum phase contrast is still defined as $C_{\phi, \max} = \phi_{\max} - \phi_{\min} = 180^\circ$ because $0^\circ = 360^\circ$ (it only makes sense to compare the phases from opposite edges in a 1D cross-section over the recess). The large dynamic range of the phase image could be highly useful for the quick identification of defects, after which higher resolution images could be recorded for the amplitude. The discontinuity at the ‘centre’ of the vortex is expected since it is the point where the horizontal components of the secondary field cancel each other, meaning the field is undefined (zero amplitude and no phase). In real measurements there may be a residual component of the rf field which contributes to the signal and generates signal.

The amplitude contrasts for the three images; (a) $C_R = 0.04$, (b) $C_R = 0.77$, and (c) $C_R = 0.79$, shows the improvement in defect detection with these three imaging configurations. As seen, the compensation and self-compensation configurations should have comparable contrasts since they both directly measure the secondary field. However, it is easier to realise the self-compensated configuration by tuning the angle between the bias field and primary field by the addition of small transverse field components. Introducing a small misalignment between the pump beam and bias field will have a negligible impact on pumping.

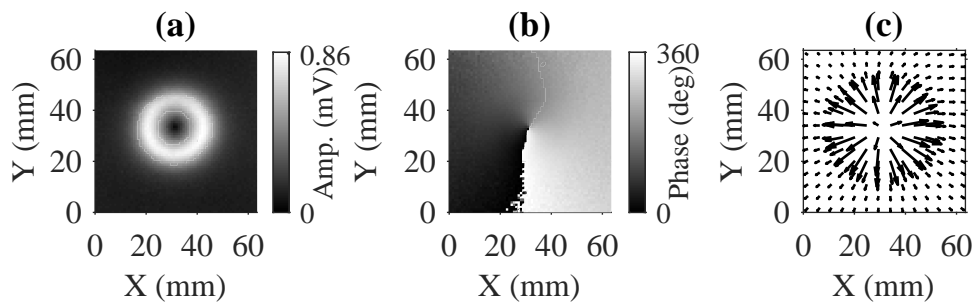


Figure 6.14: Figures of the (a) amplitude and (b) phase recorded in the self-compensated configuration [duplicated from Fig. 6.13 (e-f)]. This data is used to plot (c) a vectorial distribution of the secondary field projected on the xy -plane. For clarity the amplitude and phase images (70×70 pixels) are averaged on to a 14×14 point grid for the vector plot.

Semi-Vector Measurement

With information about the amplitude and phase of the secondary field it is possible to reconstruct the projection of the secondary field on to the plane orthogonal to the magnetometer axis. For the self-compensated configuration described above this is the xy -plane. As this is the same plane in which the pixels are recorded, this projection can be plotted and is depicted by Fig. 6.14 (c) [(a-b) same data as 6.13 (e-f)]. The value of the measured phase is somewhat arbitrary¹, but it is possible to offset the phase and create a vector map of the secondary field distribution (amplitude defines the length and phase the angle of the vector) from the expected secondary field distribution around the perimeter of the recess (perpendicular to the edge).

6.2.2 rf Compensation Factor

Since the secondary field is directly proportional to the primary field strength (below saturation), it is desirable to increase the primary field to the maximum value it is practical to realise experimentally, particularly in cases where the target object is far from the coil/ detector or if deep rf field penetration is required. However, from Sec. 3.2.3 the saturation of the atomic resonance for rf fields $> \mathbf{B}_{SAT}$ begin to decrease the SNR of the magnetometer. The compensated and self-compensated configurations can be used to generate a primary field $\mathbf{B} \gg \mathbf{B}_{SAT}$, which is undetectable by the rf magnetometer and can induce a large secondary field.

To test how well the two regimes compensate the rf field, the primary coil is aligned along the z -axis. For the compensated configuration the magnetometer axis is aligned along the y -axis and an additional coil aligned along the z -axis is used to compensate the primary field coil at the cell (Sec. 6.2.1.2). In the self-compensated regime, the magnetometer axis (non-sensitive axis) is aligned along the z -axis (Sec. 6.2.1.3). The rf spectra for the two different configurations are recorded as the primary field is increased and compared against the amplitude recorded in the normal configuration (same as the compensated configuration, but with the primary coil only). Figure 6.15 (a) and (b) shows the amplitude and linewidth of the rf spectra recorded for the normal (blue squares), compensated (green circles) and self-compensated (black triangles) configurations. For each measurement the primary field was generated once again with the $N = 1000$ turn coil with dimensions $D_o : D_i : H_{coil} = 5 : 2 : 10$ mm, located 7 mm from the cell. There is no object to generate a secondary field, so the amplitude of the measured rf spectrum corresponds directly to the primary field generated by the rf coil.

¹The polarisation rotation signal is a cosine function if the rf field is directed along the probe beam (maximum amplitude at $t = 0$) and a sine function if the rf field is perpendicular to the probe axis (zero amplitude at $t = 0$). This is discussed further in Chap. 7.

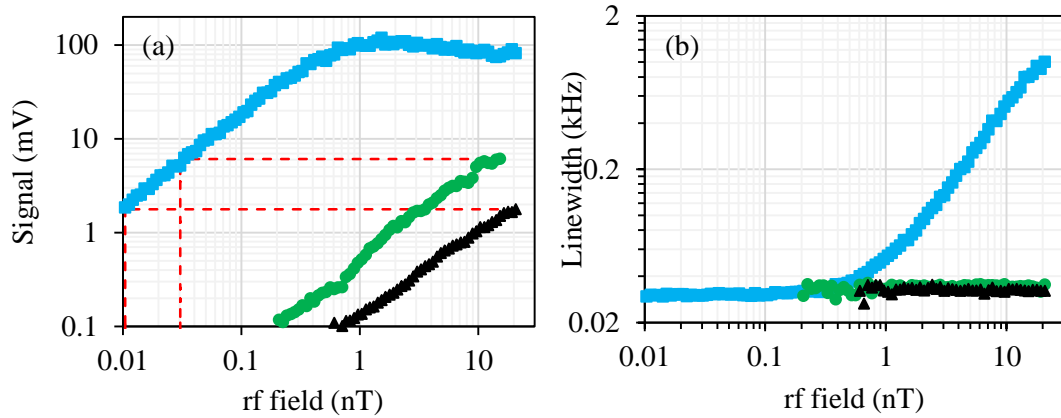


Figure 6.15: Plot of the (a) amplitude and (b) linewidth of the rf spectrum for different primary field strengths for the normal (blue squares), compensated (green circles), and self-compensated (black triangles) configurations. For each measurement the same rf coil is used to generate the primary field.

In the normal configuration for $B > 0.1$ nT the amplitude begins to depart from a linear dependence on the rf field strength and the linewidth begins to broaden. The two other cases are far from this point, even at fields of 20 nT. The compensated and self-compensated configurations demonstrated here exhibit a primary field suppression factor of 5×10^2 and 2×10^3 respectively. The difference in suppression factor between the two cases is related to how easy it is to physically realise the respective compensation geometries.

The suppression factor for the compensated configuration depends on two parameters, the degree of angular control of the compensation coil, i.e. alignment with the primary rf coil axis, and how well the compensation field strength matches the primary field. In these measurements, the compensation field strength is tuned by varying the distance of the coil to the cell. Both these parameters can only be adjusted coarsely by hand, which leads to a low suppression factor.

For the self-compensated configuration, it is only the misalignment of the primary field and magnetometer axis that is relevant. This alignment can be optimised by the addition of small transverse static fields to the bias field. The small angle created between the pump beam and the bias field has a negligible effect on the atomic pumping. There is no predicted limit on the level of compensation achievable in either configuration.

6.3 General Considerations of MIT

This section discusses issues which are generally associated with MIT. The discussion of these topics is presented in the context of rf magnetometers; however, it should be noted that they would be present regardless of what sensor is used.

6.3.1 Imaging Resolution

One of the key metrics in any imaging technique is resolution, which is a combination of the discrimination of spatial features and a change in signal strength, where the limiting cases for each are the blurring together of multiple features and when the signal is hidden by background noise. Simply put, this refers to image contrast and sharpness. In the context of MIT, resolution is related to the minimum size of the detectable defect.

The detection limit for MIT is defined when no signature of the defect is visible, i.e. when C_ϕ or $C_R = 0$. Here, qualitative comparisons will be made between images that approach this limit. It should be noted that machine learning algorithms (e.g. similar to that shown in [141]) could be trained to successfully identify signatures of defects in low contrast images where visual inspection fails.

6.3.1.1 Sub-mm Resolution

Due to the geometry of the experiment (large sensing volume far from the sample), the coil diameter limits the resolution as it defines the radius at which there is the greatest density of magnetic flux, i.e. at the average rf coil radius for an air coil or the outer diameter of the core. This is exemplified by Fig. 6.16, where rf coils of (a) $r_{\text{avg}} = 4$ mm and (b) $r_{\text{avg}} = 1$ mm were used to measure the same 24-mm-diameter recess that is 2.4-mm-deep in an aluminium plate. It is challenging to compare amplitudes as the coils have different number of turns, winding length, and diameters. However, it is clear that the spatial extent of the edge is significantly narrower for the $r_{\text{avg}} = 1$ mm coil. Coils with a diameter significantly larger than the feature will suffer from a reduced amplitude as signals from opposing edges will cancel each other. The smaller coil was used to clearly image a 1-mm-diameter recess that is 2.4-mm-deep, shown by Fig. 6.16 (c).

While the signal amplitude will decrease with increasing distance between the sample and the cell, the spatial resolution remains unchanged. The rf magnetometer makes an integrated vectorial measurement of the secondary field within the cell volume. If the secondary field is poorly defined, i.e. changes direction within the cell, then the measurement will have a low

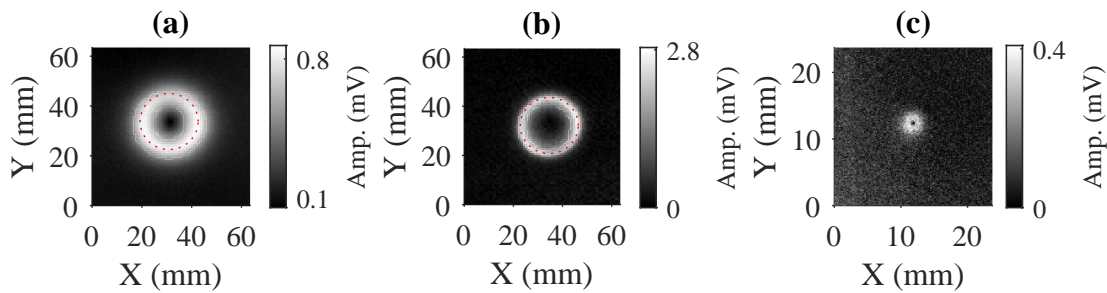


Figure 6.16: Comparison of measuring a 24-mm-diameter recess with an rf coil with an (a) 4mm and (b) 1 mm outer diameter. Figure (c) is a measurement of a 1-mm-diameter recorded with the 1-mm-diameter rf coil. Image (a) and (b) are 70×70 pixels where each pixel is $0.92 \times 0.92 \text{ mm}^2$, while (c) is 130×130 pixels where each pixel is $0.184 \times 0.184 \text{ mm}^2$. A dashed red line outlines the edge of the recess. Note: no outline for the 1 mm recess was given for clarity - the recess is ~ 5 pixels in diameter.

spatial resolution. For the case of eddy currents induced around the perimeter of a circular recess, those which flow around a larger arc length will generate a secondary field at the cell that is less well defined than those which flow around a tighter section of the perimeter. This exactly describes what happens to the eddy currents induced by large and small diameter rf coils, respectively. The same arguments hold for magnetically permeable samples. The distance of the coil to the sample will also affect the resolution, since the spatial distribution of the primary field will change with propagation distance. This distance is called lift-off and is discussed in the next section.

6.3.1.2 Lift-off

The issue of lift-off is common across all MIT measurement systems. The strength of the primary field decays and diverges rapidly with increasing distance from the source. Increasing lift-off decreases the amplitude of the induced secondary field since it is directly proportional to the amplitude of the primary field at the sample. Divergence of the rf field is equivalent to using a coil with a larger radius, which affects the spatial resolution of the measurement, as discussed in the previous section. The former impacts the contrast of the measurement, while the latter impacts the spatial resolution. These negative effects combine to create a maximum operational lift-off, after which point it is not possible to detect the target object or defect. This issue particularly limits the detection of subsurface defects or those under insulating cladding, such as corrosion under insulation. A particular advantage of rf magnetometers is their elevated sensitivity compared with pick-up coils, so they can potentially operate with a

greater lift-off.

A simple solution to the loss in primary field strength with lift-off is generating a larger primary field at the source. There is an operational limit to how much this can be increased and it is set by a combination of; available current, heating, and restrictions on coil size (resolution). It may be possible to effectively address divergence of the rf field through novel coil geometries or flux guides [151]; however, this topic is outside the scope of this thesis.

Figure 6.17 shows amplitude images recorded for a recess with a diameter of (a-c) 24 mm, (d-f) 12 mm, and 4 mm with a lift-off (a, d, g) 1 mm, (b, e, h) 3 mm, and (c, f, i) 5 mm (all the measurements were recorded with a $N = 1000$ turn, air cored coil with dimensions $D_o = 5$ mm). It can be seen that increasing lift-off broadens the amplitude profile of the recess edge in the same way as using an rf coil with a larger diameter. Broader profiles indicate that the eddy currents are not as well defined locally (i.e. lower current density), which will lead to a reduction in amplitude of the secondary field generated. This, combined with the fact that the strength of the primary field at the surface of the sample is reduced with lift-off, results in a significant reduction in amplitude contrast - leading to no visible image for the 4-mm-diameter recess with a lift-off of 5 mm [Fig. 6.17 (i)]. However, there is still information visible in the phase shown in Fig. 6.18 for the 4-mm-diameter recess with a lift-off of (a) 1 mm, (b) 3 mm, and (c) 5 mm. In each image the phase contrast is maximum, even for a lift-off of 5 mm where there was no amplitude contrast; although, there is significant noise in the phase data for this plot since the signal is weak. It should be noted that the noise in these images is because the measurements were recorded by continuously measuring a single data point for the on resonance amplitude and phase (~20 min measurement time). As the amplitude of the signal decreases, the signal noise begins to dominate the measurement. Averaging or recording and fitting to an rf spectrum would improve the quality of these images. Also, these measurements do not represent the limits of this system. They have been included to exemplify issues related to lift-off.

It should be noted that in addition to lift-off limiting the physical operational range of MIT systems and imaging resolution, the change of lift-off during a measurement can present as a false negative signal. For example, the amplitude of the secondary field generated by a crack will decrease if the lift-off is increased, when in fact no properties of the crack have changed. This is a general problem across MIT meaning that all setups would require a stable scanning rig.

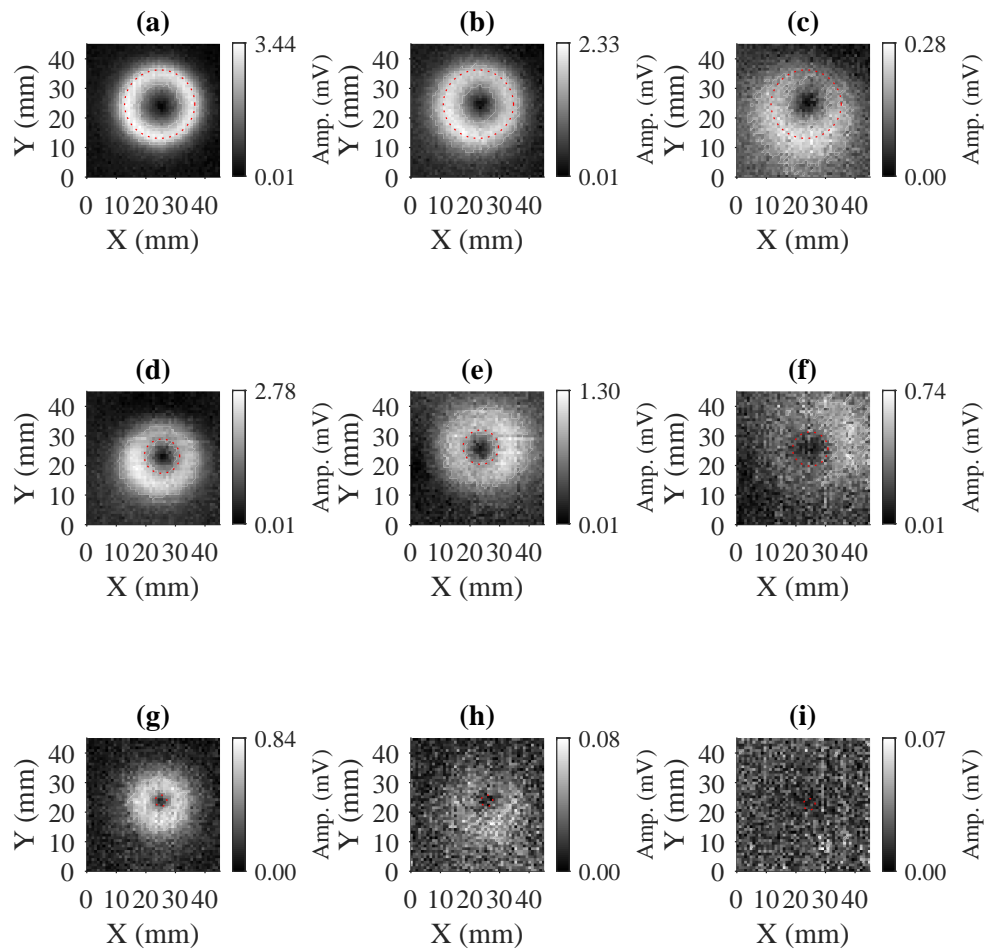


Figure 6.17: Amplitude images for a recess diameter of (a-c) 24 mm, (d-f) 12 mm, and (g-i) 4 mm with a lift-off (a, d, g) 1 mm, (b, e, h) 3 mm, and (c, f, i) 5 mm. The dashed red line in each figure outlines the edge of the defect.

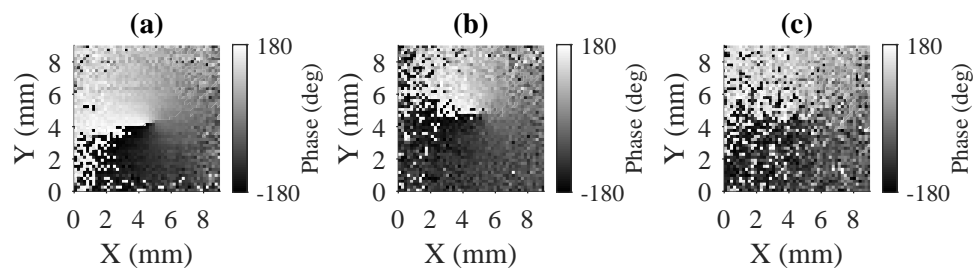


Figure 6.18: Phase images for a 4-mm-diameter recess with an (a) 1 mm, (b) 3 mm, and (c) 5 mm lift-off. These are the phase counterparts to the amplitude image shown in Fig. 6.17 (g-h), respectively.

6.3.2 Defect Characterisation

6.3.2.1 Defect Depth

The attraction of MIT is its ability to make tomographic measurements of a defect, i.e. discriminate between different defect depths. The initial motivation of this work was a challenge set by a consortium of representatives from the oil and gas sector to detect the differences between recesses that had depths of 20%, 40%, and 60% of the thickness of pipeline grade carbon steel. Figure 6.19 shows the results of using the normal configuration to measure a $150 \times 150 \text{ mm}^2$, 6-mm-thick plate with a (a-c) 24-mm-diameter recess in its centre with a depth of (a) 1.2 mm, (b) 2.4 mm, and (c) 3.6 mm. As described in Sec. 6.2.1.1 it is favourable

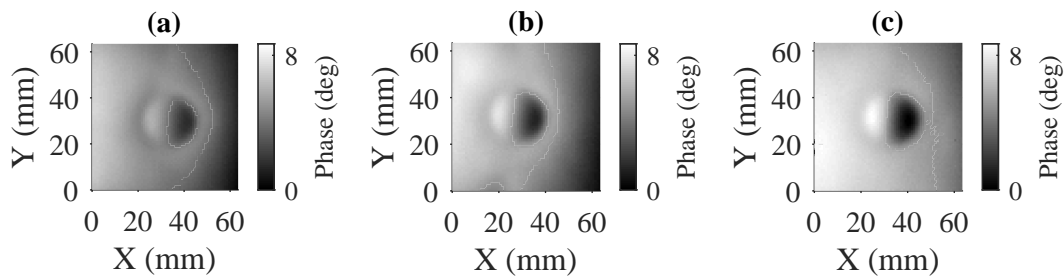


Figure 6.19: Phase images for a (a-c) 24-mm-diameter recess, recorded in the normal configuration for a 6-mm-thick steel plate with recesses with a depth of: 1.2 mm (a), 2.4 mm (b), and 3.6 mm (c).

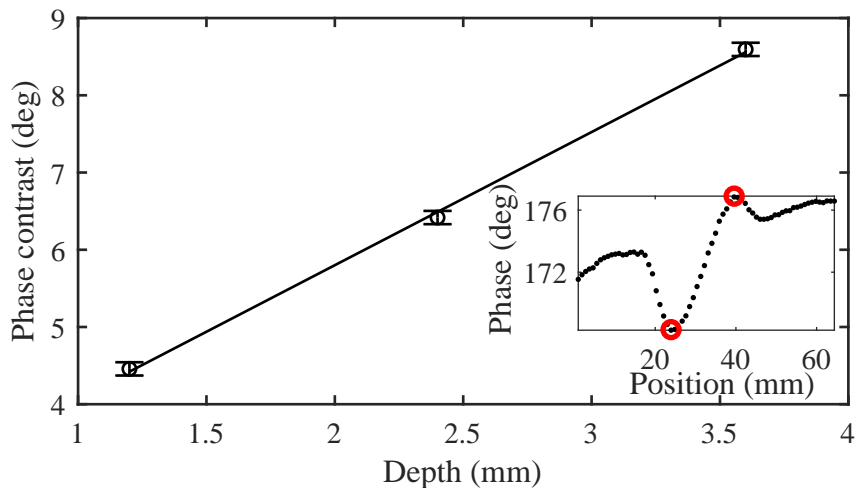


Figure 6.20: Phase contrast for the three depths of the 24-mm-diameter recess. The inset shows a cross-section of the 3.6-mm-deep recess [Fig. 6.19 (c)], marking the ϕ_{\max} and ϕ_{\min} phase value used to calculate the contrast.

to consider the phase data in the normal configuration since the amplitude contrast is poorly defined. Visual inspection of the data in Fig. 6.19 clearly shows that phase change increases with defect depth. The change in phase contrast (difference between maximum and minimum phase, measured at opposite edges of the recess and marked by red circles in the subplot in Fig. 6.20) with recess depth for the 24-mm-diameter recess is plotted in Fig. 6.20. This shows a linear dependence on the change in amplitude with recess depth. The error bars are from the uncertainty in fitting the amplitude to the rf spectrum (rf resonances are recorded since working with magnetic samples).

6.3.2.2 Optimum Operational Frequency

The main attraction of MIT measurements is for the possibility of imaging through barriers, i.e. detecting subsurface defects. To achieve this, two conditions must be met: the primary field must penetrate the barriers to induce a secondary field at the defect and a large enough secondary field needs to be generated by the defect such that it is detectable by the rf atomic magnetometer. The two regimes are mutually exclusive and can be categorised by weak and strong coupling, respectfully. Coupling strength increases with rf field frequency (Faraday's law of induction $\nabla \times \mathbf{E} = -d\mathbf{B}/dt$ means greater EC density at higher frequencies) and decreases with barrier thickness (rf field attenuated less by a thin barrier) and the optimal operational frequency occurs at the balance between the two regimes. Only aluminium samples are studied in this section since the behaviour of the secondary field generated by local magnetisation is poorly understood relative to the field generated by eddy currents. Magnetic samples will be considered in future studies as the dynamics of the penetration of local magnetisation have not yet been investigated by the author.

To investigate the optimum frequency, measurements were carried out in the self-compensation regime, imaging a defect (48-mm-diameter, 2.4-mm-deep circular recess) in an aluminium plate (area of 150×150 mm and is 6-mm-thick) covered by an aluminium barrier of varying thickness and at various operating frequencies. Examples of these measurements are given by Fig. 6.21, where the recess is measured with; (a, d, g, j) zero, (b, e, h, k) one, and (c, f, i, l) three 0.5-mm-thick aluminium sheets which act as a barrier. These measurements have been recorded at; (a-c) 0.6 kHz, (d-f) 1.3 kHz, (g-i) 2.3 kHz, and (j-l) 10 kHz. Each figure is 50×50 pixels with a step size of 1.84 mm. The asymmetry in the amplitude of the signal generated by the recess (or background) is due to partial misalignment between the surface normal of the plate (or barrier) and the rf coil axis, and the rf coil axis and the magnetometer axis - these factors amount to poor compensation. An empirical analysis of the change of two measurands

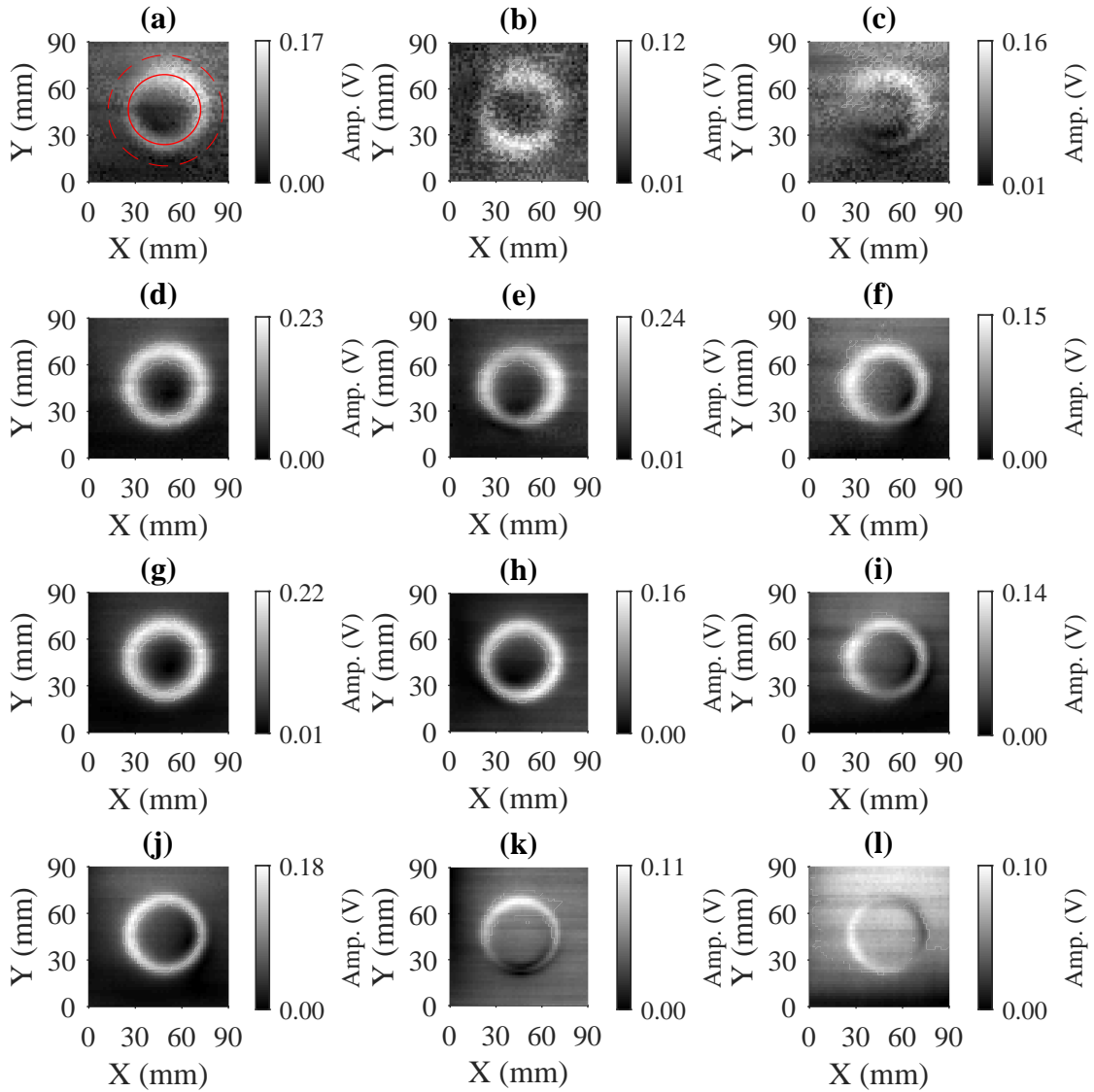


Figure 6.21: Amplitude measurements for a 48-mm-diameter recess that is 2.4 mm deep in a 6-mm-thick aluminium plate that has an area of $150 \times 150 \text{ mm}^2$ and is covered by: (a, d, g, j) zero, (b, e, h, k) one, and (c, f, i, l) three 0.5-mm-thick aluminium sheets. These measurements have been recorded at; (a-c) 0.6 kHz, (d-f) 1.3 kHz, (g-i) 2.3 kHz, and (j-l) 10 kHz. The red solid and dashed circle in (a) mark the points that were averaged to define the value R_{max} and R_{bg} , respectively (these values are described in the text).

of the amplitude image are presented. The first is the calibrated amplitude

$$R_{\text{cal}} = (R_{\text{max}} - R_{\text{bg}})/R_0, \quad (6.14)$$

where R_0 is the amplitude of the rf magnetometer signal measured without a sample (measured

in free space at the same operating frequency), which calibrates against the dependence of the amplitude on frequency. The second measurable is the amplitude contrast C_R , now defined as

$$C_R = (R_{\max} - R_{\text{bg}})/(R_{\max} + R_{\text{bg}}), \quad (6.15)$$

where the averaged amplitude of the background R_{bg} is now used instead of R_{\min} to account for the signal generated by the homogeneous surface of the barrier [e.g. seen in Fig. 6.21 (l)] and poor compensation over the recess [e.g. evidenced by an off-centre minimum in amplitude within the recess in Fig. 6.21 (a)]. To account for any asymmetry in the data, R_{\max} is the average value of data points taken on a circle around recess edge, while R_{bg} is calculated by averaging the amplitude around a circle outside the edge amplitude profile [illustrated by the solid (R_{\max}) and dashed red (R_{bg}) circle in Fig. 6.21 (a)]. Figure 6.22 shows the (a) amplitude and (b) amplitude contrast of the profiles representing the recess in the aluminium plate covered by; zero (blue circles), one (red squares), and three (orange diamonds) 0.5-mm-thick aluminium sheets, as a function operating frequency. The lift-off between the primary rf coil and the plate with a recess has been kept constant at 3 mm. The frequency dependence of the amplitude of the signatures can be divided into two parts. For frequencies below 1.5 kHz the behaviour of all three data sets show the same dependence. At low frequency there is weak coupling, hence the presence of a barrier has less effect on the signal and the measurement will follow the behaviour of an uncovered recess. For the frequencies above 1.5 kHz, the amplitude shows different behaviour depending on the thickness of the barrier. For the uncovered edge (blue circles) R increases with frequency, which is a simple consequence of the growth in induction with the frequency of the rf field. Consequently, C_R shows saturation at higher frequencies (dotted blue line for ≥ 5 kHz) since both the signal and the background are defined by the secondary field generated by the surface of the object and increase together with frequency. The frequency for which the maximum contrast is observed depends on the thickness of the barrier (dotted-dashed orange line at 1-3 kHz for 0.5-mm-thick barrier, dashed yellow line 1.3-2 kHz for 1.5-mm-thick barrier) since a thicker barrier will couple more strongly with the rf magnetic field. At high frequencies the coupling becomes stronger and the measured secondary field mostly comes from the barrier, e.g. the bright background in Fig. 6.21 (l).

The rf primary field frequency defines the penetration depth of the rf field. The larger the depth, the larger the spatial extent (spread) of the rf primary field within the object. In turn, the spread of the rf field limits the spatial resolution of the measurement - as seen with the lift-off measurements. Since the image recorded at a particular frequency integrates the contributions from different layers within the object, the total spatial resolution of the measurement is affected by the operational frequency. In particular, for high frequencies, the response from

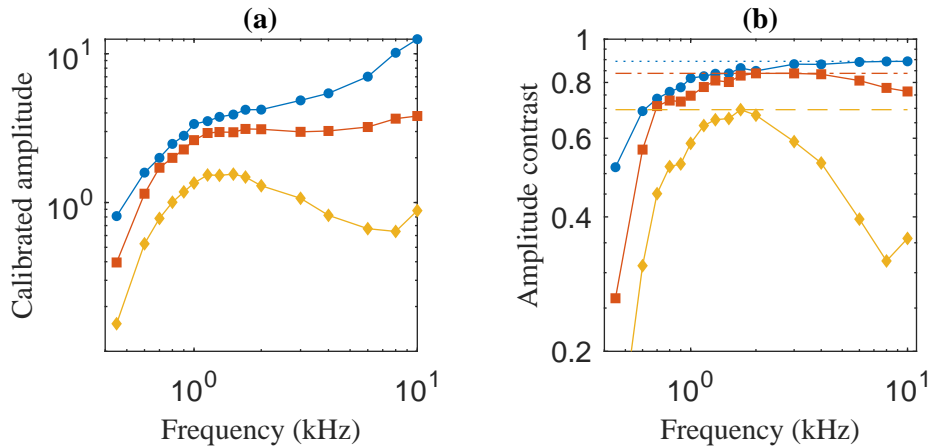


Figure 6.22: The measured change of the (a) amplitude R and (b) amplitude contrast C_R in the amplitude image of the recess as a function of the rf primary field frequency. The dependence is recorded with the recess covered by zero (blue circles), one (red squares), and three (orange diamonds) 0.5-mm-thick aluminium sheets. The horizontal lines in (b) mark the optimum contrast achieved for zero (dotted blue), one (dashed-dotted red), and three (dashed orange) 0.5-mm-thick aluminium sheets.

the object will be mostly defined by the contribution from the surface of the object and the resolution of the image will be defined by the size of the coil. Figure 6.23 shows the full width at half maximum (FWHM) of the profile in the amplitude image representing the recess as a function of the rf primary field frequency. The FWHM values were extracted from the images by fitting a Lorentzian to the amplitude profile that corresponds to the opposite edges in the cross-section of the image. It is difficult to evaluate precisely the width for frequencies below 1 kHz because of the small profile amplitude relative to the background.

It is worth pointing out that the optimum operational frequencies (~ 1 -2 kHz) are significantly higher than those reported in [91], which carry out similar measurements with pick-up coils. They observed an optimum frequency between 5 Hz and 10 Hz. The first thing to note about the results in this paper is that they are operating with steel samples at a primary field that is almost static. The paper refers to this as eddy current testing, but the contribution from eddy currents will be likely negligible and the secondary field will be generated by local magnetisation, which again highlights some of the confusion in the literature regarding the nomenclature and the understanding of the process that lead to signal generation. The dynamics of local magnetisation will be different to the eddy currents analysed for the results in this section, so it is expected that the optimum will be different. Secondly, the optimum frequency for a given penetration depth is defined by the coupling between the rf field and the object. The optimum is a balance between the induced field strength ($\propto f$) and the skin depth ($\propto 1/\sqrt{f}$). This balance implicitly includes the performance of the sensor, which for increased sensitivities

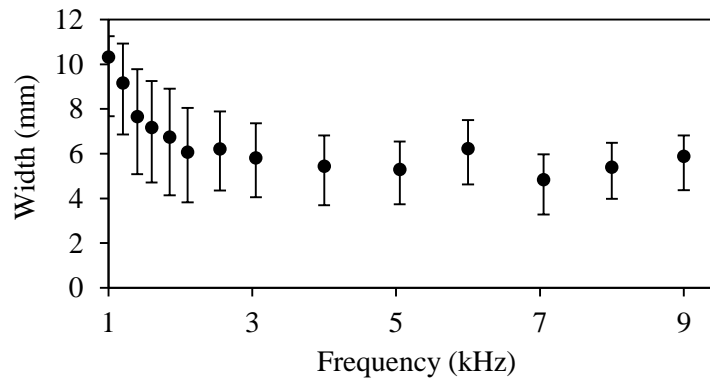


Figure 6.23: The width (FWHM) of the profiles in the amplitude images representing the edge of recess as a function the rf primary field frequency. The dependence is recorded with the recess covered by a single 0.5-mm-thick aluminium sheet (e.g. the red squares in Fig. 6.22).

will be able to detect a smaller secondary field (e.g. produced by a smaller or shallower defect) over a higher frequency range, or a deeper defect over a lower frequency range. It also includes the strength of the primary field, where a stronger (or weaker) field will be able to induce the smallest detectable secondary field deeper (or shallower) into a sample. Further study, such as using different rf field strengths and deliberately reducing the sensitivity of the rf magnetometer (e.g. use a weaker probe), is required to evaluate this hypothesis.

6.3.2.3 Defect on Inner Surfaces

To experiment with imaging through thicker barriers, a plate with a continuously varying recess was imaged. Figure 6.24 (a) is a schematic of the plate with a continuously varying recess whose depth changes from 0 mm to 5 mm. Viewed from the top, the recess is a surface feature and its depth is shown in Fig. 6.24 (b); viewed from the bottom (plate flipped by 180°), the recess is a subsurface feature and the plate thickness is given by Fig. 6.24 (c). The amplitude (d-e) and phase (f-g) have been recorded for the two respective orientations at a frequency of 1.9 kHz. The red dashed line marks the position of the edge of the recess. There is a faint modulation visible in all of the images, which is caused by the magnetic ball bearings in the trolley that supports the plate that moves with the arm of the translation stage. There are only ripples along the axis which the trolley moves. Measurement of the variation in the depth of a surface defect [Fig. 6.24 (b, d, f)] is shown to act as a benchmark comparison for the measurement of changing wall thickness. It is worth pointing out that when recording the surface defect, a non-zero signal is not only produced in the immediate vicinity of the recess edge, but also along the sloping area of the plate. Intuitively, this can be understood as a reflection of the rf primary field from the tilted recess surface, creating field components

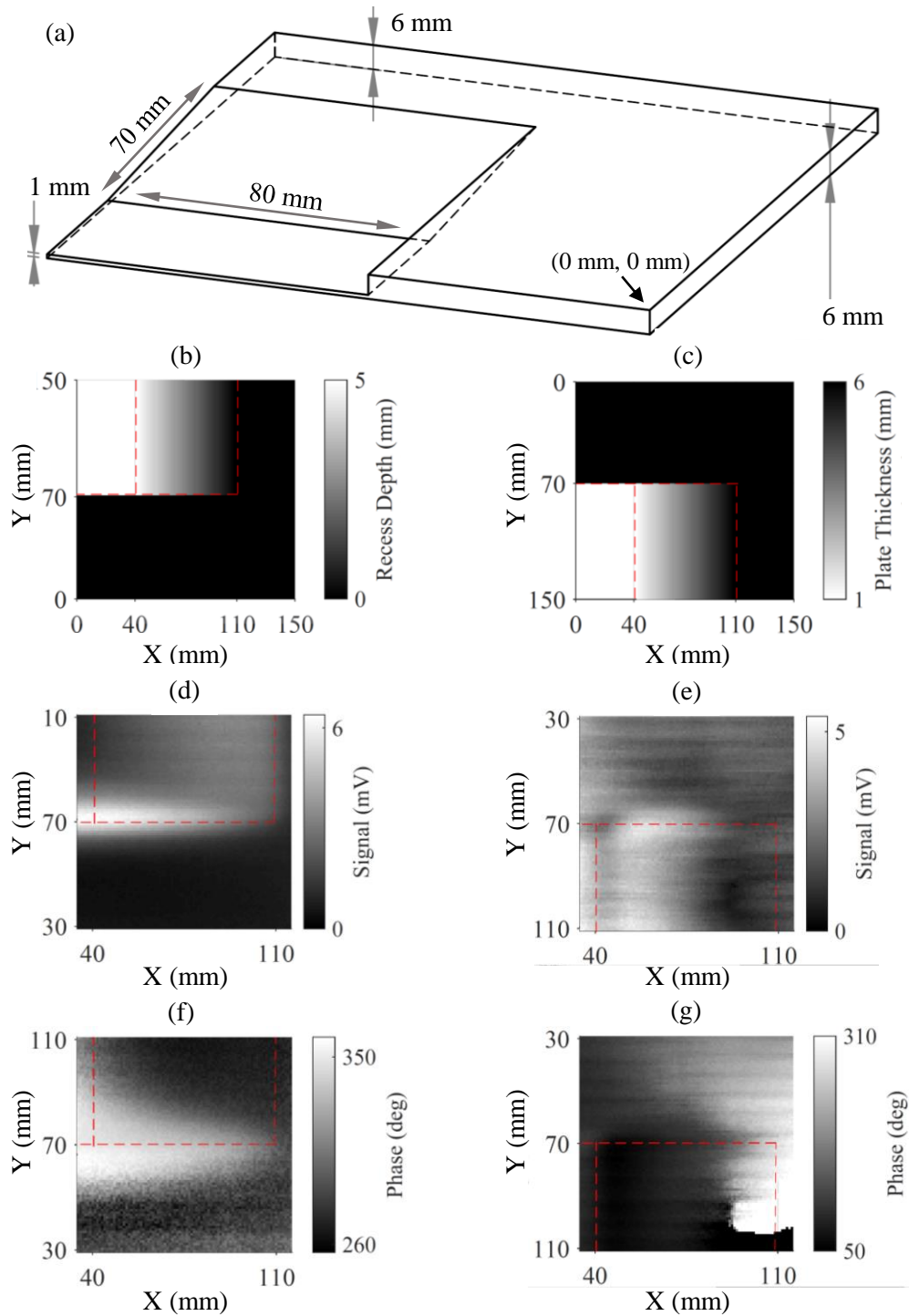


Figure 6.24: (a) Schematic of the plate with a continuously varying recess with depth, or thickness, depending on which side of the plate it is viewed from. Viewed from the top, the recess is a surface feature and its depth is shown in (b); viewed from the bottom (flipped the plate by 180°), the recess is a subsurface feature and the plate thickness is given by (c). The amplitude (d-e) and phase (f-g) have been recorded for the two respective orientations at a frequency of 1.9 kHz.

orthogonal to the bias field.

Figure 6.25 shows images of the (a-d) amplitude and (e-h) phase for a continuously varying thickness [the plate orientation is given in Fig. 6.24 (c)] for four different rf field frequencies; (a, e) 0.6kHz, (b, f) 1.3kHz, (c, g) 2.3kHz, and (d, h) 10kHz (same frequencies as shown in Fig. 6.21). In contrast to the profiles recorded where the recess is on the outer surface [shown in Fig. 6.24 (d)], the amplitude of the secondary field produced by the recess edge and the tilted area of the inner surface have a similar value. From a visual inspection of the plots it is clear that the size of the area over which there is a signal from the inner surface reduces at higher frequencies. This is simply due to the reduction in penetration depth of the primary field with increasing frequency. The strongest part of the signal is at the edge located at $Y \approx 70$ mm. At low frequencies a signal can be detected at nearly the full thickness of the plate (6mm), which is evidenced by the large spatial extent of the signal measured at 0.6kHz and 1.3kHz [Fig. 6.25 (a) and (b), respectively]. At 10kHz [Fig. 6.25 (d)] the signature is only measurable to about halfway along the edge. Here it should be noted that the depth of the recess decreases with increasing thickness. To measure the detection limit, a recess edge with the same depth would have to be measured at different thicknesses. From Fig. 6.25 (a) it can be estimated this limit would be > 6 mm.

It is worth distinguishing the effects of the secondary field at the outer surface (flat), and the inner surface (tilted in the vicinity of the recess). At the outer surface of the plate, the secondary field mostly mirrors the vertical direction of the primary field - partially compensating it. A residual component of this combined field is measured since the surface normal of the plate is not exactly parallel with the insensitive axis of the rf magnetometer, which is why the ‘background’ has a non-zero amplitude. The desired measurement ‘signal’ are the components of the secondary field generated by the recess edge and tilted area of the inner surface. In the amplitude images, there is a zero amplitude (dark) area visible [Fig. 6.25: (b) $X = 110$ mm, (c) $X = 100$ mm, and (d) $X = 70$ mm], which marks the area where the components of the secondary field compensate the residual primary field that contributes to the background signal. The zero amplitude area shifts to a smaller thickness as the frequency increases because of the change in the optimum coupling between the primary field and the plate. For this specific condition of zero amplitude, the ‘optimum’ is when the secondary field compensates the residual primary field. The change of the ratio between the components of the secondary field generated by the outer and inner surface of the plate is evidenced by the increasing dominance of the vortex in the phase images. When the secondary field from the interior of the plate dominates the signal [e.g. for Fig. 6.25 (f)], the change in phase is small (within the red dashed area relative to that seen elsewhere in the image); while, when the secondary field from the surface dominates, there is a full 360° phase change [e.g. as seen for Fig. 6.25 (h)]. The

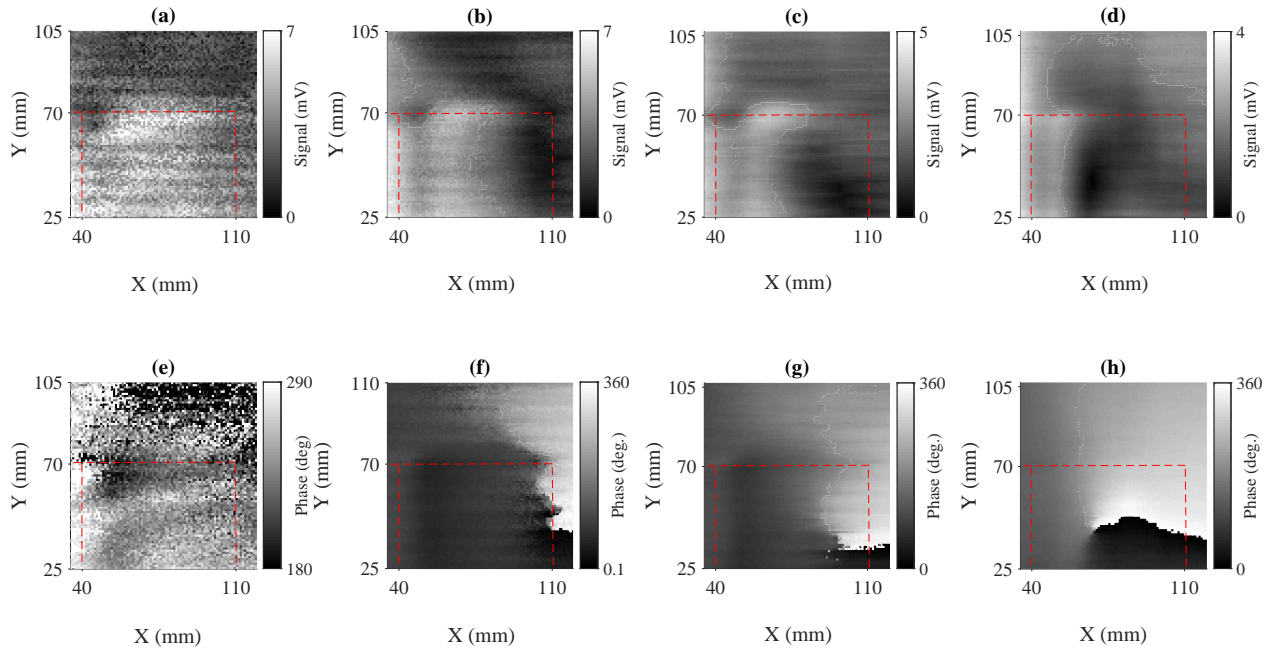


Figure 6.25: Measurement of the (a-d) amplitude and (e-h) phase for a recess with a continuously varying thickness [plate orientation given in Fig. 6.24 (c), representing a subsurface defect] for four different rf field frequencies; (a, e) 0.6 kHz, (b, f) 1.3 kHz, (c, g) 2.3 kHz, and (d, h) 10 kHz. The red dashed line marks a position of the edge of the recess on the underside of the plate. The thickness of the plate gradually increases from 1 mm at $X = 40$ mm to 6 mm at $X = 110$ mm (i.e. thickness increases from left to right), and within this range it has a constant thickness along $Y = 25$ mm at $Y = 70$ mm. Note: font size has been reduced so images could be shown at a suitable scale.

‘centre’ of the phase vortex will also shift with the position of zero amplitude, because like the self-compensation configuration, when there is zero amplitude the phase is undefined.

6.3.2.4 Concealed Defects

With what has been understood from the analysis presented so far in this chapter, the rf magnetometer can be applied to a challenging scenario: to measure mm scale cavities that are mm’s below the surface of the sample. The sample is a $140 \times 140 \text{ mm}^2$, 10-mm-thick aluminium plate that contains 2-mm-diameter cavities (drilled holes) that run parallel to the surface of the plate for 40 mm. The centre of the drilled hole offset by 1.5 mm and 2 mm from the surface of the plate on one side, and offset by 3 mm and 4 mm on the other side, i.e. there are four cavities whose shallowest points are; 0.5 mm, 1 mm, 2 mm, and 3 mm, from the surface. The measurement is again in the self-compensated configuration (rf primary field coil and the bias

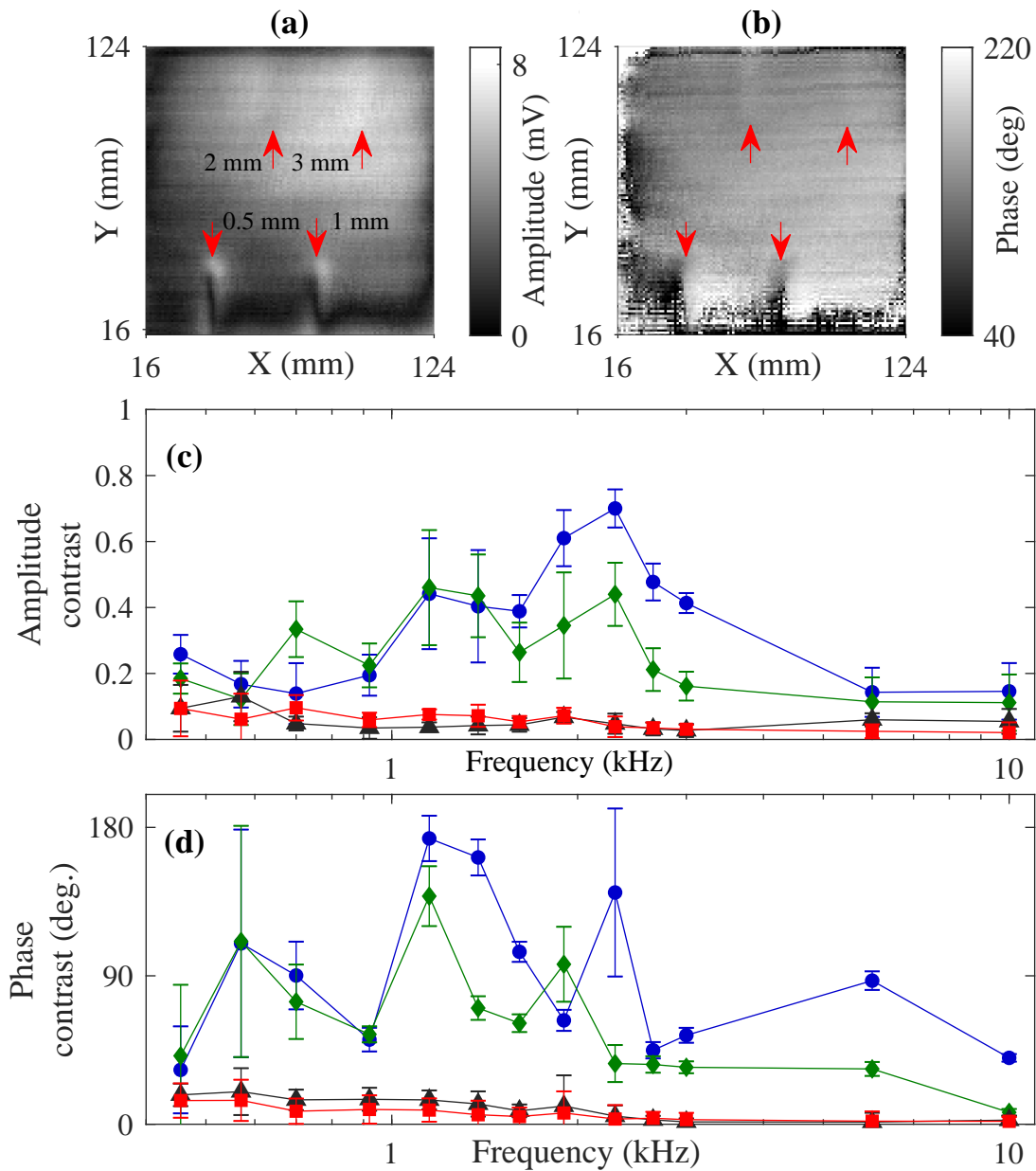


Figure 6.26: (a) Amplitude and (b) phase images recorded for 2-mm-diameter subsurface cavities (marked with red arrows). The amplitude and phase contrast are plotted in (c) and (d), respectively, for the four defects that are: 0.5 mm [(a-b) bottom left arrow, (c-d) blue circles], 1 mm [(a-b) bottom right arrow, (c-d) green diamonds], 2 mm [(a-b) top left, back triangles], and 3 mm [(a-b) top right, (c-d) red squares].

field axis parallel to the surface normal of the plate). The geometry of these cavities (cylinders) presents no hard edge to the penetrating rf field so it will produce a secondary field with a different spatial distribution to those generated by the circular recesses examined earlier.

Figure 6.26 shows images of the (a) amplitude and (b) phase recorded over the sample, measured at 1.6 kHz. The cavities are marked with red arrows (bottom left and right: 0.5 mm and 1 mm, top left and right: 2 mm and 3 mm). The signatures of all four cavities are visible in both amplitude and phase images, although the deepest two are faint. The character of the amplitude of the secondary field in this measurement is similar to that reported in the literature for a defect with a similar geometry [98]. The image has been recorded over a $108 \times 108 \text{ mm}^2$ region over the centre of the plate to minimise the influence of the signals generated by the edge of the plate. Part of the reason the signal from the two deeper defects (top two) is so weak is that the alignment of the self-compensation geometry was not fully optimised. A signature that the alignment is wrong is in the amplitude profiles for the shallow defects (bottom left and right). From the geometry of the cavity, it is expected that the signal amplitude should be symmetrical along its length (bright around the edges and dark in the centre) [98]; however, a dark strip can be seen running diagonally along their length. To be fully optimised the surface normal of the plate, the rf coil axis, and the magnetometer axis must all be parallel. The misalignment of one of these is likely causing this asymmetry and is leading to a weaker signal from the deeper recess.

Figure 6.26 (c) and (d) show the dependence of the magnetometer frequency on the amplitude contrast (C_R) and phase contrast (C_ϕ), respectively, for the 0.5 mm (blue circles), 1 mm (green diamonds), 2 mm (black triangles), and 3 mm (red squares). Since the signals are weak there is some variation in the points, but they show general trends. The frequency dependence of C_R reaches a broad maximum within the 1-2 kHz range for the cavities that lie 0.5 mm (blue dots) and 1 mm (green diamonds) under the object surface, which is in agreement with what is seen in Sec. 6.3.2.2. The dependencies for cavities that are 2 mm (yellow triangles) and 3 mm (red squares) deep indicate that the optimum is for frequencies below 1 kHz. The spatial extent of the profiles representing the cavity edge is defined by the coil diameter, lift-off distance, operating rf frequency, and conductivity of the plate. Since the size of the cavity is comparable to the diameter of the rf primary field coil, the profiles from the opposite edge of the cavities overlap. This overlap results in a reduction of the observed contrast. Since the magnitude of the bias magnetic field must be changed for each operational frequency, its direction has to be optimised each time. This leads to variation in the alignment of the self-compensation, which is responsible for the relatively large variation in the frequency dependence of the phase contrast. Nevertheless, the general trend mirrors that of the frequency dependence of the amplitude contrast. The advantage of considering the phase is that C_ϕ is

large, even for frequencies outside the optimum range (1 – 2 kHz).

6.4 Conclusions

This chapter presents the main results of this thesis: the application of an rf magnetometer for MIT. It begins by describing a geometrical configuration that significantly increases the imaging contrast and makes the rf magnetometer only sensitive to the components of the secondary field that are generated by the defect edge (for the sample geometries studied in this work). Although the compensated configuration is less effective than the self-compensation configuration (insensitive to one of the secondary field components generated by the recess) and is harder to realise experimentally, the investigations applying different compensatory fields gave a detailed insight into how the distribution of the secondary field affects the measured amplitude and phase of rf resonance and what conditions reach maximum image contrast.

An important point is that the dimensions of the rf coil define the spatial resolution of MIT. Although this fact does not solve any issues in itself, and requires the designing an appropriate rf coil, it means that the cell size can be optimised with respect to the practicality of the sensor (e.g. sensitivity and total footprint).

The rf magnetometer has been demonstrated to be able to discriminate between changing depth and size of surface defects. It should be noted that although most of the measurements looked at defects with a significant step change in dimension, the results in Fig. 6.24 show a sensitivity to an incremental change in recess depth. Future work will aim to quantify the resolution of the rf magnetometer to a change in defect size and depth, which is related to the sensitivity of rf magnetometer, and the amplitude and spatial distribution of the primary field. The investigation into looking at concealed defects showed that there is an optimum frequency of rf field that balances the penetration of the field within the sample with the inductive coupling of the field to the material to generate a secondary field. Detection of a large recess was easily demonstrated through 1.5 mm of aluminium. In a more challenging scenario it was possible to detect 2-mm-diameter cavities that were 0.5-3 mm deep in a sample. These investigations show that the rf magnetometer is extremely well suited to carry out MIT measurements and it works effectively across both magnetic and non-magnetic samples. An issue with imaging magnetic samples are drifts in the bias magnetic field as the sample (or sensors moves), which requires recording time consuming rf spectra. A solution to this issue is presented in the following chapter.

Chapter 7

Spin Maser For Defect Detection

7.1 Principle of Operation

So far the results in this thesis have been recorded with an rf magnetometer that operates with an rf field that is generated by an external source. This arrangement will be referred to as the ‘driven mode of operation’ from now on. This chapter introduces the spin maser (often called self-oscillating, or self-driven) mode of operation. Spin maser operation describes a general configuration of the sensor, but the entire focus of the discussion in this chapter is on how it benefits MIT. This work favours the term spin maser over self-oscillating since the operation is akin to a maser [4], and is the name used for a similar class of atomic magnetometers (sometimes called Zeeman masers) operating with noble gases [152, 153]. In the description of what follows it is most useful to picture the Zeeman coherences as a precessing atomic spin. The results presented for defect detection with a spin maser were first presented by the author in [10]. The dual frequency spin maser and much of the understanding of the phase matching condition was described in [15]. The results in [12] provide the demonstration of the spin maser operating in a noisy magnetic field.

7.1.1 System

Figure 7.1 is a schematic diagram of the operation of the spin maser. The same two-beam pump-probe scheme that has been used throughout this thesis is used again here. The different steps involved in the operation are described as follows and are marked by the numbers in Fig. 7.1. (1) The action of the pump beam builds a population imbalance within the hyperfine ground state level (orientation in the $F = 4$ manifold), directing the spins along the quantisation axis that is defined by the bias magnetic field (marked by the black arrow aligned along

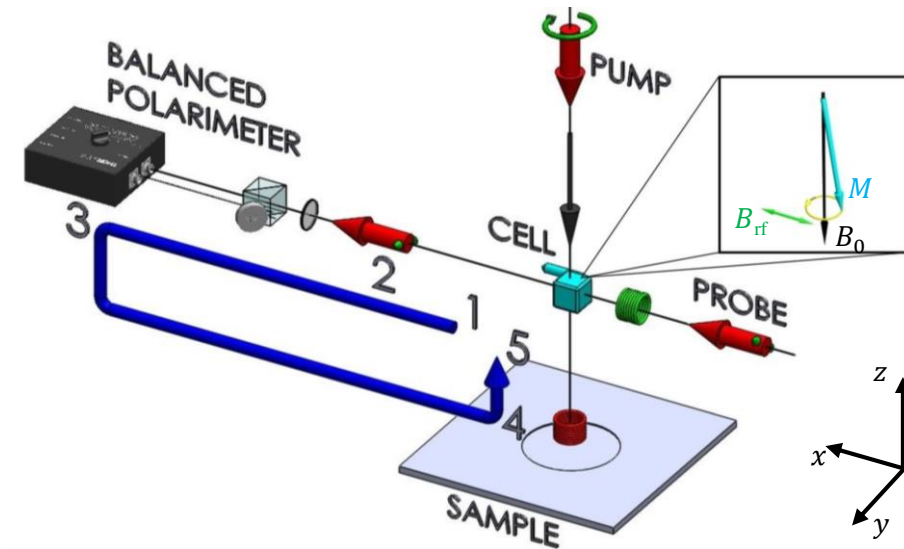


Figure 7.1: Schematic diagram of the operation of the spin maser. The inset shows the macroscopic angular momentum M (cyan arrow) directed along the quantisation axis (defined by the bias magnetic field B_0 , black arrow) by the circularly polarised pump beam. The resonant rf field B_{rf} (green double-headed arrow), which is perpendicular to B_0 , causes M to precess about the quantisation axis. The green rf coil directed along the probe is used for the normal configuration and is used to describe the operation of the spin maser. The red coil is in the geometry for self-compensation and feedback is provided by the secondary field produced by the sample. The numeric labels represent the different steps in the feedback loop, as described in the text.

the z -axis). Due to spontaneous fluctuations in the atomic spin (atomic projection noise), there is a small transverse spin component M_x precessing around the bias field at ω_L . (2) Birefringence maps the projection of the precessing M_x component on to the linear polarisation of a probe beam propagating along the x -axis, leading to a modulation of the beam's polarisation angle. (3) A balanced photodiode monitors this polarisation rotation and generates a signal with a frequency component at ω_L , (4) which is then fed to an rf coil. Consider first the green coil that is aligned along the probe beam in Fig. 7.1 (use of the secondary field for feedback will be discussed next). (5) The polarisation rotation signal from the atomic projection noise will generate an rf field that will provide feedback to the atoms, driving Zeeman coherences. If the rf field has a sufficient amplitude (gain in the feedback loop) and it is in phase with the atomic precession (phase matching condition, discussed further in the following section), then it will provide positive feedback, which increases the amplitude of the transverse spin component. This leads to an increase in the amplitude of the polarisation rotation signal and in turn the amplitude of the rf field. The feedback process continues until it reaches a steady state.

In summary, this is a self-starting system that consists of an atomic ensemble with a ground state population imbalance where spontaneous fluctuations in the atomic spin are monitored and used to drive the precession of the atomic spin. As such, this system is similar to a laser, or maser. However, for the case of the spin maser, the action of the gain and mode of the cavity is represented by the amplitude and phase of the electronic feedback loop. The amplitude of the feedback signal is controlled by the gain on the photodiode, but it is also passed through an amplifier (or attenuator, as required) and the phase is controlled by a phase-shifter (all-pass filter). The total phase shift introduced by all the elements¹ of the feedback loop is called the external phase shift. In this thesis, the rf magnetometer signal measured in the spin maser mode is called spin maser action. There is a threshold at which spin maser action is achieved, which is related to the sensitivity of the magnetometer and how close the feedback loop is to the phase matching condition. The exact relationship between these factors and the calibration of the threshold for feedback is to be the subject of further study. The system will reach a steady state when the gain of the feedback loop saturates (set by the current limit for the rf coil or when the output from the amplifier and/ or photodetector saturates) or when there is an equilibrium between signal gain and loss (loss occurs when a strong rf field saturates the amplitude of the polarisation rotation signal, e.g. as shown in Fig. 3.5).

7.1.2 Phase Matching Condition

The phase matching condition for the spin maser results that all the phase shifts in the feedback loop (spin precession, polarisation rotation signal, and external phase shift) sum to zero. The phase of the spin precession and polarisation rotation signal is set by the combination of the direction of the rf magnetic field and the detuning of the probe beam, depicted by Fig. 7.2. The diagram in Fig. 7.2 (a) shows how the sign of the polarisation rotation signal changes in time. The red arrow represents the transverse spin component M_x precessing around the bias magnetic field B_0 (directed out of the page) and the dashed cyan arrow represents the component of the rf magnetic field which is rotating at ω_L in the direction of the spin precession. From the description of birefringence in Sec. 2.2.4, the signal will have a maximum but opposite amplitude when M_x is parallel [Fig. 7.2 (a.1)] and anti-parallel [Fig. 7.2 (a.3)] to the probe, and the signal will be zero when it is perpendicular [Fig. 7.2 (a.2)]. Figure 7.2 (b) and (c) consider the signal at the beginning of the oscillation, $t = 0$. If the rf magnetic field (coil axis is shown by the double-headed dashed cyan arrow) is directed along the probe beam [Fig. 7.2 (b)], then the oscillation will begin with a maximum signal since M_x is directed

¹These are from the photodiode; any phase shift from the wiring; the amplifier/ attenuator; what has been added from the phase-shifter; the rf coil, which is an inductor; and the rf field (i.e. its direction).

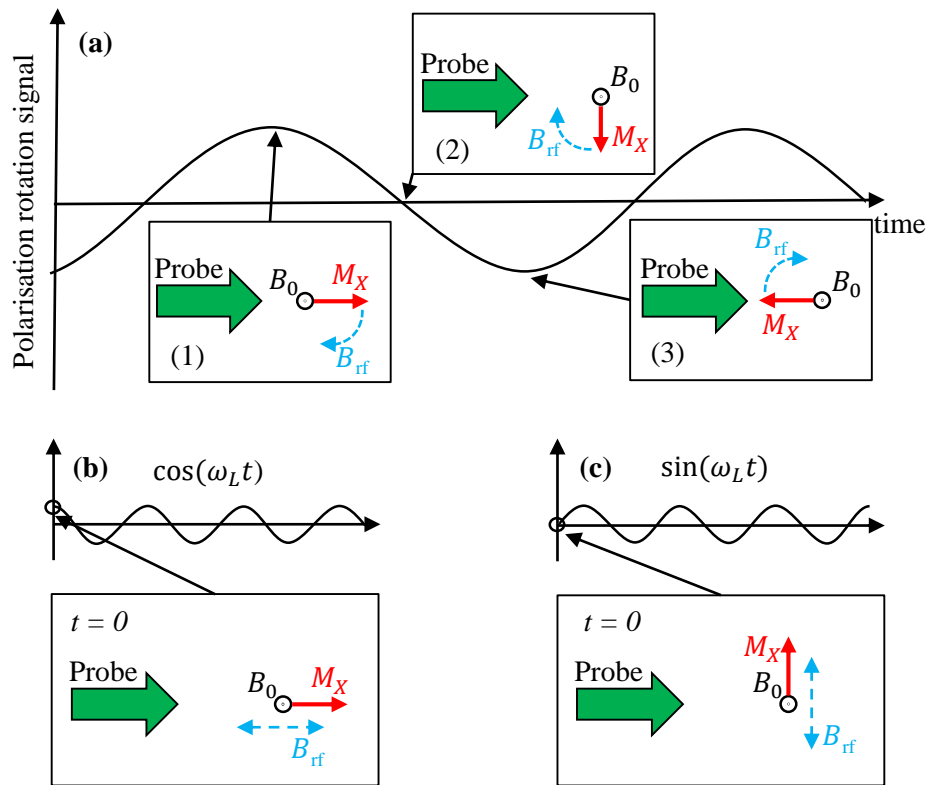


Figure 7.2: (a) Diagram showing the amplitude of the polarisation rotation signal when M_x is: (1) parallel, (2) perpendicular, and (3) anti-parallel to the probe beam. Depiction of the 90° phase difference in the polarisation rotation signal if the direction of the rf magnetic field is: (b) parallel or (c) perpendicular to the probe beam.

along the probe. If the rf magnetic field is perpendicular to the probe [Fig. 7.2 (c)], then the signal will start from zero signal. The signals recorded in these configurations will have a character described by $M_x \propto \cos(\omega_L t)$ and $\sin(\omega_L t)$, respectively. From this it is clear that $M_x \propto \cos(\omega_L t + \theta_{rf})$, where θ_{rf} is the angle between the rf magnetic field and the probe beam. Hence, θ_{rf} leads directly to a phase shift in the polarisation rotation signal. This is also shown by the phase vortex measured in the self-compensation configuration.

The positive (blue) or negative (red) detuning of the probe beam from the transitions involving the hyperfine ground state level sets whether the polarisation rotation signal is positive or negative when M_x is directed parallel or anti-parallel to the beam's direction of propagation [shown in Sec. 3.2.2.1 and again in Fig. 7.6 (a)]. The change in sign of the signal is equivalent to a 180° phase shift. Consider the case for the spin maser where the rf coil is along the probe beam and the rf field directly follows the polarisation rotation signal (i.e. there are no other phase shifts in the feedback loop), spin maser action will only occur for positive detunings. If the detuning is negative, then the rf magnetic field will be 180° out of phase with

the spin precision and spin maser action cannot occur. However, any arbitrary phase shift can be cancelled to zero by changing the external phase shift, i.e. with a variable phase-shifter.

7.2 Defect Detection

The motivation behind investigating the spin maser mode in this thesis is to apply it to MIT; however, detection of the secondary field complicates the feedback compared with using a coil. In the previous chapter it was shown that it is desirable to operate in the high contrast self-compensation configuration (depicted by the red coil in Fig. 7.1). In the self-compensation geometry, the primary field generated by the coil is undetectable by the rf magnetometer and feedback for the spin maser must be provided by the horizontal components of the secondary field. It was shown in the previous chapter that these components are only generated in the vicinity of inhomogeneities in the surface of the plate. Figure 7.3 shows the (a, c, e, g) amplitude and (b, d, f, h) phase images recorded for the $150 \times 150 \text{ mm}^2$, 6-mm-thick steel plate containing a 24-mm-diameter recess that is 2.4-mm-deep. The images are all 70×70 pixels and were recorded in the self-compensation configuration for the (a-b) driven (external source of rf field, same as the configuration described in Sec. 6.2.1.3) and (c-h) spin maser mode. The first thing that will be considered is the measurement time between these two different modes. In the driven mode [Fig. 7.3 (a-b)], the whole rf resonance needs to be recorded since the sample is magnetic and there are shifts in the position of the rf resonance due to imperfections in the active field compensation. The resonance had a span of 200 Hz so that the shifts in the bias field could be tracked and the scan had an acquisition time of 8 s per pixel, which leads to a measurement time of 12 hours. In the spin maser mode [Fig. 7.3 (c-d)], the plate can be continuously moved since the measurement is always on resonance, reducing the scan time to 20 minutes. However, in Fig. 7.3 (c) it can be seen that only a section of the recess signature is recorded in the spin maser mode relative to the driven mode (the size of this area is defined by where the phase matching condition is met and is discussed in Sec. 7.2.1). Due to the 360° [e.g. shown by the vortex visible in Fig. 7.3 (b)] phase change of the secondary field around the perimeter of the recess, the phase matching condition will always be met around the recess. The spatial extent of the image (the size of the area where there is a signal) is defined by self-adjustment of the phase through the change of the spin maser frequency, which is discussed in the following section. By adding an external phase shift it is possible to record a signal over a different region of the defect. This is shown in Fig. 7.3 (e), where there is a 180° phase shift relative to Fig. 7.3 (c). For a phase of 90° , spin maser action would be met over one of the horizontal edges (shown later in Fig. 7.7). From the circular symmetry of the recess, the change of phase shift in the feedback loop translates linearly to a change in

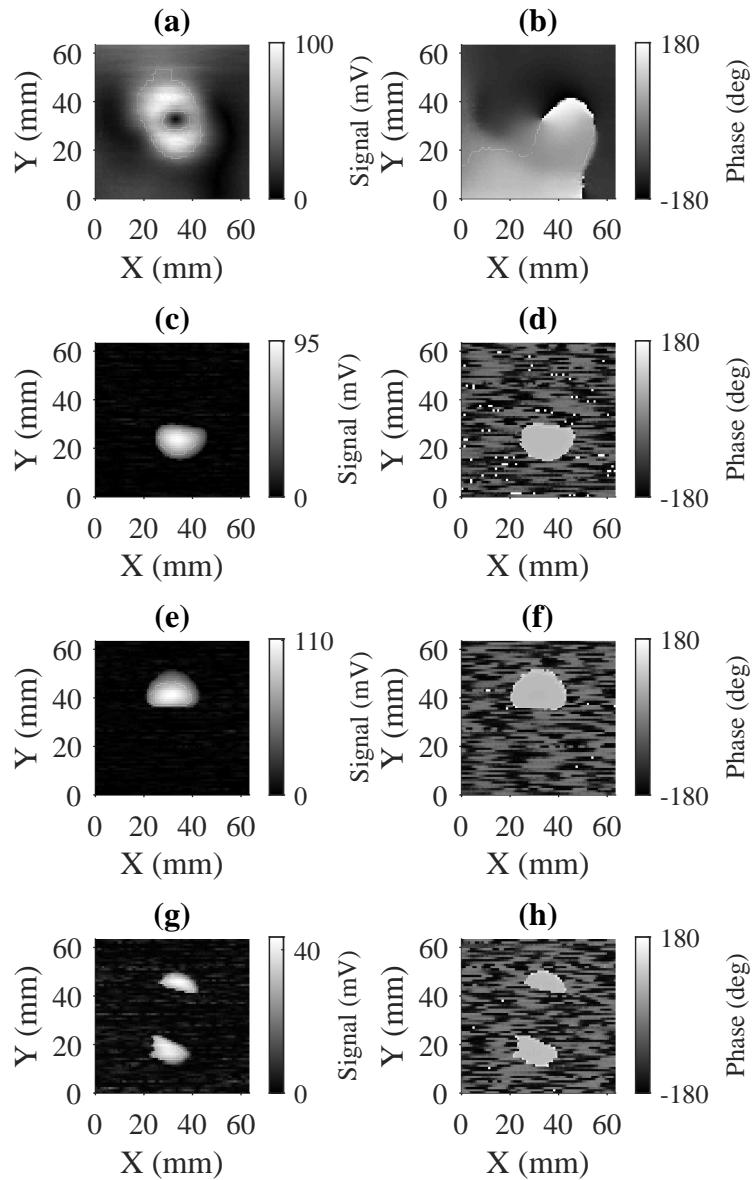


Figure 7.3: The (a, c, e, g) amplitude and (b, d, f, h) phase images recorded for the steel plate with a 24-mm-diameter recess in its centre in the driven (a-b) and spin maser (c-h) mode of operation. Both were recorded at 34kHz. The measurements for (c-d) and (e-f) were recorded with the same rf coil, but with a 180° difference between their respective external phase shifts. (g-h) The measurement was recorded with two parallel rf coils providing feedback to the atoms, simultaneously. The coils were spatially offset from each other by ~ 5 mm and had a 180° phase shift between them, i.e. they had opposite polarity.

angular position around the recess where a signal is generated. As such, the area where there is a signal is now on the opposite side of the defect.

One way to increase the area over which a signal is recorded is to use an array of coils. A double coil array was constructed, consisting of two near-identical parallel coils that were offset from each other by 5 mm and connected in series, but with opposite polarity, i.e. there is a 180° phase shift between them. Figure 7.3 (g) and (h) show the amplitude and phase recorded for the same plate with the double coil array. In this arrangement, signals from opposing edges can be recorded simultaneously. However, since the coils are directly out of phase, the primary fields generated by each coil partially compensate each other, reducing the overall signal amplitude. More complicated coil arrangements are possible with a greater number of coils, and/or different phase offsets, to image different areas of the recess; however, a more elegant solution is presented in Sec. 7.3.

In all these spin maser measurements the lock-in amplifier has been used to record the amplitude. The frequency it demodulates the polarisation rotation signal at is referenced from the polarisation rotation signal. This means when spin maser action occurs, the lock-in amplifier demodulates the signal at ω_L and will always stay on resonance. However, no phase information can be recorded from the polarisation rotation signal since it is self-referenced. The value of $\sim 80^\circ$ recorded in Fig. 7.3 (d, f, h), when there is a signal, is an arbitrary value set by the internal phase of the lock-in for demodulation. When there is no spin maser action, the lock-in is ‘unlocked’ and demodulates the signal at some frequency component that has been detected in the photodiode signal, i.e. at some frequency component of the noise. Hence when there is no spin maser action, there is a significant amount of phase noise recorded. Some amplitude noise is also visible in 7.3 (g) due to the low signal amplitude.

7.2.1 Frequency Shift

In order to provide more insight into the phase matching condition for defect detection with a spin maser, and to explain the spatial extent over which there is a signal in Fig. 7.3 (c-h), it is essential to recall the change in the phase of rf magnetometer signal around the rf resonance. To remove external variables the first set of measurements presented in this discussion were carried out within magnetic shielding. Figure 7.4 (a) shows the rf resonance (R solid black line and ϕ dotted-dashed red line) as the frequency of the rf driving field is scanned across the resonance (the data is smooth since it was recorded within shielding). The phase of the magnetometer response changes by 180° across the resonance, but a significant portion of this change ($\sim 90^\circ$) happens within a linewidth of the resonance (linewidth $\Gamma \approx 5$ Hz, the span marked by black dashed lines) where the phase change is approximately linear. Figure 7.4 (b)

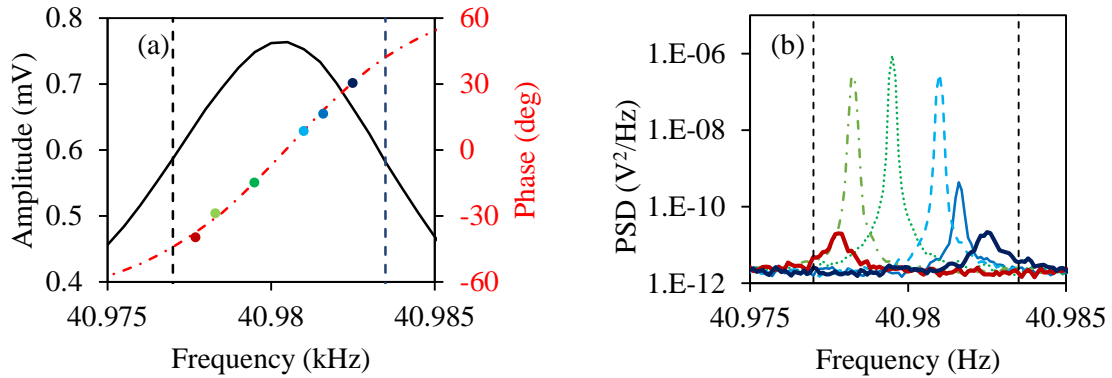


Figure 7.4: These measurements have been recorded within magnetic shielding. Figure (a) plots the different components of the rf spectrum: R (left axis, solid black line), ϕ (right axis, dotted-dashed red line), where $\nu_L = 40.98$ kHz and $\Gamma \approx 5$ Hz (span marked by black dashed lines). Figure (b) plots the power density spectrum of the spin maser signal for values of the external phase shift, which results in a shift due to the self-adjustment of the spin maser signal: $\phi = -40^\circ$ at 40.9777 kHz (red thick-solid line), $\phi = -29^\circ$ at 40.9783 kHz (dotted-dashed light-green), $\phi = -15^\circ$ at 40.9795 kHz (dotted green), $\phi = 9^\circ$ at 40.9810 kHz (dashed light-blue), $\phi = 16^\circ$ at 40.9816 kHz (solid blue line), and $\phi = 30^\circ$ at 40.9825 kHz (thick-solid dark-blue line). The frequency and phase of these spectra are marked by the circles in (a) with a colour that corresponds to the colour of the spectrum in (b).

shows the power density spectrum (PDS) of the spin maser signal. The six different lines are recorded with a different external phase shift, which results in a shift in the frequency of the spin maser signal. The frequency and phase of these spectra are marked by the circles in Fig. 7.4 (a) whose colour corresponds to the colour of the PDS in Fig. 7.4 (b). This feature shows that the spin maser can compensate an external phase shift by self-adjusting the frequency of the feedback signal. The relationship between the frequency shift and the phase follows the approximately linear phase change of the rf spectrum within the resonance linewidth. The amplitude of the signal changes as the frequency is self-adjusted due to the change in the amplitude of the rf spectrum, i.e. signal amplitude decreases away from $\nu_{\text{rf}} = \nu_L$. Note: the PDS at the furthest frequencies (red and dark-blue thick-solid lines) represent the signal measured just below the threshold for spin maser action. This shows that above the signal threshold the gain of the system rapidly increases the amplitude of the spin maser signal. Further study is required to understand the relation between the amplitude of the rf spectrum, the gain of the feedback loop, and the amplitude of the spin maser signal.

Since the spin maser action is not recorded over a single point, but over a region of the recess, and it is known that the phase (direction) of the secondary field changes linearly with angular position around the perimeter of the recess, it can be expected that the frequency of the spin maser is self-adjusting to compensate this change in phase. Since the plate measured for the

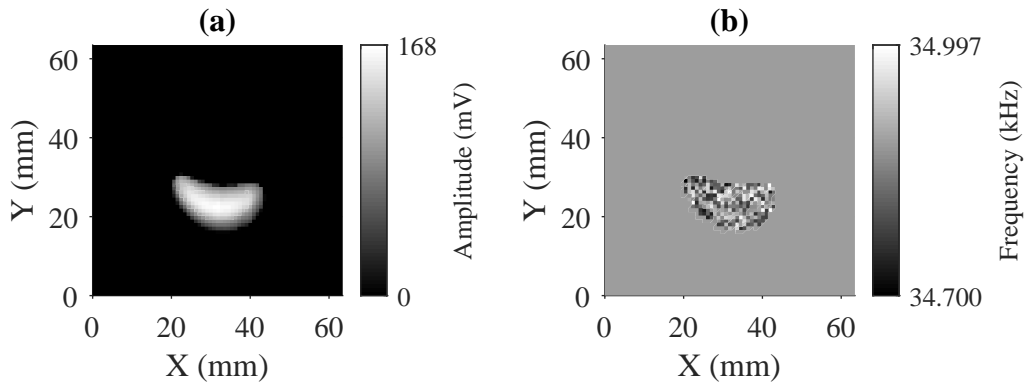


Figure 7.5: Spin maser (a) amplitude and (b) frequency recorded for an aluminium plate with a 24-mm-diameter recess. Typically a lock-in amplifier is referenced to a stable signal with an amplitude of 10 V. For these measurements the lock-in is referenced to the spin maser signal, which contains noise and has a max amplitude of 168 mV, which leads to the instabilities in the measured frequency. The resolution is not sufficient to see any significant change that could be attributed to the self-adjustment in spin maser frequency due to the known change in phase of the secondary field. When there is no spin maser action, the lock-in amplifier is unlocked and will record frequency values beyond the range of the colour-bar tick values. These points are meaningless and have been replaced with a mid-range value to remove speckle in the plot.

results in Fig. 7.3 is steel (magnetic), there is a residual change in the resonance position (100's Hz). The change in resonance position is greater than the expected change in the self-adjusted frequency due to the change in phase of the secondary field (one can assume the change in the self-adjusted frequency to be of the order of the rf resonance linewidth, which is 10's Hz). The results shown in Fig. 7.5 plot the (a) amplitude and (b) frequency recorded for an aluminium plate with a circular recess (same dimensions as recess described in Fig. 7.3). However, the stability of the frequency recorded by the lock-in amplifier is too poor to see the change in the self-adjusted spin maser frequency. It appears that the frequency values recorded at $X \approx 20$ mm is slightly darker on average than the values recorded at $X \approx 40$ mm, however this is not conclusive. The fluctuation in the measured frequency does not represent the actual fluctuation in spin maser frequency, but is due to the low voltage signal (the spin maser signal) that is being used as a reference for the lock-in (typically referenced to a 10 V signal).

The extent of the area where there is a signal recorded requires the amplitude of the rf resonance at the phase-shifted-frequency to be greater than the threshold for spin maser action. In other words if the phase shift is too great, then the amplitude of the polarisation rotation signal at the frequency that causes phase matching will be too small to cause spin maser action. This is exemplified in Fig. 7.3 (g) where the rf field is reduced (since the two coils partially cancel

each other), resulting in a smaller region where a signal is measured.

7.3 Dual Frequency Spin Maser

7.3.1 Dual Phase Matching Condition

This section describes a novel configuration where the spin maser is operated simultaneously at two frequencies and is called the dual-frequency spin maser (DFSM). This setup describes a co-magnetometer based on a single isotope, which as far as the author is aware, is the first demonstration of its kind. The element used here is caesium; however, this is a general scheme and it would be possible with other elements, e.g. rubidium.

The basis of the DFSM lies in the simultaneous generation of a population imbalance and the monitoring of the atomic spin precession in both the $F = 4$ and $F = 3$ ground state levels. This is achieved with the same two-beam pump-probe scheme used throughout this work; however, the pump beam power is reduced so the $F = 3$ manifold is not fully depopulated and the probe detuning is such that there is a measurable signal from both levels. An example of such a case is visible in Fig. 7.6 (a) (reprinted from Sec. 3.3), where the amplitude of the $F = 4$ (black diamonds) and $F = 3$ (red circles) signal is recorded as the detuning of the probe is scanned through the group of transitions involving each hyperfine ground state. This shows that the amplitude of the polarisation rotation signal from the $F = 3$ and $F = 4$ components have the same sign when they have the same sign of detuning from the relevant transitions involving the components, i.e. detuning from the $F = 3 \rightarrow F'$ for the $F = 3$ ground state level and from the $F = 4 \rightarrow F'$ for the $F = 4$ ground state level. The change in the amplitude of the signal is due to the 180° phase change of the spectrum as the detuning changes. The diagrams in Fig. 7.6 (b) and (c) show how the detuning of the probe and the direction of the rf magnetic field influence the sign of the signal. The black and red arrows represent the precessing transverse spin component for the $F = 4$ and $F = 3$ ground state levels, respectively. It should be noted that due to the difference in sign of the Landè g -factors ($g_{F=4} = 0.250390$ and $g_{F=3} = -0.251194$ from Equ. 3.1), the spins precess in opposite directions. From the difference in Landè g -factors for the two ground states, the $F = 3$ and $F = 4$ spins precess at slightly different frequencies. The difference in frequency means it is possible to distinguish between the signals generated by the two different ground states. The difference in the direction of precession is equivalent to a 180° phase shift between the two polarisation rotation signals.

From the discussion for Fig. 7.2 the direction of the rf field sets the initial direction of the spins and the amplitude of the polarisation rotation signal is maximum when the spins are directed along the propagation axis of the probe. The sign of the measured polarisation rotation signal

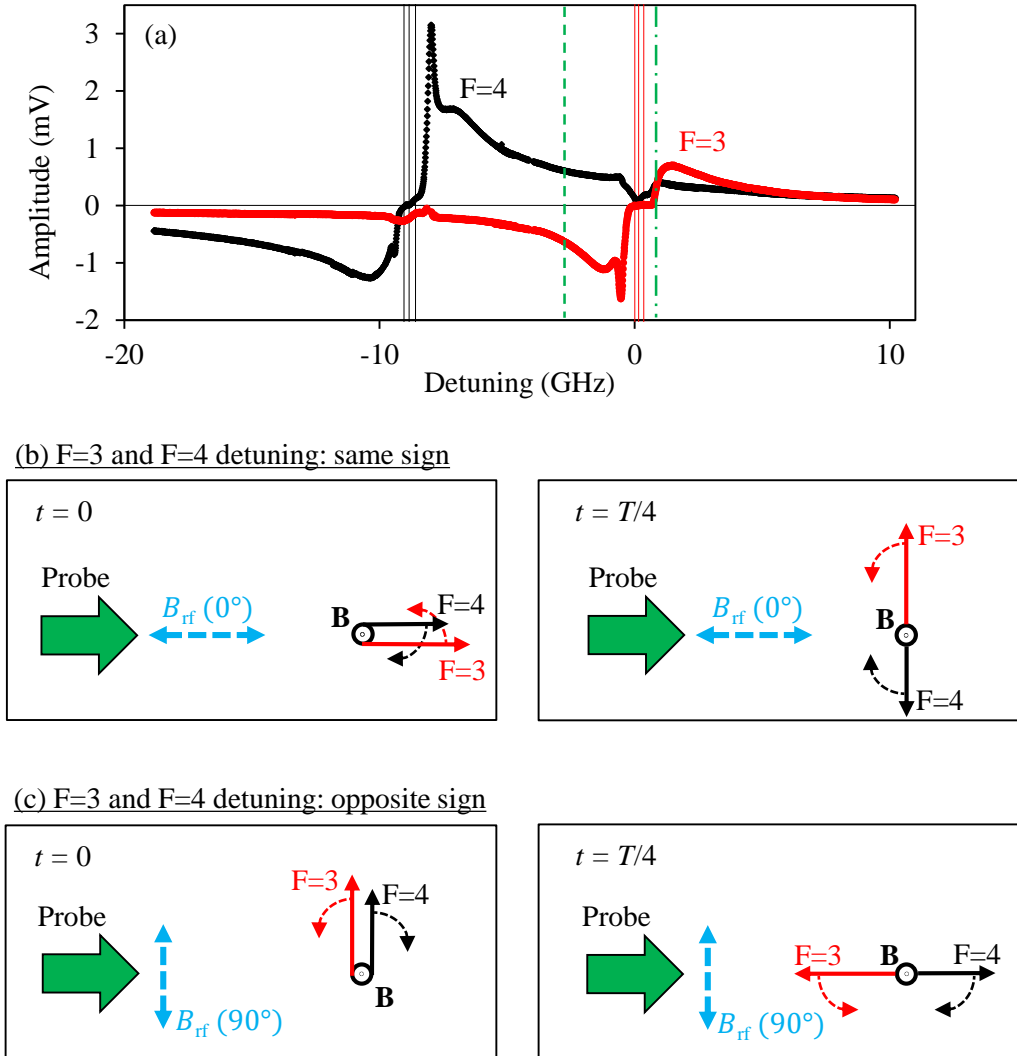


Figure 7.6: (a) Shows the change in amplitude of one of the quadrature components of the rf spectrum for the $F = 4$ (black diamonds) and $F = 3$ (red circles) ground state levels for different probe detuning (reprinted from Sec. 3.3). The black and red vertical lines represent the respective group of transitions involving the $F = 4$ and $F = 3$ hyperfine ground state levels (detuning is measured from $F = 3 \rightarrow F' = 2$). The dashed and dot-dashed green line at $\Delta = -2.75$ GHz and $\Delta = 0.89$ GHz, respectively, are the detunings used for the results presented in Fig. 7.7. The diagrams in (b) and (c) are pictorial descriptions that describe when the polarisation rotation signal for the $F = 3$ and $F = 4$ spins have the same sign, which is influenced by the direction of the rf magnetic field and the probe detuning. In (b) the rf field is parallel (0°) to the direction of propagation of the probe beam and the detuning of the probe to the group of transitions involving the $F = 4$ (black arrow) and $F = 3$ (red arrow) spins are the same. In (c) the rf field is perpendicular (90°) to the probe beam and the detuning is opposite for the $F = 4$ and $F = 3$ spins. The direction of the spins in both (b) and (c) are shown at $t = 0$ and $t = T/4$ for both configurations.

is positive when the spins are parallel with the direction of the probe, and negative when the spins are anti-parallel with the probe. The polarisation rotation signal is then multiplied by the sign (positive for blue, negative for red) of the probe detuning for the relevant spin components.

For example, in Fig. 7.6 (b) the probe beam has the same detuning for $F = 3$ and $F = 4$ from their respective group of transitions (either both red or blue detuned; e.g. the dot-dashed green line at 0.89 GHz is blue detuned for both) and the rf magnetic field (cyan arrow) is directed along the probe. Hence at $t = 0$, when both the $F = 3$ and $F = 4$ spins are directed along the probe beam, the polarisation rotation signal of both would have the same sign (in this example the signal will be positive if $\Delta = 0.89$ GHz). Once the spins precess for a quarter of a period ($t = T/4$, equivalent to a phase shift of 90°) there is no signal.

In Fig. 7.6 (c) the probe beam has the opposite detuning (one is red and the other is blue detuned, e.g. the dashed green line at -2.75 GHz is red detuned for $F = 3$ and blue detuned for $F = 4$) and the rf magnetic field is perpendicular to the probe. Now at $t = 0$ there is no signal and it is at $t = T/4$ where the polarisation rotation signal for both will reach maximum. However, due to the opposite detunings of $F = 3$ and $F = 4$ from their respective group of transitions, the amplitude of the respective polarisation rotation signals will have the same sign (in this example the signal will be positive if $\Delta = -2.75$ GHz) even though the spins are directed parallel and anti-parallel to the probe.

7.3.2 Defect Detection

The DFSM is applied to defect detection. The circular recess is a useful source of a secondary field with a variable direction, which allows for an investigation into how the phase matching condition is met for different probe detunings and rf field directions. The plots in Fig. 7.7 show the amplitude images recorded for the same 24-mm-diameter, 2.4-mm-deep recess in a 150×150 mm², 6-mm-thick aluminium plate. The recess was imaged with different detunings: Fig. 7.7 (a-c) were recorded with a detuning of 0.89 GHz [blue detuning for both $F = 4$ and $F = 3$ - marked with a dotted-dashed green line in Fig. 7.6 (a)] and is described by Fig. 7.6 (b); (d-f) were recorded for a detuning of -2.75 GHz from $F = 3 \rightarrow F' = 2$ transition [blue detuned for $F = 4$, red detuning for $F = 3$ - marked with a dotted green line in Fig. 7.6 (a)] and is described by Fig. 7.6 (c). These detunings were chosen so that the amplitude polarisation rotation signals for the $F = 3$ and $F = 4$ components were similar. The amplitude images have been recorded at their respective detunings for phase shifts of: (a, d) $\sim 0^\circ$, (b, e) $\sim 90^\circ$, and (c, f) $\sim 180^\circ$, which is shown to rotate the respective region at which spin maser action is achieved around the perimeter of the recess.

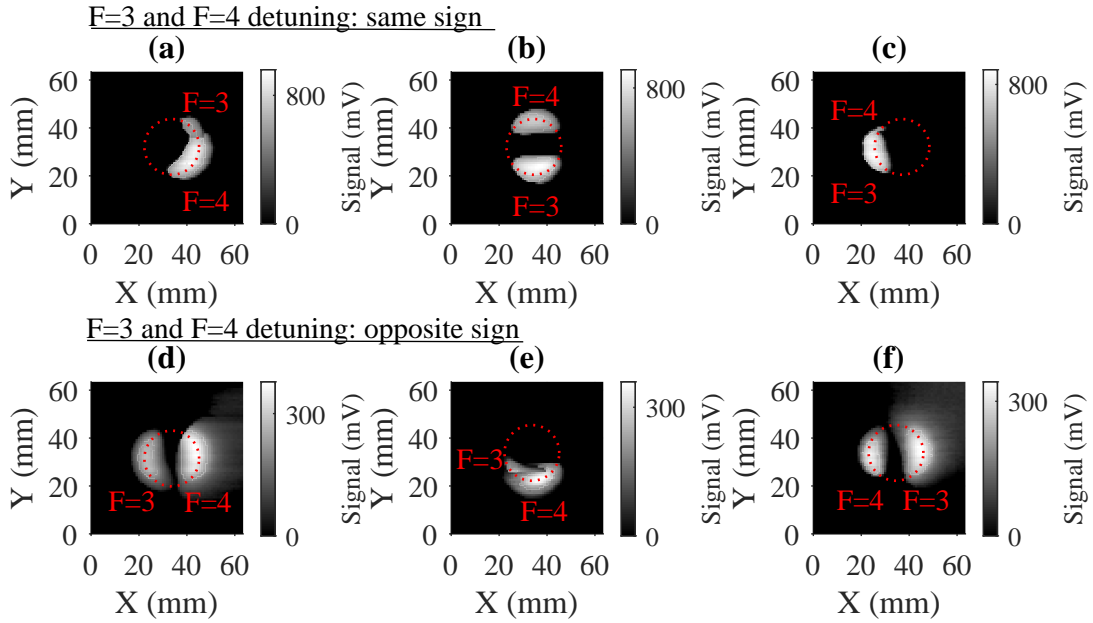


Figure 7.7: Amplitude images recorded for the DFSM for (a-c) the same and (d-f) the opposite probe beam detunings from the transitions involving the $F = 4$ and $F = 3$ ground state levels for an external phase shift of: (a, d) $\sim 0^\circ$, (b, e) $\sim 90^\circ$, and (c, f) $\sim 180^\circ$. The perimeter of the recess is marked with a dashed red circle and the respective signals from the $F = 4$ and $F = 3$ components are labelled.

Consider first a phase shift of $\sim 0^\circ$ with a probe beam with the same detuning for $F = 4$ and $F = 3$ [Fig. 7.7 (a)]. Signals from both are generated over the same region of the recess; this is equivalent to the situation described in Fig. 7.6 (b) at $t = 0$. In fact, the phase shift here is not exactly 0° , if it were then the signals would fully overlap and it would not be possible to see both since the lock-in can only demodulate the signal at a single frequency. If the detunings are opposite [Fig. 7.7 (d)], the secondary fields from opposite edges of the recess generate a signal for the $F = 4$ and $F = 3$ components. This is in agreement with what is expected from the opposite probe detuning for the $F = 4$ and $F = 3$ states. When there is a phase shift of $\sim 90^\circ$ [Fig. 7.7 (b, e)], the region where a signal is recorded for the two components also rotates by $\sim \pm 90^\circ$ for the $F = 4$ (clockwise) and $F = 3$ (counter-clockwise) signal, respectively. Figure 7.7 (e) is equivalent to the situation described in Fig. 7.6 (b) at $t = T/4$. For a phase shift of $\sim 180^\circ$ [Fig. 7.7 (c, f)], it is exactly the opposite of the case presented in Fig. 7.7 (a, d).

7.3.2.1 Active Stabilisation

The main benefit of the spin maser system is that it is self-referenced and can follow changes in ω_L so long as the phase matching condition is met. Additionally, the DFSM provides a significant advantage over the single-frequency spin maser, since it can double the area over which a signal from the defect is detectable. These two features can be combined to simplify the experimental setup, while maintaining reasonable spatial coverage for defect detection. The data presented in Fig. 7.8 are the (a, c) amplitude and (b, d) frequency images (120×120 pixels) recorded in the (a, b) driven (external source for the rf magnetic field) and (c, d) DFSM maser mode of operation for a $90 \times 90 \text{ mm}^2$, 6-mm-thick steel plate that contains a 24-mm-diameter recess that is 2.4-mm-deep in the centre of the plate. Both images have been recorded in the self-compensation mode. The amplitude image in the driven mode [Fig. 7.8 (a)] is what is expected, with strong signals generated by the edges of the plate, and the ring in amplitude at the centre representing the recess. Since the sample is magnetic, a drift of 0.61 kHz in the resonance frequency is visible in Fig. 7.8 (b) due to imperfections in the field stabilisation system. For the measurements presented in the spin maser mode, all active field stabilisation was turned off and the measurement was carried out in the ambient magnetic field, in the presence of 50-Hz magnetic field noise. Transverse static magnetic fields were applied so that the measurement was still in the self-compensation configuration (bias magnetic field parallel to

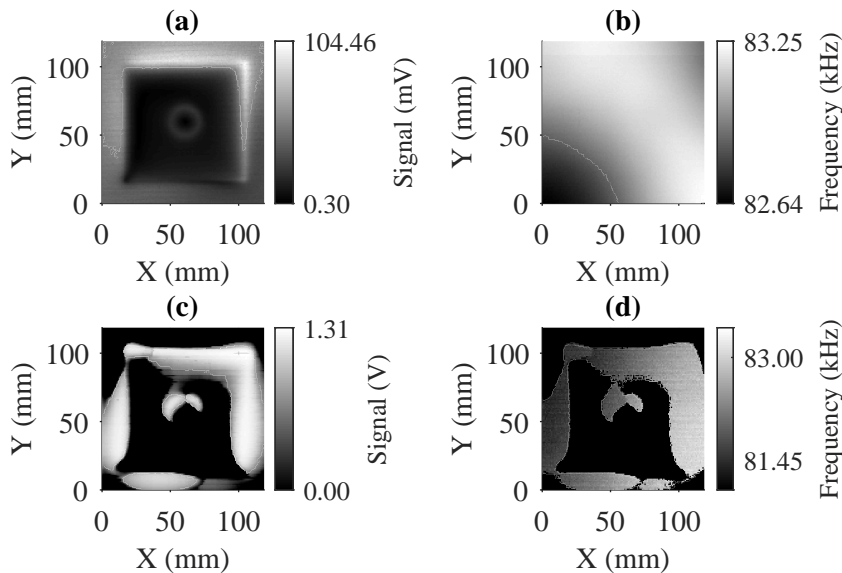


Figure 7.8: Images of the (a, c,) amplitude and (b, d) Larmor frequency recorded for a steel plate in the (a-b) driven and (c-d) DFSM mode. In the driven mode there is active stabilisation of the bias magnetic field; in the DFSM mode the active stabilisation was turned off.

the primary rf field) over the centre of the plate. The bias field is predominantly defined by the ambient magnetic field directed along the z -axis, which corresponds to a field of $\omega_L \approx 82$ kHz. In Fig. 7.8 (d) the frequency drift has increased to 1.55 kHz (the maximum and minimum frequency value are shown by the colourbar ticks, the limits are set beyond this so that the contrast of the frequency range can be discriminated from the background). However, it is still possible to record signatures of the recess and the plate edge over a significant area while in the presence of frequency drifts and 50-Hz noise.

Similarly for the results presented in Fig. 7.3, while it is required to record rf resonances for the driven mode, the DFSM could be continuously measured. As a result, Fig 7.8 (a-b) was recorded over 35 hours, compared to the 1 hour measurement time for Fig. 7.8 (c-d).

7.4 Conclusions

The operational frequency of the spin maser mode will be tuned to the rf resonance frequency so long as: (1) the phase-matching condition is met, and (2) there is enough gain in the feedback loop to provide feedback to the atoms. The ability for the spin maser to track changes in the bias magnetic field drastically increases the acquisition time when imaging magnetically permeable samples, since it removes the need to record the whole rf resonance spectrum. It also has been shown that the spin maser can work effectively without active stabilisation of the bias magnetic field (in the presence of 50Hz magnetic field noise and dc shifts in the bias magnetic field), which greatly simplifies the experimental requirements of the system. Since the phase-matching condition is only met over a limited range, not all secondary fields can be recorded by the spin maser system. However, it is possible to increase the area over which a signal is recorded by operating in the novel DFSM mode or with an array of rf coils with a relative phase shift between them.

As a co-magnetometer the DFSM mode presents the option for other interesting measurements. It is possible to make a precise frequency ratio measurement between the signal from the $F = 4$ and $F = 3$ components that will be broadly insensitive² to changes in the bias magnetic field. These types of measurement have applications in other practical sensors such as gyroscopes [154] and in fundamental searches for new physics [155]. Two other groups simultaneously presented the same concept of carrying out a frequency ratio measurement between two hyperfine ground state levels of an alkali-metal atom, but in different systems. The first group, Z. Wang et al., operated with a similar setup to this; however, the measurement was carried out in the *driven mode* [156]; while the work of P. Gomez et al. used a magnetometer

²The Larmor frequency difference ($\omega_{L,F=3} - \omega_{L,F=4}$) between the $F = 3$ and $F = 4$ states is ~ 1000 times smaller than the Larmor frequency of each state.

based on a Bose-Einstein condensate system [157]. The advantage of the spin maser system is that it is an active measurement, which means it is always on resonance and could potentially have a faster data acquisition time (high-bandwidth). The interest in the same concept from multiple groups shows that this is a pertinent area of research and it will be the focus of future studies. The results presented here for the DFSM are from preliminary studies that were recorded towards the end of this body of work. What has been presented is not complete, but it has been included because it presents a new and exciting avenue for applications of the rf magnetometer.

Chapter 8

Outlook

This work has built an rf magnetometer that can operate in an unshielded environment and has made significant progress in the study of the capabilities of rf magnetometers for applications in MIT, with particular focus on the optimisation of the sensor and the understanding of the signal response from a defect.

The rf magnetometer is attractive for MIT due to its high sensitivity, which exceeds pick-up coils of the same volume and their ability to operate at room temperature (in contrast to SQUIDs). This thesis has shown that these magnetometers are useful for this application because their insensitive axis can be aligned along the dominating primary field. In this configuration, the sensor will only measure the components of the secondary field that are generated by a defect, resulting in a high-contrast imaging scheme. Usefully, the imaging resolution of the system was also shown to be dependent on the coil size and not the size of the vapour cell used in this work, meaning the cell size can be independently optimised for the magnetometer's sensitivity and footprint. The measured signal response to the presence of a defect was confirmed with numerical modelling, enabling a robust understanding of how the spatial distribution of the secondary field affects the amplitude and phase of the magnetometer signal. This thesis has used the sensor to discriminate between defects of different sizes (diameter and depths), which could be used for tomographic characterisation of a defect once calibrated. The attraction of MIT is that rf fields can penetrate through barriers. An interesting result of this thesis is that there is an optimum frequency of rf field at which point inductive coupling (generating a strong signal) is balanced with penetration into the object (to detect deep defects). This optimum was shown to change with barrier thickness and it is expected it will also change with the sensitivity of the rf magnetometer and the strength of the primary rf field.

An outstanding issue in the field of MIT is the distinction between the dynamics of the secondary field generated by eddy currents and local magnetisation of the sample. This work

clearly identified these two different mechanisms by the difference in the direction of the secondary field. Further study is required to understand the penetration depth of the primary field through local magnetisation and its frequency dependence. Initial empirical investigations into this area have begun, and the COMSOL multi-physics software package is a promising tool to study these dynamics from a theoretical point of view.

More generally, two important findings were made concerning the operation of the rf magnetometer. The first was the identification and demonstration of a laser configuration, which reduced the two-beam optical pumping and probing scheme to a single-beam, while maintaining the same indirect-pumping and off-resonant probing action that was shown to be beneficial to the optimisation of the performance of the sensor. Although the single-beam scheme requires more optical power than the two-beam scheme, it was demonstrated to work with a VCSEL. The reduction in beam number drastically reduces the complexity of the sensor, and the use of VCSELs will significantly aid miniaturisation (reduction of size, weight, and power). The second was the demonstration of the spin maser mode for MIT. As the sensor is self-referenced, the signal is always on resonance. This meant that MIT measurements could be carried without the need for active stabilisation of the bias magnetic field. When combined, these two features relax the experimental requirements of the sensor and pave the way forward to building a practical sensor with real-world applications.

This work also presents the first demonstration of the DFSM within a single isotope, operating simultaneously on the two hyperfine ground states of caesium. This mode was shown to be useful for MIT as it increases the coverage of defect detection. However, the ability to make a frequency ratio measurement has applications in many other areas of physics, such as gyroscopes and coupling to exotic physics.

The work surrounding this thesis has generated significant output in terms of patent applications, published papers, and novel ideas in fundamental and applied physics. The existing sensor is well optimised for the applications presented here, but future research aims are to utilise the ideas and understanding gained over the last four years to develop a miniaturised sensor that has a range of applications.

References

- [1] J. Brossel and A. Kastler. Detection of magnetic resonance in excited levels-an effect of resonance radiation depolarization. *Compt. Rend. Hebd. Acad. Sci*, 229:1213, 1949.
- [2] H. G. Dehmelt. Paramagnetic resonance reorientation of atoms and ions aligned by electron impact. *Physical Review*, 103(4):1125–1126, aug 1956. doi: 10.1103/physrev.103.1125.
- [3] H. G. Dehmelt. Modulation of a light beam by precessing absorbing atoms. *Physical Review*, 105(6):1924–1925, mar 1957. doi: 10.1103/physrev.105.1924.
- [4] A. L. Bloom. Principles of operation of the rubidium vapor magnetometer. *Applied Optics*, 1(1):61, jan 1962. doi: 10.1364/ao.1.000061.
- [5] I. M. Savukov, S. J. Seltzer, M. V. Romalis, and K. L. Sauer. Tunable atomic magnetometer for detection of radio-frequency magnetic fields. *Physical Review Letters*, 95(6), aug 2005. doi: 10.1103/physrevlett.95.063004.
- [6] W. Chalupczak, R. M. Godun, S. Pustelny, and W. Gawlik. Room temperature femtotesla radio-frequency atomic magnetometer. *Applied Physics Letters*, 100(24):242401, jun 2012. doi: 10.1063/1.4729016.
- [7] P. Bevington, R. Gartman, W. Chalupczak, C. Deans, L. Marmugi, and F. Renzoni. Non-destructive structural imaging of steelwork with atomic magnetometers. *Applied Physics Letters*, 113(6):063503, aug 2018. doi: 10.1063/1.5042033.
- [8] P. Bevington, R. Gartman, and W. Chalupczak. Imaging of material defects with a radio-frequency atomic magnetometer. *Review of Scientific Instruments*, 90(1):013103, jan 2019. doi: 10.1063/1.5053959.
- [9] P. Bevington, R. Gartman, and W. Chalupczak. Enhanced material defect imaging with a radio-frequency atomic magnetometer. *Journal of Applied Physics*, 125(9):094503, mar 2019. doi: 10.1063/1.5083039.

- [10] P. Bevington, R. Gartman, and W. Chalupczak. Alkali-metal spin maser for non-destructive tests. *Applied Physics Letters*, 115(17):173502, oct 2019. doi: 10.1063/1.5121606.
- [11] P. Bevington, R. Gartman, and W. Chalupczak. Generation of atomic spin orientation with a linearly polarized beam in room-temperature alkali-metal vapor. *Physical Review A*, 101(1), jan 2020. doi: 10.1103/physreva.101.013436.
- [12] P. Bevington, R. Gartman, and W. Chalupczak. Magnetic induction tomography of structural defects with alkali-metal spin maser. *Applied Optics*, 59(8):2276, mar 2020. doi: 10.1364/ao.386499.
- [13] P. Bevington, R. Gartman, D. J. Botelho, R. Crawford, M. Packer, T. M. Fromhold, and W. Chalupczak. Object surveillance with radio-frequency atomic magnetometers. *Review of Scientific Instruments*, 91(5):055002, may 2020. doi: 10.1063/1.5145251.
- [14] P. Bevington, J. Rajroop, R. Gartman, and W. Chalupczak. Role of the probe beam in a radio-frequency atomic magnetometer. *Applied Optics*, 59(20):6054, jul 2020. doi: 10.1364/ao.396941.
- [15] P. Bevington, R. Gartman, Y. V. Stadnik, and W. Chalupczak. Dual-frequency cesium spin maser. *Physical Review A*, 102(3), sep 2020. doi: 10.1103/physreva.102.032804.
- [16] P. Bevington, R. Gartman, and W. Chalupczak. Inductive imaging of the concealed defects with radio-frequency atomic magnetometers. *Applied Sciences*, 10(19):6871, sep 2020. doi: 10.3390/app10196871.
- [17] B. Julsgaard, J. Sherson, J. L. Sorensen, and E. S. Polzik. Characterizing the spin state of an atomic ensemble using the magneto-optical resonance method. *Journal of Optics B: Quantum and Semiclassical Optics*, 6(1):5–14, sep 2004. doi: 10.1088/1464-4266/6/1/002.
- [18] S. J. Ingleby, Carolyn O’Dwyer, P. F. Griffin, A. S. Arnold, and E. Riis. Orientational effects on the amplitude and phase of polarimeter signals in double-resonance atomic magnetometry. *Physical Review A*, 96(1), jul 2017. doi: 10.1103/physreva.96.013429.
- [19] K. Jensen, M. Zugenmaier, J. Arnbak, H. Stærkind, M. V. Balabas, and M. S. Polzik. Detection of low-conductivity objects using eddy current measurements with an optical magnetometer. *Physical Review Research*, 1(3), nov 2019. doi: 10.1103/physrevresearch.1.033087.

- [20] C. Deans, L. Marmugi, and F. Renzoni. Through-barrier electromagnetic imaging with an atomic magnetometer. *Optics Express*, 25(15):17911, jul 2017. doi: 10.1364/oe.25.017911.
- [21] V. Gerginov, S. Krzyzewski, and S. Knappe. Pulsed operation of a miniature scalar optically pumped magnetometer. *Journal of the Optical Society of America B*, 34(7):1429, jun 2017. doi: 10.1364/josab.34.001429.
- [22] M. E. Limes, E. L. Foley, T. W. Kornack, S. Caliga, S. McBride, A. Braun, W. Lee, V. G. Lucivero, and M. V. Romalis. Portable magnetometry for detection of biomagnetism in ambient environments. *Physical Review Applied*, 14(1), jul 2020. doi: 10.1103/physrevapplied.14.011002.
- [23] J. C. Allred, R. N. Lyman, T. W. Kornack, and M. V. Romalis. High-sensitivity atomic magnetometer unaffected by spin-exchange relaxation. *Physical Review Letters*, 89(13), sep 2002. doi: 10.1103/physrevlett.89.130801.
- [24] S. J. Seltzer, D. M. Rampulla, S. Rivillon-Amy, Y. J. Chabal, S. L. Bernasek, and M. V. Romalis. Testing the effect of surface coatings on alkali atom polarization lifetimes. *Journal of Applied Physics*, 104(10):103116, nov 2008. doi: 10.1063/1.2985913.
- [25] C. J. Foot. *Atomic Physics*. Oxford University Press, 2005.
- [26] D. A. Steck. *Cesium D Line Data*, 2003. URL <https://steck.us/alkalidata/cesiumnumbers.1.6.pdf>.
- [27] J. Vanier and C. Audoin. *The Quantum Physics of Atomic Frequency Standards*. Adam Hilger, 1989.
- [28] B. S. Mathur, H. Tang, and W. Happer. Light shifts in the alkali atoms. *Physical Review*, 171(1):11–19, jul 1968. doi: 10.1103/physrev.171.11.
- [29] C. Cohen-Tannoudji and J. Dupont-Roc. Experimental study of zeeman light shifts in weak magnetic fields. *Physical Review A*, 5(2):968–984, feb 1972. doi: 10.1103/physreva.5.968.
- [30] A. Grosz, M. J. Haji-Sheikh, and S. C. Mukhopadhyay. *High Sensitivity Magnetometers*. Springer, 2017.
- [31] L. Young, W. T. Hill, S. J. Sibener, Stephen D. Price, C. E. Tanner, C. E. Wieman, and Stephen R. Leone. Precision lifetime measurements of Cs $6P^2P_{1/2}$ and $6P^2P_{3/2}$

- levels by single-photon counting. *Physical Review A*, 50(3):2174–2181, sep 1994. doi: 10.1103/physreva.50.2174.
- [32] T. Fernholz, H. Krauter, K. Jensen, J. F. Sherson, A. S. Sørensen, and E. S. Polzik. Spin squeezing of atomic ensembles via nuclear-electronic spin entanglement. *Physical Review Letters*, 101(7), aug 2008. doi: 10.1103/physrevlett.101.073601.
- [33] M. Auzinsh, D. Budker, and S. M. Rochester. *Optically Polarized Atoms*. Oxford University Press, 2010.
- [34] G. Di Domenico, G. Bison, S. Groeger, P. Knowles, A. S. Pazgalev, M. Rebetz, H. Saudan, and A. Weis. Experimental study of laser-detected magnetic resonance based on atomic alignment. *Physical Review A*, 74(6), dec 2006. doi: 10.1103/physreva.74.063415.
- [35] W. Chalupczak, A. Wojciechowski, S. Pustelny, and W. Gawlik. Competition between the tensor light shift and nonlinear Zeeman effect. *Physical Review A*, 82(2), aug 2010. doi: 10.1103/physreva.82.023417.
- [36] Y. Takahashi, K. Honda, N. Tanaka, K. Toyoda, K. Ishikawa, and T. Yabuzaki. Quantum nondemolition measurement of spin via the paramagnetic faraday rotation. *Physical Review A*, 60(6):4974–4979, dec 1999. doi: 10.1103/physreva.60.4974.
- [37] V. Shah, G. Vasilakis, and M. V. Romalis. High bandwidth atomic magnetometry with continuous quantum nondemolition measurements. *Physical Review Letters*, 104(1), jan 2010. doi: 10.1103/physrevlett.104.013601.
- [38] D. Budker, W. Gawlik, D. F. Kimball, S. M. Rochester, V. V. Yashchuk, and A. Weis. Resonant nonlinear magneto-optical effects in atoms. *Reviews of Modern Physics*, 74(4):1153–1201, nov 2002. doi: 10.1103/revmodphys.74.1153.
- [39] J. D. Jackson. *Classical Electrodynamics*. Wiley India Pvt. Limited, 2007. ISBN 9788126510948.
- [40] D. A. Van Baak. Resonant Faraday rotation as a probe of atomic dispersion. *American Journal of Physics*, 64(6):724–735, jun 1996. doi: 10.1119/1.18356.
- [41] W. Happer and B. S. Mathur. Off-resonant light as a probe of optically pumped alkali vapors. *Physical Review Letters*, 18(15):577–580, apr 1967. doi: 10.1103/physrevlett.18.577.

- [42] S. Jeffrey Seltzer. *Developments in Alkali-Metal Atomic Magnetometry*. PhD thesis, Princeton University, 2008.
- [43] B. Julsgaard. *Entanglement and Quantum Interactions with Macroscopic Gas Samples*. PhD thesis, University of Aarhus, 2003.
- [44] D. Budker and D. F. Jackson Kimball. *Optical Magnetometry*. Cambridge University Press, 2013. doi: 10.1017/cbo9780511846380.
- [45] F. Bloch. Nuclear induction. *Physical Review*, 70(7-8):460–474, oct 1946. doi: 10.1103/physrev.70.460.
- [46] J. B. Marion and S. T. Thornton. *Classical Dynamics of Particles and Systems*. Elsevier Science, fifth edition, 2003. ISBN 9781483272818. URL <https://books.google.co.uk/books?id=Ss43BQAAQBAJ>.
- [47] J. Belfi, G. Bevilacqua, V. Biancalana, S. Cartaleva, Y. Dancheva, and L. Moi. Cesium coherent population trapping magnetometer for cardiosignal detection in an unshielded environment. *Journal of the Optical Society of America B*, 24(9):2357, aug 2007. doi: 10.1364/josab.24.002357.
- [48] A. P. Colombo, T. R. Carter, A. Borna, Y. Y. Jau, C. N. Johnson, A. L. Dagel, and P. D. D. Schwindt. Four-channel optically pumped atomic magnetometer for magnetoencephalography. *Optics Express*, 24(14):15403, jun 2016. doi: 10.1364/oe.24.015403.
- [49] M. V. Balabas, K. Jensen, W. Wasilewski, H. Krauter, L. S. Madsen, J. H. Muller, T. Fernholz, and E. S. Polzik. High quality anti-relaxation coating material for alkali atom vapor cells. *Optics Express*, 18(6):5825, mar 2010. doi: 10.1364/oe.18.005825.
- [50] S. J. Seltzer, D. J. Michalak, M. H. Donaldson, M. V. Balabas, S. K. Barber, S. L. Bernasek, M.-A. Bouchiat, A. Hexemer, A. M. Hibberd, D. F. Jackson Kimball, C. Jaye, T. Karaulanov, F. A. Narducci, S. A. Rangwala, H. G. Robinson, A. K. Shmakov, D. L. Voronov, V. V. Yashchuk, A. Pines, and D. Budker. Investigation of antirelaxation coatings for alkali-metal vapor cells using surface science techniques. *The Journal of Chemical Physics*, 133(14):144703, oct 2010. doi: 10.1063/1.3489922.
- [51] W. Li, M. Balabas, X. Peng, S. Pustelny, A. Wickenbrock, H. Guo, and D. Budker. Characterization of high-temperature performance of cesium vapor cells with anti-relaxation coating. *Journal of Applied Physics*, 121(6):063104, feb 2017. doi: 10.1063/1.4976017.

- [52] S. J. Seltzer and M. V. Romalis. High-temperature alkali vapor cells with antirelaxation surface coatings. *Journal of Applied Physics*, 106(11):114905, dec 2009. doi: 10.1063/1.3236649.
- [53] P. Knapkiewicz. Alkali vapor MEMS cells technology toward high-vacuum self-pumping MEMS cell for atomic spectroscopy. *Micromachines*, 9(8):405, aug 2018. doi: 10.3390/mi9080405.
- [54] S. Pustelny, D. F. Jackson Kimball, S. M. Rochester, V. V. Yashchuk, and D. Budker. Influence of magnetic-field inhomogeneity on nonlinear magneto-optical resonances. *Physical Review A*, 74(6), dec 2006. doi: 10.1103/physreva.74.063406.
- [55] S. Appelt, A. Ben-Amar Baranga, C. J. Erickson, M. V. Romalis, A. R. Young, and W. Happer. Theory of spin-exchange optical pumping of ^3He and ^{129}Xe . *Physical Review A*, 58(2):1412–1439, aug 1998. doi: 10.1103/physreva.58.1412.
- [56] W. Chalupczak, P. Josephs-Franks, R. M. Godun, and S. Pustelny. Radio-frequency spectroscopy in the dark. *Physical Review A*, 88(5), nov 2013. doi: 10.1103/physreva.88.052508.
- [57] W. Chalupczak, R. M. Godun, P. Anielski, A. Wojciechowski, S. Pustelny, and W. Gawlik. Enhancement of optically pumped spin orientation via spin-exchange collisions at low vapor density. *Physical Review A*, 85(4), apr 2012. doi: 10.1103/physreva.85.043402.
- [58] S. Appelt, A. Ben-Amar Baranga, A. R. Young, and W. Happer. Light narrowing of rubidium magnetic-resonance lines in high-pressure optical-pumping cells. *Physical Review A*, 59(3):2078–2084, mar 1999. doi: 10.1103/physreva.59.2078.
- [59] W. Happer and A. C. Tam. Effect of rapid spin exchange on the magnetic-resonance spectrum of alkali vapors. *Physical Review A*, 16(5):1877–1891, nov 1977. doi: 10.1103/physreva.16.1877.
- [60] Stanford Research Systems. *Operation Manual: SR865A 2 MHz DSP Lock-in Amplifier*, 2.08 edition, 2020.
- [61] M. Auzinsh, D. Budker, D. F. Kimball, S. M. Rochester, J. E. Stalnaker, A. O. Sushkov, and V. V. Yashchuk. Can a quantum nondemolition measurement improve the sensitivity of an atomic magnetometer? *Physical Review Letters*, 93(17):173002, oct 2004. doi: 10.1103/physrevlett.93.173002.

- [62] J. M. Danet, M. Lours, S. Guérandel, and E. De Clercq. Dick effect in a pulsed atomic clock using coherent population trapping. *IEEE Transactions on Ultrasonics, Ferroelectrics, and Frequency Control*, 61(4):567–574, apr 2014. doi: 10.1109/tuffc.2014.2945.
- [63] A. Weis, S. I. Kanorsky, and J. Wurster. Quantitative interpretation of the nonlinear faraday effect as a hanle effect of a light-induced birefringence. *Journal of the Optical Society of America B*, 10(4):716, apr 1993. doi: 10.1364/josab.10.000716.
- [64] W. Gawlik, J. Kowalski, R. Neumann, and F. TrÄ€ger. Observation of the electric hexadecapole moment of free na atoms in a forward scattering experiment. *Optics Communications*, 12(4):400–404, dec 1974. doi: 10.1016/0030-4018(74)90130-8.
- [65] T. Scholtes, V. Schultze, R. IJsselsteijn, S. Woetzel, and H.-G. Meyer. Light-narrowed optically pumped Mx magnetometer with a miniaturized cs cell. *Physical Review A*, 84(4), oct 2011. doi: 10.1103/physreva.84.043416.
- [66] G. Di Domenico, H. Saudan, G. Bison, P. Knowles, and A. Weis. Sensitivity of double-resonance alignment magnetometers. *Physical Review A*, 76(2), aug 2007. doi: 10.1103/physreva.76.023407.
- [67] M. P. Ledbetter, V. M. Acosta, S. M. Rochester, D. Budker, S. Pustelny, and V. V. Yashchuk. Detection of radio-frequency magnetic fields using nonlinear magneto-optical rotation. *Physical Review A*, 75(2), feb 2007. doi: 10.1103/physreva.75.023405.
- [68] University of Strathclyde. Quantum technology showcase. In *Quantum Technology Showcase*, 2019.
- [69] Vescent. D2-100-dbr laser module, 2020. URL <https://www.vescent.com/products/lasers/d2-100-dbr-laser/>.
- [70] W. Chalupczak, R. M. Godun, and S. Pustelny. Radio-frequency spectroscopy as a tool for studying coherent spin dynamics and for application to radio-frequency magnetometry. In *Advances In Atomic, Molecular, and Optical Physics*, pages 297–336. Elsevier, 2018. doi: 10.1016/bs.aamop.2018.03.001.
- [71] M. Cerna and A. F. Harvey. *The Fundamentals of FFT-Based Signal Analysis and Measurement*, 2000.
- [72] J. Rajroop. *Radio-frequency atomic magnetometers: an analysis of interrogation regimes*. PhD thesis, University College London, 2018.

- [73] S. M. Rochester, M. P. Ledbetter, T. Zigdon, A. D. Wilson-Gordon, and D. Budker. Orientation-to-alignment conversion and spin squeezing. *Physical Review A*, 85(2), feb 2012. doi: 10.1103/physreva.85.022125.
- [74] J. Kitching. Chip-scale atomic devices. *Applied Physics Reviews*, 5(3):031302, sep 2018. doi: 10.1063/1.5026238.
- [75] D. A. Smith and I. G. Hughes. The role of hyperfine pumping in multilevel systems exhibiting saturated absorption. *American Journal of Physics*, 72(5):631–637, may 2004. doi: 10.1119/1.1652039.
- [76] Vescent. *Offset Phase Lock Servo*, 2020.
- [77] J. Singh, P. A. M. Dolph, and W. A. Tobias. Alkali metal vapor pressures and number densities for hybrid spin exchange optical pumping. Technical report, University of Virginia, 2008.
- [78] W. Chalupczak, P. Josephs-Franks, B. Patton, and S. Pustelny. Spin-exchange narrowing of the atomic ground-state resonances. *Physical Review A*, 90(4), oct 2014. doi: 10.1103/physreva.90.042509.
- [79] T. T. K. Li. *Tri-axial Square Helmholtz Coil for Neutron EDM Experiment*. Master’s thesis, Chinese University of Hong Kong, 2004.
- [80] M. E. Rudd and J. R. Craig. Optimum spacing of square and circular coil pairs. *M. Eugene Rudd Publications*, Paper 41, 1968.
- [81] P. Vigoureux. Calculation of the magnetic field strength in helmholtz systems with square and polygonal coils. *NPL Report*, DES 143.
- [82] D. Petkovic and M. Radic. Generalization of Helmholtz coil problem. *Serbian Journal of Electrical Engineering*, 12(3):375–384, 2015. doi: 10.2298/sjee1503375p.
- [83] Y. Liu, J. Xu, and Y. Wu. P-217: Designing the coil assembly to solve mask deformation. *SID Symposium Digest of Technical Papers*, 48(1):1558–1561, may 2017. doi: 10.1002/sdtp.11948.
- [84] T. W. Kornack, S. J. Smullin, S.-K. Lee, and M. V. Romalis. A low-noise ferrite magnetic shield. *Applied Physics Letters*, 90(22):223501, may 2007. doi: 10.1063/1.2737357.

- [85] B. Kuzmanovic, Z. Baus, and S. Nikolovski. Multi-layered spherical magnetic shielding. *Journal of electrical engineering*, 60(6):350–353, 2009.
- [86] S.-K. Lee and M. V. Romalis. Calculation of magnetic field noise from high-permeability magnetic shields and conducting objects with simple geometry. *Journal of Applied Physics*, 103(8):084904, apr 2008. doi: 10.1063/1.2885711.
- [87] H. Griffiths. Magnetic induction tomography. *Measurement Science and Technology*, 12, 2001.
- [88] A. J. Peyton. Electromagnetic induction tomography. In *Industrial Tomography*, pages 61–107. Elsevier, 2015. doi: 10.1016/b978-1-78242-118-4.00003-4.
- [89] X. Han-liang and X. Ling-an. Electromagnetic tomography (EMT): Theoretical analysis of the forward problem. *Applied Mathematics and Mechanics*, 21(9):1034–1044, sep 2000. doi: 10.1007/bf02459313.
- [90] P. J. Shull. *Nondestructive Evaluation Theory, Techniques, and Applications*. Marcel Dekker, Inc., 2002.
- [91] W. Yoshimura, T. Sasayama, and K. Enpuku. Optimal frequency of low-frequency eddy-current testing for detecting defects on the backside of thick steel plates. *IEEE Transactions on Magnetics*, 55(7):1–5, jul 2019. doi: 10.1109/tmag.2019.2896590.
- [92] N. Bowler. *Eddy-Current Nondestructive Evaluation*. Springer, 2019.
- [93] B. A. Auld and J. C. Moulder. Review of advances in quantitative eddy current nondestructive evaluation. *Journal of Nondestructive Evaluation*, 18(1):3–36, 1999.
- [94] S. Tumanski. *Magnetic Materials*. CRC Press, jun 2011. doi: 10.1201/b10979-4.
- [95] D. J. Griffiths. *Introduction to Electrodynamics*. Pearson, 2013.
- [96] I. M. Savukov, S. J. Seltzer, and M. V. Romalis. Detection of NMR signals with a radio-frequency atomic magnetometer. *Journal of Magnetic Resonance*, 185(2):214–220, apr 2007. doi: 10.1016/j.jmr.2006.12.012.
- [97] J. W. Mooney, S. Ghasemi-Roudsari, E. Reade Banham, C. Symonds, N. Pawlowski, and B. T. H. Varcoe. A portable diagnostic device for cardiac magnetic field mapping. *Biomedical Physics & Engineering Express*, 3(1):015008, jan 2017. doi: 10.1088/2057-1976/3/1/015008.

- [98] O. Hesse and S. Pankratyev. Usage of magnetic and field sensors and for low and frequency eddy and current testing. *Measurement Science Review*, 5, 2005.
- [99] G. Mook, O. Hesse, and V. Uchanin. Deep penetrating eddy currents and probes, 2006. URL <https://www.ndt.net/article/ecndt2006/doc/Tu.3.6.2.pdf>.
- [100] V. S. Cecco, G. Van Drunen, and F. L. Sharp. *Eddy Current Manual Volume 1*. Chalk River Nuclear Labs, 1983.
- [101] J. Garicia-Martin, J. Gomez-Gil, and E. Vazquez-Sanchez. Nondestructive techniques on eddy current testing. *Sensors*, 11:2525–2565, 2011.
- [102] T. Stepinski. Essential parameters and in eddy and current inspection. Technical report, Swedish Nuclear Power Inspectorate Project Number 97038. SKI Report 00:30, 2000.
- [103] R. Pellicer-Guridi, M. W. Vogel, D. C. Reutens, and V. Vegh. Towards ultimate low frequency air-core magnetometer sensitivity. *Scientific Reports*, 7(1), may 2017. doi: 10.1038/s41598-017-02099-z.
- [104] S. Tumanski. Induction coil sensors—a review. *Measurement Science and Technology*, 18(3):R31–R46, jan 2007. doi: 10.1088/0957-0233/18/3/r01.
- [105] T. Watanabe H. Ueda. Linearity of ferromagnetic and core solenoids. *J. Geomag. Geoelectr*, 32:285–295, 1980.
- [106] K. Kuang. *Magnetic Sensors: Principles and Applications*. IntechOpen, 2012. ISBN 9789535102328.
- [107] H. C. Seran and P. Ferreau. An optimized low-frequency three-axis search coil magnetometer for space research. *Review of Scientific Instruments*, 76(044502), 2005. doi: 10.1063/1.1884026.
- [108] Olympus. Spot probes. URL [https://www.olympus-ims.com/en/ec-probes/spot/#!cms\[focus\]=cmsContent10678](https://www.olympus-ims.com/en/ec-probes/spot/#!cms[focus]=cmsContent10678).
- [109] A. Sophian, G. Tian, and M. Fan. *Pulsed Eddy Current Non-destructive Testing and Evaluation: A Review*. Springer Science and Business Media LLC, 2017. doi: 10.1007/s10033-017-0122-4.
- [110] A. N. AbdAlla, M. A. Faraj, F. Samsuri, D. Rifai, K. Ali, and Y. Al-Douri. Challenges in improving the performance of eddy current testing: Review. *Measurement and Control*, 52(1-2):46–64, 2018. doi: 10.1177/0020294018801382.

- [111] Zetec. Handheld probes. URL <https://www.zetec.com/products/eddy-current/probes/handheld-probes/>.
- [112] E. Boto, N. Holmes, J. Leggett, G. Roberts, V. Shah, S. S. Meyer, L. Duque Munoz, K. J. Mullinger, T. M. Tierney, S. Bestmann, G. R. Barnes, R. Bowtell, and M. J. Brookes. Moving magnetoencephalography towards real-world applications with a wearable system. *Nature*, 555(7698):657–661, mar 2018. doi: 10.1038/nature26147.
- [113] R. L. Fagaly. Superconducting quantum interference device instruments and applications. *Review of Scientific Instruments*, 77(10):101101, oct 2006. doi: 10.1063/1.2354545.
- [114] E. Botto. A wearable multi-channel opm-meg system: from construction to application. In *Quantum Sensing and Magnetometry*, 2019.
- [115] D. Drung, S. Bechstein, K.-P. Franke, M. Scheiner, and Th. Schurig. Improved direct-coupled dc SQUID read-out electronics with automatic bias voltage tuning. *IEEE Transactions on Applied Superconductivity*, 11(1):880–883, mar 2001. doi: 10.1109/77.919485.
- [116] H. Weinstock. A review of SQUID magnetometry applied to nondestructive evaluation. *IEEE Transactions on Magnetics*, 27(2):3231–3236, mar 1991. doi: 10.1109/20.133898.
- [117] W. G. Jenks, S. S. H. Sadeghi, and J. P. Wikswo. SQUIDs for nondestructive evaluation. *Journal of Physics D: Applied Physics*, 30(3):293–323, feb 1997. doi: 10.1088/0022-3727/30/3/002.
- [118] W. N. Podney. Performance measurements of a superconductive microprobe for eddy current evaluation of subsurface flaws. *IEEE Transactions on Applied Superconductivity*, 3(1):1914–1917, mar 1993. doi: 10.1109/77.233587.
- [119] Y. Hatsukade, K. Hayashi, Y. Shinyama, Y. Kobayashi, S. Adachi, K. Tanabe, and S. Tanaka. Characteristics of an HTS-SQUID gradiometer with ramp-edge josephson junctions and its application on robot-based 3d-mobile compact SQUID NDE system. *Physica C: Superconductivity and its Applications*, 471(21-22):1228–1233, nov 2011. doi: 10.1016/j.physc.2011.05.166.
- [120] K. Yotsugi, Y. Hatsukade, and S. Tanaka. Robot-arm-based mobile HTS SQUID system for NDE of structures. *Journal of Physics: Conference Series*, 97:012134, feb 2008. doi: 10.1088/1742-6596/97/1/012134.

- [121] C. H. Smith and R. W. Schneider. Low-field magnetic sensing with GMR sensors. In *Sensors EXPO-Baltimore*, pages 1–13, 1999.
- [122] D. Samal and A. P. S. Kumar. Giant magnetoresistance. *Resonance*, 13(4):343–354, April 2008. doi: 10.1007/s12045-008-0015-z.
- [123] NVE. How GMR works. URL <https://www.nve.com/Downloads/intro.pdf>.
- [124] J. Lenz and S. Edelstein. Magnetic sensors and their applications. *IEEE Sensors Journal*, 6(3):631–649, June 2006. doi: 10.1109/jsen.2006.874493.
- [125] G. Mook, O. Hesse, and V. Uchanin. Deep penetrating eddy currents and probes. *Materials Testing*, 49(5):258–264, May 2007. doi: 10.3139/120.100810.
- [126] F. Hankard, J. Gattacceca, C. Fermon, M. Pannetier-Lecoeur, B. Langlais, Y. Quesnel, P. Rochette, and S. A. McEnroe. Magnetic field microscopy of rock samples using a giant magnetoresistance-based scanning magnetometer. *Geochemistry, Geophysics, Geosystems*, 10(10), oct 2009. doi: 10.1029/2009gc002750.
- [127] M. Pannetier-Lecoeur, C. Fermon, H. Polovy, H. Dyvorne, N. Sergeeva-Chollet, and J. Paul. Gmr based sensors for ultra-sensitive magnetometry. In *EEE Sensors*. IEEE, oct 2009. doi: 10.1109/ICSENS.2009.5398408.
- [128] M. Djamal and R. Ramli. *Magnetic Sensors - Development Trends and Applications*. InTech, nov 2017. doi: 10.5772/intechopen.70548.
- [129] T. Dogaru, C. S. Smith, R. W. Schneider, and S. T. Smith. New directions in eddy current sensing technology. *Sensors Mag.*, 18(6):56–63, 2001. URL http://web.hep.uiuc.edu/home/serrede/P435/Lecture_Notes/New_Directions_in_Eddy_Current_Sensing.pdf.
- [130] L. S. Rosado, F. A. Cardoso, S. Cardoso, P. M. Ramos, P. P. Freitas, and M. Piedade. Eddy currents testing probe with magneto-resistive sensors and differential measurement. *Sensors and Actuators A: Physical*, 212:58–67, June 2014. doi: 10.1016/j.sna.2014.03.021.
- [131] M. Le, J. Kim, H. S. Do, and J. Lee. 2-d vector field visualization of corrosion in a small-bore piping system using bobbin-type integrated hall and GMR sensors arrays. *IEEE*, feb 2014. doi: 10.1109/SAS.2014.6798913.

- [132] T. Dogaru and S. T. Smith. Edge crack detection using a giant magnetoresistance based eddy current sensor. *Nondestructive Testing and Evaluation*, 16(1):31–53, jan 2000. doi: 10.1080/10589750008953062.
- [133] T. Dogaru and S. T. Smith. Giant magnetoresistance-based eddy-current sensor. *IEEE Transactions on Magnetics*, 37(5):3831–3838, 2001. doi: 10.1109/20.952754.
- [134] W. W. Ward and J. C. Moulder. *Low Frequency, Pulsed Eddy Currents for Deep Penetration*, pages 291–298. Springer US, Boston, MA, 1998. ISBN 978-1-4615-5339-7. doi: 10.1007/978-1-4615-5339-7_37.
- [135] A. L. Ribeiro, D. Pasadas, T. Rocha, and H. M. Ramos. GMR versus differential coils in velocity induced eddy current testing. In *IEEE International Instrumentation and Measurement Technology Conference (I2MTC) Proceedings*, 2014.
- [136] M. Pelkner, R. Pohl, M. Kreuzbruck, and C. Commandeur. Development of adapted gmr-probes for automated detection of hidden defects in thin steel sheets. In *AIP Conference Proceedings*. AIP Publishing LLC, 2016. doi: 10.1063/1.4940464.
- [137] V. Shah, S. Knappe, P. D. D. Schwindt, and J. Kitching. Subpicotesla atomic magnetometry with a microfabricated vapour cell. *Nature Photonics*, 1(11):649–652, nov 2007. doi: 10.1038/nphoton.2007.201.
- [138] R. Zhang, T. Dyer, N. Brockie, R. Parsa, and R. Mhaskar. Subpicotesla scalar atomic magnetometer with a microfabricated cell. *Journal of Applied Physics*, 126(12):124503, sep 2019. doi: 10.1063/1.5113520.
- [139] A. Wickenbrock, S. Jurgilas, A. Dow, L. Marmugi, and F. Renzoni. Magnetic induction tomography using an all-optical ^{87}Rb atomic magnetometer. *Optics Letters*, 39(22):6367, nov 2014. doi: 10.1364/ol.39.006367.
- [140] C. Deans, L. Marmugi, S. Hussain, and F. Renzoni. Electromagnetic induction imaging with a radio-frequency atomic magnetometer. *Applied Physics Letters*, 108(10):103503, 2016. doi: 10.1063/1.4943659.
- [141] C. Deans, L. D. Griffin, L. Marmugi, and F. Renzoni. Machine learning based localization and classification with atomic magnetometers. *Physical Review Letters*, 120(3), jan 2018. doi: 10.1103/physrevlett.120.033204.
- [142] S. Y. Hussain. *Application of Quantum Magnetometers to Security and Defence Screening*. phdthesis, University College London, 2018.

- [143] C. Deans. *Electromagnetic Induction Imaging with Atomic Magnetometers*. phdthesis, 2018.
- [144] C. Deans, L. Marmugi, and F. Renzoni. Sub-sm–1 electromagnetic induction imaging with an unshielded atomic magnetometer. *Applied Physics Letters*, 116(13):133501, mar 2020. doi: 10.1063/5.0002146.
- [145] A. Wickenbrock, N. Leefer, J. W. Blanchard, and D. Budker. Eddy current imaging with an atomic radio-frequency magnetometer. *Applied Physics Letters*, 108(18):183507, may 2016. doi: 10.1063/1.4948534.
- [146] G. Chatzidrosos, A. Wickenbrock, L. Bougas, H. Zheng, O. Tretiak, Y. Yang, and D. Budker. Eddy-current imaging with nitrogen-vacancy centers in diamond. *Physical Review Applied*, 11(1), jan 2019. doi: 10.1103/physrevapplied.11.014060.
- [147] M. W. Mitchell and S. P. Alvarez. Colloquium : Quantum limits to the energy resolution of magnetic field sensors. *Reviews of Modern Physics*, 92(2), apr 2020. doi: 10.1103/revmodphys.92.021001.
- [148] Olympus. *Pencil Surface Probes*, 2020. URL <https://www.olympus-ims.com/en/ec-probes/pencil-surface-probes/>.
- [149] Zetec. *SURF-X Flexible Eddy Current Array Probes*, 2020. URL <https://www.bergeng.com/mm5/downloads/zetec/Zetec-Surf-X-Brochure.pdf>.
- [150] D. W. Allan. Statistics of atomic frequency standards. *Proceedings of the IEEE*, 54(2): 221–230, 1966.
- [151] Y. Jin Kim and I. Savukov. Ultra-sensitive magnetic microscopy with an optically pumped magnetometer. *Scientific Reports*, 6(1), apr 2016. doi: 10.1038/srep24773.
- [152] M. G. Richards, B. P. Cowan, M. F. Secca, and K. Machin. The ^3He nuclear Zeeman maser. *Journal of Physics B: Atomic, Molecular and Optical Physics*, 21(4):665, 1988.
- [153] D. Bear, T. E. Chupp, K. Cooper, S. DeDeo, M. Rosenberry, R. E. Stoner, and R. L. Walsworth. Improved frequency stability of the dual-noble-gas maser. *Physical Review A*, 57(6):5006–5008, jun 1998. doi: 10.1103/physreva.57.5006.
- [154] T. W. Kornack, R. K. Ghosh, and M. V. Romalis. Nuclear spin gyroscope based on an atomic comagnetometer. *Physical Review Letters*, 95(23), nov 2005. doi: 10.1103/physrevlett.95.230801.

-
- [155] T. Sato, Y. Ichikawa, S. Kojima, C. Funayama, S. Tanaka, T. Inoue, A. Uchiyama, A. Gladkov, A. Takamine, Y. Sakamoto, Y. Ohtomo, C. Hirao, M. Chikamori, E. Hikota, T. Suzuki, M. Tsuchiya, T. Furukawa, A. Yoshimi, C. P. Bidinosti, T. Ino, H. Ueno, Y. Matsuo, T. Fukuyama, N. Yoshinaga, Y. Sakemi, and K. Asahi. Development of co-located ^{129}Xe and ^{131}Xe nuclear spin masers with external feedback scheme. *Physics Letters A*, 382(8):588–594, feb 2018. doi: 10.1016/j.physleta.2017.12.003.
- [156] Z. Wang, X. Peng, R. Zhang, H. Luo, J. Li, Z. Xiong, S. Wang, and H. Guo. Single-species atomic comagnetometer based on $\text{Rb}87$ atoms. *Physical Review Letters*, 124(19), may 2020. doi: 10.1103/physrevlett.124.193002.
- [157] P. Gomez, F. Martin, C. Mazzinghi, D. Benedicto Orenes, S. Palacios, and M. W. Mitchell. Bose-einstein condensate comagnetometer. *Physical Review Letters*, 124(17), apr 2020. doi: 10.1103/physrevlett.124.170401.

Appendix A

Instrumentation

A.1 Translation Stage

Many results presented in this work are images constructed of the amplitude and phase of individual rf spectra, measured at different positions over the surface of an object. This is achieved by raster scanning the object underneath the magnetometer using an two orthogonally orientated, electronically controlled, belt driven stepper motors (Ooznest NEMA 1705HS200A). This device makes a 0.184mm (1.8°) step when it receives a 1 V pulse. Two stepper motors were combined to create a 2D translation stage. Each motor creates a directional magnetic field when in action, which is detectable by the magnetometer. As a result, the stepper motors are located ~ 1 m away from the sensor and the scanning direction is kept constant during measurements. As a 2D image is created by scanning a line along one axis before taking an incremental step along the other, the stepper motor must return to its origin along the first scanned axis before scanning the next line, doubling the overall measurement time.